Damping of Torsional Beam Vibrations

Hoffmeyer, David

Publication date:
2019

Document Version
Publisher's PDF, also known as Version of record

Citation (APA):
Hoffmeyer, D. (2019). *Damping of Torsional Beam Vibrations*. Technical University of Denmark. DCAMM Special Report No. S263

DTU Mechanical Engineering
Department of Mechanical Engineering

Damping of Torsional Beam Vibrations

David Hoffmeyer

PhD Thesis

Damping of Torsional Beam Vibrations

David Hoffmeyer

Technical University of Denmark
Department of Mechanical Engineering
Section of Solid Mechanics
August 2019

Technical University of Denmark
Department of Mechanical Engineering
Section of Solid Mechanics
Nils Koppels Allé, Building 404
2800 Kongens Lyngby, Denmark
Phone (+45) 4525 4250, Fax (+45) 4525 1961
http://www.mek.dtu.dk/

Publication Reference Data
David Hoffmeyer
Damping of Torsional Beam Vibrations
PhD Thesis
Technical University of Denmark
Department of Mechanical Engineering
August, 2019
ISBN: 978-87-7475-569-2
DCAMM Special Report No. S263
Keywords: Damping, structural dynamics, thin-walled beams, torsion, coupled vibrations, warping, viscous damping, positive position feedback, active control, stability, tuned mass absorber, finite element method

Preface

This thesis is submitted in partial fulfilment of the PhD degree from the Technical University of Denmark. The work has been carried out at the Section of Solid Mechanics, Department of Mechanical Engineering. The work has been performed in the period of September 2016 to August 2019 under the supervision of Associate Professor Jan Høgsberg, and the project has been internally funded.

I owe my deepest gratitude to my supervisor Jan Høgsberg for his guidance and support throughout the project. I am especially thankful for being trained in the art of teaching and for many fruitful discussions.

I would like to thank Professor Paolo Ermanni at the Swiss Federal Institute of Technology (ETH) in Zürich, Switzerland for giving me the opportunity of spending three months at the CMASLab, and thank you to Oleg Testoni for being my daily colleague.

Furthermore I would like to thank my colleagues at the department for their companionship and for creating a nice atmosphere at the office.

Finally I must express a thanks to my close ones and family for enduring me throughout the project. A special thanks to my wife Sarah for her unconditional support and encouragement, and for keeping my spirit high.

Kongens Lyngby, August 2019

David Hoffmeyer

Abstract

This thesis contains an extended summary describing damping of torsional and coupled bending-torsion vibrations in flexible beam structures by supplemental damping devices. Torsion occurs in various large structures and it is shown how to apply both passive and active dissipation mechanisms to control the dynamic response.

The first part of the thesis considers different modelling aspects of torsional beam vibrations. A novel concept is presented where damping is introduced by restraining the out-of-plane axial warping displacements associated with torsion. Modelling such local forces typically requires a three-dimensional description. Solving the corresponding equations in state-space may be computationally very inefficient and emphasis is thus on equivalent yet simpler and computationally efficient models. An analytical procedure is presented together with finite element models consisting of beam elements and 3D isoparametric elements for dynamic analysis.

Damping of pure torsional vibrations by restraining warping with viscous dampers is presented in the second part of the thesis. A 3D FE model is set up with discrete viscous dampers and the results are used to calibrate an analytical model with the discrete dampers modelled by an equivalent viscous bimoment. The partial restraining of warping caused by the local dampers gives rise to a residual flexibility incorporated into the equivalent analytical model. Significant damping ratios are obtained for cross-sections with open contours and the residual flexibility is easily determined based on the 3D model.

The third part considers damping of coupled bending-torsion vibrations by active feedback control. A 3D model with discrete actuators is again used to calibrate a beam element model with positive position feedback control. The apparent negative stiffness component of the applied linear filter increases the damping potential, and when only restraining the warping component of the coupled response, noticeable damping ratios are obtained for the effective beam element model.

The final and fourth part considers multiple tuned mass absorbers targeting the same fully coupled mode. The non-resonant background modes contribute to the support motion of the absorbers, and this effect is represented by two additional terms and calibrated based on information from the complete structure. An approximate balancing procedure furthermore indicates the necessity of inhomogeneous sizing of the absorbers.

Resumé

Denne afhandling indeholder et udvidet resumé, der beskriver dæmpning af vridnings- og koblede bøjning-vridningssvingninger i fleksible bjælkekonstruktioner ved hjælp af supplerende dæmperanordninger. Vridning forekommer i forskellige store konstruktioner, og det vises, hvordan både passive og aktive dissipationsmekanismer kan anvendes til at kontrollere det dynamiske respons.

Den første del af afhandlingen omfatter forskellige modelleringsaspekter af vridningssvingninger. Et nyt koncept præsenteres, hvor dæmpning introduceres ved at fastholde de aksiale hvælvningsflytninger forbundet med vridning. Modellering af sådanne lokale kræfter kræver typisk en tredimensionel beskrivelse. Den tilsvarende løsning ved tilstandvariable kan være beregningsmæssigt meget ineffektiv, og der lægges derfor vægt på ækvivalente, men enklere og beregningseffektive modeller. En analytisk procedure sammen med elementmetodemodeller bestående af bjælkeelementer og isoparametriske 3D-elementer til dynamisk analyse præsenteres.

Dæmpning af rene vridningssvingninger ved fastholdelse af hvælvning med viskose dæmpere præsenteres i anden del af afhandlingen. En 3D FE-model sættes op med diskrete viskose dæmpere, og resultaterne bruges til at kalibrere en analytisk model med de diskrete dæmpere modelleret som et ækvivalent viskost bimoment. Den delvise fastholdelse af hvælvning forårsaget af dæmpernes lokale karakter giver anledning til en residual fleksibilitet, der indarbejdes i den ækvivalente analytiske model. Betydelige dæmpningsforhold opnås for tværsnit med åbne konturer, og den residuale fleksibilitet bestemmes let på baggrund af 3D-modellen.

Den tredje del behandler dæmpning af koblede bøjning-vridningssvingninger ved aktiv feedback-kontrol. En 3D-model med diskrete aktuatorer bruges igen til at kalibrere en bjælkeelementmodel med positiv positionsfeedbackkontrol. Den tilsyneladende negative stivhedskomponent i det anvendte lineære filter øger dæmpningspotentialet, og når kun hvælvningskomponenten i det koblede respons fastholdes, opnås betydelige dæmpningsforhold for den effektive bjælkeelementmodel.

Den sidste og fjerde del omfatter multiple tunede masseabsorbere, rettet mod samme fuldt koblede svingningsform. Bidraget til understøtningsflytningerne af absorberne på grund af de ikke-resonante baggrundssvingningsformer, kalibreres med to tillægskonstanter bestemt på baggrund af information fra den komplette konstruktion. En approksimativ balanceringsprocedure indikerer endvidere nødvendigheden af inhomogen balancering af absorberne.

Publications

Journal papers

[P1] Hoffmeyer, D. and Høgsberg, J., Damping of Torsional Vibrations in Thin-Walled Beams by Viscous Bimoments, *Mechanics of Advanced Materials and Structures*, published online: February 1, 2019.

[P2] Hoffmeyer, D. and Høgsberg, J., Damping of Coupled Bending-Torsion Beam Vibrations by Spatially Filtered Warping Position Feedback, 2019, (submitted).

[P3] Hoffmeyer, D. and Høgsberg, J., Calibration and Balancing of Multiple Tuned Mass Absorbers for Damping of Coupled Bending-Torsion Beam Vibrations, 2019, (submitted).

Conference papers

[C1] Hoffmeyer, D. and Høgsberg, J., Numerical Investigation of Damping of Torsional Beam Vibrations by Viscous Bimoments, *VIII ECCOMAS Thematic Conference on Smart Structures and Materials*, June 5-8, 2017.

[C2] Hoffmeyer, D. and Høgsberg, J., Active Warping Control for Damping of Torsional Beam Vibrations, *IX ECCOMAS Thematic Conference on Smart Structures and Materials*, July 8-11, 2019.

Contents

1 | Introduction

Methods for alleviating structural vibrations have been a vivid area of research for the past many decades [46]. Vibrations in structures induced by wind, rain, earthquake, humans, traffic etc. are generally inexpedient and associated with a number of disadvantages. For structures intended for human interaction too large accelerations may cause discomfort and vibrations should therefore be limited to low frequencies. Vibrations may additionally lead to fatigue damage [34] which for larger structures may cause collapse or reduced structural life-time. Slender beam structures like bridge girders [1, 3, 57] as in Fig. 1.1, wind turbine blades [11, 56] as in Fig. 1.2 and airplane wings may furthermore be prone to aeroelastic instabilities like flutter [25, 18] where apparent negative damping is induced. Hereby an otherwise small structural motion may develop over time to vibrations with excessive amplitudes. For bridge girders and wind turbine blades tuned mass dampers [4, 44] and viscous-type dampers [22, 11] have been used to damp vibrations.
When the inherent material damping does not suffice, the use of supplemental dampers is a widely recognized way to effectively reduce the dynamic response of a flexible structure. There is a large variety of damping devices with different characteristics [49]. They can be categorised in several groups where two of them encompass passive and active devices. Passive systems may enhance energy dissipation without any power source and operate on principles such as sliding or friction [42]. A well-known passive damping mechanism is the viscous damper which is proportional to the instantaneous velocity [31]. Viscous damper models may lead to theoretically

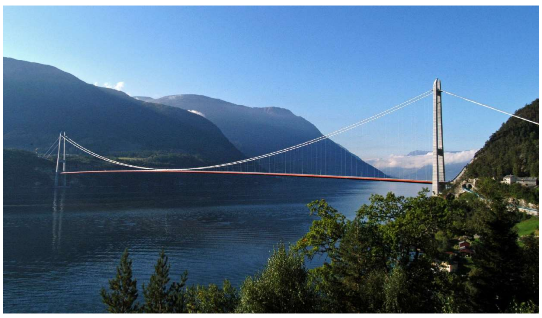


Figure 1.1. Left: Hardanger Bridge, Norway.[1] Right: London Millennium Bridge, UK.[2]

[1]Source: https://en.hardangerfjord.com/eidfjord/things-to-do/hardanger-bridge-p1680333.
[2]Source: https://www.triphobo.com/places/london-united-kingdom/millennium-bridge.

Figure 1.2. Wind turbine rotor.[3]

neat results and therefore comprise practical rules of thumb, e.g. as for the case of a discrete viscous damper on a cable [35]. Viscous dampers, however, represent to a great extent a mathematical convenience rather than a physical damping mechanism, and thus often serve to illustrate the mechanisms behind damping and the associated potential to alleviate vibration amplitudes. Pure viscous damping may however be realized actively by direct velocity feedback [5], which requires an active control strategy.

Active control devices, on the other hand, are force delivering systems typically applied with real-time processing of sensor data [50]. They usually require a power source and must therefore also undergo maintenance and be constructed in a robust manner in the case of a power outage. The advantage of active control is an increased effect and greatly enhanced damping. But when addressing civil engineering structures there are uncertainties due to deviations in geometry, wear of devices and structure etc., all to be captured by a limited number of sensors [26]. The tuning and calibration of such a device is therefore important in order for it to be fail-safe.

Common for the slender beam structures in Figs. 1.1 and 1.2 is that they partly vibrate in torsion [47]. This motion is typically induced either because the load acts with an eccentricity to the shear centre or if the cross-section lacks double symmetry whereby torsion couples with bending [21]. For thin-walled beam cross-sections axial and out-of-plane warping due to inhomogeneous torsion is an intrinsic part of the static and dynamic response [53]. For cross-sections with an open contour these displacements are non-vanishing at the boundary.

The increase in frequency due to restraining warping at a beam boundary is often significant [6]. Introducing a dissipative mechanism proportional to the warping at the end of a beam is therefore an effective means of alleviating torsional vibrations. This is used in [28] to introduce substantial modal damping for pure torsional vibrations for beams with open cross-sections. The governing differential equation is solved and a viscous boundary condition derived and applied directly to the pure bimoments [53] at the beam support. In practice, however, restraining the warping of the entire cross-section of a beam is not feasible and an alternative is to apply a number of discrete devices placed in configurations constituting pure bimoments, in

[3]Source: https://www.bioinformatics.dtu.dk/news/nyhedid=1BAFD1FA-4578-4AB9-B212-D01A5E204260&utm_device=web&utm_source=RelatedNews&utm_campaign=More-than-DKK-100-million-for-independent-research.

order not to induce any resulting normal forces or bending moments.
A special feature of applying such device configurations on a beam cross-section is that warping is only restrained at the point of application of the specific device. The remaining of the cross-section is thereby able to warp in between and this lowers the frequency compared to full restrainment of the entire cross-section warping. This partial warping restrainment is thus associated with an excess flexibility and must be included in the model in order to be able to tune and calibrate the device properly. This effect corresponds to a beam with an elastic boundary condition [2, 51].

Outline of the thesis

The work presented in this thesis considers the damping of torsional and coupled bending-torsion vibrations in thin-walled beam structures. The emphasis is partly on utilising the increase in stiffness and thereby frequency associated with restraining the axial warping displacements from torsion occurring at the beam boundary, and partly on balancing multiple damper devices working together, e.g. in the case of several tuned mass absorbers.

Restraining warping by discrete devices gives rise to very local effects and the increase in stiffness is very much dependent on the positions of the devices on the cross-section. It is therefore necessary to establish a detailed three-dimensional (3D) finite element (FE) model which accurately captures the local effects when partially restraining warping. Such a model is a powerful tool to analyse the dynamic behaviour of a beam structure including effects that simpler models are not able to capture. When performing a damping analysis of a structure the system equations will typically be formulated in state-space, which doubles the number of variables. A numerical 3D model of a simple beam may easily contain several thousand degrees-of-freedom and solving the corresponding eigenvalue problem is not without considerable computational cost when using a high-level programming language. Retrieving the complex frequencies and mode shapes may therefore be intractable. Because of that, calibrating simpler models such as analytical models or beam element models to match the complex behaviour of a full 3D model is emphasized in this work. When realizing that the residual flexibility from the partial warping restrainment directly constitutes a decrease in frequency, simpler models may be calibrated based on this reduction in stiffness. Thereby they represent computationally more efficient models that may be used in initial design situations where several geometric designs and damper placements are investigated. The following two main objectives are therefore defined:

- Investigate the potential of damping torsional beam vibrations by restraining warping.
- Establish computationally efficient and simple models as alternatives to full 3D FE models.

The damping potential in the case of pure torsional vibrations is investigated by viscous dampers. This passive mechanism is sufficient to introduce significant modal

damping ratios, even when warping is just partially restrained. The associated residual warping is modelled as a fictitious spring in series with the damper device. In the case of coupled vibrations, torsion only constitutes a part of the coupled response, and restraining warping alone therefore has a reduced effect. In order to accommodate this reduction, an active concept is applied in the form of positive position feedback (PPF) control [23, 40, 45]. Warping displacements are typically small, and as the PPF control increases the actuator deflection locally it is advantageous for small deformation problems like warping control.
The analytical equations for pure torsional vibrations are easily obtained and solved iteratively. Combined with a viscous boundary condition taking the actual damper configuration into account as an equivalent viscous bimoment, the analytical solutions serve as a computationally efficient method of analysis. In the case of coupled vibrations the analytical solutions become unmanageable and a simple beam element model with PPF feedback control is set up for efficient analysis. In both cases these models are calibrated with respect to a full 3D FE model with isoparametric elements [13] and compared with the results from the 3D model.

A second part of the thesis presents initial investigations of the use of multiple tuned mass absorbers for damping coupled beam vibrations. Multiple devices associated with both translation and rotation tuned to the same mode require inhomogeneous balancing to achieve the desired damping behaviour. An approximate balancing procedure is applied, and the contribution from the non-resonant background modes is included by calibrating an additional flexibility and inertia term.

Structure of the thesis

The thesis consists of an extended summary covering the objectives described above. It is based on two journal papers [P1] and [P2], a technical brief [P3] and two conference proceedings [C1] and [C2], and thus summarises the main methods and results presented in the papers. Chapter 1 gives an introduction to the different methods used for analysing torsional and coupled vibrations, namely an analytical method, a beam element model and a full 3D FE model with isoparametric elements. Chapter 2 covers the main content of [C1] and [P1] with excerpts from [P2], and describes damping of pure torsional vibrations by viscous dampers, both in configurations of the actual spatial distributions on the cross-section for the 3D FE model, as well as an equivalent viscous bimoment for the analytical model. Chapter 3 expands to coupled bending-torsion vibrations, as described in [C2] and [P2], with active control introduced as a PPF filter on a beam element model. In both Chapter 2 and 3 the simpler models are calibrated with respect to a full 3D model and the results of the two models are compared. Chapter 4 presents initial investigations of multiple tuned mass absorbers calibrated and balanced to the same mode, and is covered in [P3]. Finally Chapter 5 gives concluding remarks about the main results and provides suggestions for possible future extensions of the work.

2 Torsional and Coupled Beam Vibrations

The basic dynamic characteristics of beam structures vibrating in either pure torsion or coupled bending and torsion are conveniently described by the governing differential equations. Modelling of thin-walled beams by the use of beam theory with the corresponding cross-sectional parameters assumes the beam to be sufficiently slender, in order for the beam theory to accurately represent the actual behaviour. For pure torsional vibrations the governing differential equation can effectively be solved analytically [20]. This yields an expression for the spatial behaviour with four integration constants to be determined based on the boundary conditions. The corresponding transcendental equation is then solved iteratively as studied in [P1]. For coupled vibrations three coupled differential equations govern the dynamics through the distance between the elastic and shear centre. Analytical solutions to these equations are typically not manageable and the beam structure may therefore conveniently be discretized with beam elements for a numerical solution, as emphasized in [P2] and [P3].

For more detailed analyses where cross-sectional effects like restrained axial warping and in-plane distortion become important, three-dimensional finite element analyses with isoparametric elements may be used. To capture the warping across the flange thickness linear interpolation is sufficient, and for ideal boundary conditions four nodes along a flange part is sufficient, [P1].

For all analyses in the following chapters some form of solution to the governing beam equations or equivalent solid description is used. Therefore an outline of the applied ways to analyse beam vibrations including torsion is given in the following.

2.1 Pure torsional vibrations

For beams with double symmetric cross-sections pure torsional vibrations may occur for prismatic beams when the elastic centre and shear centre coincide. For thin-walled cross-sections axial warping is an intrinsic and important part of the torsional motion. Excluding the warping in beams with open cross-sections is associated with a significant modelling error [6].

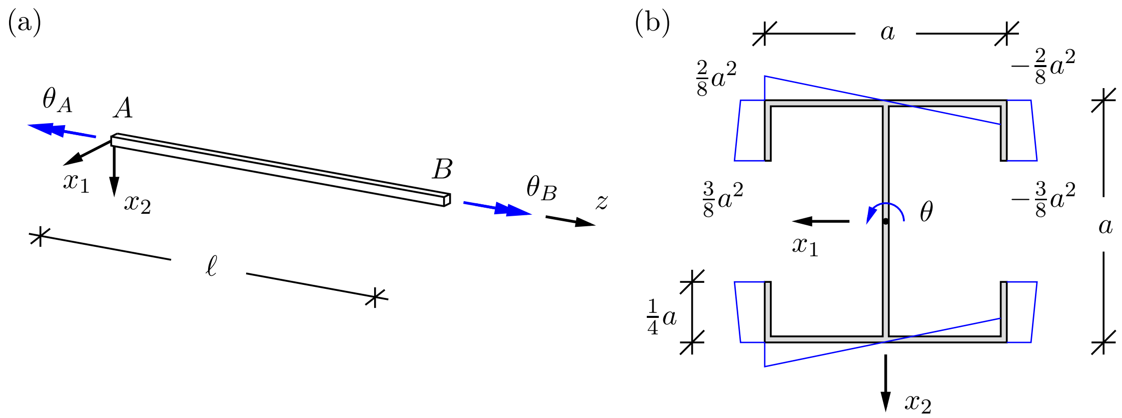

Figure 2.1. (a) Beam with length ℓ, transverse coordinate axes $\{x_1, x_2\}$ and angle of twist θ. (b) Modified I-profile cross-section with sector-coordinate ψ and indicated shear centre at $(x_1, x_2) = (0, 0)$.

Assume a beam with length ℓ, transverse axes $\{x_1\,,\,x_2\}$ and longitudinal axis z as shown in Fig. 2.1a. The governing differential equation for pure torsional motion with the angle of twist $\theta(t)$ is

$$EI_\psi\theta''''(t) - GK\theta''(t) + \rho J\ddot{\theta}(t) = 0 \tag{2.1}$$

where E is Young's modulus, I_ψ is the warping moment of inertia, G is the shear modulus, K is the torsion stiffness parameter, ρ is the material density and J is the polar moment of inertia. The spatial dependence (z) will in general be omitted, while $(\,)' = \partial(\,)/\partial z$ denotes differentiation with respect to z and $\dot{(\,)} = \partial(\,)/\partial t$ represents differentiation with respect to time t. The torsional stiffness GK accounts for homogeneous torsion, while EI_ψ represents the warping stiffness from inhomogeneous torsion. The cross-sectional warping is associated with the sector-coordinate ψ and defined in the case of free homogeneous torsion. For the modified I-profile cross-section in Fig. 2.1b the sector-coordinate ψ is indicated.
The spatial solution to (2.1) is obtained by assuming a time harmonic solution of the form

$$\theta(t) = \varphi e^{i\omega t} \tag{2.2}$$

with ω being the angular frequency and φ representing the amplitude along the beam. The spatial solution may be written as

$$\varphi = D_1\cosh(\alpha z) + D_2\sinh(\alpha z) + D_3\cos(\beta z) + D_4\sin(\beta z) \tag{2.3}$$

where the integration constants D_1 to D_4 are determined based on the boundary conditions. The two apparent wave numbers are given as

$$\alpha^2 = \sqrt{\tfrac{1}{4}k^4 + \lambda^4} + \tfrac{1}{2}k^2 \quad , \quad \beta^2 = \sqrt{\tfrac{1}{4}k^4 + \lambda^4} - \tfrac{1}{2}k^2 \tag{2.4}$$

defining the warping length scale k, wave speed v and normalized wave number λ as

$$k^2 = \frac{GK}{EI_\psi} \quad , \quad v^2 = \frac{GK}{\rho J} \quad , \quad \lambda^4 = \left(\frac{k\omega}{v}\right)^2 \tag{2.5}$$

The dynamics of the torsional vibrations are governed by the parameter $k\ell$, according to the specific boundary conditions. Ideal and standard boundary conditions consist of a free end, a fully fixed end, a 'simple' end where rotation is restrained but warping is free and a 'no warp' end where warping is restrained but with rotation allowed. A comprehensive yet not exhaustive list of transcendental equations is given in Appendix B. These equations are solved iteratively for the frequencies ω_j and subsequently the spatial vibration forms φ_j.

2.2 Coupled bending-torsion vibrations

In many applications of beam structures, torsional vibrations are an inherent part of a response coupled with bending. This is usually due to non-coinciding elastic centre and shear centre when the cross-section lacks symmetry [21]. A single line of symmetry couples torsion with bending in one direction, leaving the motion in the remaining transverse direction uncoupled, while full asymmetry couples the transverse motion in both principal directions with torsion. Inhomogeneous material distribution as in the case of some aircraft wings and varying cross-section and pretwist as in the case of wind turbine blades also leads to coupling between torsion and bending [24, 54]. The different displacement components may be more or less pronounced but still require the solution of three coupled differential equations.
A generally asymmetric cross-section is seen in Fig. 2.2a with ξ_1 and ξ_2 denoting the transverse displacements in the x_1- and x_2-direction, respectively, while the shear centre A defines the origin of the coordinate system and $C = (c_1\,,\, c_2)$ represents the elastic centre. When applying summation over repeated Greek index, the coupled differential equations can be written as

$$\begin{aligned} EI_{\gamma\mu}\xi_\mu'''' + \rho A\ddot{\xi}_\gamma - \rho A c_\mu \ddot{\theta} = 0 \quad , \quad \gamma, \mu = 1, 2 \\ EI_\psi \theta'''' - GK\theta'' + \rho A c_1 \ddot{\xi}_2 - \rho A c_2 \ddot{\xi}_1 + \rho J \ddot{\theta} = 0 \end{aligned} \tag{2.6}$$

where $I_{\gamma\mu}$ are the moments of inertia, A is here the cross-sectional areal, c_μ are the distances between the elastic centre and shear centre and $J = I_{11} + I_{22} + (c_1^2 + c_2^2)A$ now denotes the polar moment of inertia with respect to the shear centre.

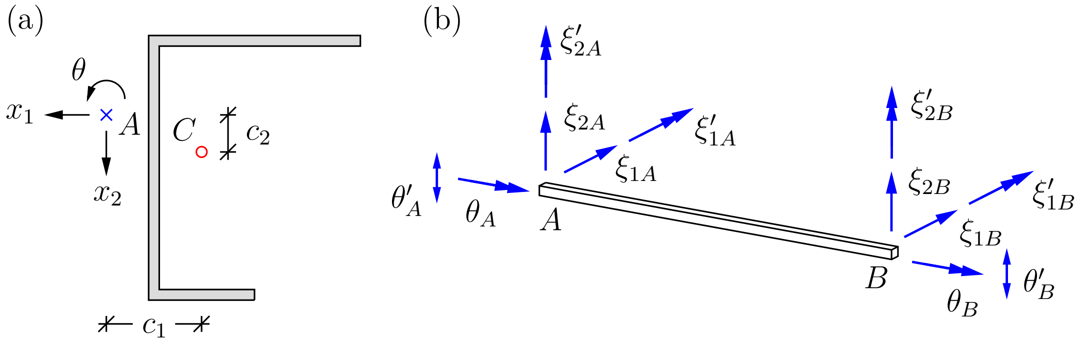

Figure 2.2. (a) Asymmetric cross-section with elastic centre C and shear centre A and (b) beam element degrees-of-freedom.

Analytical solutions to (2.6) are non-trivial to obtain and may not be feasible to handle. Approximate methods may be used [21] but usually require specification of some expansion functions, where the accuracy of the solution depends on the ability of the expansion functions to represent the actual vibration forms. A convenient method of solving the governing equations in (2.1) and (2.6) is the finite element method. This approach may provide frequencies and mode shapes for various boundary conditions, representing the exact results to the differential equations with high accuracy for a sufficiently dense discretization. Two typical types of elements will be illustrated in the next section.

2.3 Beam vibrations by finite elements

Approximate yet very accurate solutions to the governing differential equations in (2.1) and (2.6) for slender beams may be obtained by finite elements using simple beam elements as convenient alternative to analytical solutions, see. e.g. [17, 43, 52]. Even though explicit and often simple transcendental equations may be found for (2.1) describing pure torsional vibrations, each transcendental equation depends on the particular boundary conditions. Modelling pure torsional vibrations with beam elements may be practical as boundary conditions can be changed.
For a more detailed description of the dynamic behaviour of beams a model with three-dimensional, isoparametric elements can be used. A suitable three-dimensional discretization allows for analyses of actual structures, where in-plane distortion may have a significant influence for shorter beams. The cost, however, is a substantial increase in system size, typically with many thousand degrees-of-freedom. Solving the corresponding eigenvalue problem to obtain the dynamic characteristics is therefore not without considerable effort - especially when including damping terms in the equation of motion. Using simple beam elements for preliminary analyses therefore constitutes a good alternative.

2.3.1 Simple beam elements

Discretization of a beam structure with beam elements is advantageous in situations where three-dimensional effects like distortion of the cross-section and local restraining of axial warping is without importance and the boundary conditions are ideal. For pure torsional vibrations a two-dimensional beam element may suffice if the beam structure is straight and thus without corners [C2]. But in the general case a three-dimensional beam element must be used to capture the relation between torsion and bending in corners and junctions of a frame structure.
Without the axial degree-of-freedom the general beam element has six degrees-of-freedom per node as shown in Fig. 2.2b, including the warping intensity θ' indicated by the vertical double arrow. With $s = z/\ell$ being a normalized coordinate, interpolation between the nodes is performed by the cubic Hermitian shape functions,

$$\mathbf{N} = \left[2s^3 - 3s^2 + 1 \ , \ s(s-1)^2 \ , \ -2s^3 + 3s^2 \ , \ s^2(s-1) \right] \tag{2.7}$$

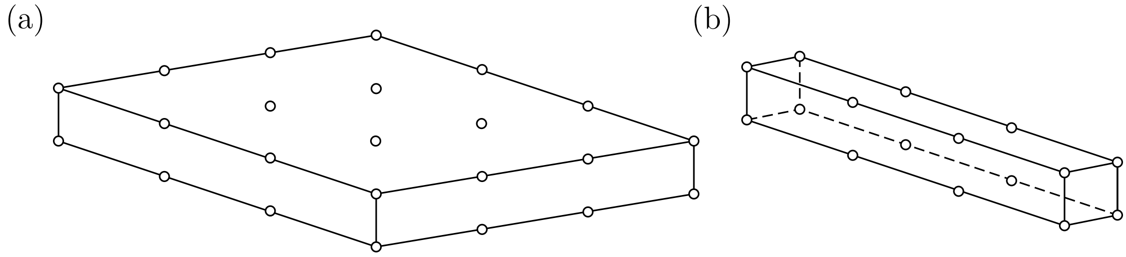

Figure 2.3. Three-dimensional isoparametric elements. (a) Bi-cubic-linear and (b) cubic-bi-linear.

as the differential equations are of quartic order. As the beam structure is represented by the displacement components at the nodes, the size of the global system is usually very small and the eigenvalue problems are easily solved with standard solvers. For straight and prismatic beams explicit mass and stiffness matrices can be derived [C2, P2], making the need for numerical integration obsolete.
The warping of the beam cross-section is represented by its warping intensity θ' retrieved directly from the beam element model. The corresponding axial warping displacements are defined through the relation

$$u = -\psi\theta' \tag{2.8}$$

where the sector-coordinate ψ is a function of the geometry of the cross-section and may be found by analytical [53] or numerical [30] means.

2.3.2 Three-dimensional elements

For more detailed analyses three-dimensional isoparametric elements may be used as they can capture the warping across the flange thickness [13]. Possible elements are shown in Fig. 2.3 and consist of a bi-cubic-linear element for flange parts and a cubic-bi-linear element for corners and junctions. A single bi-cubic-linear element per flange part in the cross-sectional plane is in many cases sufficient to get reasonably accurate results [P1], and two may be used for increased accuracy. However, a single element is recommended for preliminary analyses. These elements are sufficient to capture the quadratic shear stress distribution in static analyses, and they capture the dynamic characteristics of undamped beams with ideal boundary conditions very well. The internal nodes in the bi-cubic-linear element are recommended to get a regular convergence behaviour and as described in [P1] care must be taken when discretizing a structure with local actuator forces or point-wise supports.

2.3.3 Equations of motion

Regardless of the elements chosen for discretization the dynamic properties are governed by the global mass matrix $\mathbf{M}$ and global stiffness matrix $\mathbf{K}$. The n degrees-of-freedom are collected in the displacement vector $\mathbf{q}(t)$ and the equation of motion for free and undamped vibrations is then given as

$$\mathbf{M}\ddot{\mathbf{q}}(t) + \mathbf{K}\mathbf{q}(t) = \mathbf{0} \tag{2.9}$$

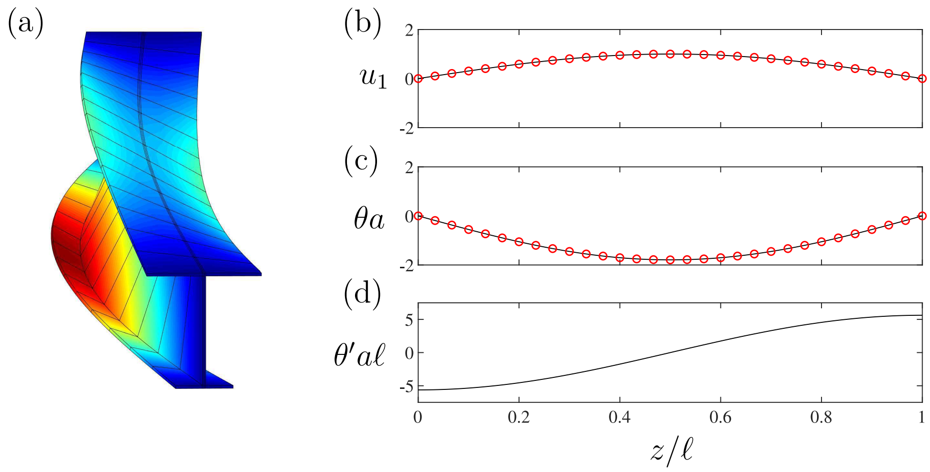

Figure 2.4. (a) Patch plot of the first vibration mode and (b-d) displacement components of the beam element model with a being the height of the cross-section.

The modal properties are obtained by assuming a harmonic frequency solution of the form $\mathbf{q}(t) = \tilde{\mathbf{q}}e^{i\omega t}$, where the tilde will indicate the vibration amplitude if not mentioned otherwise. This leads to the eigenvalue problem

$$\Big(-\omega_{0,j}^2 \mathbf{M} + \mathbf{K} \Big) \tilde{\mathbf{q}}_{0,j} = \mathbf{0} \tag{2.10}$$

The solutions to the above generalised eigenvalue problem consist of the undamped frequencies $\omega_{0,j}$ and the corresponding undamped mode shape vectors $\tilde{\mathbf{q}}_{0,j}$.
For a beam simply supported in both bending and torsion (see Section 2.1) and with an I-profile cross-section with a vertical line of symmetry, the lowest vibration mode is seen in Fig. 2.4. The patch plot is from a full 3D model where the colors indicate the absolute displacements, and the coupling between bending in the horizontal direction and torsion is clearly observed. From an equivalent model with beam elements the relevant normalized displacement components are seen to the right in Fig. 2.4, where also the warping displacements at the beam extremities are seen to be non-vanishing due to the non-zero rate of twist in Fig. 2.4d. The red markers in Fig. 2.4b,c are values from the 3D model averaged over the cross-section, indicating good agreement between the two models.

These models constitute the backbone of the analyses performed in the various parts of the thesis. A full 3D model with the presence of damping terms is inefficient to solve. Therefore particular emphasis is given towards a comparison between a 3D FE model and the analytical solutions to (2.1) in the case of pure torsional vibrations or a model with beam elements for coupled bending-torsion vibrations. Special effects like partial restraining of warping [P1, P2] and active measures of damping [P2] can be implemented as special boundary conditions or can supplement the equations of motion in state-space. In this way very detailed analyses can be carried out without the use of a 3D model as demonstrated in the following chapters.

3 | Passive Damping by Viscous Bimoments

Axial warping is an intrinsic part of torsional vibrations of thin-walled beams, and efficient damping of a particular vibration mode can be achieved by restraining the warping displacements at the end cross-section of a beam structure. The warping displacements in (2.8) are given as the sector-coordinate ψ times the rate of twist θ', representing the warping intensity along the beam. The sector-coordinate describes the cross-sectional distribution of the axial displacements, as shown in Fig. 2.1b. Preventing axial warping increases the stiffness of the beam and leads to large shifts in the natural frequency. As the attainable damping by viscous dampers is proportional to the relative increase in frequency, substantial amounts of damping can be obtained by restraining the warping of the entire cross-section by a pure viscous boundary condition, as demonstrated in [28].
In practice it will typically not be possible to construct a damping mechanism able to restrain the warping of the entire cross-section. A realistic alternative is to apply a set of discrete devices placed in a specific configuration on the cross-section, as shown in Fig. 3.1a. With discrete devices applied, the remaining part of the cross-section is still able to warp in between the dampers. The effect of using discrete devices to restrain the warping is thus reduced, compared to restraining the warping of the entire cross-section. However, the configuration in Fig. 3.1a is still effective and introduces substantial damping, as investigated in [C1] and [P1]. This partial warping restraint [12] is associated with a residual flexibility, which in the following is taken into account.

The analysis of a beam with discrete damping devices on the cross-section, as shown in Fig. 3.1a, requires a detailed discretization of the structure in order to capture the influence from the local dampers. The number of degrees-of-freedom for a complete beam structure therefore rapidly increases to an unmanageable size. Alternatively the solution to the governing differential equation in (2.1) may be used, with the specific distribution of the discrete viscous dampers accounted for by an equivalent bimoment B_d, as shown in Fig. 3.1b. The corresponding transcendental equation is effectively solved iteratively and requires limited computational effort. It is therefore an appealing alternative to solving the equations in state-space for the full three-dimensional structure.
This chapter focusses on pure torsional vibrations, and investigates the accuracy of

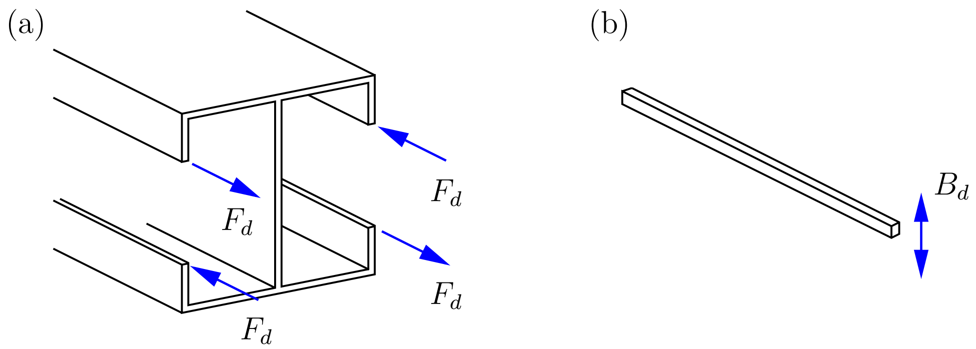

Figure 3.1. (a) Cross-section with discrete damper forces and (b) beam element model with equivalent damper bimoment.

the governing differential equation when a boundary condition for dissipating energy is used for obtaining the transcendental equation. This condition is formulated as an effective bimoment, taking all the discrete viscous dampers in Fig. 3.1a into account, and thus comprising their actual positions on the full 3D structure. The results from solving the transcendental equation are compared with the full 3D model with isoparametric elements, as described in Section 2.3.2, and the chapter thus presents the main features of [P1].

3.1 Discrete viscous dampers

The applied discrete viscous dampers in Fig. 3.1a provide a configuration of axial forces on the beam cross-section. A given set of axial viscous forces may result in both a normal force and bending moments. If these resulting section forces are not vanishing, the viscous forces will introduce extension and bending.
For a set of discrete axial forces, the resulting normal forces is given by the sum

$$N_d(t) = \sum_k F_{d,k}(t) \tag{3.1}$$

where $F_{d,k}$ is the k'th viscous damper force. Similarly, the bending moments $M_{d,\gamma}$ are determined by their distance to the elastic centre as

$$M_{d,\gamma}(t) = \sum_k F_{d,k}(t)(x_{\gamma,k} - c_\gamma) \qquad , \qquad \gamma = 1,2 \tag{3.2}$$

In the present context only pure torsional vibrations are considered, without coupling to extension or bending. Thus, a resulting normal force or bending moments should not be introduced. For the symmetric cross-section in Fig. 3.1a with the corresponding symmetric configuration of the damper forces, the summations in (3.1) and (3.2) yield both vanishing normal force and bending moments.
However, the force configuration in Fig. 3.1a still counteracts twist of the beam through the axial warping deformation. As shown in [P1] this twist is introduced by the bimoment

$$B_d(t) = \sum_k \psi_k F_{d,k}(t) \tag{3.3}$$

From (3.3) it is thus evident, that even a single viscous force $F_{d,k}$ will generate a bimoment, while all four forces are needed to retain the double symmetry to avoid elongation and bending. Force configurations generating a pure bimoment, for which the sums in (3.1) and (3.2) are zero, therefore result in pure torsional vibrations.

3.1.1 Boundary condition

The integration constants in the spatial solution in (2.3) are determined based on the boundary conditions for the particular beam configuration. The applied bimoment B_d in Fig. 3.1b represents the set of discrete, axial dampers in Fig. 3.1a and is in the following introduced as a viscous boundary condition for the partial differential equation in (2.1).
The discrete viscous force $F_{d,k}(t)$ is proportional to a viscous gain or damping coefficient c_0, as expressed by the relation

$$F_{d,k}(t) = \pm\, \alpha_k c_0 \dot{u}_{d,k}(t) \tag{3.4}$$

where $\dot{u}_{d,k}$ is the axial velocity at the location of the k'th damper force, while the particular sign in (3.4) changes between the beam ends in either $z = 0$ or $z = \ell$. When multiple dampers are present as in the case of Fig. 3.1a the factors α_k in (3.4) are introduced to enable individual balancing of the k'th damper force, as described in Section 3.3.2. The damper gain is therefore given as $c_k = \alpha_k c_0$ with c_0 being a common damper gain for all discrete dampers.
According to (3.3) the viscous force in (3.4) will generate a bimoment. When equating the rate of work produced by the discrete viscous forces in (3.4) with the rate of work produced by the equivalent bimoment B_d in (3.3), the bimoment caused by the discrete dampers is given as

$$B_d(t) = \mp\, \dot{\theta}'_d(t) \sum_k \alpha_k c_0 \psi_k^2 \tag{3.5}$$

The resulting boundary condition is used with the spatial solution in (2.3), and therefore the time harmonic representation in (2.2) is introduced. For the beam the external bimoment (3.5) is counteracted by the internal section bimoment, and as demonstrated in [P1] the boundary condition then appears as

$$\varphi''_d \mp i\omega\eta\varphi'_d = 0 \tag{3.6}$$

in which the effective damping parameter

$$\eta = \sum_k \alpha_k c_0 \frac{\psi_k^2}{EI_\psi} \tag{3.7}$$

combines the individual damper forces in Fig. 3.1a according to their sector-coordinate ψ_k, whereby η represents the viscous coefficient for the resulting bimoment B_d in Fig. 3.1b. By using the boundary condition in (3.6), the transcendental equations in Appendix B are obtained and solved iteratively for the wave numbers in (2.4) or the corresponding angular frequency ω.

3.1.2 FE model with discrete dampers

The transcendental equations are effectively solved with limited computational effort, in which the actual discrete dampers are taken into account by the effective damping parameter η in (3.7), while neglecting the local effect of these forces on the cross-section. These effects could result in in-plane distortion [7, 33] of the cross-section in the case of short beams, or partial restraining of the warping caused by the local dampers. To investigate the influence of these effects, a full 3D finite element model with isoparametric elements is established. The results from solving the differential equation may then be effectively compared with and assessed by the 3D FE results.

The basis of the 3D FE analyses is the discretized system in (2.9). The damper forces $F_{d,k}$ are introduced and the equation of motion for the full 3D system with external damper forces is then given as

$$\mathbf{M}\ddot{\mathbf{q}}(t) + \mathbf{K}\mathbf{q}(t) = -\sum_k \mathbf{w}_k F_{d,k}(t) \tag{3.8}$$

where the individual damper forces are added to the nodal points of the discretized structure by the connectivity vector $\mathbf{w}_k$, containing all zero entries except for a unit value at the single degree-of-freedom associated with the location of the specific damper.

By use of (3.4) the dissipative term on the right-hand side of (3.8) may be expressed by an effective damping matrix

$$\mathbf{C}_d = \sum_k \alpha_k c_0 \mathbf{w}_k \mathbf{w}_k^T \tag{3.9}$$

The damping matrix $\mathbf{C}_d$ will be non-proportional and contain the balancing factors α_k in the diagonal, corresponding to the degree-of-freedom associated with damper force $F_{d,k}$ and with c_0 as a common factor. The equation of motion (3.8) with the added local dampers in (3.9) is then given by the classic form

$$\mathbf{M}\ddot{\mathbf{q}}(t) + \mathbf{C}_d\dot{\mathbf{q}}(t) + \mathbf{K}\mathbf{q}(t) = \mathbf{0} \tag{3.10}$$

which constitutes a quadratic eigenvalue problem that is solved in state-space form for the modal natural frequencies ω_j, as described in [P1].

For finite values of the viscous gain c_0 the solutions to (3.10) will be complex-valued with the imaginary part of the damped frequency ω_j representing the damping associated with the j'th vibration mode, conveniently expressed by the damping ratio as

$$\zeta_j = \frac{\mathrm{Im}[\omega_j]}{|\omega_j|} \tag{3.11}$$

For vanishing gain $c_0 = 0$ the dampers will have no effect and the modal frequencies ω_j will recover the undamped (real-valued) frequencies $\omega_{0,j}$. For the viscous boundary condition in (3.6) this undamped limit corresponds to $\eta = 0$, resulting in real-valued frequencies and mode shapes. Oppositely when the gain becomes

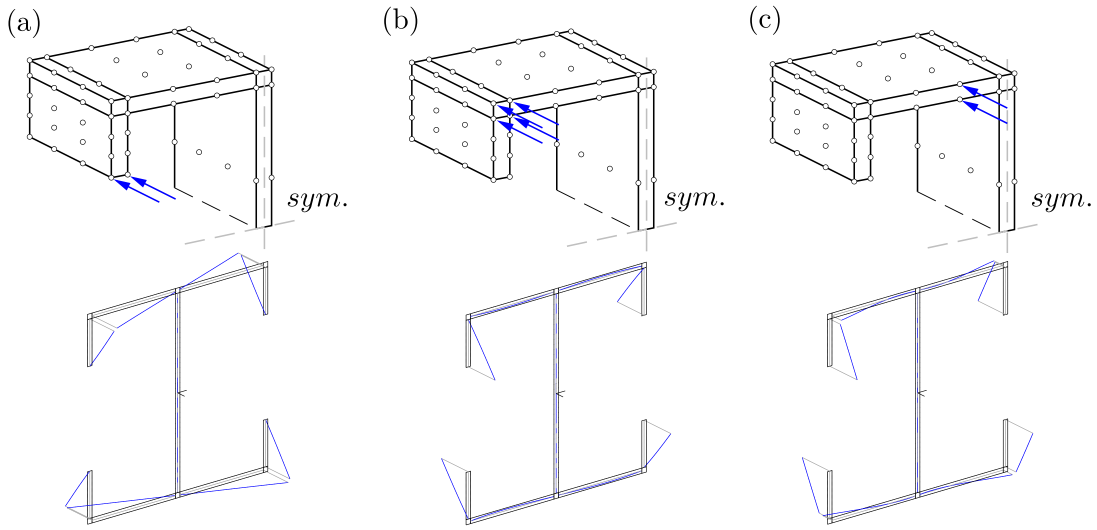

Figure 3.2. Section of the modified I-profile with three different configurations of dampers, and the associated warping displacements (artificially amplified).

infinitely large ($c_0 \to \infty$) the dampers lock and fully restrain the associated degrees-of-freedom connected to the dampers. In this case the frequencies will be referred to as the infinitely damped frequencies $\omega_{\infty,j}$, corresponding to $\eta \to \infty$ for the viscous boundary condition in (3.6).
Due to the very local placement of the discrete damper forces, care must be taken when discretizing the 3D domain. In [P1] an investigation of the applicability of the elements in Fig. 2.3 is performed, concluding that a fine discretization of the beam end in the longitudinal beam direction leads to converging results. With a too coarse discretization near the cross-section where the local forces are attached, significant deviations are expected. Furthermore, the internal nodes of the bi-cubic-linear Lagrange element in Fig. 2.3a ensure a consistent convergence behaviour.

3.2 Restraining warping

The ability of the set of axial dampers in Fig. 3.1a to fully restrain warping at the beam end is an important measure of the damping efficiency. The top row of Fig. 3.2 shows a quarter model of the double-symmetric cross-section in Fig. 2.1b, with three different damper configurations (a-c). The best damper performance is obtained when the warping deformation can be restrained over the entire cross-section. However, for $c_0 \to \infty$ the discrete dampers in Fig. 3.2 will only fully restrain the axial motion exactly at the degrees-of-freedom where the dampers are attached. This leaves a non-vanishing warping function, as the remaining part of the cross-section is still able to warp in between the damper locations, as illustrated in the bottom row of Fig. 3.2.
The analytical beam solution represented by the boundary condition in (3.6) is associated with a vanishing warping intensity $\theta' = 0$ in the limit of infinite gain $c_0 \to \infty$. Thus, in the analytical model, $\eta \to \infty$ completely prevents warping of the entire

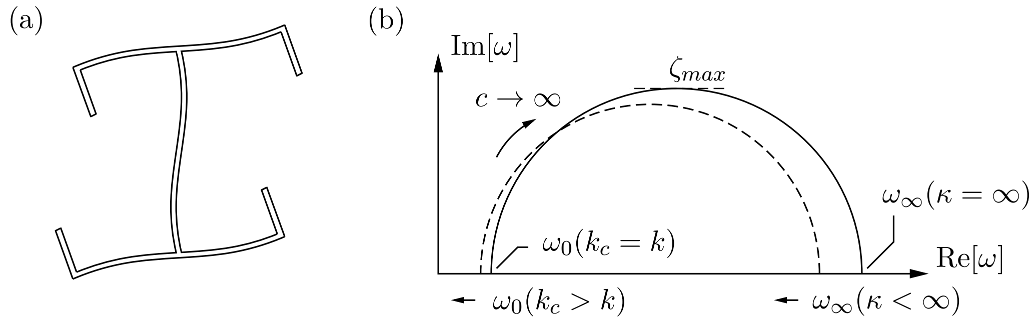

Figure 3.3. (a) In-plane distortion of the modified I-profile when vibrating in pure torsion and (b) frequency locus in the complex plane and effect of parameters κ and k_c.

cross-section, while in reality and in the 3D FE model residual warping appears because of the local restraining by the dampers, shown in the bottom row of Fig. 3.2. In order for the analytical model to accurately represent this local damper effect, an excess flexibility is therefore included in the mathematical model in Section 3.3.1 and [P1,P2].

For external dampers the tuning and placing is an important aspect of the design. The dampers will yield maximum modal damping when maximizing the separation of ω_0 for $c_0 = 0$ and ω_∞ for $c_0 \to \infty$. If the gain $c_k = \alpha_k c_0$ is chosen such that the k'th damper provides too little resistance, or if it is placed redundantly, it will have vanishing effect. Too large resistance will instead lock the damper, also without any damping effect. The three damper configurations in Fig. 3.2 result in different damping efficiency as they will prevent warping in different ways. For the configuration (c) the dampers are placed indirectly where the warping displacements are small, whereas the configurations (a) and (b) have better authority. Table 3.1 provides the infinitely damped frequency ω_∞ obtained by the numerical 3D finite element model for the lowest torsional mode of the beam structure used in the example in Section 3.4. This frequency is given relative to the undamped frequency ω_0 without dampers. The influence of the damper configuration and thereby damping efficiency is directly proportional to the relative increment $(\omega_\infty - \omega_0)/\omega_0$, which shows that configuration (b) outperforms (a) and (c). For the analytical solution, this increment will be larger due to complete restrainment of the warping by B_d, while the residual warping shown in the bottom row of Fig. 3.2 inherently reduces the frequency ω_∞ and thus the attainable damping.

Table 3.1. Relative frequency increments due to damper locking.

	(a)	(b)	(c)	(∞)
$(\omega_\infty - \omega_0)/\omega_0$	0.318	0.368	0.225	0.480

3.3 Model calibration

As the discrete damper forces have a very local nature and thus allow residual warping deformation in the cross-section, the 3D FE model is considered as the exact representation of the actual behaviour of the beam structure. The analytical model comprised of the differential equation in (2.1) describes the idealized motion without any possibility for the in-plane distortion shown in Fig. 3.3a or the residual warping illustrated in Fig. 3.2. However, as the effective analytical solution method is favourable, it should be calibrated to better represent the behaviour of the 3D model and include these supplemental effects. For short beams the analytical model should therefore be corrected for distortion of the cross-section in Fig. 3.3a as well as partial restraining of warping due to the specific damper configuration in Fig. 3.2.

3.3.1 Calibration of model parameters

Figure 3.3b schematically shows the semi-circular root locus trajectory of the damped frequency in the complex plane. When increasing c_0 from 0 to ∞, the complex natural frequency ω moves along the trajectory from ω_0 to ω_∞. The accuracy of the analytical model relies on the ability of its root locus to initiate and terminate at the same frequencies as for the full 3D FE model. Calibration of the model parameters, such that these frequencies are identical between the two models, is therefore necessary. A proper procedure is now described for adjusting the theoretical beam model to represent the limiting frequencies.

In [P1] it is described how to calibrate the warping length scale k defined in (2.5) with respect to a corrected value k_c, to account for distortion (Fig. 3.3a) based on results from the 3D FE model. This reduces the undamped frequency ω_0, as shown in Fig. 3.3b.

To take the partial restrainment of the warping in Fig. 3.2 into account, a fictitious spring with spring stiffness κ is placed in series with the damper element as shown in Fig. 3.4 and described in [P2]. This spring is not physically present, but merely represents the excess flexibility associated with the partial warping for $\eta \to \infty$. The bimoment associated with this fictitious spring is given by the relation

$$B_d(t) = \mp \kappa \varphi'_\kappa(t) \tag{3.12}$$

The combination of the bimoment in (3.5) with the total displacement over the boundary condition in Fig. 3.4, given by $\varphi'_{d*}(t) = \varphi'_\kappa(t) + \varphi'_d(t)$, yields the augmented boundary condition with residual flexibility correction,

$$\varphi''_{d*} \mp \left(\frac{1}{i\omega\eta} + \frac{1}{\bar{\kappa}} \right)^{-1} \varphi'_{d*} = 0 \tag{3.13}$$

where $\bar{\kappa} = \kappa / EI_\psi$ is a normalized spring stiffness. The effect of the flexibility $1/\bar{\kappa}$ is illustrated in Fig. 3.3b, resulting in a reduction of the infinitely damped frequency ω_∞ obtained from the analytical model for finite values of the stiffness κ. When the

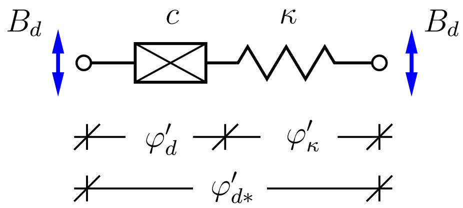

Figure 3.4. Boundary condition with a damping element with gain c in series with a spring with stiffness κ.

warping of the entire cross-section of the 3D model is restrained, no excess flexibility is available, whereby for $\kappa \to \infty$ the flexibility term in (3.13) vanishes. Residual warping is however allowed by the discrete damper configuration as shown in the bottom row of Fig. 3.2. This reduces the frequency ω_∞ and the stiffness therefore attains a finite value $\kappa < \infty$ when the dampers lock for $c_0 \to \infty$.
Determination of the residual stiffness κ requires information about the natural frequencies for the actual 3D FE model in the limit $c_0 \to \infty$ with the dampers fully locked. When the root locus of the analytical model terminates at this frequency ω_∞^{3D} of the 3D model with the dampers locked, the accuracy of the analytical model is retained. The transcendental equations appearing from (2.3) do not have a closed-form solution due to the frequency appearing in both the arguments to the trigonometric and hyperbolic functions and in the boundary condition in (3.13). In the limit $\eta \to \infty$ the first term in the paranthesis in (3.13) vanishes. Thus only $1/\bar{\kappa}$ is left, whereby the stiffness $\bar{\kappa}$ may be determined explicitly by simply substituting the frequency $\omega_\infty^{\mathrm{3D}}$ into the wave number expression (2.4), as demonstrated by the following example in Section 3.4.
The availability of the computationally efficient analytical model comes at the cost of determining the frequency $\omega_\infty^{\mathrm{3D}}$, which usually requires a detailed 3D finite element model. With the analytical model properly calibrated, it is however not necessary to perform an expensive full root locus analysis with the large 3D FE model.

3.3.2 Balancing of dampers

The calibration of the parameters in Section 3.3.1 ensures that the root locus of the analytical model initiates and terminates at the frequencies ω_0 and ω_∞ obtained from the full 3D model. However, this assumes a semi-circular trajectory in the complex frequency plane when the dampers work optimally together on the same vibration mode. As the dampers in Fig. 3.2 are located at different points on the cross-section, they should not be balanced identically and thus have different α_k. The balancing does not change the frequencies ω_0^{3D} and $\omega_\infty^{\mathrm{3D}}$ but ensures an optimal root locus trajectory where all dampers act collectively to obtain the desired semi-circular trajectory in Fig. 3.3b, see [41].
For viscous dampers an approximate yet accurate method for the relative sizing of discrete dampers on a flexible structure is described in [41]. The method relies on the constraint forces ρ_{jk} for the j'th mode and k'th damper in the limit of $c_0 \to \infty$,

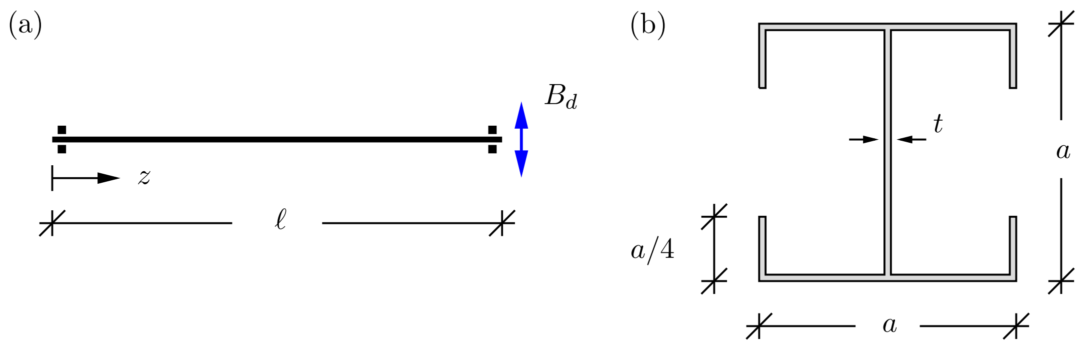

Figure 3.5. (a) 'Simple-simple' beam with damping treatment at $z = \ell$, and (b) modified I-profile.

where all dampers are replaced with rigid links. These constraint forces can be determined as

$$\rho_{jk} = \mathbf{w}_k^T \left(\omega_{\infty,j}^2 \mathbf{M} - \mathbf{K}\right) \tilde{\mathbf{q}}_{\infty,j} \tag{3.14}$$

The gain $c_k = \alpha_k c_0$ is then determined relative to an arbitrary gain by its constraint force and the corresponding modal displacement $\mathbf{w}_k^T \tilde{\mathbf{q}}_{0,j}$ by

$$\frac{c_k}{c_1} = \frac{\rho_{jk}}{\rho_{j1}} \frac{\mathbf{w}_1^T \tilde{\mathbf{q}}_{0,j}}{\mathbf{w}_k^T \tilde{\mathbf{q}}_{0,j}} \tag{3.15}$$

When all dampers are balanced relative to damper $k = 1$, then $c_0 = c_1$ in (3.4) and (3.9), whereby the balancing factor $\alpha_k = c_k / c_1$ is given directly by the expression in (3.15). This balancing causes the dampers to lock uniformly and thus act collectively.

3.4 Example: Damping of pure torsional vibrations

The efficiency of the analytical model with calibrated parameters compared to the full 3D model is conveniently demonstrated by an example. In [C1] an I-profile is analysed with three substantially different damper configurations, exhibiting a significant reduction of the infinitely damped frequency $\omega_\infty^{3\mathrm{D}}$ by damper configurations that leave large parts of the cross-section unrestrained for $c_0 \to \infty$. In [P1] a beam with length $\ell/a = 30$ and with the modified I-profile in Fig. 3.5b is analysed, and the main results are now summarised with emphasis on the model calibration and the accuracy between the two models.

A 'simple-simple' beam structure is shown in Fig. 3.5a, where the rotation of the two beam ends is restrained but warping is allowed. Viscous damping is introduced by a single viscous bimoment B_d at the right end at $z = \ell$. The governing transcendental equation is given as

$$\begin{aligned} &\Big((\alpha\ell)^2 + (\beta\ell)^2\Big) \sinh(\alpha\ell)\sin(\beta\ell) - \\ &\left(\frac{1}{i\omega\eta\ell} + \frac{1}{\bar{\kappa}\ell}\right)^{-1} \cosh(\alpha\ell)\cos(\beta\ell)\Big[\beta\ell\tanh(\alpha\ell) - \alpha\ell\tan(\beta\ell)\Big] = 0 \end{aligned} \tag{3.16}$$

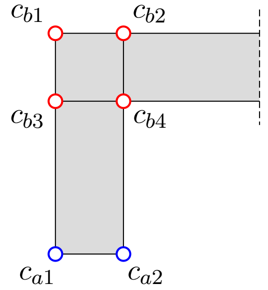

Figure 3.6. Order of the damping coefficients.

For vanishing damping ($\eta = 0$) this equation recovers the 'simple-simple' case in Table B.2, while for $\eta \to \infty$ the solution can be found from Table B.4 with 'fixed-simple' supports. The effective damping parameter η given in (3.7) is determined based on the balancing of the dampers and their sector-coordinate. The two different damper configurations indicated in Fig. 3.6 are applied to investigate the influence of the position of the dampers on the cross-section. In case a eight dampers are placed on the cross-section, placed in pairs of two at the bottom of each vertical flange part. This configuration is denoted B_a and shown in blue. For case b sixteen dampers are placed in groups of four in each of the four corners. This configuration is denoted B_b and is shown with the red circles in Fig. 3.6.
The calibration procedure requires the frequencies ω_0^{3D} and $\omega_\infty^{\mathrm{3D}}$ from the full 3D FE model. Distortion is initially corrected by calibrating k_c so that ω_0 for the beam model recovers ω_0^{3D}. This effect is however vanishing for long beams with a beam length to cross-section height ratio above 10.
The excess flexibility from the partial restraining of the warping is then determined by substituting $\omega_\infty^{\mathrm{3D}}$ for the frequency in (3.16) for $\eta \to \infty$, which leads to

$$\bar{\kappa}\ell = \frac{\big((\alpha\ell)^2 + (\beta\ell)^2\big)\tanh(\alpha\ell)\tan(\beta\ell)}{\beta\ell\tanh(\alpha\ell) - \alpha\ell\tan(\beta\ell)} \tag{3.17}$$

in which $\alpha\ell$ and $\beta\ell$ now depend on ω_∞^{3D}. Thus this expression gives two different $\bar{\kappa}\ell$-values for the two damper configurations. The balancing factors from (3.15) are given in Table 3.2, and large ratios between the damper coefficients are obtained for configuration B_b, ensuring uniform locking of the dampers, as shown next.

With the balancing factors determined from the 3D model and the model parameters k_c and $\bar{\kappa}\ell$ calibrated for the analytical model, the root loci in Fig. 3.7a are obtained when varying the common viscous damping coefficient in the interval $c_0 \in [0\,;\infty[$ and solving the eigenvalue problem. Results from the 3D FE model are indicated by

Table 3.2. Balancing factors.

Bimoment	B_a		B_b			
Damping coefficient	c_{a1}	c_{a2}	c_{b1}	c_{b2}	c_{b3}	c_{b4}
α_k	1.0	0.8	1.0	7.5	70.2	141.9

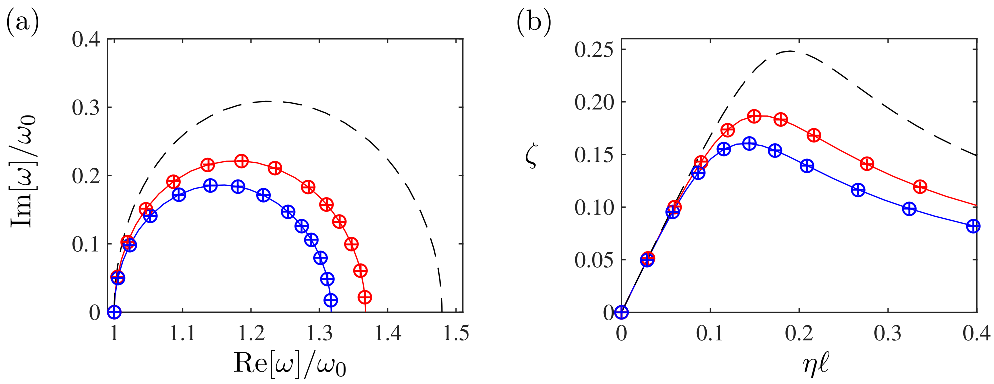

Figure 3.7. Complex frequency loci (a) and damping ratio (b). Results from 3D FE analysis (○) and (○) and differential equation (— , +) and (— , +). Blue and red corresponds to B_a and B_b respectively. (– –) indicates fully restrained cross-sections.

the (○)-markers and the analytical model from solving (3.16) are represented by the solid lines and (+)-markers. The effect of the model calibration is clear as the root loci initiate and terminate at identical frequencies. The reduction of the frequency ω_∞ due to the residual warping is furthermore significant compared to the dashed line indicating a fully restrained cross-section, obtained by (3.16) for $\bar{\kappa} \to \infty$.
The damper configuration B_b is the better of the two as it yields the largest frequency increment of 0.368 compared to 0.318 for configuration B_a, see Table 3.1. Thus B_b results in the largest imaginary value of the natural frequency, and thereby produces the largest maximal damping ratio of $\zeta_b \simeq 0.19$, compared to $\zeta_a \simeq 0.16$ for configuration B_a, as shown in Fig. 3.7b. In the case where warping is fully restrained, the frequency increment is 0.480 and the corresponding maximal damping ratio is $\zeta = 0.248$. The residual warping thus has a significant influence and reduces both the frequency increment $(\omega_\infty - \omega_0)/\omega_0$ and the damping ratio substantially. A complete analytical model therefore needs to take the residual warping into account by the fictitious stiffness κ in Fig. 3.4 and the augmented boundary condition in (3.13).
The markers for the two models in Fig. 3.7 coincide almost perfectly, concluding that initial design considerations with respect to damper configurations, damping ratios and frequency increments may conveniently be performed with the analytical model, as long as the various parameters are calibrated based on frequency results from a full 3D FE model. The coinciding markers furthermore verify the proper parameter calibration and the applied balancing of the individual dampers.

4 | Active Damping by Warping Position Feedback

For torsional vibrations of beams with open cross-sections discrete viscous dampers placed in suitable configurations on the end cross-section constitute a convincing method of damping, as significant damping ratios may be obtained, see [C1,P1] or [28]. However situations may arise in which viscous-type dampers are insufficient, as in the case of a cross-section without double symmetry where torsion couples with bending or for closed cross-sections as demonstrated by an example in Appendix A. In the case of coupling, the torsion component only represents a part of the coupled response and the effect of dampers working only on the torsion part may be insufficient. Using an active approach in terms of a feedback control may therefore be beneficial, as such strategies can introduce apparent negative stiffness that greatly increases the damping potential [29].

As the warping displacements from the torsion part of coupled vibrations are small, a positive position feedback control strategy [16, 29] will be adopted in this chapter. A linear filter [8] controls the actuator force with the collocated axial displacement as input from structural measurements obtained by e.g. a laser or piezoelectric sensor. The filter has advantageous properties and a well defined stability limit caused by the active force delivered to the structure, below which a bounded response at all times is secured. The residual flexibility described in Section 3.2 and 3.3 from the partial restrainment of the cross-sectional warping due to the configuration of discrete actuators, is accounted for as it adjusts the stability limit. The flexibility is calibrated based on 3D FE results, as described in Chapter 3
This chapter focusses on the damping of beams with open cross-sections. In [C2] pure torsional vibrations have been investigated and in [P2] damping of coupled bending-torsion vibrations are investigated. The issue of coupled vibrations is emphasised in the chapter, especially how to spatially filter the coupled response in order for the actuators to only restrain the part of the axial displacements related to torsional warping, thus leaving elongation and bending unaffected.
Analytical expressions for the vibration characteristics for coupled beam vibrations are not feasible to handle. The active concept is therefore used in connection with the computationally efficient beam element model described in Section 2.3. The chapter thus presents the main features of [P2].

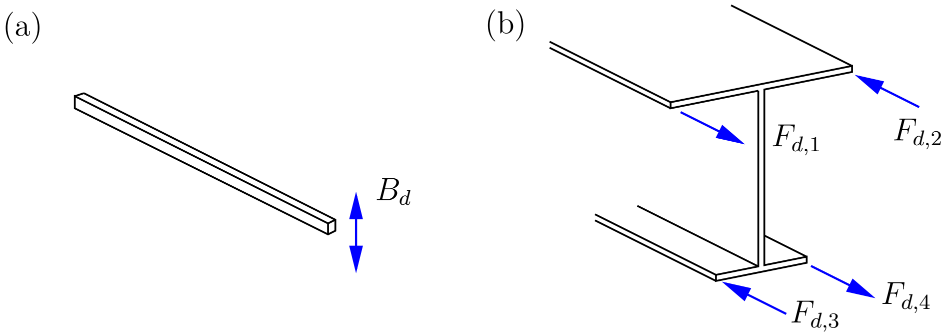

Figure 4.1. (a) Beam element model with equivalent actuator bimoment and (b) 3D structure with discrete axial actuators.

4.1 PPF control with flexibility

The beam structure in Fig. 4.1a is discretized with the beam elements in Fig. 2.2b and represents the behaviour of the full 3D model in Fig. 4.1b. The configuration of the discrete axial actuators F_d in the 3D model is represented by the single equivalent actuator bimoment B_d. The governing equation of motion is analogous to (3.8) and for the beam model given as

$$\mathbf{M}\ddot{\mathbf{q}}(t) + \mathbf{K}\mathbf{q}(t) = -\mathbf{w}B_d(t) \tag{4.1}$$

where the connectivity vector $\mathbf{w}$ contains a single unit value at the warping degree-of-freedom associated with the single actuator bimoment B_d. The control law governing the active actuator bimoment is composed of a linear filter with positive position feedback given by the scalar equation

$$B_d(t) + \tau\dot{B}_d(t) = g\theta_d'(t) \tag{4.2}$$

where g is the actuator gain, τ is a filter constant specifying a cut-off frequency at $1/\tau$ and $\theta_d'(t)$ is the warping intensity representing the axial displacement through the sector-coordinate ψ by (2.8). In the frequency domain equation (4.2) can be written as $\widetilde{B}_d = H(\omega)\widetilde{\theta}_d'$, where H is a gain-dependent transfer function taking the form

$$H = \frac{g}{1 + i\omega\tau} \tag{4.3}$$

The phase angle φ, the absolute value of the transfer function and the real and imaginary parts are shown in Fig. 4.2. Dissipation of energy requires $\mathrm{Im}[H] > 0$ whereas it follows from Fig. 4.2b that $g < 0$. This results in the apparent stiffness function $\mathrm{Re}[H] < 0$ being negative. The filter therefore gives a force that acts ahead of velocity with a phase $\varphi > \pi/2$, as seen in Fig. 4.2a. This greatly increases the attainable damping as the PPF increases the actuator stroke and thereby improves energy dissipation by $\mathrm{Im}[H]$. Furthermore noisy high-frequency components are filtered away because $|H| \to 0$ for $\omega \to \infty$. These properties make the PPF a suitable choice for small deformation problems as in the case of active warping control.

The equivalent actuator bimoment B_d in (4.2) represents the actual configuration of axial actuators in Fig. 4.1b. Therefore, the residual flexibility due to the partial warping restrainment must be taken into account. The procedure in Section 3.3.1 described in [C2] and [P2], introduces a fictitious spring with stiffness κ as previously shown in Fig. 3.4. This leads to the augmented control equation that can be written as

$$\left(\frac{1}{g}+\frac{1}{\kappa}\right) B_d(t)+\frac{\tau}{g}\dot{B}_d(t)=\theta'_{d*}(t) \tag{4.4}$$

where c in Fig. 3.4 is replaced by H with gain g in (4.3). The fictitious stiffness κ is determined such that the frequency for the beam element model at infinite gain $g \to -\infty$ recovers the correct frequency obtained by the full 3D model when locking the local actuators in Fig. 4.1b. The stiffness κ is therefore determined based on the infinitely damped frequency ω_∞ in the limit of infinite gain. In this limit the eigenvalue problem with contribution from the augmented control equation in (4.4) reduces to a contribution from the spring which appears as an addition to the stiffness matrix for the beam element model,

$$\Big(-\omega_{\infty,j}^2\mathbf{M}+\mathbf{K}+\kappa\mathbf{w}\mathbf{w}^T\Big)\tilde{\mathbf{q}}_{\infty,j}=\mathbf{0} \tag{4.5}$$

The infinitely damped frequency $\omega_{\infty,j}$ and corresponding mode shape vector $\tilde{\mathbf{q}}_{\infty,j}$ for the beam element model in the limit of infinite gain $g \to -\infty$, are thus determined from (4.5) that depends on the the fictitious stiffness κ. As the warping of the cross-section of the full 3D model is only partially restrained, the frequency ω_∞^{3D} is thus lowered and results in a finite value of κ. The stiffness is thus determined by the equivalence $\omega_{\infty,j}=\omega_\infty^{3D}$. As demonstrated in [P2] applying the matrix determinant lemma from the Sherman-Morrison formula [10] to (4.5) gives the fictitious stiffness as

$$\kappa=-\frac{1}{\mathbf{w}^T\Big[-(\omega_\infty^{3D})^2\mathbf{M}+\mathbf{K}\Big]^{-1}\mathbf{w}} \tag{4.6}$$

This expression explicitly determines the influence of the residual flexibility based on the mass matrix $\mathbf{M}$, stiffness matrix $\mathbf{K}$ and connectivity vector $\mathbf{w}$ for the beam

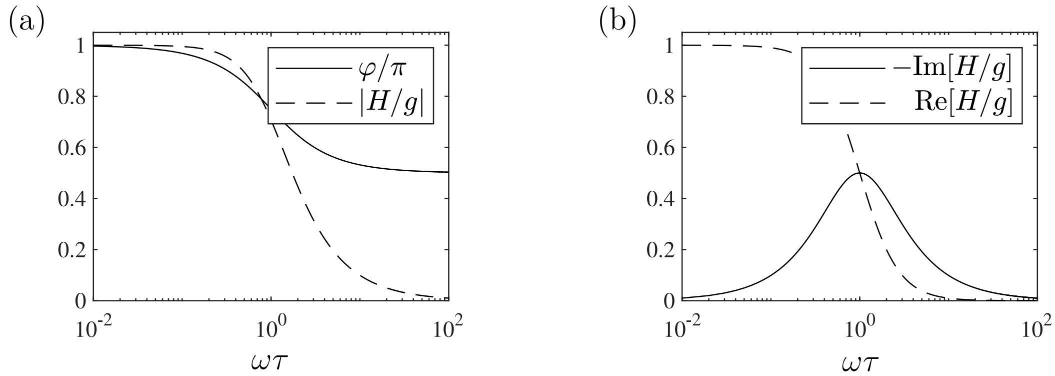

Figure 4.2. (a) Magnitude and phase angle and (b) real and imaginary part of the transfer function H.

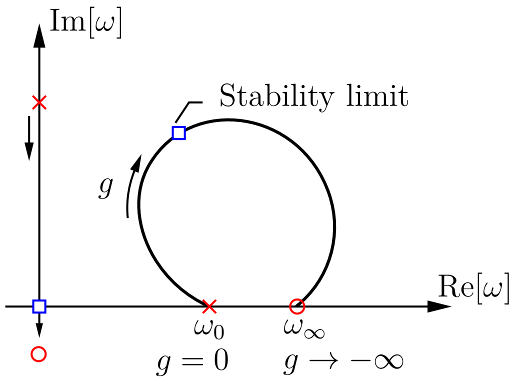

Figure 4.3. Root locus and indication of the stability limit when the purely imaginary eigenvalue becomes negative.

element model, and the frequency ω_∞^{3D} from the full 3D FE model in the limit of infinite gain. For the beam element model the mass and stiffness matrices have a limited size, whereby the inversion in (4.6) is computationally inexpensive.

4.2 System stability

The augmented control equation in (4.4) exerts an active force on the structure with an apparent negative stiffness component as represented by $\mathrm{Re}[H] < 0$. This negative stiffness cannot in magnitude exceed the structural stiffness at the location of the actuator. When that occurs the response will become unbounded and the combined system therefore unstable. The actuator force is proportional to the gain g and a limit on the gain must therefore be determined in order to secure a bounded response and thereby a stable system at all times.

Figure 4.3 shows a root locus for a particular mode tracing the damped frequency in the complex plane from the undamped frequency ω_0 (×) to the infinitely damped frequency ω_∞ (∘). The trajectory of the root locus is in the case of PPF not semicircular due to the apparent negative stiffness part of the control equation. Solutions to the combined system comprised of the structural equations (4.1) and the augmented control equation (4.4) are typically found from a state-space format. This format implies that a purely imaginary root is added to the family of complex natural frequencies, as indicated in Fig. 4.3. Stability requires all roots to have a positive imaginary part, and instability therefore occurs when one of these purely imaginary roots become negative. This transition defines the limit of stability by the corresponding gain $g = g_{\mathrm{stab}}$, indicated by the blue square (□) in Fig. 4.3.

The point of instability can be determined based on the elastic energy contained within the system. This energy is comprised of contributions from the structural stiffness through the stiffness matrix of the beam element model and the negative stiffness and fictitious flexibility from the controller through g and κ. The elastic energy can be expressed as

$$V_e = \begin{bmatrix} \mathbf{q}^*(t)^T & B_d(t) \end{bmatrix} \begin{bmatrix} \mathbf{K} & -g\nu^{-1}\mathbf{w} \\ -g\nu^{-1}\mathbf{w}^T & -g\nu^{-1} \end{bmatrix} \begin{bmatrix} \mathbf{q}^*(t) \\ B_d(t) \end{bmatrix} \tag{4.7}$$

where $\nu = \left(1 + \frac{g}{\kappa}\right)$ contains the correction from the fictitious stiffness κ. Stability requires the elastic energy in (4.7) to be positive [37]. When rewriting the energy it is seen that only a single term may become negative for gains above a certain level. As demonstrated in [P2] this gives the following explicit requirement for the gain

$$\frac{1}{g_{\text{stab}}} = -\mathbf{w}^T\mathbf{K}^{-1}\mathbf{w} - \frac{1}{\kappa} \tag{4.8}$$

Thus, instability occurs when the structural flexibility at the location of the actuator represented by $\mathbf{w}^T\mathbf{K}^{-1}\mathbf{w}$ is eliminated by the equivalent flexibility of the control equation with the added fictitious flexibility $1/\kappa$. The added flexibility $1/\kappa$ thus reduces the allowable gain, and is therefore important to include as it is otherwise ignored by the original PPF control equation for the beam model in (4.2).

4.3 Warping control and connectivity

The emphasis in this chapter has been on establishing a beam element model with a single actuator bimoment working on the gradient of the angle twist, and representing a configuration of discrete axial actuators on the actual 3D cross-section. The accuracy of this model is contained within the exact calibration of the fictitious stiffness κ by frequency matching. Thus a 3D FE model of the actual beam structure and actuator configuration is required to obtain the infinitely damped frequency $\omega_\infty^{3\text{D}}$ used for calibration of κ. In the 3D model, however, bending couples with torsion, and the axial displacements at the end cross-section therefore consist of warping displacements from torsion as well as displacements from the inclination of the cross-section due to bending, as shown in Fig. 4.4. In order for the beam

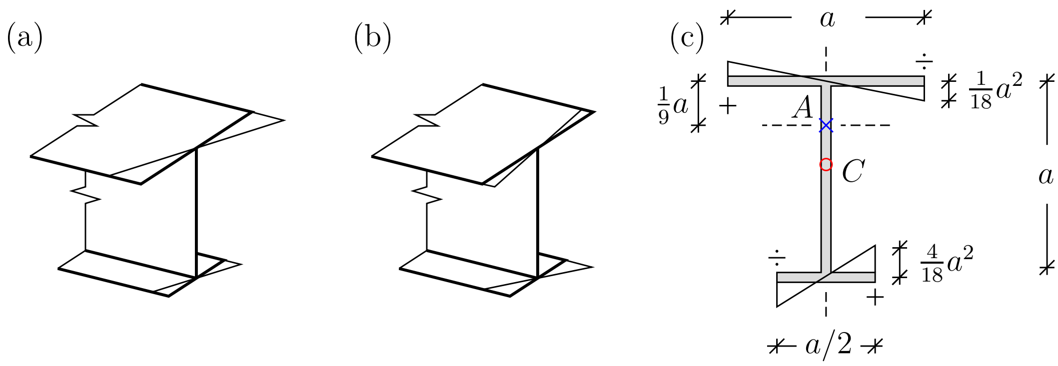

Figure 4.4. (a) Inclination from bending, (b) warping and (c) sign of the analytical sector-coordinate ψ.

element model to represent the 3D model it is necessary to set up a spatial filter such that the discrete axial actuators in Fig. 4.1b only restrain the warping part of the coupled response. This corresponds to the single actuator bimoment in Fig. 4.1a only restraining the warping intensity through the rate of twist θ', and not the inclination from bending.

Details about the 3D model are found in Chapter 2 and in [P1]. In (3.8) the discrete dampers have been modelled individually, but in order for the active actuators to work on relative displacements, they are constructed as an equivalent bimoment in a single connectivity vector $\mathbf{w}_{3D}$ with proper balancing factors. In Fig. 4.4c an I-profile cross-section with a single line of symmetry is shown with the associated sector-coordinate ψ. Different parts of the cross-section warp in different directions and the crucial step is to ensure that the signs in $\mathbf{w}_{3D}$ correspond to these displacements, whereby the control leaves elongation and bending unaffected. These signs are given by the sector-coordinate and will be contained within the balancing factors α_k. The connectivity vector takes the form

$$\mathbf{w}_{3D} = [\,\dots\,,\, \alpha_k\,,\, \dots\,]^T \tag{4.9}$$

with contributions from all actuators. As the actuators now work on relative displacements, the balancing method adopted in Chapter 3 and used in [P1] cannot be applied. However, a suitable balancing is secured when setting the balancing factors α_k in $\mathbf{w}_{3D}$ proportional to the square root of the sector-coordinate at the actuator locations. The balancing factor for actuator k can then be determined as

$$\alpha_k = \mathrm{sign}(\psi_k)\sqrt{|\psi_k|} \tag{4.10}$$

where the sign function provides the correct spatial filtering and the square root ensures that the sector-coordinate does not appear squared in the outer product $\mathbf{w}\mathbf{w}^T$. With this filtering the targeted natural frequency ω_∞^{3D} in the limit of $g_{3D} \to -\infty$ can be determined by solving the structural equations and controller equation for the 3D model in state-space, as shown in [P2]. The frequency ω_∞^{3D} is effectively determined by imposing a constraint on the relative warping displacements by the use of a Lagrange multiplier [19]. The connectivity vector $\mathbf{w}_{3D}$ is conveniently used for the constraint equation $\mathbf{w}_{3D}\tilde{\mathbf{q}} = 0$ resulting in a generalised eigenvalue problem of size $n + 1 \times n + 1$ that yields real-valued natural frequencies $\omega_{\infty,j}^{3D}$.

When considering the four-actuator configuration in Fig. 4.1b, with the analytical sector-coordinate given in Fig. 4.4c, the four non-zero entries in the connectivity vector $\mathbf{w}_{3D}$ are given by $\pm a/\sqrt{18}$ for $F_{d,1}$ and $F_{d,2}$, respectively, while for $F_{d,3}$ and $F_{d,4}$ they are respectively $\mp 2a/\sqrt{18}$. The connectivity vector then takes the normalized form

$$\mathbf{w}_{3D} = [\,\dots\,,\, 1\,,\, -1\,,\, -2\,,\, 2\,,\, \dots\,]^T \tag{4.11}$$

where the common factor $a/\sqrt{18}$ has been absorbed by the gain g_{3D}. The connectivity vector thus contains the ratios between the individual balancing factors given in (4.10). For more complicated cross-sections or when the warping across the thickness of the flanges is accounted for, a more detailed numerical cross-sectional analysis may be performed [30], as conducted for the example in [P2].

4.4 Example: Damping of coupled vibrations

The efficiency of the active feedback control is demonstrated by analysing the damping potential of a beam with length $\ell/a = 30$ and the I-profile cross-section shown in Fig. 4.4c. Warping control is applied and the example summarises the results in [P2].

The beam is simply supported in both ends with respect to torsion and bending in the horizontal x_1-direction. Vertical vibrations do not couple with torsion due to the vertical line of symmetry for the cross-section in Fig. 4.4c. These specific boundary conditions are realized in the 3D model by locking all cross-sectional nodes in the vertical x_2-direction, thereby effectively preventing torsion, while the nodes along a line in the vertical x_2-direction at $x_1 = 0$ are constrained in the horizontal x_1-direction to secure the transverse displacements. The end cross-section may therefore rotate with respect to the vertical line of symmetry allowing axial displacements.

A patch plot of the lowest vibration mode is shown in Fig. 2.4a. A single actuator bimoment is applied at one end of the beam element model and the 3D model therefore contains eight discrete actuators, two at the end of each of the four horizontal flanges.

In order for the beam element model to effectively represent the 3D FE model, the fictitious stiffness κ must be determined, as it represents the effect of partial restrained warping. Figure 4.5a shows the resulting axial displacements for the lowest undamped coupled mode of the beam. The inclinations of the two horizontal flanges are clearly not identical, indicating a response comprised of both inclination from bending and torsional warping, as depicted in Figs. 4.4a,b.

When the warping part of the response at the location of the actuators is restrained completely, the axial displacements are reduced to the displacement field shown in Fig. 4.5b where the inclinations of the two flanges with respect to the outer points on the flanges are now identical. This is associated with the infinitely damped frequency $\omega_\infty = \omega_\infty^{3D}$, for which the fictitious stiffness κ is then calibrated by (4.6).

The damping results are shown by the root loci in Fig. 4.6, where the two lowest coupled modes are analysed with the same actuator configuration. The beam element model is represented by the solid line and circle markers (— , ∘), where (– –) indicates the case of fully restrained warping with assumed $\kappa \to \infty$. The 3D model is represented by the red markers (+) and the blue square (□) represents the point

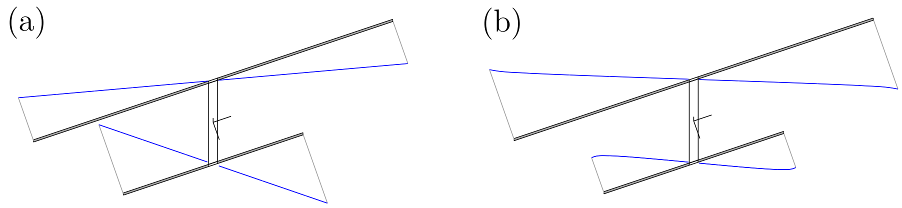

Figure 4.5. Axial displacements for (a) the first undamped mode and (b) the infinitely damped mode.

of instability according to (4.8).

Due to the apparent negative stiffness of the control equation in (4.4), the semicircular behaviour is expanded to a shape with a circle center placed above the real axis. Thus the general size of the root locus is amplified, thereby also increasing the modal damping ratio. As the warping of the cross-section merely represents a part of the coupled response, the effect of the partial warping restrainment is therefore less significant, when compared to the analyses of pure torsional vibrations in [C2] and [P1]. However, the consequence of the reduction of the relative frequency increment $(\omega_\infty - \omega_0)/\omega_0$ is apparent from the reduced root loci. For the beam model the relative frequency increment is reduced from 0.092 to 0.086 for the first mode due to the partial warping restrainment, and for the second mode it is reduced from 0.136 to 0.123. Similarly the damping ratio at instability is reduced from $\zeta_1 = 0.189$ to 0.174 for the first mode and from $\zeta_2 = 0.301$ to 0.188 due to the partial warping restraining.

In terms of stability, the added flexibility reduces the allowable value of the gain. To the left in Fig. 4.6 the pure imaginary root is seen. This root was introduced by the single equivalent actuator bimoment present in both the beam element model and 3D model. As seen by the blue square marker instability occurs exactly when this imaginary root attains a zero imaginary part.

The markers for the two models match quite well, and the small difference is attributed partly to the difference in undamped frequency by the lack of correcting for in-plane distortion, and partly because of discrepancies in the modelling of the boundary conditions in the 3D model.

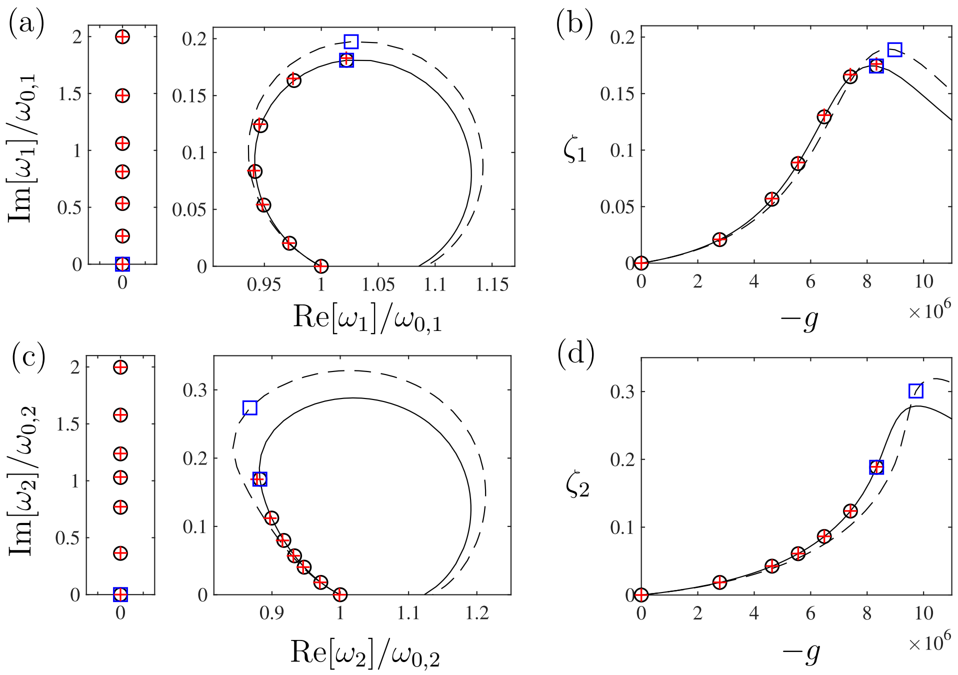

Figure 4.6. Frequency loci (a,c) and damping ratio (b,d) for the first mode (a,b) and second mode (c,d) of the beam model. Red markers represent the 3D FE model and the blue square indicates the gain limit. Dashed line represents $\kappa \to \infty$.

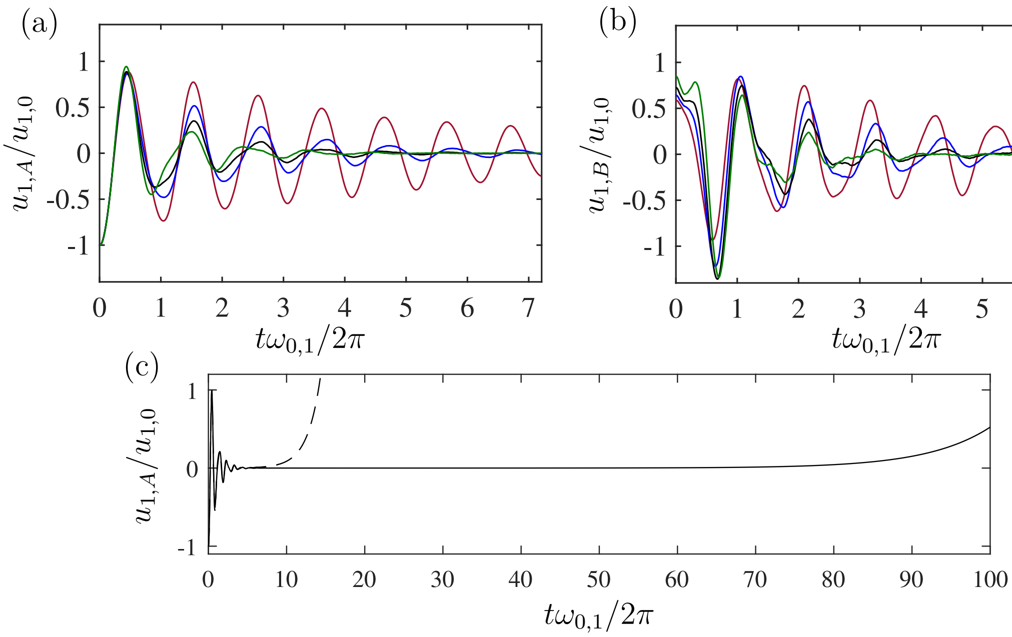

Figure 4.7. Free response from an initial displacement showing the horizontal displacement of (a) the shear centre and (b) the junction of the web and lower horizontal flange for $0.40 \cdot g_{\rm stab}$ (red), $0.65 \cdot g_{\rm stab}$ (blue), $0.80 \cdot g_{\rm stab}$ (black) and $0.95 \cdot g_{\rm stab}$ (green). (c) shows the horizontal displacement of the shear centre for $1.01 \cdot g_{\rm stab}$ (solid) and $1.05 \cdot g_{\rm stab}$ (dashed).

As torsion and bending couple the total response will inherently be affected by the warping control. Figure 4.7 shows the free response when vibrations of the beam element model are initiated by an initial displacement. For a point on the middle of the beam the figure then shows (a) the horizontal displacement of the shear centre and (b) the linearized horizontal displacement of the junction between the web and lower horizontal flange of the cross-section. The curves represent the gains $0.40 \cdot g_{\rm stab}$ (red), $0.65 \cdot g_{\rm stab}$ (blue), $0.80 \cdot g_{\rm stab}$ (black) and $0.95 \cdot g_{\rm stab}$ (green) with $g_{\rm stab}$ representing the gain limit. These selected gains approximately correspond to the mode 1 damping ratios: $\zeta_1 = 2.9\,\%$, $8.3\,\%$, $13.8\,\%$ and $17.4\,\%$. Figure 4.7b includes the torsional part of the response, and it is thus clear that the total response is effectively damped by the proposed warping control.

A crucial part of the design of the actuator system is to avoid an unstable structural system at any cost. The gain limit is governed by (4.8) when perfect actuator and sensor dynamics are assumed. A gain above this limit $g_{\rm stab}$ results in an unbounded response as shown in Fig. 4.7c. The response may build up slowly when the gain is only slightly above the limit, as indicated by the solid line. However, significant violations may cause a rapidly increasing response, and the stability limit should be obeyed with a sufficient margin.

5 | Tuned Mass Absorbers for Coupled Vibrations

A widely used device for mitigating vibrations in civil engineering structures is the tuned mass absorber [15, 36]. Figure 5.1a shows the basic absorber structure with a suspended mass with a spring and a viscous dashpot. The mass absorber is relatively easy to install in large-scale structures such as bridges [9], wind turbine blades [4] and tall buildings [55].

When introducing a mass absorber in a structure, the targeted structural mode splits into two coupled structure-absorber modes. The original tuning procedure of Den Hartog [14] is based on a frequency tuning with respect to the selected resonant vibration mode, where two neutral frequencies independent of the damping are selected to attain equal dynamic amplification of the two coupled modes. Subsequently the damping parameter is chosen to obtain a flat plateau of the dynamic amplification around resonance. This corresponds to equal modal damping of the two structural modes associated with the targeted vibration form, and this tuning serves as a good compromise between high modal damping and limited response amplification [36]. This tuning procedure assumes that the response of the structure can be represented by a single targeted vibration mode. For flexible structures or for indirect positioning of the absorber, the remaining non-resonant modes will contribute to the support motion of the absorber, deteriorating the accuracy of the tuning procedure.

As shown in [38] the effect of the background modes can be accounted for by two supplemental terms in the absorber equation, representing excess flexibility and inertia. These terms can be calibrated based on two frequencies for the actual structure with representative absorbers mounted. This approach has been used for inerter-based absorbers in [27], and will be used in this chapter for mass absorbers.

When torsion couples with bending [39] multiple absorbers may be applied targeting the same vibration mode [32]. For fully coupled beam vibrations a three-component absorber can be used, consisting of two translational absorbers and a single rotational absorber. As an alternative to the classic configuration in Fig. 5.1a, the translational absorbers may be realized as the crucifix-absorber in [48], while the rotational absorber may be designed as a fly-wheel type disc with electromagnetic or eddy current dampers. Multiple absorbers require a proper and inhomogeneous balancing to work optimally together and to ensure the desired properties of the tuning. As described in [P3] an approximate method is used for individual balanc-

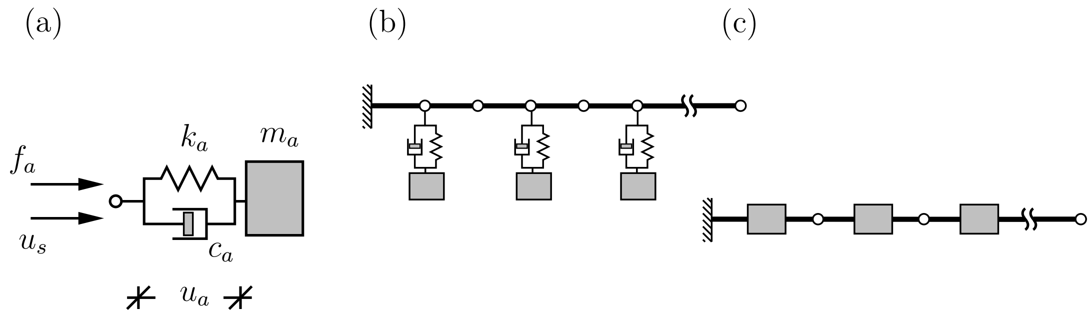

Figure 5.1. (a) Tuned mass absorber, (b) structure with multiple absorbers and (c) locking of the absorber mass to the structure at $c_a \to \infty$.

ing of the three absorbers. This chapter therefore describes the main features of the calibration and balancing procedure adopted in [P3].

5.1 Tuning with residual mode correction

The tuning procedure with correction for the residual non-resonant background modes is described in the following. The governing structural and absorber equations are presented and the modal properties are obtained by an expansion in the infinitely damped vibration form. The approach is based on an initially determined absorber mass m_a, which remains constant throughout the tuning procedure. The tuning and calibration of the residual mode corrections are independent of the balancing factors once the modal properties have been obtained, and the tuning formulas thus appear as scalar relations.

5.1.1 Governing equations

The structural system is similar to (3.8) but with the absorber forces contained in the vector $\mathbf{f}_a$ and external loads in $\mathbf{f}_e$. In the frequency domain the general response equation can be written as

$$\Big(-\omega^2\mathbf{M} + \mathbf{K}\Big)\tilde{\mathbf{q}} + \mathbf{W}\tilde{\mathbf{f}}_a = \tilde{\mathbf{f}}_e \tag{5.1}$$

For the single absorber in Fig. 5.1a, m_a is the absorber mass, k_a is the spring stiffness, c_a is the viscous damping coefficient, u_s is the structural displacement and u_a is the relative absorber displacement. When n_a absorbers are mounted on the structure as in Fig. 5.1b, the attachment to the structure is specified by the connectivity array $\mathbf{W}$, containing the individual connectivity vectors,

$$\mathbf{W} = [\, \mathbf{w}_1\, ,\, \mathbf{w}_2\, ,\, \dots\, ,\, \mathbf{w}_{n_a} \,] \tag{5.2}$$

where each $\mathbf{w}$ contains a single unit entry at the associated degree-of-freedom. The absorber forces are determined either from the parallel configuration of the spring and dashpot or from the accelerated mass as

$$\widetilde{\mathbf{f}}_a = -\Big(k_a + i\omega c_a\Big)\boldsymbol{\alpha}\widetilde{\mathbf{u}}_a = -\omega^2 m_a \boldsymbol{\alpha}\Big(\widetilde{\mathbf{u}}_a + \widetilde{\mathbf{u}}_s\Big) \tag{5.3}$$

The relative balancing of the multiple absorbers is specified by the balancing factors α_k contained in the matrix

$$\boldsymbol{\alpha} = \mathrm{diag}[\,\alpha_1\,,\,\alpha_2\,,\,\dots\,,\,\alpha_{n_a}\,] \tag{5.4}$$

The absorber parameters m_a, c_a and k_a thus serve as common factors and the effect of the individual absorbers are given by the balancing matrix $\boldsymbol{\alpha}$.
When eliminating the absorber force $\widetilde{\mathbf{f}}_a$ in (5.1) by the latter equality in (5.3), and introducing the structural displacements at each absorber as $\widetilde{\mathbf{u}}_s = \mathbf{W}^T\widetilde{\mathbf{q}}$ in (5.3), the structural and absorber equations can be written as

$$\begin{aligned} \Big(\mathbf{K} - \omega^2\mathbf{M}_\infty\Big)\widetilde{\mathbf{q}} - \omega^2 m_a \mathbf{W}\boldsymbol{\alpha}\widetilde{\mathbf{u}}_a &= \widetilde{\mathbf{f}}_e \\ \Big(k_a + i\omega c_a - \omega^2 m_a\Big)\boldsymbol{\alpha}\widetilde{\mathbf{u}}_a - \omega^2 m_a \boldsymbol{\alpha}\mathbf{W}^T\widetilde{\mathbf{q}} &= \mathbf{0} \end{aligned} \tag{5.5}$$

where the augmented mass matrix

$$\mathbf{M}_\infty = \mathbf{M} + m_a \mathbf{W}\boldsymbol{\alpha}\mathbf{W}^T \tag{5.6}$$

contains contributions from the absorber masses, as illustrated in Fig. 5.1c. For $c_a \to \infty$ the equation (5.5a) recovers the undamped structure, with all masses locked to the structure and contained in the mass matrix in (5.6). The eigenvalue problem corresponding to the homogeneous form of (5.5a) when $\widetilde{\mathbf{u}}_a = \mathbf{0}$ is thus a consistent representation of the dynamics of the structure.

5.1.2 Augmented modal response

The classic tuning in [14, 36] is based on a single representative vibration mode $j = r$ of the structure. For flexible structures the residual non-resonant background modes ($j \neq r$) contribute as well to the support motion of the absorber because of the presence of the absorber. This effect thus needs to be taken into account when tuning the absorber. As demonstrated in [38] the effect of the background modes can be represented by additional flexibility and inertia terms, which are added to the modal absorber equation (5.5b).
The homogeneous form of the structural equation (5.5a) for $\widetilde{\mathbf{u}}_a = \mathbf{0}$ is associated with an eigenvalue problem similar to (2.10), but with the mass matrix $\mathbf{M}_\infty$ from (5.6). This eigenvalue problem represents the structure when the absorber mass is locked to the structure, as indicated in Fig. 5.1c. The corresponding eigenvectors $\widetilde{\mathbf{q}}_{\infty,j}$ are thus suitable for the modal expansions

$$\widetilde{\mathbf{q}} = \sum_{j=1}^{n} \widetilde{\mathbf{q}}_{\infty,j}\frac{x_j}{\nu_{\infty,j}} \quad , \quad \widetilde{\mathbf{u}}_a = \mathbf{W}^T\widetilde{\mathbf{q}}_{\infty,r}\frac{y_r}{\nu_{\infty,r}} \tag{5.7}$$

where x_j and y_r are the corresponding modal coordinates for the structure and absorbers, respectively. The factor $\nu_{\infty,j}$ represents a combined modal displacement as discussed in [P3]. The absorber displacements are expanded directly in terms of the targeted vibration form $j = r$. As demonstrated in [P3] the introduction of the expansions in (5.7) into the equations (5.5) yields the modal equations

$$\begin{aligned} \Big(k_j - \omega^2 m_j\Big) x_j - \omega^2 m_a \eta_{jr} y_r &= f_j \\ \Big(k_a + i\omega c_a - \omega^2 m_a\Big) y_r - \omega^2 m_a \sum_{j=1}^{n} \eta_{rj} x_j &= 0 \end{aligned} \tag{5.8}$$

where m_r, k_r and f_r are the modal mass, stiffness and load, respectively. The parameter η_{jr} is a coupling term that takes the background modes into account. It is normalized so that $\eta_{rr} = 1$ for the targeted mode $j = r$.

As an alternative to a direct truncation of the sum in (5.8) the non-resonant modes $j \neq r$ can be represented by a flexibility $1/k'_r$ term and inertia $1/m'_r\omega^2$ term, as demonstrated in [38]. Hereby the sum can be approximated as

$$\sum_{j=1}^{n} \eta_{rj} x_j = x_r + \sum_{j \neq r}^{n} \eta_{rj} x_j = x_r + k_a \left(\frac{1}{k'_r} - \frac{1}{m'_r \omega^2} \right) y_r \tag{5.9}$$

where the correction terms k'_r and m'_r appear as supplemental modal stiffness and mass, respectively. The modal truncation with the residual mode corrections in (5.9) thus eliminates the sum in the absorber equation in (5.8b), whereby the modal equations only include $j = r$.

By substituting the representation in (5.9) with the residual mode corrections into the modal equations in (5.8) and then eliminating the modal coordinates between the two equations, the characteristic equation can be obtained as

$$\mu_* \Big(1 - \kappa_* \frac{\mu_r}{\kappa_r}\Big) \xi^4 - (\mu_* + \kappa_*) \xi^2 + \kappa_* + i\xi\beta_*(1 - \xi^2) = 0 \tag{5.10}$$

in which the parameters κ_*, μ_* and β_* represent the total stiffness, mass and damper ratios including corrections as

$$\frac{1}{\mu_*} = \frac{1}{\mu_r} + \frac{1}{\mu'_r} \quad , \quad \frac{1}{\kappa_*} = \frac{1}{\kappa_r} + \frac{1}{\kappa'_r} \quad , \quad \beta_* = \beta_r \frac{\kappa_*}{\kappa_r} \frac{\mu_*}{\mu_r} \tag{5.11}$$

where $\mu_r = m_a/m_r$ and $\kappa_r = k_a/k_r$ are the modal mass and stiffness ratios, describing the relation between the absorber parameters and the modal mass and stiffness. Similarly, the mass and stiffness correction ratios μ'_r and κ'_r represent the residual mode contributions m'_r and k'_r introduced in (5.9). The viscous damping coefficient c_a is contained in the modal damper ratio $\beta_r = c_a/\sqrt{k_r m_r}$. The characteristic equation is furthermore normalized with respect to the frequency associated with locking of the absorber masses to the structure,

$$\xi = \frac{\omega}{\omega_{\infty,r}} = \omega \sqrt{\frac{m_r}{k_r}} \tag{5.12}$$

Because of the structural equation in (5.5a) with the mass matrix in (5.6) the characteristic equation in (5.10) remains within a fourth-order polynomial format. For a classic modal expansion based on the undamped mode shapes $\tilde{\mathbf{q}}_{0,r}$, the residual mode correction implies a fifth-order polynomial, whereby the calibration requires an approximation [38].

5.1.3 Absorber tuning

The total absorber ratios including corrections κ_* and μ_* are tuned according to a desired tuning principle. The classic tuning procedure leads to a semi-circular root locus trajectory, where two initial branches meet at a bifurcation point and then split into a branch approaching the real axis at the frequency $\omega_\infty = \omega_r$ and an other branch approaching the imaginary axis. This behaviour is shown in Fig. 5.3d of the example in Section 5.3. With n_a absorbers, $n_a - 1$ modes will be redundant absorber modes with high modal damping approaching the imaginary axis along a central backbone locus. The two other modes, indicated with ($\circ$) and ($\square$) markers in Fig. 5.3c, are the coupled structure-absorber modes that determine the attainable damping and thus the absorber performance.
The largest modal damping ratio is obtained at the bifurcation point where the two semi-circular paths meet. However, this point is associated with constructive interference, leading to high dynamic response amplification. A good compromise between high modal damping and limited amplification is achieved by the equal modal damping principle described in [37]. This method leads to a lower damping ratio as indicated by the asterisks, but ensures a flat response plateau.

The equal modal damping principle can be expressed by a generic characteristic equation, as given in [37] and used in [P3]. The tuning formulas are obtained by direct comparison of the factors to this generic equation and the factors to the characteristic equation in (5.10).
The procedure assumes a constant absorber mass m_a, whereby the total mass ratio μ_* including correction in (5.11) does not redefine the mass ratio μ_r. However, when the background corrections have been determined, the stiffness and damper ratios are re-tuned by the relations

$$\frac{\kappa_*}{\mu_*} = \frac{1}{1 + \mu_* \dfrac{\mu_r}{\kappa_r}} \quad , \quad \frac{\beta_*}{\kappa_*} = \sqrt{2\mu_* \frac{\mu_r}{\kappa_r}} \tag{5.13}$$

where details on the derivation are given in [P3]. When the residual modes are not included in the tuning, the correction ratios κ_r' and μ_r' disappear, whereby $\kappa_* = \kappa_r$ and $\mu_* = \mu_r$. In this case the tuning formulas (5.13) are simplified and recover the basic tuning formulas in e.g. [36].
As the absorber mass is kept constant, the tuning is not based on a specified modal damping ratio or a selected amplification level. The updated modal damping ratio for the structural modes can however be estimated as

$$\zeta_r^{\text{est}} \simeq \sqrt{\tfrac{1}{8}\mu_* \frac{\mu_r}{\kappa_r}} \tag{5.14}$$

The above expressions ensure equal modal damping for the two structural modes based on the specified mass ratio μ_r, and (5.14) can be used to roughly estimate a mass ratio μ_r that secures a sufficient modal damping ratio.

5.1.4 Calibration and design

Determination of the residual mode corrections k_r' and m_r' and thereby the total stiffness and mass ratios κ_* and μ_* including corrections requires information about the complete structure, which includes the non-resonant modes. When the absorbers are mounted on the structure without damper effect ($c_a = 0$) the structural mode splits into two coupled modes. In Fig. 5.3c the two undamped frequencies ω_A and ω_B, associated with structure-absorber interaction, contain contributions from all modes. The correction parameters k_r' and m_r' may therefore be calibrated based on these two frequencies. When the absorber parameters are subsequently modified, the frequencies will change. However, as long as this change is moderate the correction ratios κ_r' and μ_r' are most likely obtained with sufficient accuracy.

The design procedure consists of choosing an absorber mass $\widetilde{m}_a$, which hereafter is kept constant. The infinitely damped mode shapes with the absorber masses locked to the structure are hereafter determined, resulting in the modal equations in (5.8). Based on the absorber mass, the uncorrected stiffness ratio and damper ratio are tuned by (5.13) for $\kappa_* = \kappa_r$ and $\mu_* = \mu_r$, as the correction ratios κ_r' and μ_r' have not yet been determined. From the tuned stiffness ratio the corresponding spring stiffness k_a without residual mode corrections is then calculated. The approximate absorber mass $\widetilde{m}_a$ and tuned absorber stiffness $\widetilde{k}_a$ are then assumed to be representative for the structure with absorbers, and denoted with a tilde to indicate that they are initial estimates.
The frequencies ω_A and ω_B are then calculated based on the representative parameters $\widetilde{m}_a$ and $\widetilde{k}_a$, and the characteristic equation in (5.10) without damping $\beta_* = 0$ is then solved to obtain the representative estimates $\widetilde{\mu}_*$ and $\widetilde{\kappa}_*$. These parameters are determined by matching the frequency solutions to the characteristic equation (5.10) for the two representative frequencies ω_A and ω_B. The resulting mass and stiffness ratios including background corrections then appear as

$$\widetilde{\mu}_* = \frac{\widetilde{\kappa}_r}{\widetilde{\mu}_r} \frac{\xi_A^2 \xi_B^2 - \xi_A^2 - \xi_B^2 + 1}{\xi_A^2 \xi_B^2 - \xi_A^2 - \xi_B^2} \quad , \quad \widetilde{\kappa}_* = -\frac{\widetilde{\kappa}_r}{\widetilde{\mu}_r} \frac{\xi_A^2 \xi_B^2 - \xi_A^2 - \xi_B^2 + 1}{\xi_A^2 \xi_B^2} \tag{5.15}$$

where $\xi_{A,B} = \omega_{A,B}/\omega_r$ are the normalized frequencies. When $\widetilde{\mu}_*$ and $\widetilde{\kappa}_*$ from (5.15) are assumed to accurately represent the structure including background modes, the correction ratios κ_r' and μ_r' are calculated from (5.11), and then assumed to represent the influence from the residual modes ($j \neq r$).
The stiffness ratio κ_* and damper ratio β_* are now re-tuned according to (5.13), in which $\mu_* = \widetilde{\mu}_*$ includes residual mode correction by the expression (5.15). Subsequently this gives the absorber stiffness k_a and damping coefficient c_a, now corrected with respect to the interaction with the other modes. As the absorber mass m_a is

kept constant, the total mass ratio μ_* will not give a corrected value of the absorber mass m_a. Further details on the design procedure can be found in [P3].

5.2 Absorber balancing

When multiple absorbers are placed on the structure targeting the same vibration mode, inhomogeneous balancing factors should be introduced for the individual absorbers. The balancing factors in the balancing matrix $\boldsymbol{\alpha}$ in (5.4) are functions of the modal displacement due to different stiffness in the different directions of the beam, as well as the influence from the boundary conditions. In this section the approximate method for balancing viscous dampers derived in [41] and used in Section 3.3.2 is applied.

An analogy to the viscous damper may be drawn for the mass absorber. With constant absorber parameters, the absorber forces may be given by a frequency function $H(\omega)$ as

$$\widetilde{\mathbf{f}}_a = i\omega m_a \frac{i\omega(k_a + i\omega c_a)}{-\omega^2 m_a + k_a + i\omega c_a} \boldsymbol{\alpha}\widetilde{\mathbf{u}}_s = i\omega H(\omega)\boldsymbol{\alpha}\widetilde{\mathbf{u}}_s \tag{5.16}$$

For pure viscous dampers the frequency function $H(\omega)$ would become real-valued, as considered in [41]. The mass absorbers are tuned to a selected resonant mode. Assuming resonance therefore gives an estimate of the working behaviour of the absorbers. At resonance the stiffness and inertia terms in the denominator of (5.16) cancel as $k_a \simeq m_a\omega^2$, whereby the frequency function is approximated as

$$H(\omega) \simeq m_a \frac{i\omega(k_a + i\omega c_a)}{i\omega c_a} \simeq m_a \frac{k_a}{c_a} \tag{5.17}$$

The last approximation assumes $\omega c_a \ll k_a$. The tuned mass absorber therefore acts as a viscous damper around resonance, with the viscous parameter $m_a k_a / c_a$. Thus, around resonance it seems appropriate to determine the relative balancing of the absorbers by the method presented in Section 3.3.2. In many cases this approach provides seemingly good estimates for the individual balancing of the mass absorbers.

5.3 Example: Damping by multiple absorbers

The use of multiple mass absorbers for damping of fully coupled flexible beam vibrations is illustrated by an example, and the section summarises the results from [P3]. The cantilever beam in Fig. 5.2 is mounted with three absorbers; one rotational and two translational. They are placed in the fourth node along the beam and attached to the origin of the beam axes to remain within a single-unit-value construction of the connectivity vectors $\mathbf{w}$. In the present case the origin of the beam axes is placed in the shear centre A to obtain a simple structural model. For another absorber

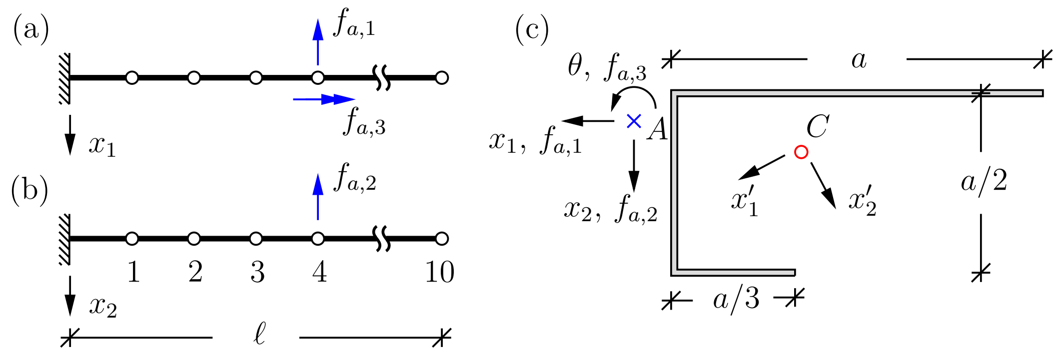

Figure 5.2. (a,b) Cantilever beam with three absorber forces and (c) beam cross-section.

location, the beam axes must simply be placed at the different location. The cross-section is the asymmetric C-profile in Fig. 5.2c. The material is isotropic and the length of the beam is $\ell/a = 40$. The structure is modelled with the beam elements shown in Fig. 2.2b.

First step is to balance the individual absorbers. Based on the analogy to the viscous dampers in Section 5.2, the balancing factors are according to Section 3.3.2 found to be $\boldsymbol{\alpha} = \mathrm{diag}[\,1\,,\,1.735\,,\,0.038a^2\,]$. The factor a^2 on the rotational absorber appears because the rotational inertia is described by a mass moment of inertia. The balancing factors change according to the positioning along the beam and on the cross-section, whereby they must be re-calculated for a new absorber position.

Due to the indirect positioning of the absorbers the residual mode corrections are calibrated based on initial estimates of the absorber parameters. These parame-

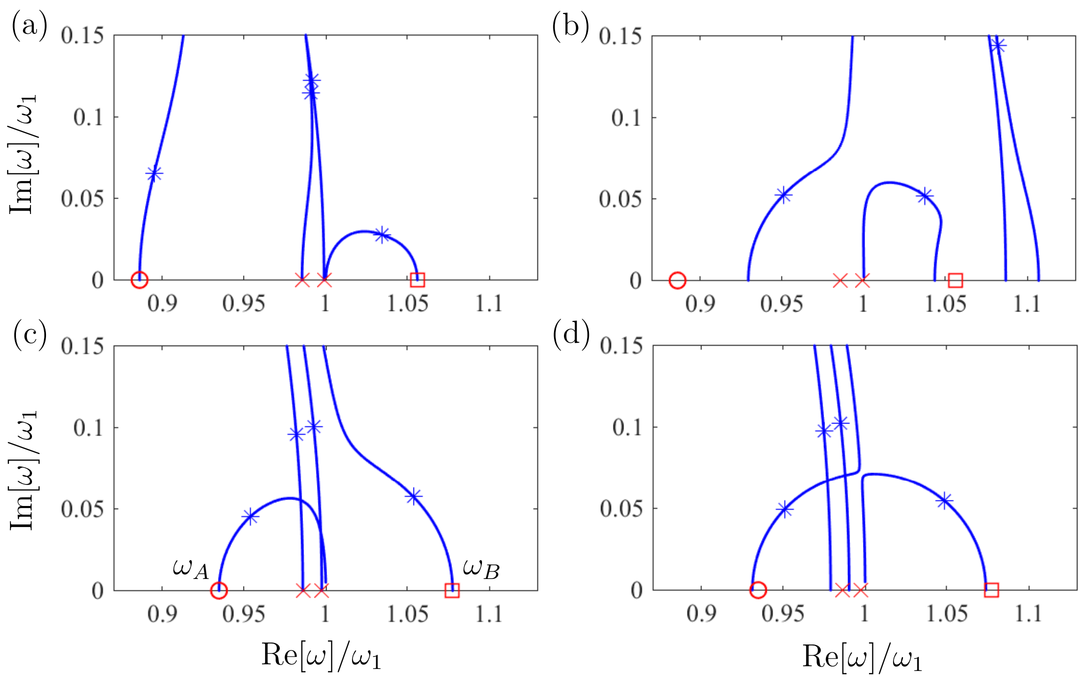

Figure 5.3. Root loci (a,c) without correction, (b,d) with correction, (a,b) not balanced and (c,d) balanced.

ters are determined based on a tuning without the corrections. For an initially desired modal damping ratio the corresponding mass ratio and absorber mass can be calculated and then kept constant for the remaining analysis. For a desired damping ratio of $\zeta_{\text{des}} = 0.05$ the mass ratio is $\mu_r = 0.0206$ and the stiffness ratio is $\kappa_r = \mu_r(1 - \mu_r) = 0.0202$ according to (5.13). From these ratios the fixed absorber mass m_a and estimated absorber stiffness $\widetilde{k}_a$ are used to calculate ω_A and ω_B, from which the corrected mass ratio $\widetilde{\mu}_*$ is obtained. After a re-tuning the final absorber parameters are then determined.
The residual mode correction and balancing changes the behaviour of the frequencies in the complex plane. Figure 5.3 shows the trajectories of the root locus without correction (a,c) and with correction (b,d). The two top subplots are for homogeneous balancing $\boldsymbol{\alpha} = \text{diag}[\,1\,,\,1\,,\,1\,]$ while the bottom two are for inhomogeneous balancing obtained by Section 5.2. The frequencies ω_A ($\circ$) and ω_B ($\square$) are identified in Fig. 5.3c with the inhomogeneous balancing, whereas the homogeneous balancing in Fig. 5.3a obscures the semi-circular behaviour of the root locus. With calibrated parameters, Fig. 5.3d shows the desired semi-circular behaviour, with the asterisks indicating the equal modal damping ratios for the structural modes, while the frequencies marked with the circle and square markers are only changed slightly due to the calibrated residual mode parameters κ_r' and μ_r'. Without balancing but with calibrated parameters, Fig. 5.3b shows that the balancing indeed is necessary in order to achieve the fully semi-circular curves with a bifurcation point in Fig. 5.3d.
The damping ratio after correcting the absorber parameters are according to (5.14) determined to be $\zeta_1^{\text{est}} = 0.05210$. The actual damping ratios of the two structural modes are subsequently found to be $\zeta_1 = 0.0527$ and 0.0525, while the two redundant absorber modes have twice as large damping ratios of $\zeta_1^a = 0.1005$ and 0.1043. As shown in [P3] the balancing and calibration furthermore results in flat plateaus of the frequency response curves when loaded by a spatially distributed load orthogonal to the other modes.

6 | Conclusions

This thesis considers damping of torsional and coupled bending-torsion vibrations in thin-walled beams by supplemental and discrete damping devices. The main emphasis has been on a novel concept of introducing damping by restraining the warping displacements associated with torsion by viscous dampers and by active actuators with PPF control. To accommodate the local effects of the discrete devices it has been demonstrated how to establish equivalent and computationally efficient models as alternatives to full 3D FE models. Thirdly it has been shown how to calibrate and balance multiple mass absorbers to account for background effects and different positioning.

For pure torsional vibrations viscous dampers were used. In practice warping is easily restrained by suitable configurations of discrete dampers constituting pure bimoments. These dampers only restrain warping at their point of application, and a 3D FE model was set up to model the residual warping. Such a model easily has several thousand degrees-of-freedom and is computationally inefficient. Therefore the analytical solutions to the differential equation governing torsional vibrations was supplemented by a viscous boundary condition taking the actual configuration of dampers into account by a single equivalent viscous bimoment. The residual flexibility associated with the partial warping restrainment was conveniently modelled as a fictitious spring in series with the damper. This fictitious spring stiffness was calibrated from 3D FE results and included in the analytical boundary condition. When calibrating the analytical model properly it is computationally superior to the full 3D model, as it may easily be solved iteratively. Good agreement between the two models was shown together with significant damping ratios.

For coupled vibrations the analytical solutions become unmanageable and therefore a beam element model was set up as alternative to the 3D model. When torsion couples with bending the displacements at the beam end is mixed and restraining only the warping part gives less effect. Therefore an active PPF concept was applied and the beam model was supplemented by the residual flexibility from the partial warping restrainment. This flexibility lowered the allowable value of the actuator gain ensuring a stable system and bounded response. In order to only restrain the warping part of the coupled response, the actuators in the 3D model were spatially filtered combining them as a single dissipative bimoment. This resulted in noticeable damping ratios and good agreement between the two models was observed.

Due to the good compliance with the full 3D model, the calibration of the simpler analytical and beam element models constitute solid alternatives for initial designs where several geometries and actuator configurations are investigated. The method therefore seems promising for structures where the beam end cross-section is suitable for installation of discrete devices.

Multiple mass absorbers were furthermore investigated for damping of the same targeted beam vibration mode. The background effect from the non-resonant modes was calibrated by two terms representing the excess absorber support motion. Approximate balancing of the mass absorbers showed the need for non-identical balancing. Proper calibration and balancing of the absorbers resulted in the desired properties of the applied equal modal damping principle.

Suggestions for future work

Investigation of the following topics is among others suggested in order to extend and improve the current work:

- Closed cross-sections are more rigid in torsion and restraining warping at a beam boundary has a limited effect. As several relevant civil engineering type structures are constructed with closed cross-section, it is suggested to perform similar analyses for such structures. The viscous damping concept may be insufficient, but an active concept may prove to introduce sufficient damping.
- The configuration of discrete actuators in Chapter 4 used to restrain the warping part of the coupled response, may as well be applied for the bending part of the cross-section displacements. Establishing a filter which relatively works on both torsional warping and the inclination from bending will yield even greater damping potentials. This can be achieved by two spatial filters, but requires a relative balancing.
- For beam structures where the beam end is not suitable for applying discrete devices an alternative is to use devices working on the relative motion and therefore could be placed between the beam ends, and eventually inside a closed cross-section contour.
- The balancing method proposed for the tuned mass absorbers is derived for viscous dampers, and a proper balancing principle for mass absorbers should be investigated.

References

[1] Achkire, Y., Bossens, F. and Preumont, A., Active damping and flutter control of cable-stayed bridges, *Journal of WInd Engineering and Industrial Aerodynamics.*, vol. 74-76, pp. 913-921, 1998.

[2] Al-Jumaily, A.M. and Faulkner, L.L., Vibration of continuous systems with compliant boundaries, *Journal of Sound and Vibration*, vol. 54, no. 2, 203-213, 1977.

[3] Andersen, M.S. et. al., Aerodynamic stability of long span suspension bridges with low torsional natural frequencies, *Engineering Structures*, vol. 120, pp. 82-91, 2016.

[4] Arrigan, J. et. al., Control of flapwise vibrations in wind turbine blades using semi-active tuned mass dampers, *Structural Control and Health Monitoring*, vol. 18, no. 8, pp. 840-851, 2011.

[5] Balas, M.J., Direct velocity feedback control of large space structures, *Journal of Guidance, Control and Dynamics*, vol. 2, no. 3, pp. 252-253, 1979.

[6] Banerjee, J.R., Guo, S. and Howson, W.P., Exact dynamic stiffness matrix of a bending-torsion coupled beam including warping, *Computers and Structures*, vol. 59, no. 4, pp. 613-621, 1996.

[7] Barr, A.D.S. and Duthie, T., Influence of cross-section distortion on the bending vibration of thin-walled beams of H section, *Journal of Mechanical Engineering Science*, vol. 6, no. 3, pp. 211-218, 1964.

[8] Baz, A. and Poh, S., Optimal vibration control with modal positive position feedback, *Optimal Control Applications and Methods*, vol. 17, no. 2, pp. 141-149, 1996.

[9] Casalotti, A., Arena, A. and Lacarbonara, W., Mitigation of post-flutter oscillations in suspension bridges by hysteretic tuned mass dampers, *Engineering Structures*, vol. 69, pp. 62-71, 2014.

[10] Cha, P.D. and Yoder, N.C., Applying Sherman-Morrison-Woodbury formulas to analyze the free and forced responses of a linear structure carrying lumped elements, *Journal of Vibration and Acoustics*, vol. 129, no. 3, pp. 307-316, 2007.

[11] Chen, B. et. al., Enhancement of flutter stability in wind turbines with a new type of passive damper of torsional rotation of blades, *Journal of Wind Engineering and Industrial Aerodynamics*, vol. 173, pp. 171-179, 2018.

[12] Christiano, P. and Salmela, L., Frequencies of Beams with Elastic Warping Restraint, *Journal of the Structural Division*, vol. 97, no. 6, pp. 1835-1840, 1971.

[13] Cook, R.D. et. al., Concepts and Applications of Finite Element Analysis, Wiley, 4th ed., 2002.

[14] Den Hartog, J.P., *Mechanical Vibrations*, 4th ed. New York, McGraw-Hill, 1956, (reprinted by Dover, New York, 1985).

[15] Elias, S. and Matsagar, V., Research developments in vibration control of structures using passive tuned mass dampers, *Annual Reviews in Control*, vol. 44, pp. 129-156, 2017.

[16] Fanson, J.L. and Caughey, T.K., Positive position feedback control for large space structures, *AIAA Journal*, vol. 28, no. 4, 1990.

[17] Friberg, P.O., Beam element matrices derived from Vlasov's theory of open thin-walled elastic beams, *International Journal for Numerical Methods in Engineering*, vol. 21, pp. 1205-1228, 1985.

[18] Ge, Y.J. and Tanaka, H., Aerodynamic flutter analysis of cable-supported bridges by multi-mode and full-mode approaches, *Journal of Wind Engineering and Industrial Aeridynamics*, vol. 8, no. 2-3, pp. 123-153, 2000.

[19] Géradin, M. and Cardona, A., Flexible Multibody Dynamics, A Finite Element Approach, Wiley, 2001.

[20] Gere, J.M., Torsional vibrations of beams of thin-walled open section, *ASME Journal of Applied Mechanics*, vol. 21, no. 4, pp. 381-387, 1954.

[21] Gere, J.M. and Lin, Y.K., Coupled vibrations of thin-walled beams of open cross-section, *Journal of Applied Mechanics*, vol. 25, pp. 373-378, 1958.

[22] Geurts, C., Vrouwenvelder, T., van Staalduinen, P. and Reusink, J., Numerical modelling of rain-wind induced vibrations: Erasmus Bridge, Rotterdam, *Structural Engineering International (IABSE)*, 2, pp. 129-135, 1998.

[23] Goh, C.J. and Caughey, T.K., On the stability problem caused by finite actuator dynamics in the collocated control of large space structures, *International Journal of Control*, vol. 41, no. 3, pp. 787-802, 1985

[24] Hajianmaleki, M. and Qatu, M.S., Vibrations of straight and curved composite beams: A review, *Composite Structures*, vol. 100, pp. 218-232, 2013.

[25] Hansen, M.H., Aeroelastic instability problems for wind turbines, *Wind Energy*, vol. 10, pp. 551-577, 2007.

[26] Housner, G.W. et. al., Structural control: Past, present, and future, *Journal of Engineering Mechanics*, vol. 123, no. 9, pp. 897-971, 1997.

[27] Høgsberg, J., A robust calibration procedure for multiple electromechanical shunt absorbers on a flexible structure, *Proceedings of the IX ECCOMAS Thematic Conference on Smart Structures and Materials*, July, 2019.

[28] Høgsberg, J., Hoffmeyer, D. and Ejlersen, C., Damping of torsional beam vibrations by control of warping displacement, *Journal of Vibration and Acoustics*, vol. 138, no. 1, pp. 014501, 2016.

[29] Høgsberg, J. and Krenk, S., Linear control strategies for damping of flexible structures, *Journal of Sound and Vibration*, vol. 293, no. 1-2, pp. 59-77, 2006.

[30] Høgsberg, J. and Krenk, S., Analysis of moderately thin-walled beam cross-sections by cubic isoparametric elements, *Computers and Structures*, vol. 134, pp. 88-101, 2014.

[31] Inman, D., Engineering Vibration, Pearson, 4th ed., 2014.

[32] Jangid, R.S. and Datta, T.K., Performance of multiple tuned mass dampers for torsionally coupled systems, *Earthquake Engineering and Structural Dynamics*, vol. 26, no. 3, pp. 307-317, 1997.

[33] Jönsson, J., Determination of shear stresses, warping functions and section properties of thin-walled beams using finite elements, *Computers and Structures*, vol. 68, no. 4, pp. 393-410, 1998.

[34] Keller, P., Higgins, C. and Lovejoy, S.C., Evaluation of torsional vibrations in steel truss bridge members" *Journal of Bridge Engineering*, vol. 20, no. 9, p. 04014102, 2015.

[35] Krenk, S., Vibrations of a taut cable with an external damper, *Journal of Applied Mechanics*, vol. 67, no. 4, pp. 772-776, 2000.

[36] Krenk, S., Frequency analysis of the tuned mass damper, *Journal of Applied Mechanics*, vol. 72, no. 6, pp. 936-942, 2005.

[37] Krenk, S. and Høgsberg, J., Equal modal damping design for a family of resonant vibration control formats, *Journal of Vibration and Control*, vol. 19, no. 9, pp. 1294-1315, 2013.

[38] Krenk, S. and Høgsberg, J., Tuned resonant mass or inerter-based absorbers: unified calibration with quasi-dynamic flexibility and inertia correction, *Proceedings of the Royal Society A - Mathematical, Physical and Engineering Sciences*, vol. 472, no. 2185, pp. 20150718, 2016.

[39] Li, C. and Qu, W., Optimum properties of multiple tuned mass dampers for reduction of translational and torsional response of structures subject to ground acceleration, *Engineering Structures*, vol. 28, no. 4, pp. 472-494, 2006.

[40] Mahmoodi, N. and Mehdi, A., Active vibration control with modified positive position feedback, *Journal of Dynamic Systems, Measurement and Control*, vol. 131, no. 4, pp. 1-8, 2009.

[41] Main, J.A. and Krenk, S., Efficiency and tuning of viscous dampers on discrete systems, *Journal of Sound and Vibration*, vol. 286, no. 1-2, pp. 97-122, 2005.

[42] Makris, N. and Chang, S.P., Effect of viscous, viscoplastic and friction damping on the response of seismic isolated structures, *Earthquake Engineering and Structural Dynamics*, vol. 29, no. 1, pp. 85-107, 2000.

[43] Mei, C., Coupled vibrations of thin-walled beams of open section using the finite element method, *International Journal of Mechanical Sciences*, vol. 12, no. 10, pp. 883-891, 1970.

[44] Mokrani, B. et. al., Passive damping of suspension bridges using multi-degree of freedom tuned mass dampers, *Engineering Structures*, vol. 153, pp. 749-756, 2017.

[45] Preumont, A., Vibration control of active structures, Springer, 3rd ed., 2011.

[46] Saeed, T.E. et. al., A state-of-the-art review of structural control systems, *Journal of Vibration and Control*, vol. 21, no. 5, pp. 919-937, 2015.

[47] Sapountzakis, E.J., Bars under torsional loading: A generalized beam theory approach, *ISRN Civil Engineering*, vol. 2013, pp. 1-39, 2013.

[48] Snowdon, J.C., The cruciform dynamic vibration absorber, *Journal of the Acoustical Society of America*, vol. 75, no. 6, pp. 1792-1799, 1984.

[49] Soong, T.T. and Spencer Jr., B.F., Supplemental energy dissipation: state-of-the-art and state-of-the-practice, *Engineering Structures*, vol. 24, pp. 243-259, 2002.

[50] Spencer, B.F. and Nagarajaiah, S., State of the art of structural control, *Journal of Structural Engineering*, vol. 129, no. 7, pp. 845-856, 2003.

[51] Svedholm, C. et. al., Vibration of damped uniform beams with general end conditions under moving loads, *Engineering Structures*, vol. 126, pp. 40-52, 2016.

[52] Tanaka, M. and Bercin, A.N., Finite element modelling of the coupled bending and torsional free vibration of uniform beams with an arbitrary cross-section, *Applied Mathematical Modelling*, vol. 21, no. 6, pp. 339-344, 1997.

[53] Vlasov, V.Z., Thin-walled elastic beams, Israel Program for Scientific Translation, Jerusalem, 1961.

[54] Vo, T.P. and Lee, J., Flexural-torsional coupled vibration and buckling of thin-walled open section composite beams using shear-deformable beam theory, *International Journal of Mechanical Sciences*, vol. 51, no. 9-10, pp. 631-641, 2009.

[55] Zheng, L., Zhang, H., Zhao, B. and Xianjie, L., Shaking table test and numerical simulation on vibration control effects of TMD with different mass ratios on a super high-rise structure, *Structural Design of Tall and Special Buildings*, vol. 27, no. 9, pp. e1470, 2018.

[56] Zuo, H., Bi, K. and Hao, H., Mitigation of tower and out-of-plane blade vibrations of offshore monopile wind turbines by using multiple tuned mass dampers, *Structure and Infrastructure Engineering*, vol. 15, no. 2, pp. 269-284, 2019.

[57] Øiseth, O. and Sigbjörnsson, R., An alternative analytical approach to prediction of flutter stability limits of cable supported bridges, *Journal of Sound and Vibration*, vol. 330, no. 12, pp. 2784-2800, 2011.

A Damping of a Beam with Closed Cross-Section

This appendix contains an example of damping of the lowest pure torsional mode of a beam element model with a symmetric closed cross-section. Two simply supported beam configurations are investigated; the beam in Fig. A.1a with a single bimoment and the beam in Fig. A.1b with two bimoments. The beam has length $\ell/a = 30$, the geometry as shown in Fig. A.1c, overall thickness $t = a/40$ and isotropic material. As the cross-section is not quadratic, it warps with the sector-coordinate shown in the figure, with identical corner-values of $\psi_c = a^2/24$. The two bimoments in Fig. A.1b are identical due to symmetry.

The two beam configurations are damped by viscous bimoments by the method in Chapter 3, and by active actuators with PPF control as in Chapter 4. The bimoments restrain the warping of the entire cross-section due to the increased torsional rigidity and vanishing warping displacements. The corresponding root loci and damping ratios are seen in Fig. A.2. The viscous analysis yields two semi-circular root loci, where case (b) has a larger relative frequency increment due to the two bimoments. The relative frequency increments are $(\omega_\infty - \omega_0)/\omega_0 = 0.0041$ and 0.0082, respectively, and the damping ratios are $\zeta = 0.002$ and 0.0041, respectively. Introducing an additional bimoment thus approximately doubles the maximum damping ratio.

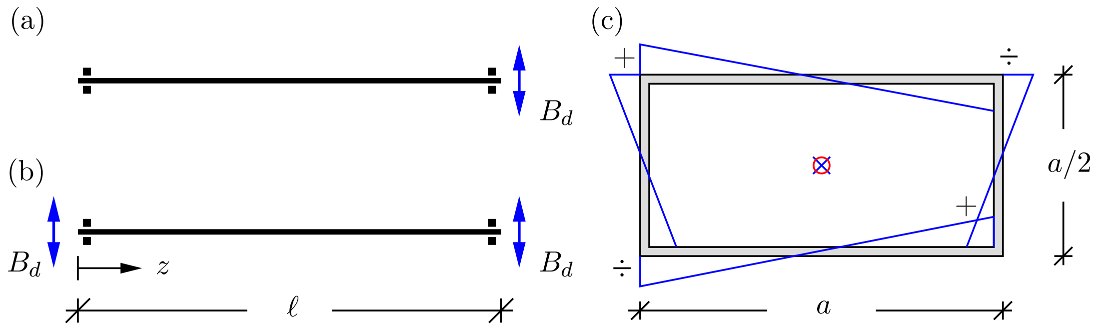

Figure A.1. Simply supported beam with (a) a single bimoment and (b) two bimoments. (c) Cross-section and sector-coordinate with corner-value $\psi_c = a^2/24$.

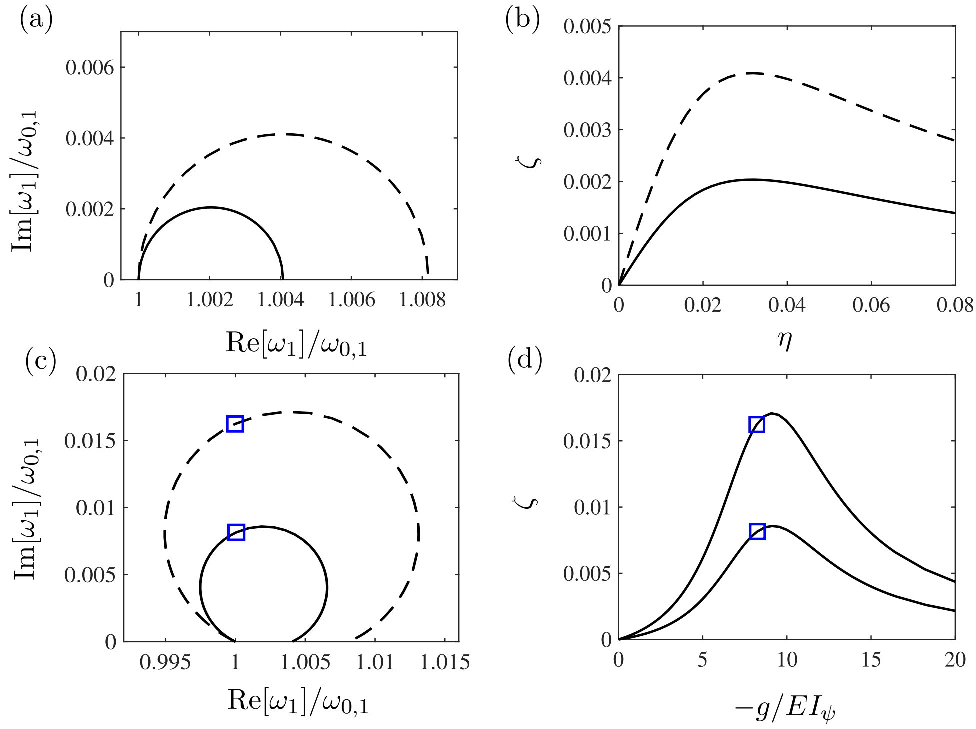

Figure A.2. Root loci (a,c) and damping ratio (b,d) by the viscous analysis (a,b) and the PPF control (c,d).

For the PPF control the relative frequency increments are identical to the viscous analysis, but the maximum damping ratios at the point of instability are $\zeta = 0.0086$ and 0.017. Due to the nature of the closed cross-section the effect of restraining warping is thus limited, as the warping effect becomes very localized at the support.

B | Transcendental Equations

This appendix contains a series of transcendental equations obtained from solving the differential equation (2.1) governing pure torsional vibrations. Ordinary boundary conditions as well as added torsion and warping springs and damping treatment are applied. The following tables are organized in a structured manner such that most tables contain a specific boundary condition at the left end. Even though some cases are repeated the equations are presented in a consistent manner.

B.1 Beams with ordinary boundary conditions

The ordinary and typical boundary conditions consist of a free end, a fixed end, and 'simple' end where torsion is restrained but warping is allowed and a 'no warp' end where warping is restrained but torsion allowed. The requirements to the angle of twist φ and its derivatives follow as,

$$\begin{aligned} k^2\varphi'(z) - \varphi'''(z) &= 0 \quad , \quad \text{Free rotation} \\ \varphi''(z) &= 0 \quad , \quad \text{Free warping} \\ \varphi'(z) &= 0 \quad , \quad \text{Restrained warping} \\ \varphi(z) &= 0 \quad , \quad \text{Restrained rotation} \end{aligned} \tag{B.1}$$

where k is given in (2.5). A rotation restraint is indicated by two markers as for the right end of the *Free-simple* beam in Table B.1, a restraint on warping is indicated by a vertical line as for the *Free-no warp* beam and a restraint on both torsion and warping are indicated by the clamped end as for the *Free-fixed* beam.

Table B.1. Beams with a free left end.

Free-free beam.

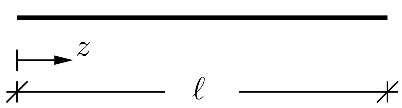

$$k^2\varphi'(0) - \varphi'''(0) = 0 \qquad k^2\varphi'(\ell) - \varphi'''(\ell) = 0$$
$$\varphi''(0) = 0 \qquad \varphi''(\ell) = 0$$

$$\big((\alpha\ell)^6 - (\beta\ell)^6\big)\sinh(\alpha\ell)\sin(\beta\ell) + 2(\alpha\ell)^3(\beta\ell)^3\big(\cosh(\alpha\ell)\cos(\beta\ell) - 1\big) = 0$$

Free-simple beam.

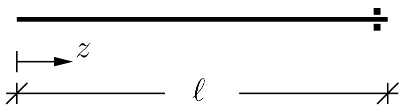

$$k^2\varphi'(0) - \varphi'''(0) = 0 \qquad \varphi(\ell) = 0$$
$$\varphi''(0) = 0 \qquad \varphi''(\ell) = 0$$

$$(\alpha\ell)^3\tanh(\alpha\ell) - (\beta\ell)^3\tan(\beta\ell) = 0$$

Free-no warp beam.

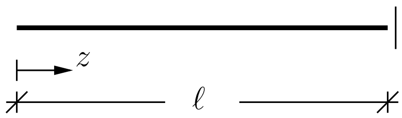

$$k^2\varphi'(0) - \varphi'''(0) = 0 \qquad k^2\varphi'(\ell) - \varphi'''(\ell) = 0$$
$$\varphi''(0) = 0 \qquad \varphi'(\ell) = 0$$

$$(\beta\ell)^3\tanh(\alpha\ell) + (\alpha\ell)^3\tan(\beta\ell) = 0$$

Free-fixed beam.

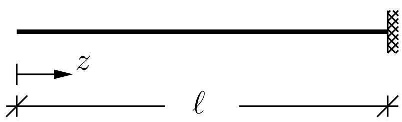

$$k^2\varphi'(0) - \varphi'''(0) = 0 \qquad \varphi(\ell) = 0$$
$$\varphi''(0) = 0 \qquad \varphi'(\ell) = 0$$

$$\frac{(\alpha\ell)^4 + (\beta\ell)^4}{(\alpha\ell)^2(\beta\ell)^2}\cosh(\alpha\ell)\cos(\beta\ell) + \frac{(\alpha\ell)^2 - (\beta\ell)^2}{(\alpha\ell)(\beta\ell)}\sinh(\alpha\ell)\sin(\beta\ell) + 2 = 0$$

Table B.2. Beams with a simple left end.

Simple-free beam.

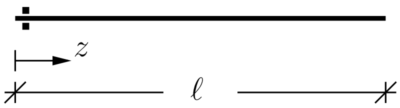

$$\varphi(0) = 0 \qquad k^2\varphi'(\ell) - \varphi'''(\ell) = 0$$
$$\varphi''(0) = 0 \qquad \varphi''(\ell) = 0$$

$$(\alpha\ell)^3 \tanh(\alpha\ell) - (\beta\ell)^3 \tan(\beta\ell) = 0$$

Simple-simple beam.

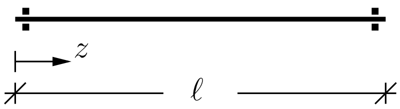

$$\varphi(0) = 0 \qquad \varphi(\ell) = 0$$
$$\varphi''(0) = 0 \qquad \varphi''(\ell) = 0$$

$$\sin(\beta\ell) = 0$$

Simple-no warp beam.

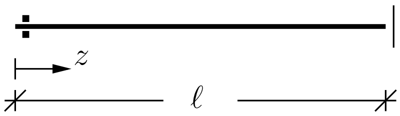

$$\varphi(0) = 0 \qquad k^2\varphi'(\ell) - \varphi'''(\ell) = 0$$
$$\varphi''(0) = 0 \qquad \varphi'(\ell) = 0$$

$$\cos(\beta\ell) = 0$$

Simple-fixed beam.

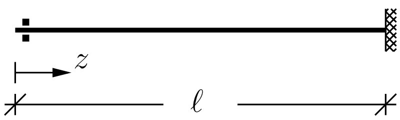

$$\varphi(0) = 0 \qquad \varphi(\ell) = 0$$
$$\varphi''(0) = 0 \qquad \varphi'(\ell) = 0$$

$$(\beta\ell) \tanh(\alpha\ell) - (\alpha\ell) \tan(\beta\ell) = 0$$

Table B.3. Beams with a 'no warp' left end.

No warp-free beam.

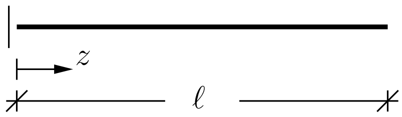

$$k^2\varphi'(0) - \varphi'''(0) = 0 \qquad k^2\varphi'(\ell) - \varphi'''(\ell) = 0$$
$$\varphi'(0) = 0 \qquad \varphi''(\ell) = 0$$

$$(\beta\ell)^3 \tanh(\alpha\ell) + (\alpha\ell)^3 \tan(\beta\ell) = 0$$

No warp-simple beam.

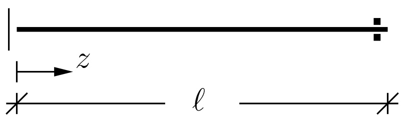

$$k^2\varphi'(0) - \varphi'''(0) = 0 \qquad \varphi(\ell) = 0$$
$$\varphi'(0) = 0 \qquad \varphi''(\ell) = 0$$

$$\cos(\beta\ell) = 0$$

No warp-no warp beam.

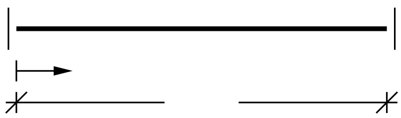

$$k^2\varphi'(0) - \varphi'''(0) = 0 \qquad k^2\varphi'(\ell) - \varphi'''(\ell) = 0$$
$$\varphi'(0) = 0 \qquad \varphi'(\ell) = 0$$

$$\sin(\beta\ell) = 0$$

No warp-fixed beam.

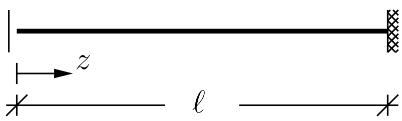

$$k^2\varphi'(0) - \varphi'''(0) = 0 \qquad \varphi(\ell) = 0$$
$$\varphi'(0) = 0 \qquad \varphi'(\ell) = 0$$

$$(\alpha\ell) \tanh(\alpha\ell) + (\beta\ell) \tan(\beta\ell) = 0$$

Table B.4. Beams with a fixed left end.

Fixed-free beam.

$$\varphi(0) = 0 \qquad k^2\varphi'(\ell) - \varphi'''(\ell) = 0$$
$$\varphi'(0) = 0 \qquad \varphi''(\ell) = 0$$

$$\frac{(\alpha\ell)^4 + (\beta\ell)^4}{(\alpha\ell)^2(\beta\ell)^2}\cosh(\alpha\ell)\cos(\beta\ell) + \frac{(\alpha\ell)^2 - (\beta\ell)^2}{(\alpha\ell)(\beta\ell)}\sinh(\alpha\ell)\sin(\beta\ell) + 2 = 0$$

Fixed-simple beam.

$$\varphi(0) = 0 \qquad \varphi(\ell) = 0$$
$$\varphi'(0) = 0 \qquad \varphi''(\ell) = 0$$

$$(\beta\ell)\tanh(\alpha\ell) - (\alpha\ell)\tan(\beta\ell) = 0$$

Fixed-no warp beam.

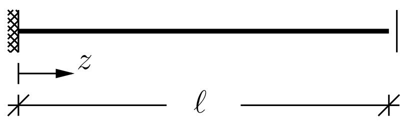

$$\varphi(0) = 0 \qquad k^2\varphi'(\ell) - \varphi'''(\ell) = 0$$
$$\varphi'(0) = 0 \qquad \varphi'(\ell) = 0$$

$$(\alpha\ell)\tanh(\alpha\ell) + (\beta\ell)\tan(\beta\ell) = 0$$

Fixed-fixed beam.

$$\varphi(0) = 0 \qquad \varphi(\ell) = 0$$
$$\varphi'(0) = 0 \qquad \varphi'(\ell) = 0$$

$$\big((\alpha\ell)^2 - (\beta\ell)^2\big)\sinh(\alpha\ell)\sin(\beta\ell) + 2(\alpha\ell)(\beta\ell)\big(1 - \cosh(\alpha\ell)\cos(\beta\ell)\big) = 0$$

B.2 Beams with rotation and warping springs

In the case of non-ideal boundary conditions where a complete restraint is not present, the dynamic behaviour of torsional beam vibrations can be modelled by added springs. A resistance on the rotation of a beam end can be established by the condition,

$$k^2 EI_\psi \varphi'(z) - EI_\psi \varphi'''(z) = -k_\varphi \varphi(z) \tag{B.2}$$

where k_φ is the rotational spring constant. Equivalently a resistance on the warping of a beam end may be implemented by the condition,

$$- EI_\psi \varphi''(z) = k_\psi \varphi'(z) \tag{B.3}$$

where k_ψ is the warping spring stiffness. An comprehensive yet not exhaustive list of corresponding transcendental equations is presented in the following tables.
The equations are structured such that for vanishing spring stiffness and transcendental equations recover the ones in Section B.1, whereas when the spring stiffness become finitely large, the transcendental equations reduce to the term (usually) in the { }-brackets. Several equations may however be reduced if not retaining this structure, but it is believed to give a greater overview.

Table B.5. Beams with a free left end.

Free-free beam with rotation spring.

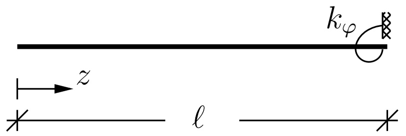

$$k^2 EI_\psi \varphi'(\ell) - EI_\psi \varphi'''(\ell) = -k_\varphi \varphi(\ell)$$
$$k^2\varphi'(0) - \varphi'''(0) = 0 \qquad \varphi''(\ell) = 0$$
$$\varphi''(0) = 0$$

$$\big((\alpha\ell)^6 - (\beta\ell)^6\big)\sinh(\alpha\ell)\sin(\beta\ell) + 2(\alpha\ell)^3(\beta\ell)^3\big(\cosh(\alpha\ell)\cos(\beta\ell) - 1\big) - \ell^3 \frac{k_\varphi}{EI_\psi}\frac{(\alpha\ell)^2 + (\beta\ell)^2}{(\alpha\ell)(\beta\ell)}\cosh(\alpha\ell)\cos(\beta\ell)\Big\{(\alpha\ell)^3\tanh(\alpha\ell) - (\beta\ell)^3\tan(\beta\ell)\Big\} = 0$$

Free-free beam with warping spring.

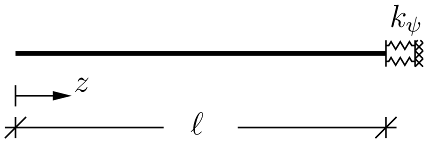

$$k^2\varphi'(0) - \varphi'''(0) = 0 \qquad k^2\varphi'(\ell) - \varphi'''(\ell) = 0$$
$$\varphi''(0) = 0 \qquad -EI_\psi\varphi''(\ell) = k_\psi\varphi'(\ell)$$

$$\big((\alpha\ell)^6 - (\beta\ell)^6\big)\sinh(\alpha\ell)\sin(\beta\ell) + 2(\alpha\ell)^3(\beta\ell)^3\big(\cosh(\alpha\ell)\cos(\beta\ell) - 1\big) - \ell\frac{k_\psi}{EI_\psi}\big((\alpha\ell)^2 + (\beta\ell)^2\big)\cosh(\alpha\ell)\cos(\beta\ell)\Big\{(\beta\ell)^3\tanh(\alpha\ell) + (\alpha\ell)^3\tan(\beta\ell)\Big\} = 0$$

Free-no warp beam with rotation spring.

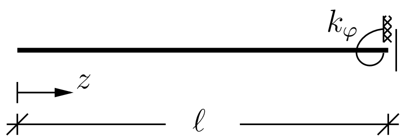

$$k^2 EI_\psi \varphi'(\ell) - EI_\psi \varphi'''(\ell) = -k_\varphi \varphi(\ell)$$
$$k^2\varphi'(0) - \varphi'''(0) = 0 \qquad \varphi'(\ell) = 0$$
$$\varphi''(0) = 0$$

$$(\beta\ell)^3\tanh(\alpha\ell) + (\alpha\ell)^3\tan(\beta\ell) - \ell^3\frac{k_\varphi}{EI_\psi}\frac{(\alpha\ell)(\beta\ell)}{(\alpha\ell)^2 + (\beta\ell)^2}\frac{1}{\cosh(\alpha\ell)\cos(\beta\ell)}\cdot \left\{\frac{(\alpha\ell)^4 + (\beta\ell)^4}{(\alpha\ell)^2(\beta\ell)^2}\cosh(\alpha\ell)\cos(\beta\ell) + \frac{(\alpha\ell)^2 - (\beta\ell)^2}{(\alpha\ell)(\beta\ell)}\sinh(\alpha\ell)\sin(\beta\ell) + 2\right\} = 0$$

Free-simple beam with warping spring.

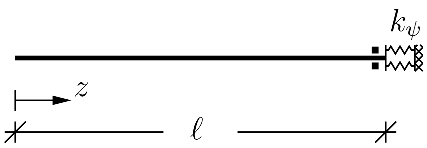

$$k^2\varphi'(0) - \varphi'''(0) = 0 \qquad \varphi(\ell) = 0$$
$$\varphi''(0) = 0 \qquad -EI_\psi\varphi''(\ell) = k_\psi\varphi'(\ell)$$

$$(\alpha\ell)^3\tanh(\alpha\ell) - (\beta\ell)^3\tan(\beta\ell) + \ell\frac{k_\psi}{EI_\psi}\frac{(\alpha\ell)^2(\beta\ell)^2}{(\alpha\ell)^2 + (\beta\ell)^2}\frac{1}{\cosh(\alpha\ell)\cos(\beta\ell)}\cdot \left\{\frac{(\alpha\ell)^4 + (\beta\ell)^4}{(\alpha\ell)^2(\beta\ell)^2}\cosh(\alpha\ell)\cos(\beta\ell) + \frac{(\alpha\ell)^2 - (\beta\ell)^2}{(\alpha\ell)(\beta\ell)}\sinh(\alpha\ell)\sin(\beta\ell) + 2\right\} = 0$$

Table B.6. Beams with a simple left end.

Simple-free beam with rotation spring.

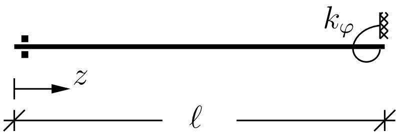

$$\begin{aligned} \varphi(0) &= 0 \quad & k^2 EI_\psi \varphi'(\ell) - EI_\psi \varphi'''(\ell) &= -k_\varphi \varphi(\ell) \\ \varphi''(0) &= 0 & \varphi''(\ell) &= 0 \end{aligned}$$

$$(\alpha\ell)^3 \tanh(\alpha\ell) - (\beta\ell)^3 \tan(\beta\ell) + \ell^3 \frac{k_\varphi}{EI_\psi} \frac{(\alpha\ell)^2 + (\beta\ell)^2}{(\alpha\ell)(\beta\ell)} \frac{\tanh(\alpha\ell)}{\cos(\beta\ell)} \Big\{ \sin(\beta\ell) \Big\} = 0$$

Simple-free beam with warping spring.

$$\begin{aligned} \varphi(0) &= 0 \quad & k^2 \varphi'(\ell) - \varphi'''(\ell) &= 0 \\ \varphi''(0) &= 0 & -EI_\psi \varphi''(\ell) &= k_\psi \varphi'(\ell) \end{aligned}$$

$$(\alpha\ell)^3 \tanh(\alpha\ell) - (\beta\ell)^3 \tan(\beta\ell) + \ell \frac{k_\psi}{EI_\psi} \left((\alpha\ell)^2 + (\beta\ell)^2\right) \frac{1}{\cos(\beta\ell)} \Big\{ \cos(\beta\ell) \Big\} = 0$$

Simple-no warp beam with rotation spring.

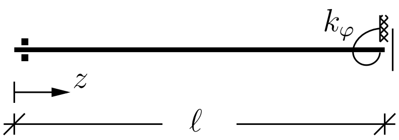

$$\begin{aligned} \varphi(0) &= 0 \quad & k^2 EI_\psi \varphi'(\ell) - EI_\psi \varphi'''(\ell) &= -k_\varphi \varphi(\ell) \\ \varphi''(0) &= 0 & \varphi'(\ell) &= 0 \end{aligned}$$

$$\cos(\beta\ell) - \ell^3 \frac{k_\varphi}{EI_\psi} \frac{1}{(\alpha\ell)(\beta\ell)\left((\alpha\ell)^2 + (\beta\ell)^2\right)} \cos(\beta\ell) \Big\{ (\beta\ell) \tanh(\alpha\ell) - (\alpha\ell) \tan(\beta\ell) \Big\} = 0$$

Simple-simple beam with warping spring.

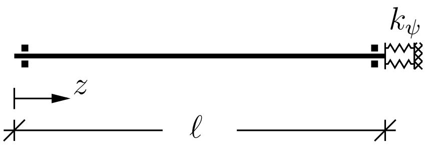

$$\begin{aligned} \varphi(0) &= 0 \quad & \varphi(\ell) &= 0 \\ \varphi''(0) &= 0 & -EI_\psi \varphi''(\ell) &= k_\psi \varphi'(\ell) \end{aligned}$$

$$\sin(\beta\ell) + \ell \frac{k_\psi}{EI_\psi} \frac{1}{(\alpha\ell)^2 + (\beta\ell)^2} \frac{\cos(\beta\ell)}{\tanh(\alpha\ell)} \Big\{ (\beta\ell) \tanh(\alpha\ell) - (\alpha\ell) \tan(\beta\ell) \Big\} = 0$$

Table B.7. Beams with a 'no warp' left end.

No warp-free beam with rotation spring.

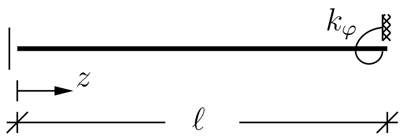

$$k^2 \varphi'(0) - \varphi'''(0) = 0 \qquad k^2 EI_\psi \varphi'(\ell) - EI_\psi \varphi'''(\ell) = -k_\varphi \varphi(\ell)$$

$$\varphi'(0) = 0 \qquad \varphi''(\ell) = 0$$

$$(\beta\ell)^3 \tanh(\alpha\ell) + (\alpha\ell)^3 \tan(\beta\ell) - \ell^3 \frac{k_\varphi}{EI_\psi} \frac{(\alpha\ell)^2 + (\beta\ell)^2}{(\alpha\ell)(\beta\ell)} \frac{1}{\cos(\beta\ell)} \Big\{ \cos(\beta\ell) \Big\} = 0$$

No warp-free beam with warping spring.

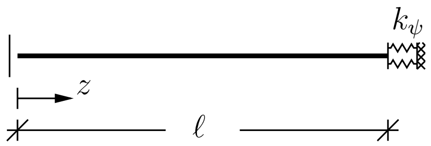

$$k^2 \varphi'(0) - \varphi'''(0) = 0 \qquad k^2 \varphi'(\ell) - \varphi'''(\ell) = 0$$

$$\varphi'(0) = 0 \qquad -EI_\psi \varphi''(\ell) = k_\psi \varphi'(\ell)$$

$$(\beta\ell)^3 \tanh(\alpha\ell) + (\alpha\ell)^3 \tan(\beta\ell) + \ell \frac{k_\psi}{EI_\psi} \big((\alpha\ell)^2 + (\beta\ell)^2\big) \frac{\tanh(\alpha\ell)}{\cos(\beta\ell)} \Big\{ \sin(\beta\ell) \Big\} = 0$$

No warp-no warp beam with rotation spring.

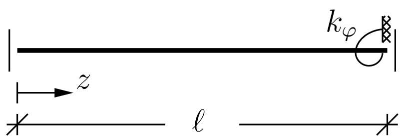

$$k^2 \varphi'(0) - \varphi'''(0) = 0 \qquad k^2 EI_\psi \varphi'(\ell) - EI_\psi \varphi'''(\ell) = -k_\varphi \varphi(\ell)$$

$$\varphi'(0) = 0 \qquad \varphi'(\ell) = 0$$

$$\sin(\beta\ell) - \ell^3 \frac{k_\varphi}{EI_\psi} \frac{1}{(\alpha\ell)(\beta\ell)\big((\alpha\ell)^2 + (\beta\ell)^2\big)} \frac{\cos(\beta\ell)}{\tanh(\alpha\ell)} \Big\{ (\alpha\ell)\tanh(\alpha\ell) + (\beta\ell)\tan(\beta\ell) \Big\} = 0$$

No warp-simple beam with warping spring.

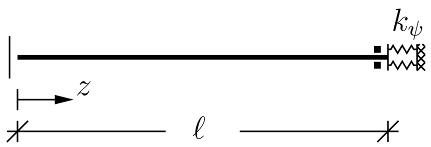

$$k^2 \varphi'(0) - \varphi'''(0) = 0 \qquad \varphi(\ell) = 0$$

$$\varphi'(0) = 0 \qquad -EI_\psi \varphi''(\ell) = k_\psi \varphi'(\ell)$$

$$\cos(\beta\ell) + \ell \frac{k_\psi}{EI_\psi} \frac{1}{(\alpha\ell)^2 + (\beta\ell)^2} \cos(\beta\ell) \Big\{ (\alpha\ell)\tanh(\alpha\ell) + (\beta\ell)\tan(\beta\ell) \Big\} = 0$$

Table B.8. Beams with a fixed left end.

Fixed-free beam with rotation spring.

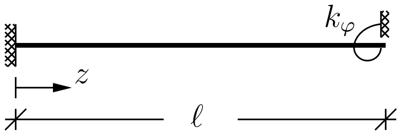

$$\varphi(0) = 0 \qquad k^2 EI_\psi \varphi'(\ell) - EI_\psi \varphi'''(\ell) = -k_\varphi \varphi(\ell)$$
$$\varphi'(0) = 0 \qquad \varphi''(\ell) = 0$$

$$\frac{(\alpha\ell)^4 + (\beta\ell)^4}{(\alpha\ell)^2(\beta\ell)^2} \cosh(\alpha\ell)\cos(\beta\ell) + \frac{(\alpha\ell)^2 - (\beta\ell)^2}{(\alpha\ell)(\beta\ell)} \sinh(\alpha\ell)\sin(\beta\ell) + 2+$$
$$\ell^3 \frac{k_\varphi}{EI_\psi} \frac{(\alpha\ell)^2 + (\beta\ell)^2}{(\alpha\ell)^3(\beta\ell)^3} \cosh(\alpha\ell)\cos(\beta\ell)\Big\{(\beta\ell)\tanh(\alpha\ell) - (\alpha\ell)\tan(\beta\ell)\Big\} = 0$$

Fixed-free beam with warping spring.

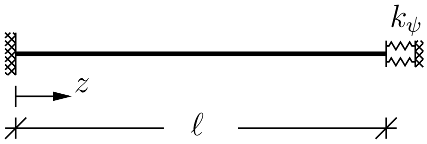

$$\varphi(0) = 0 \qquad k^2 \varphi'(\ell) - \varphi'''(\ell) = 0$$
$$\varphi'(0) = 0 \qquad -EI_\psi \varphi''(\ell) = k_\psi \varphi'(\ell)$$

$$\frac{(\alpha\ell)^4 + (\beta\ell)^4}{(\alpha\ell)^2(\beta\ell)^2} \cosh(\alpha\ell)\cos(\beta\ell) + \frac{(\alpha\ell)^2 - (\beta\ell)^2}{(\alpha\ell)(\beta\ell)} \sinh(\alpha\ell)\sin(\beta\ell) + 2+$$
$$\ell \frac{k_\psi}{EI_\psi} \frac{(\alpha\ell)^2 + (\beta\ell)^2}{(\alpha\ell)^2(\beta\ell)^2} \cosh(\alpha\ell)\cos(\beta\ell)\Big\{(\alpha\ell)\tanh(\alpha\ell) + (\beta\ell)\tan(\beta\ell)\Big\} = 0$$

Fixed-no warp beam with rotation spring.

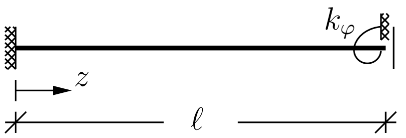

$$\varphi(0) = 0 \qquad k^2 EI_\psi \varphi'(\ell) - EI_\psi \varphi'''(\ell) = -k_\varphi \varphi(\ell)$$
$$\varphi'(0) = 0 \qquad \varphi'(\ell) = 0$$

$$(\alpha\ell)\tanh(\alpha\ell) + (\beta\ell)\tan(\beta\ell) + \ell^3 \frac{k_\varphi}{EI_\psi} \frac{1}{(\alpha\ell)(\beta\ell)\big((\alpha\ell)^2 + (\beta\ell)^2\big)} \frac{1}{\cosh(\alpha\ell)\cos(\beta\ell)} \cdot$$
$$\Big\{\big((\alpha\ell)^2 - (\beta\ell)^2\big)\sinh(\alpha\ell)\sin(\beta\ell) + 2(\alpha\ell)(\beta\ell)\big(1 - \cosh(\alpha\ell)\cos(\beta\ell)\big)\Big\} = 0$$

Fixed-simple beam with warping spring.

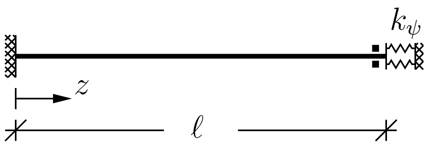

$$\varphi(0) = 0 \qquad \varphi(\ell) = 0$$
$$\varphi'(0) = 0 \qquad -EI_\psi \varphi''(\ell) = k_\psi \varphi'(\ell)$$

$$(\beta\ell)\tanh(\alpha\ell) - (\alpha\ell)\tan(\beta\ell) - \ell \frac{k_\psi}{EI_\psi} \frac{1}{(\alpha\ell)^2 + (\beta\ell)^2} \frac{1}{\cosh(\alpha\ell)\cos(\beta\ell)} \cdot$$
$$\Big\{\big((\alpha\ell)^2 - (\beta\ell)^2\big)\sinh(\alpha\ell)\sin(\beta\ell) + 2(\alpha\ell)(\beta\ell)\big(1 - \cosh(\alpha\ell)\cos(\beta\ell)\big)\Big\} = 0$$

Table B.9. Beams with a rotation spring at both ends.

Free-free beam.

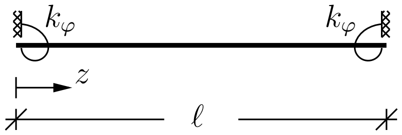

$$\begin{aligned} k^2 EI_\psi \varphi'(0) - EI_\psi \varphi'''(0) &= -k_\varphi \varphi(0) \quad \varphi''(0) = 0 \\ k^2 EI_\psi \varphi'(\ell) - EI_\psi \varphi'''(\ell) &= -k_\varphi \varphi(\ell) \quad \varphi''(\ell) = 0 \end{aligned}$$

$$\big((\alpha\ell)^6 - (\beta\ell)^6\big)\sinh(\alpha\ell)\sin(\beta\ell) + 2(\alpha\ell)^3(\beta\ell)^3\big(\cosh(\alpha\ell)\cos(\beta\ell) - 1\big) + \left(\ell^3 \frac{k_\varphi}{EI_\psi}\right)^2 \left(2 + \frac{(\alpha\ell)^4 + (\beta\ell)^4}{(\alpha\ell)^2(\beta\ell)^2}\right)\sinh(\alpha\ell)\Big\{\sin(\beta\ell)\Big\} = 0$$

No warp-no warp beam.

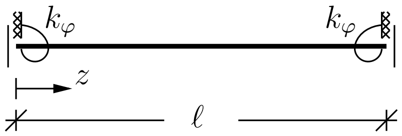

$$\begin{aligned} k^2 EI_\psi \varphi'(0) - EI_\psi \varphi'''(0) &= -k_\varphi \varphi(0) \quad \varphi'(0) = 0 \\ k^2 EI_\psi \varphi'(\ell) - EI_\psi \varphi'''(\ell) &= -k_\varphi \varphi(\ell) \quad \varphi'(\ell) = 0 \end{aligned}$$

$$\sin(\beta\ell) + \left(\ell^3 \frac{k_\varphi}{EI_\psi}\right)^2 \frac{1}{(\alpha\ell)^2(\beta\ell)^2\big((\alpha\ell)^2 + (\beta\ell)^2\big)^2} \frac{1}{\sinh(\alpha\ell)} \cdot \Big\{\big((\alpha\ell)^2 - (\beta\ell)^2\big)\sinh(\alpha\ell)\sin(\beta\ell) + 2(\alpha\ell)(\beta\ell)\big(1 - \cosh(\alpha\ell)\cos(\beta\ell)\big)\Big\} = 0$$

Free-no warp beam.

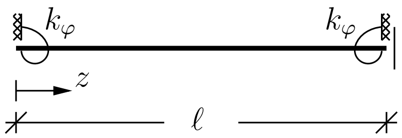

$$\begin{aligned} k^2 EI_\psi \varphi'(0) - EI_\psi \varphi'''(0) &= -k_\varphi \varphi(0) \quad \varphi''(0) = 0 \\ k^2 EI_\psi \varphi'(\ell) - EI_\psi \varphi'''(\ell) &= -k_\varphi \varphi(\ell) \quad \varphi'(\ell) = 0 \end{aligned}$$

$$(\beta\ell)^3 \tanh(\alpha\ell) + (\alpha\ell)^2 \tan(\beta\ell) - \ell^3 \frac{k_\varphi}{EI_\psi} \frac{1}{(\alpha\ell)^2 + (\beta\ell)^2} \frac{1}{\cosh(\alpha\ell)\cos(\beta\ell)} \cdot \Big\{\big((\alpha\ell)^2 - (\beta\ell)^2\big)\sinh(\alpha\ell)\sin(\beta\ell) + 2(\alpha\ell)(\beta\ell)\big(1 - \cosh(\alpha\ell)\cos(\beta\ell)\big)\Big\} - \left(\ell^3 \frac{k_\varphi}{EI_\psi}\right)^2 \frac{1}{(\alpha\ell)^2(\beta\ell)^2}\Big\{(\beta\ell)\tanh(\alpha\ell) - (\alpha\ell)\tan(\beta\ell)\Big\} = 0$$

Table B.10. Beams with a warping spring at both ends.

Free-free beam.

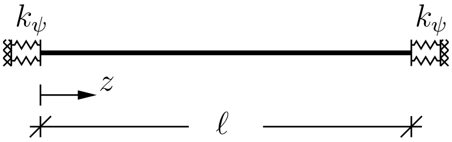

$$k^2\varphi'(0) - \varphi'''(0) = 0 \qquad -EI_\psi\varphi''(0) = k_\psi\varphi'(0)$$
$$k^2\varphi'(\ell) - \varphi'''(\ell) = 0 \qquad -EI_\psi\varphi''(\ell) = k_\psi\varphi'(\ell)$$

$$\big((\alpha\ell)^6 - (\beta\ell)^6\big)\sinh(\alpha\ell)\sin(\beta\ell) + 2(\alpha\ell)^3(\beta\ell)^3\big(\cosh(\alpha\ell)\cos(\beta\ell) - 1\big) -$$
$$\left(\ell\frac{k_\psi}{EI_\psi}\right)^2 \big((\alpha\ell)^2 + (\beta\ell)^2\big)\sinh(\alpha\ell)\Big\{\sin(\beta\ell)\Big\} = 0$$

Simple-simple beam.

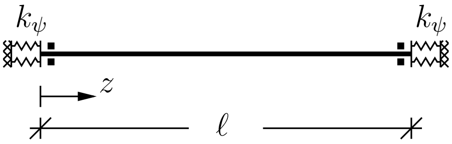

$$\varphi(0) = 0 \qquad -EI_\psi\varphi''(0) = k_\psi\varphi'(0)$$
$$\varphi(\ell) = 0 \qquad -EI_\psi\varphi''(\ell) = k_\psi\varphi'(\ell)$$

$$\sin(\beta\ell) - \left(\ell\frac{k_\psi}{EI_\psi}\right)^2 \frac{1}{(\alpha\ell)^2 + (\beta\ell)^2}\frac{1}{\sinh(\alpha\ell)}\cdot$$
$$\Big\{\big((\alpha\ell)^2 - (\beta\ell)^2\big)\sinh(\alpha\ell)\sin(\beta\ell) + 2(\alpha\ell)(\beta\ell)\big(1 - \cosh(\alpha\ell)\cos(\beta\ell)\big)\Big\} = 0$$

Free-simple beam.

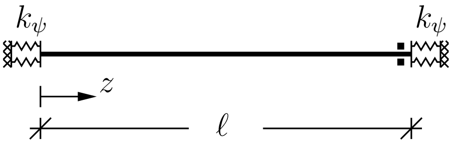

$$k^2\varphi'(0) - \varphi'''(0) = 0 \qquad -EI_\psi\varphi''(0) = k_\psi\varphi'(0)$$
$$\varphi(\ell) = 0 \qquad -EI_\psi\varphi''(\ell) = k_\psi\varphi'(\ell)$$

$$(\alpha\ell)^3\tanh(\alpha\ell) - (\beta\ell)^2\tan(\beta\ell) + \ell\frac{k_\psi}{EI_\psi}\frac{(\alpha\ell)(\beta\ell)}{(\alpha\ell)^2 + (\beta\ell)^2}\cosh(\alpha\ell)\cos(\beta\ell)\cdot$$
$$\Big\{\big((\alpha\ell)^2 - (\beta\ell)^2\big)\sinh(\alpha\ell)\sin(\beta\ell) + 2(\alpha\ell)(\beta\ell)\big(1 - \cosh(\alpha\ell)\cos(\beta\ell)\big)\Big\} -$$
$$\left(\ell\frac{k_\psi}{EI_\psi}\right)^2 \Big\{(\alpha\ell)\tanh(\alpha\ell) + (\beta\ell)\tan(\beta\ell)\Big\} = 0$$

B.3 Beams with damping treatment

The last section of tables lists a series of transcendental equations where damping treatment according to Chapter 3 is applied. This boundary condition has the form,

$$\varphi''(z) \mp \eta\varphi'(z) = 0 \tag{B.4}$$

where η identifies the specific form of the damping while the $'+'$ refers to the left end at $z = 0$ and the $'-'$ refers to the right end at $z = \ell$. In the case of the damping treatment being applied at both ends, symmetric boundary conditions results in identical balancing of the two damping functions, while for asymmetric boundary conditions a balancing factor ν is applied for the left beam end.

Table B.11. Beams with a free left end.

Free-free beam with damping at the right end.

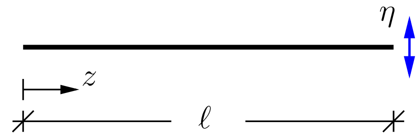

$$
\begin{aligned}
k^2\varphi'(0) - \varphi'''(0) &= 0 & k^2\varphi'(\ell) - \varphi'''(\ell) &= 0\\
\varphi''(0) &= 0 & \varphi''(\ell) + \eta\varphi'(\ell) &= 0
\end{aligned}
$$

$$
\begin{aligned}
&\big((\alpha\ell)^6 - (\beta\ell)^6\big)\sinh(\alpha\ell)\sin(\beta\ell) + 2(\alpha\ell)^3(\beta\ell)^3\big(\cosh(\alpha\ell)\cos(\beta\ell) - 1\big) +\\
&\eta\ell\big((\alpha\ell)^2 + (\beta\ell)^2\big)\cosh(\alpha\ell)\cos(\beta\ell)\Big\{(\beta\ell)^3\tanh(\alpha\ell) + (\alpha\ell)^3\tan(\beta\ell)\Big\} = 0
\end{aligned}
$$

Free-free beam with damping at both ends.

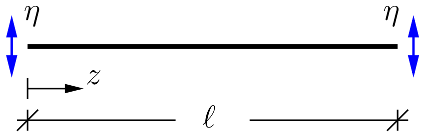

$$
\begin{aligned}
k^2\varphi'(0) - \varphi'''(0) &= 0 & k^2\varphi'(\ell) - \varphi'''(\ell) &= 0\\
\varphi''(0) - \eta\varphi'(0) &= 0 & \varphi''(\ell) + \eta\varphi'(\ell) &= 0
\end{aligned}
$$

$$
\begin{aligned}
&\big((\alpha\ell)^6 - (\beta\ell)^6\big)\sinh(\alpha\ell)\sin(\beta\ell) + 2(\alpha\ell)^3(\beta\ell)^3\big(\cosh(\alpha\ell)\cos(\beta\ell) - 1\big) +\\
&2\eta\ell\big((\alpha\ell)^2 + (\beta\ell)^2\big)\cosh(\alpha\ell)\cos(\beta\ell)\Big\{(\beta\ell)^3\tanh(\alpha\ell) + (\alpha\ell)^3\tan(\beta\ell)\Big\} +\\
&(\eta\ell)^2\big((\alpha\ell)^2 + (\beta\ell)^2\big)\sinh(\alpha\ell)\Big\{\sin(\beta\ell)\Big\} = 0
\end{aligned}
$$

Free-simple beam with damping at the right end.

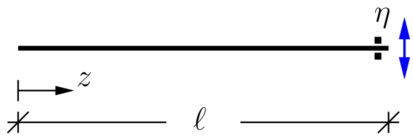

$$
\begin{aligned}
k^2\varphi'(0) - \varphi'''(0) &= 0 & \varphi(\ell) &= 0\\
\varphi''(0) &= 0 & \varphi''(\ell) + \eta\varphi'(\ell) &= 0
\end{aligned}
$$

$$
\begin{aligned}
&(\alpha\ell)^3\tanh(\alpha\ell) - (\beta\ell)^3\tan(\beta\ell) + \eta\ell\frac{(\alpha\ell)^2(\beta\ell)^2}{(\alpha\ell)^2 + (\beta\ell)^2}\frac{1}{\cosh(\alpha\ell)\cos(\beta\ell)}\cdot\\
&\left\{\frac{(\alpha\ell)^4 + (\beta\ell)^4}{(\alpha\ell)^2(\beta\ell)^2}\cosh(\alpha\ell)\cos(\beta\ell) + \frac{(\alpha\ell)^2 - (\beta\ell)^2}{(\alpha\ell)(\beta\ell)}\sinh(\alpha\ell)\sin(\beta\ell) + 2\right\} = 0
\end{aligned}
$$

Free-simple beam with damping at both ends.

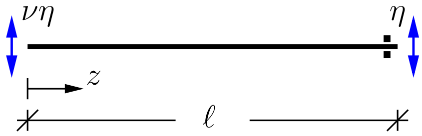

$$
\begin{aligned}
k^2\varphi'(0) - \varphi'''(0) &= 0 & \varphi(\ell) &= 0\\
\varphi''(0) - \nu\eta\varphi'(0) &= 0 & \varphi''(\ell) + \eta\varphi'(\ell) &= 0
\end{aligned}
$$

$$
\begin{aligned}
&(\alpha\ell)^3\tanh(\alpha\ell) - (\beta\ell)^3\tan(\beta\ell) + \eta\ell\frac{(\alpha\ell)^2(\beta\ell)^2}{(\alpha\ell)^2 + (\beta\ell)^2}\frac{1}{\cosh(\alpha\ell)\cos(\beta\ell)}\cdot\\
&\left\{\frac{(\alpha\ell)^4 + (\beta\ell)^4}{(\alpha\ell)^2(\beta\ell)^2}\cosh(\alpha\ell)\cos(\beta\ell) + \frac{(\alpha\ell)^2 - (\beta\ell)^2}{(\alpha\ell)(\beta\ell)}\sinh(\alpha\ell)\sin(\beta\ell) + 2 +\right.\\
&\left.\nu\cosh(\alpha\ell)\cos(\beta\ell)\left(\frac{(\alpha\ell)^2 + (\beta\ell)^2}{(\alpha\ell)(\beta\ell)}\right)^2\right\} + \nu(\eta\ell)^2\Big\{(\alpha\ell)\tanh(\alpha\ell) + (\beta\ell)\tan(\beta\ell)\Big\} = 0
\end{aligned}
$$

Table B.12. Beams with a simple left end.

Simple-free beam with damping at the right end.

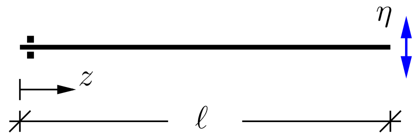

$$\varphi(0)=0 \qquad k^2\varphi'(\ell)-\varphi'''(\ell)=0$$
$$\varphi''(0)=0 \qquad \varphi''(\ell)+\eta\varphi'(\ell)=0$$

$$(\alpha\ell)^3\tanh(\alpha\ell)-(\beta\ell)^3\tan(\beta\ell)+\eta\ell((\alpha\ell)^2+(\beta\ell)^2)\frac{1}{\cos(\beta\ell)}\Big\{\cos(\beta\ell)\Big\}=0$$

Simple-free beam with damping at both ends.

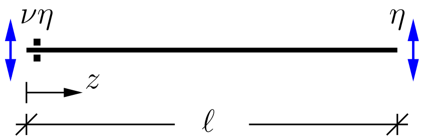

$$\varphi(0)=0 \qquad k^2\varphi'(\ell)-\varphi'''(\ell)=0$$
$$\varphi''(0)-\nu\eta\varphi'(0)=0 \qquad \varphi''(\ell)+\eta\varphi'(\ell)=0$$

$$(\alpha\ell)^3\tanh(\alpha\ell)-(\beta\ell)^3\tan(\beta\ell)+\nu\eta\ell\frac{(\alpha\ell)^2(\beta\ell)^2}{(\alpha\ell)^2+(\beta\ell)^2}\frac{1}{\cosh(\alpha\ell)\cos(\beta\ell)}\cdot$$
$$\Bigg\{\frac{(\alpha\ell)^4+(\beta\ell)^4}{(\alpha\ell)^2(\beta\ell)^2}\cosh(\alpha\ell)\cos(\beta\ell)+\frac{(\alpha\ell)^2-(\beta\ell)^2}{(\alpha\ell)(\beta\ell)}\sinh(\alpha\ell)\sin(\beta\ell)+2+$$
$$\frac{1}{\nu}\cosh(\alpha\ell)\cos(\beta\ell)\left(\frac{(\alpha\ell)^2+(\beta\ell)^2}{(\alpha\ell)(\beta\ell)}\right)^2\Bigg\}+\nu(\eta\ell)^2\Big\{(\alpha\ell)\tanh(\alpha\ell)+(\beta\ell)\tan(\beta\ell)\Big\}=0$$

Simple-simple beam with damping at the right end.

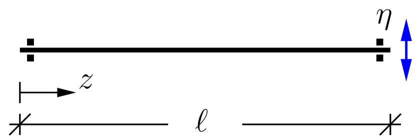

$$\varphi(0)=0 \qquad \varphi(\ell)=0$$
$$\varphi''(0)=0 \qquad \varphi''(\ell)+\eta\varphi'(\ell)=0$$

$$\sin(\beta\ell)-\eta\ell\frac{1}{(\alpha\ell)^2+(\beta\ell)^2}\frac{\cos(\beta\ell)}{\tanh(\alpha\ell)}\Big\{(\beta\ell)\tanh(\alpha\ell)-(\alpha\ell)\tan(\beta\ell)\Big\}=0$$

Simple-simple beam with damping at both ends.

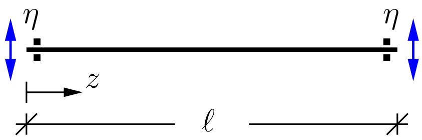

$$\varphi(0)=0 \qquad \varphi(\ell)=0$$
$$\varphi''(0)-\eta\varphi'(0)=0 \qquad \varphi''(\ell)+\eta\varphi'(\ell)=0$$

$$\sin(\beta\ell)-2\eta\ell\frac{1}{(\alpha\ell)^2+(\beta\ell)^2}\frac{\cos(\beta\ell)}{\tanh(\alpha\ell)}\Big\{(\beta\ell)\tanh(\alpha\ell)-(\alpha\ell)\tan(\beta\ell)\Big\}+$$
$$(\eta\ell)^2\frac{1}{(\alpha\ell)^2+(\beta\ell)^2}\frac{1}{\sinh(\alpha\ell)}\Big\{((\alpha\ell)^2-(\beta\ell)^2)\sinh(\alpha\ell)\sin(\beta\ell)+$$
$$2(\alpha\ell)(\beta\ell)(1-\cosh(\alpha\ell)\cos(\beta\ell))\Big\}=0$$

Table B.13. Beams with a 'no warping' or fixed left end.

No warping-free beam.

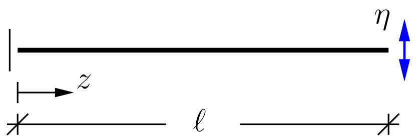

$$k^2\varphi'(0) - \varphi'''(0) = 0 \qquad k^2\varphi'(\ell) - \varphi'''(\ell) = 0$$
$$\varphi'(0) = 0 \qquad \varphi''(\ell) + \eta\varphi'(\ell) = 0$$

$$(\beta\ell)^3 \tanh(\alpha\ell) + (\alpha\ell)^3 \tan(\beta\ell) + \eta\ell((\alpha\ell)^2 + (\beta\ell)^2)\frac{\tanh(\alpha\ell)}{\cos(\beta\ell)}\Big\{\sin(\beta\ell)\Big\} = 0$$

No warping-simple beam.

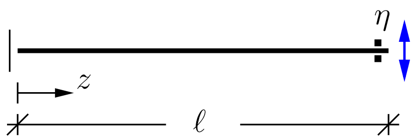

$$k^2\varphi'(0) - \varphi'''(0) = 0 \qquad \varphi(\ell) = 0$$
$$\varphi'(0) = 0 \qquad \varphi''(\ell) + \eta\varphi'(\ell) = 0$$

$$\cos(\beta\ell) + \eta\ell\frac{1}{(\alpha\ell)^2 + (\beta\ell)^2}\cos(\beta\ell)\Big\{(\alpha\ell)\tanh(\alpha\ell) + (\beta\ell)\tan(\beta\ell)\Big\} = 0$$

Fixed-free beam.

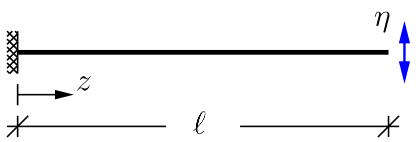

$$\varphi(0) = 0 \qquad k^2\varphi'(\ell) - \varphi'''(\ell) = 0$$
$$\varphi'(0) = 0 \qquad \varphi''(\ell) + \eta\varphi'(\ell) = 0$$

$$\frac{(\alpha\ell)^4 + (\beta\ell)^4}{(\alpha\ell)^2(\beta\ell)^2}\cosh(\alpha\ell)\cos(\beta\ell) + \frac{(\alpha\ell)^2 - (\beta\ell)^2}{(\alpha\ell)(\beta\ell)}\sinh(\alpha\ell)\sin(\beta\ell) + 2+$$
$$\eta\ell\frac{(\alpha\ell)^2 + (\beta\ell)^2}{(\alpha\ell)^2(\beta\ell)^2}\cosh(\alpha\ell)\cos(\beta\ell)\Big\{(\alpha\ell)\tanh(\alpha\ell) + (\beta\ell)\tan(\beta\ell)\Big\} = 0$$

Fixed-simple beam.

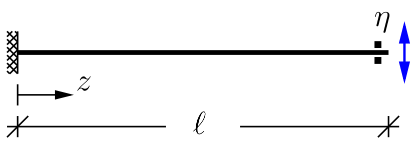

$$\varphi(0) = 0 \qquad \varphi(\ell) = 0$$
$$\varphi'(0) = 0 \qquad \varphi''(\ell) + \eta\varphi'(\ell) = 0$$

$$(\beta\ell)\tanh(\alpha\ell) - (\alpha\ell)\tan(\beta\ell) - \eta\ell\frac{1}{(\alpha\ell)^2 + (\beta\ell)^2}\frac{1}{\cosh(\alpha\ell)\cos(\beta\ell)}\cdot$$
$$\Big\{((\alpha\ell)^2 - (\beta\ell)^2)\sinh(\alpha\ell)\sin(\beta\ell) + 2(\alpha\ell)(\beta\ell)(1 - \cosh(\alpha\ell)\cos(\beta\ell))\Big\} = 0$$

P1

Damping of Torsional Vibrations in Thin-Walled Beams
by Viscous Bimoments

David Hoffmeyer and Jan Høgsberg

Mechanics of Advanced Materials and Structures,
Published online: February 1, 2019
DOI: 10.1080/15376494.2019.1567885

MECHANICS OF ADVANCED MATERIALS AND STRUCTURES
https://doi.org/10.1080/15376494.2019.1567885

Taylor & Francis
Taylor & Francis Group

Check for updates

ORIGINAL-ARTICLE

Damping of torsional vibrations in thin-walled beams by viscous bimoments

David Hoffmeyer and Jan Høgsberg

Department of Mechanical Engineering, Technical University of Denmark, Kongens Lyngby, Denmark

ABSTRACT
Torsional vibrations in beams are damped by discrete, axial viscous dampers in configurations constituting bimoments. The bimoments act on warping displacements and partial restraining of warping suggests the inclusion of a flexibility parameter, calibrated from numerical results. Correcting for distortion is incorporated in a similar manner. The use of the governing differential equation with calibrated parameters as an alternative to a full complex analysis by a FE model is justified by an example. It is demonstrated that the differential equation determines the damped frequencies and damping ratios with great accuracy. Significant damping ratios of the lowest torsional mode are obtained.

ARTICLE HISTORY
Received 9 October 2018
Accepted 7 January 2019

KEYWORDS
Torsional vibrations; damping; warping; thin-walled beams; bimoment; finite element method

1. Introduction

In slender thin-walled beam structures, torsional vibrations may be induced by e.g. wind, earthquakes—and in the case of bridges—also by excitations from pedestrians or traffic. For beams with symmetric cross-sections torsional vibrations may be initiated when the load acts with an eccentricity to the cross-sectional shear center. For cross-sections without double symmetry, the elastic and shear centers do not coincide, whereby the torsional and flexural vibrations inherently couple. In either case, the mitigation of vibrations may lead to a reduction in fatigue stresses [1], improvements in comfort levels and even removal of aerodynamic instabilities such as flutter for structures exposed to wind. During flutter an initial small or moderate motion develops over time to vibrations with large amplitudes, possibly damaging a structure to failure. Flutter is usually a combination of torsion and flexure, but also pure torsional flutter may occur [2]. The phenomenon is associated with apparent negative damping that typically cannot be sufficiently compensated by the inherent material damping. In the design procedure for slender cable-stayed bridges substantial effort is put into avoiding flutter, as it may be a limiting factor for the overall span of suspension bridges [3]. A remedy for avoiding the onset of flutter is by simply increasing the governing flutter limit, e.g. by separating the main girder in two with connecting beams [4]. For an aerodynamic analysis of bridges with slotted box girders see [5], while an active control strategy for bridge cable vibrations has been proposed in [6], resulting in an increase in the critical flutter wind speed. If geometric changes with the purpose of reducing the flutter limit are deemed inappropriate, flutter may instead be compensated by adding a supplemental damping mechanism or device. For example, damping the critical torsional mode of a bridge deck may be of particular interest when it is economically cheaper than producing a closed box girder [3]. The phenomenon of flutter in bridge decks is treated in greater detail in [7–11]. Recently, it was shown in [12] that the flutter critical rotational speed of a wind turbine rotor may be increased by the use of a viscous type eddy current damper working on the torsional motion of the turbine blades.

Torsional vibrations in thin-walled beams are associated with inhomogeneous torsion that generates out-of-plane, axial warping displacements. For beams with open cross-sections these displacements are often non-vanishing at the boundaries of the beam. For very long beams, inhomogeneous torsion has little influence and solutions based on pure homogeneous torsion are therefore adequate. However, for beams of short to moderate length, relative to the size of the cross-section, the contribution from inhomogeneous torsion may be significant [13]. The vibration characteristics of uncoupled torsional vibrations, including the effect of warping, were originally investigated by Gere [14], who solved for the natural frequencies and the associated mode shapes of beams with various natural boundary conditions. Subsequently, Gere and Lin [15] studied the coupling between flexural and torsional vibrations in beams with non-coinciding elastic and shear centers. A thorough review of torsion in beams has been given in [16].

The problem of torsional vibrations not only occurs in civil and wind engineering structures, but may also yield structure-borne sound and noise in power trains inside ships and in vehicles [17], while even in drillstrings used for drilling of oil or gas wells the torsional dynamic behavior may cause severe problems [18]. Furthermore, in the aerospace and aviation industry, composite materials are vastly used and torsional vibrations in for example plate-like structures

CONTACT David Hoffmeyer davhoff@mek.dtu.dk Nils Koppels Alle, Building 404, DK-2800, Kongens Lyngby, Denmark.
Color versions of one or more of the figures in the article can be found online at www.tandfonline.com/umcm.
This article has been republished with minor changes. These changes do not impact the academic content of the article.

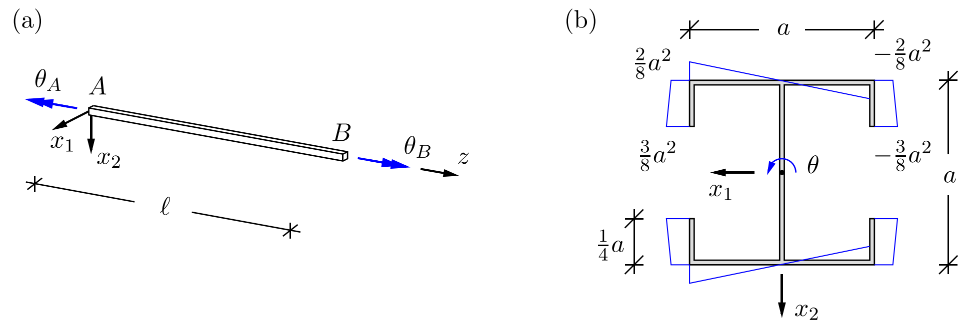

Figure 1. (a) Beam with length ℓ, transverse coordinate axes $\{x_1, x_2\}$ and angle of twist θ. (b) Modified I-profile cross-section with sector-coordinate ψ and indicated shear center.

may be damped and/or mitigated by viscoelastic constraining layers [19] or piezoelectric patches [20] and [21].

The warping effect was taken into account by Christiano and Salmela [22], expanding the original work of Gere [14] by introducing the concept of partially restrained warping at the boundary, specifically by adding supplemental stiffness locally to the out-of-plane axial warping displacements. A similar approach, with a localized viscous effect acting on the warping motion was used to introduce supplemental damping in [23], where the viscous boundary condition was applied directly to the pure bimoments at the beam supports. In [23], the eigenvalue problem associated with the free vibrations of the damped beam was solved with respect to the complex-valued natural frequency, whereby the corresponding damping ratio could be determined subsequently. It was demonstrated that significant damping ratios could be realized by applying viscous bimoments at the beam supports. Recently, Hoffmeyer and Høgsberg [24] showed by a finite element comparison that the location of discrete axial viscous dampers on the cross-section in fact has a great influence on the attainable damping ratios when the dampers are balanced properly [25]. For general details on viscous dampers see e.g. [25–28]. Even though the finite element method may be the most popular numerical method, Sapountzakis [29] applied a boundary element method for solving the torsion problem for beams with variable cross-section.

In the present article, the efficiency of torsional damping by viscous warping control is investigated by detailed numerical analysis, where a supplemental flexibility parameter is introduced in the damper model to take into account the inability of local forces on a beam cross-section to fully restrain axial warping. Thus, the flexibility parameter describes the remaining flexibility of the beam due to partly restrained warping at a boundary when the applied viscous dampers lock at infinite damping. The locking changes the infinitely damped natural frequency of the beam, reflecting the presence of the axial dampers and their particular spatial configuration. The inclusion of such a flexibility parameter corresponds to the effect of flexible boundary conditions as described in e.g. [30–34]. The supplemental flexibility parameter is calibrated by dedicated finite element results, and thus an additional correction parameter may even be included in the spatial solution of the differential equation to account for in-plane distortion of the cross-section. The resulting analytical model for torsional vibrations of thin-walled beams is therefore accurate and includes important supplemental effects. The linear finite element model used for both calibration and comparison is based on isoparametric elements with cubic-linear interpolation [35], especially suitable for modeling of thin-walled beams. Configurations with pure bimoments are easily represented by symmetrically located axial dampers, representing a pure viscous damping term in the governing equation due to direct proportionality with conjugated velocity. The damped eigenvalue problem is obtained by setting up the numerical equations of motion in state-space form, whereby the complex natural frequencies and the corresponding damping ratios can be obtained directly from the eigenvalues. It is demonstrated by an example how different bimoment configurations influence the damping properties of the first torsional mode and how an optimal location of the dampers on the cross-section may be estimated. The example furthermore shows that when designed properly, viscous bimoments are a very effective means for damping torsional vibrations in thin-walled beams.

2. Uncoupled torsional vibrations

The design and calibration of beam structures is conveniently based on an analytical approach and thus the theoretical solutions are initially derived. The characteristics of torsional vibrations in thin-walled beams may be analyzed by considering the free response of a beam element. The beam has the length ℓ, axial coordinate z, and in-plane coordinates $\{x_1, x_2\}$. The angle of twist $\theta(z, t)$ and coordinate system are seen in Figure 1a. In the remainder of the article, the independent spatial coordinates are not depicted to maintain a compact notation.

2.1. Governing equation

The governing differential equation may be established by the elastic and kinetic energy. In order to take the warping effect into account the elastic strain energy receives contributions from both homogeneous torsion (St. Venant) and inhomogeneous torsion (Vlasov). It then takes the form,

$$U(t) = \frac{1}{2}\int_\ell \theta'(t) GK \theta'(t)\, dz + \frac{1}{2}\int_\ell \theta''(t) EI_\psi \theta''(t)\, dz \qquad (1)$$

where G is the shear modulus, K is the torsion stiffness parameter, E is Young's modulus, I_ψ is the warping moment of

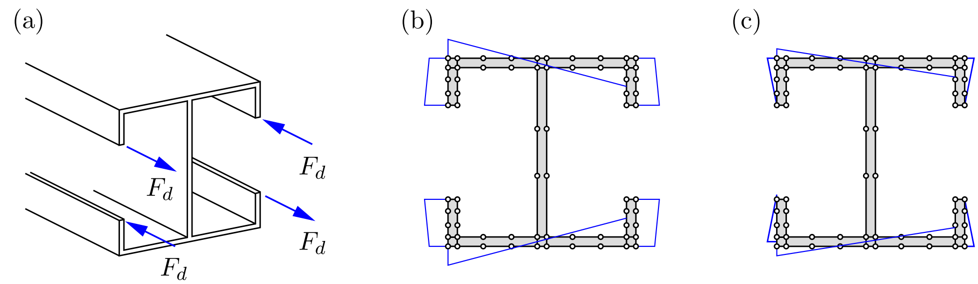

Figure 2 (a) Modified I-profile with axial, viscous forces in a pure bimoment configuration and warping functions (b) for $c_j = 0$ and (c) for $c_j = \infty$.

inertia with ψ indicating the warping function, or sector-coordinate, of the cross-section and $()' = \partial()/\partial z$ indicates differentiation with respect to z. The part of the elastic energy describing inhomogeneous torsion relates to the out-of-plane axial displacements described by the sector-coordinate. For a modified I-profile with added vertical flanges, the sector-coordinate is shown in Figure 1b. The kinetic energy contains the torsional inertia,

$$T(t) = \frac{1}{2}\int_\ell \dot{\theta}(t)\rho J\dot{\theta}(t)\,dz \tag{2}$$

where ρ is the mass density, J is the polar moment of inertia, and $\dot{()} = \partial()/\partial t$ indicates differentiation with respect to t. Energy is dissipated through idealized discrete viscous dampers located at an end cross-section. Each damper j is associated with a particular viscous damping coefficient c_j, while several dampers may act on the same cross-section. Hereby the dissipated energy D may be expressed as

$$D(t) = \sum_j \dot{\theta}_j(t)c_j\dot{\theta}_j(t) \tag{3}$$

with the summation taking into account the individual contributions from all dampers acting on the cross-section. In case of damped vibrations, the change in mechanical energy is balanced by the dissipated energy: $\dot{U} + \dot{T} = -D$. However, as the dissipated energy enters the equilibrium equation through the boundary conditions, the governing differential equation for the beam remains undamped as

$$EI_\psi\theta''''(t) - GK\theta''(t) + \rho J\ddot{\theta}(t) = 0 \tag{4}$$

A time harmonic solution of the form $\theta(t) = \varphi e^{i\omega t}$ may in the following be assumed with ω as the natural frequency and φ representing the spatial solution. Following the classic approach in [14] the spatial solution may be written as

$$\varphi = D_1\cosh(\alpha z) + D_2\sinh(\alpha z) + D_3\cos(\beta z) + D_4\sin(\beta z) \tag{5}$$

where D_1 to D_4 are integration constants. The two apparent wave numbers are written as in [23],

$$\alpha^2 = \sqrt{\frac{1}{4}k^4 + \lambda^4} + \frac{1}{2}k^2, \quad \beta^2 = \sqrt{\frac{1}{4}k^4 + \lambda^4} - \frac{1}{2}k^2 \tag{6}$$

defining the warping length scale k, wave speed v, and scaled wave number λ, respectively, as

$$k^2 = \frac{GK}{EI_\psi}, \quad v^2 = \frac{GK}{\rho J}, \quad \lambda^4 = \left(\frac{k\omega}{v}\right)^2 \tag{7}$$

Depending on the boundary conditions the integration constants in (5) are determined, yielding the transcendental equation for the specific beam problem. This equation must be solved iteratively for a combined set of α and β together with the relations in (6) and (7). See [23] for transcendental equations for various beam configurations.

2.2. Bimoment from axial forces

With the differential equation defined in (4), damping is now introduced as a boundary condition to be used together with the spatial solution in (5). The damping effect is applied by placing concentrated viscous forces on the end cross-section acting in the axial direction of the beam, as illustrated in Figure 2a. A number of viscous forces may be placed symmetrically or even asymmetrically, whereby a given set of axial damping forces may result in both a normal force and bending moments alongside the desired bimoment, see e.g. [36]. However, if the force configuration yields vanishing normal force and bending moments, the produced bimoment will in the following be referred to as a pure bimoment. Besides the resulting normal force and bending moments, a general geometrically asymmetric configuration of a set of axial dampers may furthermore contribute with additional effects like distortion or higher order warping modes. These effects are not captured by the differential equation but will inherently be a part of a three-dimensional solid (finite element) model. It is in the present work not of interest to set-up configurations that introduce a normal force or a bending moment as this complicates the comparison with the solutions derived from the uncoupled differential equation (4). Therefore, only symmetric configurations without a resulting normal force and bending moment will be considered in the present analysis.

The principle of virtual work may be used to quantify whether a certain damper configuration also introduces a normal force or bending moment. Let the jth damper force be $F_{d,j}$ and multiply with a virtual displacement δu_j to obtain the virtual work $F_{d,j}\delta u_j$. The total virtual work is therefore obtained as the sum of the individual contributions from all dampers acting on the cross-section,

$$\delta W_d(t) = \sum_j F_{d,j}(t)\delta u_j(t) \tag{8}$$

where subscript d indicates the cross-section with the damper(s) applied at either end of the beam. The contribution to a normal force N_d is derived from (8) by assuming that

$\delta u_j = \delta u_c$, where δu_c is the axial virtual displacement at the elastic center $C = \{c_1, c_2\}$ of the cross-section. Thereby, the relation $\delta W_d = N_d \delta u_c$ defines the normal force as

$$N_d(t) = \sum_j F_{d,j}(t) \tag{9}$$

Similarly, a contribution to the bending moment with respect to a principle cross-sectional axis can be obtained by introducing the virtual damper displacement $\delta u_j = (x_1 - c_1)\delta\theta_1 + (x_2 - c_2)\delta\theta_2$ expressed in terms of the damper coordinates $\{x_1, x_2\}$ and the cross-section inclinations θ_1 and θ_2 in the two corresponding in-plane directions, see Figure 1. The virtual work relation $\delta W_d = M_{d,1}\delta\theta_1 + M_{d,2}\delta\theta_2$ then identifies the bending moments as

$$M_{d,\alpha}(t) = \sum_j F_{d,j}(t)(x_{\alpha,j} - c_\alpha), \quad \alpha = 1, 2 \tag{10}$$

For the configuration in Figure 2a the resulting normal force and bending moments vanish as the forces and moments add up to zero according to the summations in (9) and (10). Thus, for a symmetric cross-section a corresponding symmetric configuration of passive or collocated active dampers produce a pure bimoment without coupling to section forces associated with extension and bending.

In the present work only pure bimoments will be generated for pure torsional motion. The virtual work produced by a bimoment B_d is given as

$$\delta W_d(t) = -B_d(t)\delta\theta'(t) \tag{11}$$

The axial out-of-plane displacement is expressed in terms of the sector coordinate ψ as

$$\delta u_j(t) = -\psi_j \delta\theta'(t) \tag{12}$$

where ψ_j is the intensity of the sector-coordinate at the location of the jth damper. Substitution of (8) into (11) then defines the bimoment as

$$B_d(t) = \sum_j \psi_j F_{d,j}(t) \tag{13}$$

From (13) it is evident that even a single applied axial force will generate a bimoment, while only force configurations satisfying the conditions in (9) and (10) will result in a pure torsional moment with vanishing normal force and bending moments.

2.3. Boundary condition

The set of axial viscous forces that produce a pure bimoment works on the axial warping displacements generated by the twisting motion of the beam. This viscous bimoment constitutes the boundary condition and the axial viscous force $F_{d,j}$ at the boundary is therefore given as

$$F_{d,j}(t) = \pm\, \alpha_j c_0 \dot{u}_{d,j}(t) \tag{14}$$

where $\dot{u}_{d,j}$ is the axial velocity at the location of the damper, defined positive in the axial z-direction as shown in Figure 1a. Furthermore, c_0 is the viscous coefficient and α_j is a balancing factor in the case of multiple dampers not placed symmetrically. In that case all viscous damping coefficients are balanced relative to the reference coefficient c_0. The axial force is defined positive in tension, and the "+" in (14) therefore refers to the left end of the beam at $z = 0$, while the "–" indicates the right end of the beam at $z = \ell$. According to (12) the axial velocity is represented by the sector-coordinate ψ as

$$\dot{u}_{d,j}(t) = -\psi_j \dot{\theta}'_d(t) \tag{15}$$

The rate of external work produced by the viscous forces is found by multiplying the viscous force $F_{d,j}$ with the energy conjugate velocity $\dot{u}_{d,j}$ followed by summation over the applied viscous forces. This work is equated with the work produced by a bimoment: $D = -\dot{\theta}'_d B_d$. This gives the resulting bimoment produced by the axial viscous forces as

$$B_d(t) = \mp\, \dot{\theta}'_d(t) \sum_j \alpha_j c_0 \psi_j^2 \tag{16}$$

This bimoment must be counteracted by the section bimoment when EI_ψ is the warping stiffness as

$$B_d(t) = -EI_\psi \theta''_d(t) \tag{17}$$

By assuming the frequency solution $\theta(t) = \varphi e^{i\omega t}$ and inserting (16) into (17) the boundary condition appears as

$$\varphi'' \mp i\omega\eta\varphi' = 0 \tag{18}$$

where

$$\eta = \sum_j \alpha_j c_0 \frac{\psi_j^2}{EI_\psi} \tag{19}$$

is an effective damping parameter that collects the damping forces. The boundary condition (18) may be applied directly to determine the integration constants in (5), thereby establishing a transcendental equation to be solved for the wave number or natural frequency. In the case of infinite damping $\eta \to \infty$ and for the damper configuration in Figure 2a the warping function in Figure 2b, associated with no damping, will approach the one in Figure 2c.

3. Finite element model

The differential equation (4) governs the torsional vibrations of the continuous beam model with damping applied as a boundary condition. It is effectively solved and may conveniently be used for calibration and optimization of the damper design. However, as the dampers act locally on the cross-section at discrete positions, some effects may occur which are not captured by the differential equation derived on the basis of simplified kinematic assumptions with a resulting bimoment (16) acting proportionally to the gradient of the angle of twist. These local effects could include in-plane distortion of the cross-section, local bending of flanges, etc. When modeling a complex structure it is of interest to be able to do simple, yet fairly accurate preliminary analyses, rather than performing the relevant investigations on a full three-dimensional finite element model—which may be computationally very expensive or even intractable. Therefore a finite element model is set up in

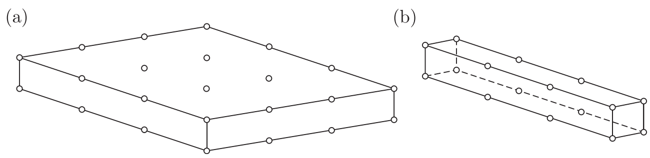

Figure 3. (a) Bi-cubic-linear and (b) cubic-bi-linear isoparametric Lagrange-elements for thin-walled flanges.

order to investigate the effect of applying local dampers, and to compare with the results from solving the differential equation.

The finite element model is based on a discretization of the three-dimensional beam structure into finite elements, as indicated in Figure 2b, where the geometry is defined by a number of nodes. At these nodes concentrated damping forces F_d may be placed, introducing damping at discrete locations on the cross-section. The present model considers viscous dampers, as defined in (14), but in a finite element formulation general passive or active dampers may as well be applied. In the structural model for the beam any inherent structural damping is neglected, whereby the model only consists of the stiffness matrix $\mathbf{K}$, the mass matrix $\mathbf{M}$ and n degrees-of-freedom collected in the column vector $\mathbf{q}$. For the structure without dampers, the equations of motion can therefore be written in the general form as

$$\mathbf{M}\,\ddot{\mathbf{q}}(t) + \mathbf{K}\mathbf{q}(t) = \mathbf{0} \tag{20}$$

Free vibration solutions are obtained by assuming the harmonic representation $\mathbf{q}(t) = \tilde{\mathbf{q}}e^{i\omega t}$, where the tilde indicates harmonic amplitudes and ω is the free vibration angular frequency. Substitution of the harmonic representation into (20) yields the associated eigenvalue problem

$$\left(\mathbf{K}-\omega_{0,n}^2\mathbf{M}\right)\tilde{\mathbf{q}}_n = \mathbf{0} \tag{21}$$

which determines the undamped natural frequency $\omega_{0,n}$ and the corresponding mode shape $\tilde{\mathbf{q}}_n$ for the nth vibration form of the structure.

Concentrated and discrete dampers are now applied in the numerical model, as indicated by the arrows with F_d in Figure 2a. These forces are added to the system by a connectivity vector $\mathbf{w}_j$ for the jth damper, with all zero entries except for a unit value at the single degree-of-freedom where the specific damper is located. Thus, the connectivity vector governs the location, direction and scaling of the damper force $F_{d,j}$, as discussed in greater detail for viscous dampers in [25]. For the structure with dampers the equation of motion (20) is extended to

$$\mathbf{M}\ddot{\mathbf{q}}(t) + \mathbf{K}\mathbf{q}(t) = -\sum_j \mathbf{w}_j F_{d,j}(t) \tag{22}$$

In (14) the local damper velocity $\dot{u}_{d,j} = \mathbf{w}_j^T\,\dot{\mathbf{q}}$ for the jth damper is as well determined by the connectivity vector. Hereby the dissipative term on the right hand side of (22) can be expressed as

$$\sum_j \mathbf{w}_j F_{d,j}(t) = \mathbf{C}_d\,\dot{\mathbf{q}}(t) \tag{23}$$

introducing the damping matrix

$$\mathbf{C}_d = \sum_j \alpha_j c_0 \mathbf{w}_j \mathbf{w}_j^T \tag{24}$$

with c_0 being the viscous reference value and α_j the balancing factor for the jth damper—thus $c_j = \alpha_j c_0$ and c_0 may be chosen arbitrarily among all dampers. Substitution of (23) into the right hand side of (22) then yields the equations of motion with added local dampers as

$$\mathbf{M}\ddot{\mathbf{q}}(t) + \mathbf{C}_d\dot{\mathbf{q}}(t) + \mathbf{K}\mathbf{q}(t) = \mathbf{0} \tag{25}$$

This equation constitutes a quadratic eigenvalue problem for the solution of the natural frequency, conveniently expressed in state-space form as

$$\frac{d}{dt}\begin{bmatrix}\mathbf{q}(t)\\ \dot{\mathbf{q}}(t)\end{bmatrix} = \begin{bmatrix}\mathbf{0} & \mathbf{I}\\ -\mathbf{M}^{-1}\mathbf{K} & -\mathbf{M}^{-1}\mathbf{C}_d\end{bmatrix}\begin{bmatrix}\mathbf{q}(t)\\ \dot{\mathbf{q}}(t)\end{bmatrix} \tag{26}$$

where $\mathbf{I}$ is the $n \times n$ identity matrix. These coupled equations may be written in compact form by introducing the state vector as $\mathbf{z} = [\mathbf{q}\,,\,\dot{\mathbf{q}}]^T$ and the state matrix in (26) as $\mathbf{A}$. When assuming frequency dependent harmonic solutions, the eigenvalue problem for the damped structure can be written in the standard form

$$(\mathbf{A}-i\omega_n\mathbf{I})\tilde{\mathbf{z}}_n = \mathbf{0} \tag{27}$$

with $\tilde{\mathbf{z}}$ being the eigenvector and $i\omega_n$ the eigenvalue. For finite values of the viscous coefficients c_j, the solution to (27) will be complex-valued, with the imaginary part of the natural frequency ω_n representing the damping associated with the nth vibration form. For vanishing viscous damping, ω_n retains $\omega_{0,n}$ determined by (21), while for all $c_j \to \infty$ the damped natural frequency ω_n approaches $\omega_{n,\infty}$, representing the real-valued natural frequency of mode n associated with full restrainment of the degrees-of-freedom connected to a damper.

A disadvantage of the state-space form is that the state-matrix is $2n \times 2n$ whereby the size of the system is doubled. Thus solving the system for large structures imposes a substantial numerical effort. For instance, a three-dimensional finite element model may easily have several thousand degrees-of-freedom, whereby this method may be computationally heavy or even infeasible. In a design scenario, it may therefore be necessary to establish a faster—yet approximate—tool, such as solving the transcendental equation associated with the differential equation in Section 2.

With the damping matrix $\mathbf{C}_d$ added to the equations of motion in (25) the damped frequency may be expressed through the damping ratio ζ as

$$\omega_n = |\omega_n|\left(\sqrt{1-\zeta_n^2} + i\zeta_n\right) \tag{28}$$

The damping ratio can therefore be obtained directly from (28) as the relative imaginary part of the damped frequency,

$$\zeta_n = \frac{\mathrm{Im}[\omega_n]}{|\omega_n|} \tag{29}$$

The mode shapes obtained from (27) are in general also complex, with the real part representing the physical vibration form and the imaginary part representing the spatial phase

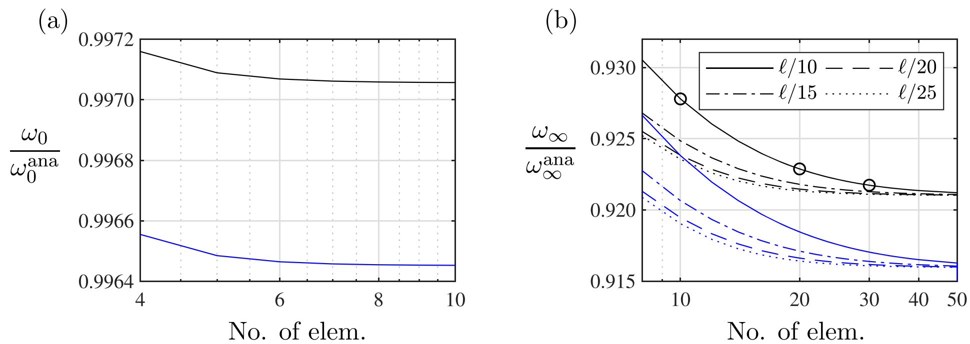

Figure 4. Convergence of ω_0 (a) and ω_∞ (b) as a function of the number of lengthwise elements and local discretization. Black line is one in-plane element per flange part and blue line is two.

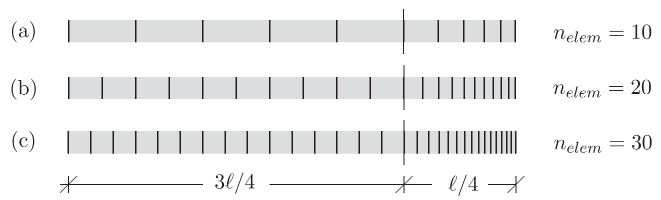

Figure 5. Discretization with lengthwise elements. One fourth of the beam is discretized with an equal amount of elements as the remaining part, but with lengths of decaying exponential type.

shift due to the presence of the energy dissipating dampers. The remaining part of the article only considers the first torsional mode, whereby the subscript $n = 1$ is omitted.

An effective and systematic way of modeling thin-walled beams is by use of the isoparametric Lagrange-elements shown in Figure 3. They consist of a bi-cubic-linear element with eight internal nodes for flange parts, and a cubic-bi-linear element for corners and junctions. They have four nodes in the flange-wise direction and two across the thickness. As long as the flanges are thin or of moderate thickness, the linear interpolation across the thickness is assumed sufficient. In a static analysis, a single element across a web or flange part yields a cubic interpolation, capturing the sufficient order of the shear stress distribution, see e.g. [35]. In the present context, the advantage of using such solid elements rather than shell elements is that they represent the warping displacements more accurately as the warping across the flange thickness is not necessarily constant. In the top row of Figure 6 it may be seen how a section of the modified I-profile may be discretized with these elements.

Figure 4a and b show the convergence of the first undamped and infinitely damped torsional frequencies ω_0 and ω_∞ relative to the corresponding analytical frequencies ω^{ana} from Section 2.1 as a function of the number of elements in the lengthwise direction. The beam has "simple" supports that restrain rotation but allow warping, with a geometry as described in Section 5. The black line indicates an in-plane discretization of one element per flange part as in Figure 6, while the blue line represents two elements. As seen the frequency converges with relatively few elements, and the difference between using one or two elements per flange part is minimal. In the top row of Figure 6 it may be seen how local damping forces are applied as concentrated forces acting at specific nodes. When the viscous coefficient for these dampers is infinitely high the dampers lock and act as axial supports. These discrete supports have a very local nature and a significant influence on the convergence of the infinitely damped frequency ω_∞. The element topology and discretization of the structural domain in the lengthwise direction then becomes important. If the beam was to be discretized with equally sized elements in the lengthwise direction, a very high amount of elements are needed for sufficient convergence. Therefore, it is proposed to perform a finer discretization close to the damped end of the beam. Figure 5 shows such a local discretization, for dampers acting at the right end cross-section with one fourth of the beam with length ℓ being discretized with the same amount of elements as the remaining part of the beam. The three discretizations (a)–(c) in Figure 5 are depicted with (○) in Figure 4b. Within the densely discretized zone, the element lengths decrease exponentially towards the beam end. Figure 4b shows the convergence of the infinitely damped frequency ω_∞ as a function of the number of lengthwise elements. The two groups of curves represent in-plane discretization with one (black) or two (blue) elements per flange part. Each group contains four curves, obtained for different relative lengths of the zone with finer discretization: $\ell/10$ (—), $\ell/15$ (– –), $\ell/20$ (— ·) and $\ell/25$ (· · ·). It is seen that the convergence is much slower. For the modified I-profile sufficient convergence is obtained with one in-plane element per flange part, 30 lengthwise elements and $\ell/25$ with finer discretization.

4. Damper design

The placing and tuning of external dampers is often a crucial process during the design. If the damper is placed in a position with no motion at all or if the damping parameter is chosen so that it provides too little resistance, it will have no effect. On the contrary if it provides too large resistance it will act as a rigid link. In a tuning procedure it is obviously of interest to reach maximum modal damping, which is reached by maximizing ω_∞ when $c_j \to \infty$ for the particular damper placement.

4.1. Balancing of dampers

In the case with more than one damper mounted on the structure, the dampers should be balanced such that they work optimally together. For symmetric structures and

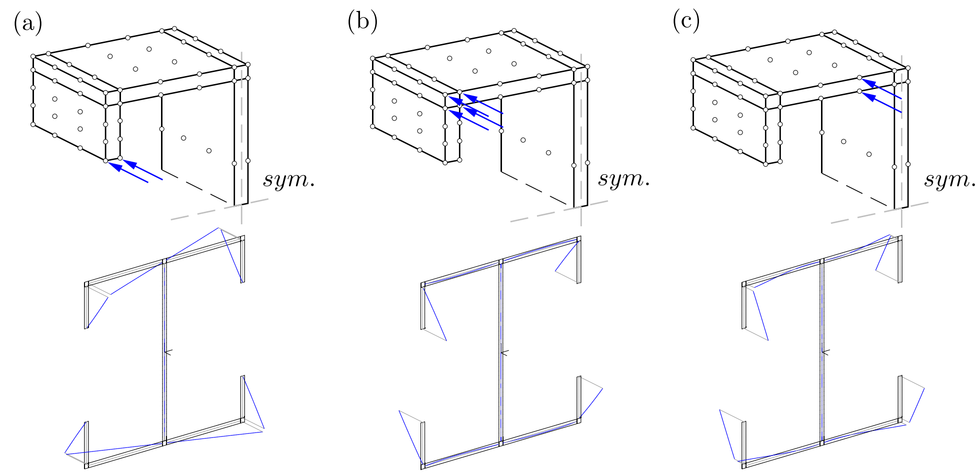

Figure 6. Section of the modified I-profile with three different configurations of dampers, and the associated warping displacements (scaled for visual reason).

Table 1. Relative frequency increments due to damper locking.

		(a)	(b)	(c)
ω_∞/ω_0	[–]	1.318	1.368	1.225

symmetric locations they should all have equal gain, whereas in the case of asymmetry they should not. An approximate yet accurate procedure is described in [25], balancing a set of viscous dampers against an arbitrarily chosen reference damper. The method is based on a reduction technique using the undamped mode n associated with the eigenvalue problem in (21). In the other limiting case where $c_j \to \infty$ for all dampers they lock and act as rigid links providing constraint forces at the damper locations which enters the eigenvalue problem. When using the papers two-component approximation technique the constraint force $\rho_{n,j}$ for the jth rigid link in vibration mode n may be determined as

$$\rho_{n,j} = \mathbf{w}_j^T \left(\omega_{\infty,n}^2 \mathbf{M} - \mathbf{K}\right) \tilde{\mathbf{q}}_{\infty,n} \tag{30}$$

The idea is then to minimize the residual forces leading to the following rule for distributing the relative gains of the viscous dampers acting together,

$$\frac{c_j}{c_1} = \frac{\rho_{n,j}}{\rho_{n,1}} \frac{\mathbf{w}_1^T \tilde{\mathbf{q}}_{0,n}}{\mathbf{w}_j^T \tilde{\mathbf{q}}_{0,n}} \tag{31}$$

When all dampers are balanced relative to damper $j = 1$, then $c_0 = c_1$ in (14) and (24), whereby balancing factor $\alpha_j = c_j/c_1$ is given directly as the expression in (31).

4.2. Restraining warping

An important measure for damping efficiency is the ability of the dampers to fully restrain warping. Restraining warping of the entire cross-section at one or possibly both ends of a beam by the chosen set of dampers yields the highest possibly value of ω_∞. This damper configuration will therefore provide the largest attainable damping ratio for a particular beam vibrating in pure torsion. For the analytical beam solution, the fully locked limit is represented by a support condition that fully restrains the rate of twist: $\theta'(t) = 0$. In reality and in the numerical finite element model, the limit $c_j \to \infty$ implies that only the degrees-of-freedom connected to a damper are fully restrained by the locking of the dampers, thus allowing the cross-section to warp between the damper locations with a non-vanishing warping function different from the kinematic representation used in the analytical beam solution. In the numerical finite element model an optimal distribution the local dampers is therefore associated with minimizing the residual warping when $c_j \to \infty$ and thereby maximizing the locked natural frequency ω_∞.

Figure 6 illustrates the warping functions associated with locked dampers for different damper configurations acting on the modified I-profile. The top row of the figure shows a quarter of the double symmetric cross-section with three different configurations of axial damping forces, that by construction are placed symmetrically to avoid a resulting normal force or bending moments. The forces therefore produce a pure bimoment in all three configurations. The second row of Figure 6 shows plots of the corresponding out-of-plane warping displacements (artificially amplified) with restrained axial displacement at the damper locations. The axial displacement is averaged across the thickness of the flanges to illustrate representative center line distributions of the axial warping function. It is initially verified that the axial displacements are in fact zero at the location of the dampers. Two or four local forces are applied in the finite element model to avoid unnecessary distortion across the wall thickness. It is seen that finite out-of-plane warping still is present, although the dampers are fully locked. Thus, a certain degree of flexibility in the locked limit $c_j \to \infty$ remains in the finite element model, while for the analytical boundary condition in (18) the rate of twist $\varphi_d' = 0$ by a supporting bimoment governed by (17).

Assume a continuous beam model with "simple–simple" support conditions for the torsional problem and dampers acting on the warping displacement at the right free end. The cross-section of the beam is shown in Figure 6 and the length of the slender beam is equal to thirty times the cross-section height, while the remaining cross-section properties are given in Section 5. Table 1 provides the natural

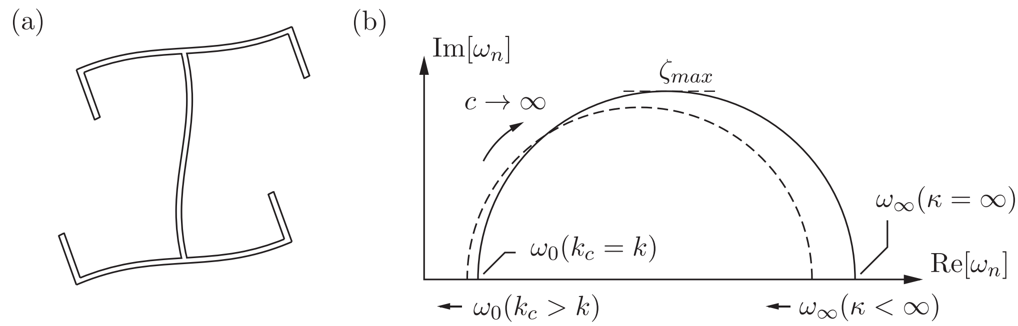

Figure 7. (a) In-plane distortion of the modified I-profile when vibrating in pure torsion and (b) frequency locus in the complex plane and consequence of parameters κ and k_c.

frequency ω_∞ for the first torsional mode obtained by the numerical finite element model. The results are presented relative to the corresponding natural frequency ω_0 without dampers. The warping function without dampers is shown in Figure 2b, which shows that the largest warping occurs at the free end of the small vertical flange. Thus, the damper placement depicted in Figure 6a may be expected to provide the best authority and thereby the largest relative frequency increase. It is seen in the table that for this configuration (a) the frequency ratio is $\omega_\infty/\omega_0 = 1.318$, providing almost a 32% increase due to locking of the dampers. However, it is seen from the warping distribution in Figure 6a that the out-of-plane displacement is fairly large at the corner and non-vanishing along the flanges. When instead placing the dampers as in Figure 6b the displacement is almost fully restrained along the horizontal flanges, while only non-vanishing along the small vertical flanges. Apparently, this configuration is better at restraining the warping displacement and Table 1 also confirms a small increase in the frequency ratio $\omega_\infty/\omega_0 = 1.368$ for case (b). The optimal placement is therefore not necessarily dictated by the largest value of the sector coordinate ψ, but instead by the ability to restrain warping when the dampers are fully locked. In Figure 6c, the dampers are placed closer to the junction with the web, whereby the warping function appears to be qualitatively similar to that in Figure 1b, although with visible displacements at the horizontal flange. Therefore, the frequency increase for this configuration (c) is less than for the previous case (b). Another location of dampers may however be even better than case (b), indicating that finding the optimal placement is a non-trivial task. The efficiency of the individual damper configurations is analyzed in much greater detail in Section 5.

4.3. Calibration of parameters

When modeling thin-walled beams by the use of beam theory, it is commonly assumed that the beam is sufficiently slender for the beam theory to apply and be represented with sufficient accuracy by the associated cross-sectional parameters. However, for short or very flexible beams, distortional effects, as illustrated by the in-plane deformations in Figure 7a, may have great influence on the vibration characteristics [37] and [38]. The influence of distortional effects on the torsional vibration characteristics can be corrected in the differential equation by adding relevant terms. Unfortunately, this severely complicates the analytical work and increase the complexity of the transcendental equations that will then be much more difficult to solve. The warping length scale k in (7) solely determines the undamped natural frequency ω_0. Thus, a way to account for the possible effects from distortion is to calibrate k by comparison with either experimental results or accurate finite element solutions.

The attainable damping depends very much on the half-circular trajectory of the natural frequency in the complex plane, as indicated in Figure 7b. Thus, in order for the differential equation to represent the finite element solutions as accurately as possible, the complex frequency locus should initiate and terminate at the correct frequencies ω_0 and ω_∞, respectively. As demonstrated in the previous section, the placement of the dampers has a great impact on the locked natural frequency ω_∞. Thus, the warping length scale is conveniently calibrated to capture the exact natural frequency ω_0, containing all distortional effects from the finite element model. The natural frequency ω_0 for the analytical beam model is obtained by solving the continuous eigenvalue problem based directly on the differential equation in Section 2.1. A modified warping length scale k_c is then determined by for example a simple numerical search until the exact natural frequency ω_0 from the finite element model is retained.

In the sketch in Figure 7b the solid curve represents the half-circular root locus associated with the analytical solution to the continuous eigenvalue problem when the original wave length scale $k = \sqrt{GK/EI_\psi}$ is used. The dashed locus instead indicates the exact complex root trajectory obtained by solving the full eigenvalue problem (27) in state-space form for the finite element structure. The analytical beam problem slightly overestimates ω_0, because distortional effects constitute non-represented flexibility, whereby the corrected wave length parameter k_c must be larger than the original k determined by the basic cross-section parameters. This effect is analyzed in more detail in the subsequent example, which shows that this correction due to distortional effects is mainly required for relatively short beams.

In the case of infinite damping the out-of-plane warping is completely restrained at the particular points on the cross-section where the dampers are placed. Thus, between these points the cross-section will still be able to warp, as

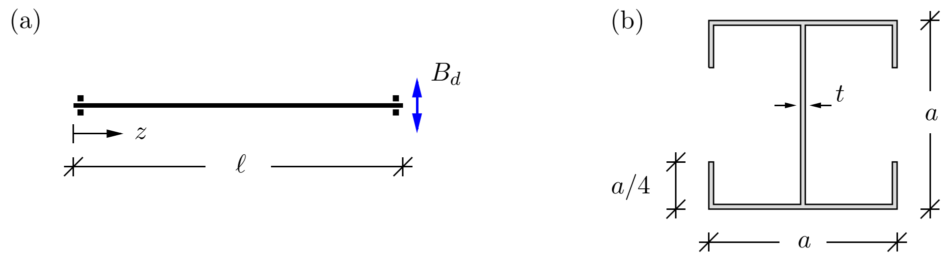

Figure 8. (a) "Simple–simple" beam with damping treatment at $z = \ell$, and (b) modified I-profile.

illustrated in Figure 6. This excess deformation is associated with additional flexibility relative to the full restrainment of the cross-section when solving the differential equation. This additional flexibility is represented by the artificial stiffness κ, introduced to the boundary condition in (18) as

$$\varphi'' \mp \left(\frac{1}{i\omega\eta} + \frac{1}{\kappa}\right)^{-1} \varphi' = 0 \tag{32}$$

The effect of the additional flexibility $1/\kappa$ is illustrated in Figure 7b, resulting in a reduction of the natural frequency from the differential equation. The correction constant κ may be calibrated as for k_c, based on a simple numerical search routine that retains the correct natural frequency ω_∞ obtained from the finite element model. The correct κ is calibrated so that the continuous eigenvalue problem with the flexible boundary condition

$$\varphi'' \mp \kappa \varphi' = 0 \tag{33}$$

exactly recovers the numerically determined ω_∞ associated with $\eta \to \infty$. In practice, the state-space problem in (27) is not conveniently solved to get ω_∞. Instead axial support conditions are added to the finite element model at damper locations, whereby the natural frequency ω_∞ may be readily obtained from a generalized eigenvalue problem similar to (21).

In the limiting case of infinite damping with $\eta \to \infty$, the boundary condition (32) dictates that $\varphi' = 0$, thus without excess warping displacement, when neglecting the correction term $1/\kappa$ in the parenthesis. However, with the concentrated dampers applied at discrete points on the cross-section, the partially restrained warping will inherently reduce the infinitely damped frequency due to the remaining flexibility, as the cross-section will obviously warp between damper locations. This further implies that the warping displacements are linear combinations of the sector-coordinates associated with the undamped beam in Figure 2b and the remaining warping function in Figure 2c for infinite damping. The axial displacements in (15) are therefore only an approximation, leaving a slightly altered warping stiffness to be used for the section bimoment in (17). However, as the actual warping displacements at infinite damping vanish, the current model actually predicts the damping behavior with great accuracy, as demonstrated by the numerical example in the next section. Thus, instead of conducting a full root locus analysis with the large finite element model, the eigenvalue solution from the partial differential equation may effectively be used to design the damper system, as long as the two correction parameters k_c and κ are calibrated accurately.

5. Damping of a "simple–simple" beam

To illustrate the attainable damping properties by restraining the warping displacements—and to demonstrate the accuracy of using the differential equation with calibrated parameters rather than doing a full root locus analysis—a beam is analyzed with the two different bimoment configurations in Figure 6a and b, from now denoted as B_a and B_b, respectively. The beam in Figure 8a is with "simple–simple" supports which represent restrained rotation and free warping at both ends. Viscous damping is applied at $z = \ell$. The cross-section in Figure 8b has a height and width a, thickness $t = a/40$ and added vertical flanges of length $a/4$. Possion's ratio is $\nu = 0.3$. According to [23] the transcendental equation governing the simple-simple beam may be written as

$$\left((\alpha\ell)^2 + (\beta\ell)^2\right)\sinh(\alpha\ell)\sin(\beta\ell) - \left(\tfrac{1}{i\omega\eta\ell} + \tfrac{1}{\kappa\ell}\right)^{-1}\cosh(\alpha\ell)\cos(\beta\ell)\left[\beta\ell\,\tanh(\alpha\ell) - \alpha\ell\,\tan(\beta\ell)\right] = 0 \tag{34}$$

The first step is to calibrate k_c and κ based on the established finite element model of the beam. Figure 9a shows the variation of k_c relative to the original $k = \sqrt{GK/EI_\psi}$ for different lengths of the beam. The graph basically shows the influence of cross-section distortion on the undamped frequencies, as a function of the beam length to the height of the cross-section. It shows that distortion has a significant effect when the beam is sufficiently short. With increasing length the ratio k_c/k approaches unity, without the distortional effect. Based on the calibrated k_c the stiffness parameter κ may subsequently be calibrated. Figure 9b shows the variation of $\kappa\ell$ for the two bimoment configurations as they give different infinitely damped frequencies. The specific value of $\kappa\ell$ ensures that the infinitely damped frequency ω_∞ obtained by the transcendental equation matches the corresponding frequency from the finite element analysis. Figure 9b shows that κ increases with the slenderness ratio ℓ/a as the warping effect is less important in long beams, whereby the term $1/\kappa\ell \to 0$ in (32) as $\kappa\ell \to \infty$.

5.1. Optimal balancing of dampers

The damper configurations B_a in Figure 6a and B_b in Figure 6b involve 8 and 16 dampers, respectively. The dampers are placed asymmetrically on the quarter cross-section as shown

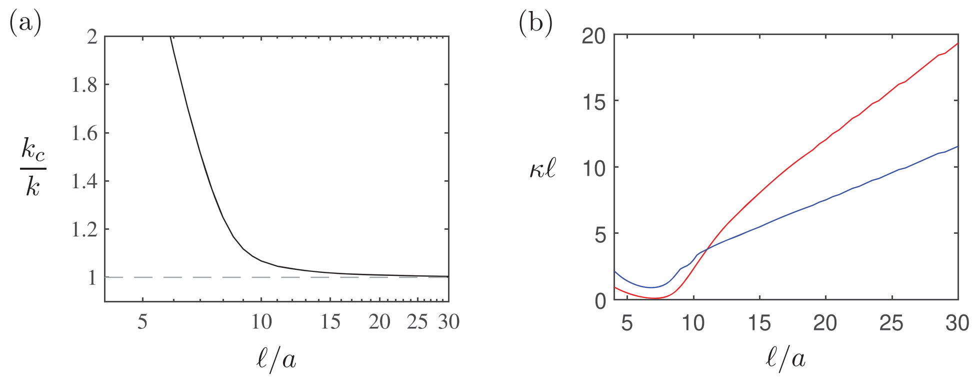

Figure 9. (a) Calibrated k_c and (b) $\kappa\ell$ for B_a (blue line) and B_b (red line) based on finite element results.

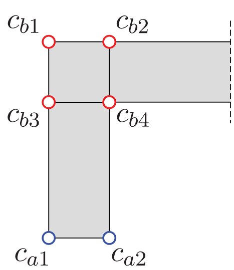

Figure 10. Order of the damping coefficients.

Table 2. Parameters used for analysis.

Bimoment Damping coefficient	B_a c_{a1}	c_{a2}	B_b c_{b1}	c_{b2}	c_{b3}	c_{b4}
α_j	1.0	0.8	1.0	7.5	70.2	141.9
$\kappa\ell$	0.385		0.645			
k_c/k	1.004		1.004			

in Figure 10 where $c_{a1} - c_{a2}$ are associated with B_a and $c_{b1} - c_{b4}$ are associated with B_b. As the warping amplitudes are different at all six locations in Figure 10 the dampers must be balanced relative to each other according to (31). The configuration B_a is balanced relative to c_{a1} and B_b is balanced relative to c_{b1}. The balancing factors α_j are seen in Table 2. For B_a the balancing factors are within the same order of magnitude, and only a vanishing deviation would be observed if the dampers were not balanced. In the case of B_b the necessity of balancing is obvious as c_{b3} and c_{b4} are much larger than c_{b1} and c_{b2} and if all dampers had the same damping coefficient the root locus would consist of multiple smaller semicircles as illustrated in [25] with less effect.

5.2. Root locus analysis

With the parameters k_c and κ calibrated, a full root locus analysis may be performed by solving the transcendental equation (34) by varying the viscous damping parameter in the interval $c_0 \in [0\,;\infty[$. The real part of the complex frequency will then shift from ω_0 to ω_∞. The frequency loci and damping ratios obtained from the transcendental equation are compared to similar analyses in the finite element format, see Figure 11. The analyses are based on $\ell/a = 30$. The results are not dependent of the size of the cross-section if the ratio ℓ/a is kept constant, neither does the material have an influence on the relative frequency increment $(\omega_\infty - \omega_0)/\omega_0$, and thereby the maximum attainable damping ratio. However, the optimal value of the viscous damping parameter and absolute frequencies are sensitive to changes in geometry and material and will therefore change accordingly.

The black dashed line indicates a fully restrained cross-section, therefore representing the maximum frequency and damping ratio. The parameters needed for solving the transcendental equation are given in Table 2. Considering the frequency loci it may be observed that the frequencies coincide at ω_0 and ω_∞ as expected due to the calibration of k_c and $\kappa\ell$. It may furthermore be observed by the blue lines, indicating that the dampers are placed in the outermost points of the cross-section (Figure 6a) yield a lower ω_∞ than having the dampers placed at the corners (Figure 6b), represented by the red lines. The damping ratio is determined based on the imaginary part of the frequency, see (29), and thus the larger the imaginary part the larger the damping ratio. The ($\circ$)-markers and solid lines with the (+)-markers representing FE results and results from solving the transcendental equation respectively match perfectly.

Table 3 presents the relative frequency increments and maximum damping ratios, $\zeta_{\max}$. The results from the full finite element analysis and from solving the transcendental equation are presented for comparison. From the relative frequency increments $(\omega_\infty - \omega_0)/\omega_0$ it may be seen that warping has a significant influence on the natural frequency. Relative increments of 30–50% are observed in this particular case, merely by restraining warping partially at one end of the beam. The maximum damping ratio $\zeta_{\max}$ corresponds approximately to the top point of the frequency loci in Figure 11a and thus to half of the relative frequency increment [26] and [39],

$$\zeta^* = \frac{1}{2}\frac{\omega_\infty - \omega_0}{\omega_0} \tag{35}$$

From Table 3 it may be seen that this estimate fits well with the results from the root locus analyses. Thus, in a preliminary design situation the maximum damping ratio is easily estimated from ω_0 and ω_∞, obtained without solving the full complex problem in (27).

If transient analyses are to be performed in a preliminary design stage, the motion of the beam must also be

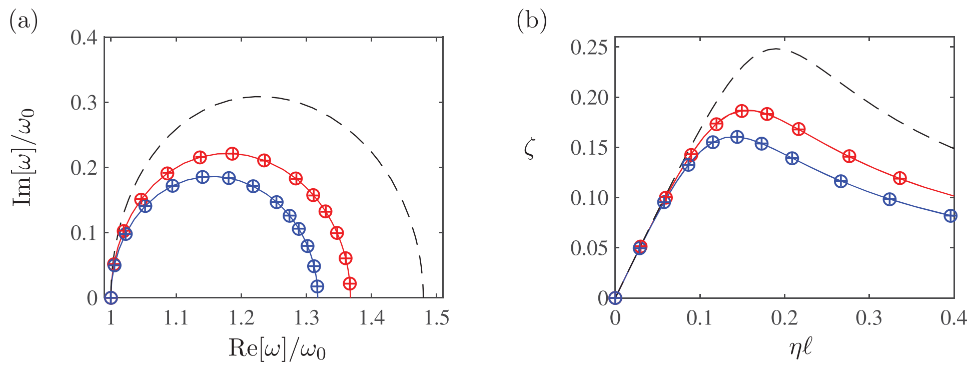

Figure 11. Complex frequency loci (a) and damping ratio (b). Results from finite element analysis (blue circle) and (red circle) and differential equation (blue line, blue plus symbol) and (red line, red plus symbol). Blue and red corresponds to B_a and B_b respectively. (– –) indicates fully restrained cross-sections.

sufficiently represented by the differential equation. The undamped and infinitely damped mode shapes from the differential equation are shown with $(+)$-markers in Figure 12a and b, in which the rotations from the finite element model are plotted with $(\circ)$-markers. These rotations are determined based on an average displacement of the eight junction nodes at the connection between the cross-section web and the two flanges, see Figure 2b. In Figure 12 it may be seen that the rotations from the two methods match almost perfectly, and the differential equation therefore accurately represents the vibration form as well. From the curves it is also evident that restraining warping partially at the right end of the beam causes the gradient of the rotation to decrease, which also can be seen in the mode shapes from the finite element model in Figure 12c and d, with colors indicating the absolute displacements. If the right end cross-section was fully prevented from warping the rotation curve would have been flat at the right end of Figure 12b as the gradient would then be zero, $\varphi'(\ell) = 0$.

5.3. Optimal damper location

From the root locus analysis it is evident that the maximum damping ratio depends very much on the damper location, and it has previously been demonstrated that the optimal position is not directly proportional with the magnitude of the warping displacements. The largest damping ratio is however obtained when placing the dampers such that the flexibility of the beam is lowered as much as possible, thereby increasing the infinitely damped frequency ω_∞. Therefore, the bimoment configuration B_b yields the largest damping ratios during the root locus analysis. However, determining the position of the dampers such that ω_∞ is increased as much as possible is as mentioned earlier not a trivial task.

An optimal position of the dampers is robustly estimated by simply sweeping over locations along the flanges of the profile and determining ω_∞ when replacing the dampers with axial supports. Comparing ω_∞ with ω_0 as in (35) gives a good estimate of an optimal position that maximizes the damping ratio. In the current example the dampers may be placed at six different locations, either as a horizontal pair as in Figure 6a, as four dampers as in Figure 6b or as a vertical pair as in Figure 6c. For each of the six positions, ω_∞ may be found by either solving the transcendental equation or by the finite element model, which only requires solving a real-valued problem. Figure 13 shows the ratios ω_∞/ω_0 of which two are recovered in Table 3. This analysis again shows that placing the dampers at the corner is more effective than at the bottom of the vertical flange. However, the actual optimal damper location is seemingly on the vertical flange just below the corner element.

Table 3. Frequency increments and damping ratios from the root locus analysis.

Bimoment	$(\omega_\infty - \omega_0)/\omega_0$	ζ^{FEM}_{max}	$\zeta^{Diff.eq.}_{max}$	ζ^*
B_a	0.318	0.160	0.161	0.159
B_b	0.368	0.186	0.187	0.184
∞	0.480	–	0.248	0.240

6. Conclusions

A method for damping torsional vibrations in thin-walled beams by restraining the out-of-plane axial warping displacements has been expanded by including a flexibility term in the viscous boundary condition, to be used in relation with the governing differential equation. The flexibility term alters the infinitely damped frequency for a given bimoment configuration and may be calibrated by supplemental finite element results. Furthermore, the warping length scale k has been calibrated according to finite element results to take the in-plane distortional effects associated with short beams into account in the modified value k_c. Hereby the frequency loci produced by the differential equation are obtained, which initiate and terminate at the correct frequencies, as obtained by the finite element model. Almost identical results in terms of maximum damping ratios and the associated viscous damping coefficients are obtained by the differential equation and the finite element model. As the axial dampers have a very local nature caution must be taken when meshing the structure. It is proposed to mesh $25/\ell$ of the beam end with the dampers applied with as many elements as the rest of the beam. Furthermore, the eight internal nodes of the bi-cubic-linear element ensure a consistent convergence behavior.

The finite element model of the beam from the example has more than 18.500 degrees-of-freedom. A full root locus analysis of a three-dimensional finite element model may

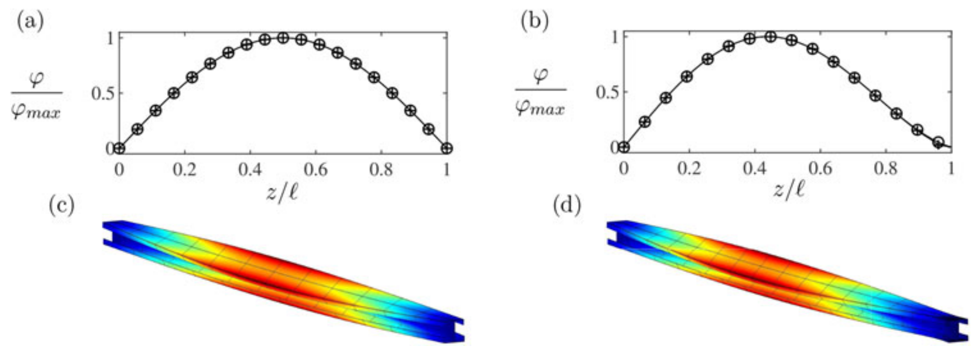

Figure 12. Undamped (a, c) and infinitely damped (b, d) mode shapes. (a, b) Shows the rotation relative to the shear center from the FE results (○) and from the differential equation (—, +) and (c, d) shows patch plots from the FE model.

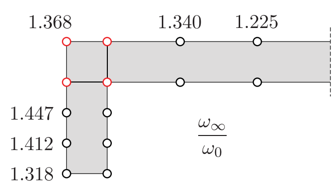

Figure 13. Relative frequency increments for different damper locations.

therefore be computationally very heavy and time consuming, and even in some cases practically impossible. This suggests that preliminary analyses may be performed by using the differential equation with calibrated parameters obtained by solving only two undamped eigenvalue problems. This allows for an investigation of damper configurations, different geometries, etc., retrieving damping ratios, frequencies and optimal values of viscous damping coefficients with great accuracy. With a single or few final designs a more detailed analysis may then be conducted in the full finite element format.

It has furthermore been demonstrated how different damper configurations on the cross-section may influence the attainable damping properties. For a chosen beam configuration the dampers should be placed to minimize the flexibility of the beam and thereby increase the relative frequency increment between the undamped and infinitely damped frequencies. A substantial amount of damping has been demonstrated, and the differential equation and the finite element model shows very good conformity. Though, it still remains a challenge to determine the flexibility parameter κ explicitly. As it requires information about the beam configuration and the cross-section, it may be achieved with the hierarchical Carrera Unified Formulation [40] exploiting some higher-order theory to capture the altered warping of the cross-section. Finally, a simply way of estimating the optimal location of the dampers was presented.

As the warping displacements are generally quite small, damping could be realized with e.g. piezoelectric transducers as presented in [41], where large forces may be generated at small stroke levels. If the beam is small, piezoelectric patches [21] could be placed in pairs on the beam flanges where one acts as the sensor and the other as actuator. Although these would act on the relative displacements, they should still be able to control warping and thus introduce damping.

ORCID

David Hoffmeyer http://orcid.org/0000-0003-2499-1964

References

[1] P. Keller, C. Higgins, and S. C. Lovejoy, "Evaluation of torsional vibrations in steel truss bridge members," J. Bridge Eng., vol. 20, no. 9, p. 04014102, 2015.
[2] A. Larsen, "Bridge deck flutter analysis," Proceedings of the Danish Society for Structural Science and Engineering, vol. LXXXVII, no. 2–4, June 2016.
[3] A. Larsen, Private communication, Chief Specialist, Aero and Structural Dynamics, Bridge, Tunnel and Marine Structures, COWI, October 2017.
[4] M. N. Svendsen, Private communication, Chief Consultant, International Bridges, Ramboll, October 2017.
[5] H. Sato, S. Kusuhara, K. Ogi, and H. Matsufuji, "Aerodynamic characteristics of super long-span bridges with slotted box girder," J. Wind Eng. Ind. Aerodyn., vol. 88, no. 2–3, pp. 297–306, 2000.
[6] Y. Achkire, F. Bossens, and A. Preumont, "Active damping and flutter control of cable-stayed bridges," J. Wind Eng. Ind. Aerodyn., vol. 74–76, pp. 913–921, 1998.
[7] O. Øiseth and R. Sigbjörnsson, "An alternative analytical approach to prediction of flutter stability limits of cable supported bridges," J. Sound Vib., vol. 330, no. 12, pp. 2784–2800, 2011.
[8] J. Náprstek and S. Pospíšil, "Response types and general stability conditions of linear aero-elastic system with two degrees-of-freedom," J. Wind Eng. Ind. Aerodyn., vol. 111, pp. 1–13, 2012.
[9] M. S. Andersen, J. Johansson, A. Brandt, and S. O. Hansen, "Aerodynamic stability of long span suspension bridges with low torsional natural frequencies," Eng. Struct., vol. 120, pp. 82–91, 2016.
[10] Z. Zhang, X. Zhang, Y. Yang, and Y. Ge, "Nonlinear aerodynamic and energy input properties of a twin-box girder bridge deck section," J. Fluids Struct., vol. 74, pp. 413–426, 2017.
[11] M. N. Svendsen and S. M. Johannesen, "Multi-modal flutter analysis of a long floating bridge," 40th IABSE Symposium, 19–21 September, Nantes, France, 2018.
[12] B. Chen, Z. Zhang, X. Hua, S. R. K. Nielsen, and B. Basu, "Enhancement of flutter stability in wind turbines with a new type of passive damper of torsional rotation of blades," J. Wind Eng. Ind. Aerodyn., vol. 173, pp. 171–179, 2018.
[13] J. R. Banerjee, S. Guo, and W. P. Howson, "Exact dynamic stiffness matrix of a bending-torsion coupled beam including warping," Comput. Struct., vol. 59, no. 4, pp. 613–621, 1996.
[14] J. M. Gere, "Torsional vibrations of beams of thin-walled open section," ASME J. Appl. Mech., vol. 21, no. 4, pp. 381–387, 1954.

[15] J. M. Gere and Y. K. Lin, "Coupled vibrations of thin-walled beams of open cross-section," ASME J. Appl. Mech., vol. 25, no. 3, pp. 373–378, 1958.

[16] E. J. Sapountzakis, "Bars under torsional loading: a generalized beam theory approach," ISRN Civ. Eng., vol. 2013, p. 1, 2013.

[17] M. Matthias, D. Schlote, and H. Atzrodt, "Active structures to reduce torsional vibrations," Proc. SPIE, vol. 8690, p. 869001, 2013.

[18] J. D. Jansen and L. van den Steen, "Active damping of self-excited torsional vibrations in oil well drillstrings," J. Sound Vib., vol. 179, no. 4, pp. 647–668, 1995.

[19] I. Y. Shen, "Bending and torsional vibration control of composite beams through intelligent constrained-layer damping treatments," Smart Mater. Struct., vol. 4, no. 4, pp. 340–355, 1995.

[20] E. Augustyn and M. S. Kozień, "A study on possibility to apply piezoelectric actuators for active reduction of torsional beams vibrations," Acta Phys. Pol. A, vol. 125, no. 4, pp. A164–A168, 2014.

[21] J. Toftekær, A. Benjeddou, J. Høgsberg, and S. Krenk, "Optimal piezoelectric resistive-inductive shunt damping of plates with residual mode correction," J. Intell. Mater. Syst. Struct., vol. 29, no. 16, pp. 3346–3370, 2018.

[22] P. Christiano and L. Salmela, "Frequencies of beams with elastic warping restraint," J. Struct. Div., vol. 97, no. 6, pp. 1835–1840, 1971.

[23] J. Høgsberg, D. Hoffmeyer, and C. Ejlersen, "Damping of torsional beam vibrations by control of warping displacement," J. Vib. Acoust., vol. 138, p. 014501, 2016.

[24] D. Hoffmeyer and J. Høgsberg, "Numerical investigation of damping of torsional beam vibrations by viscous bimoments," presented at the VIII ECCOMAS Thematic Conference on Smart Structures and Materials, June 5–8, 2017.

[25] J. A. Main and S. Krenk, "Efficiency and tuning of viscous dampers on discrete systems," J. Sound Vib., vol. 286, no. 1–2, pp. 97–122, 2005.

[26] K. Engelen, H. Ramon, W. Saeys, W. Franssens, and J. Anthonis, "Positioning and tuning of viscous damper on flexible structure," J. Sound Vib., vol. 304, no. 3–5, pp. 845–862, 2007.

[27] S. Krenk, "Complex modes and frequencies in damped structural vibrations," J. Sound Vib., vol. 270, no. 4–5, pp. 981–996, 2004.

[28] M. Gürgöze and H. Erol, "Dynamic response of a viscously damped cantilever with a viscous end condition," J. Sound Vib., vol. 298, no. 1–2, pp. 132–153, 2006.

[29] E. J. Sapountzakis, "Torsional vibrations of composite bars of variable cross-section by BEM," Comput. Methods Appl. Mech. Eng., vol. 194, no. 18–20, pp. 2127–2145, 2005.

[30] C. Svedholm, A. Zangeneh, C. Pacoste, S. François, and R. Karoumi, "Vibration of damped uniform beams with general end conditions under moving loads," Eng. Struct., vol. 126, pp. 40–52, 2016.

[31] J. C. MacBain and J. Genin, "Effect of support flexibility on the fundamental frequency of vibrating beams," J. Franklin Inst., vol. 296, no. 4, pp. 259–273, 1973.

[32] A. M. Al-Jumaily and L. L. Faulkner, "Vibration of continuous systems with compliant boundaries," J. Sound Vib., vol. 54, no. 2, pp. 203–213, 1977.

[33] M. J. Maurizi, R. E. Rossi, and P. M. Bellés, "Free vibrations of uniform Timoshenko beams with ends elastically restrained against rotation and translation," J. Sound Vib., vol. 141, no. 2, pp. 359–362, 1990.

[34] S. Naguleswaran, "Transverse vibration of an Euler–Bernoulli uniform beam on up to five resilient supports including ends," J. Sound Vib., vol. 261, no. 2, pp. 372–384, 2003.

[35] J. Høgsberg and S. Krenk, "Analysis of moderately thin-walled beam cross-sections by cubic isoparametric elements," Comput. Struct., vol. 134, pp. 88–101, 2014.

[36] C. F. Kollbrunner and N. Hajdin, Dünnwandige stäbe, Band 1, Stäbe mit undeformierbaren querschnitten. Berlin, Heidelberg: Springer, 1972.

[37] A. D. S. Barr and T. Duthie, "Influence of cross-section distortion on the bending vibration of thin-walled beams of H section," Mech. Eng., vol. 6, no. 3, pp. 211–218, 1964.

[38] J. Jönsson, "Determination of shear stresses, warping functions and section properties of thin-walled beams using finite elements," Comput. Struct., vol. 68, no. 4, pp. 393–410, 1998.

[39] J. Høgsberg, "Modelling of dampers and damping in structures," PhD thesis, Department of Mechanical Engineering, Technical University of Denmark, 2007.

[40] E. Carrera and M. Petrolo, "Refined beam elements with only displacement variables and plate/shell capabilities," Meccanica, vol. 47, no. 3, pp. 537–556, 2012.

[41] A. Preumont, B. de Marneffe, A. Deraemaeker, and F. Bossens, "The damping of a truss structure with a piezoelectric transducer," Comput. Struct., vol. 86, no. 3–5, pp. 227–239, 2008.

P2

Damping of Coupled Bending-Torsion Beam Vibrations
by Spatially Filtered Warping Position Feedback

David Hoffmeyer and Jan Høgsberg

(Submitted)

Damping of Coupled Bending-Torsion Beam Vibrations by Spatially Filtered Warping Position Feedback

David Hoffmeyer[a,*], Jan Høgsberg[a]

[a] *Department of Mechanical Engineering,*
Technical University of Denmark,
DK-2800 Kongens Lyngby, Denmark
Nils Koppels Allé, Building 404

Abstract

Damping of coupled bending-torsion beam vibrations is realized by local actuators, operating axially on an end cross-section of a fully three-dimensional structure by a collective positive position feedback control with a spatial filter that specifically targets the out-of-plane warping component of the coupled response. To reduce the computational effort, a beam element model is introduced, in which a single control bimoment is supplemented by a fictitious stiffness that accounts for the inability of the local actuators to fully restrain warping. This fictitious stiffness is conveniently calibrated by frequency matching in the limit of infinite control gain and it enables accurate estimation of both complex roots and the stability limit from beam element analysis. It is demonstrated by a numerical example that substantial modal damping is attained by positive position feedback of the torsional warping component from the fully coupled response.

Keywords:

Damping, coupled vibrations, positive position feedback, active control, thin-walled beams, finite element method

1. Introduction

Many beam structures exhibit properties which inherently couple basic deformation modes. Varying cross-sectional properties, pretwist, inhomogeneous material distribution and lack of cross-sectional symmetry may all lead to coupling between axial, bending and/or torsional deformation modes of beam structures. Areas of application in large-scale structures may include wind turbine blades, bridges and tall buildings [1]. In all of these areas, structural vibrations may be an issue and supplemental damping by discrete devices may be required to increase the life-time of structures prone to fatigue damage, reduce the risk of aeroelastic instabilities like flutter and secure accelerations below comfort levels.

*Corresponding author
Email address: davhoff@mek.dtu.dk (David Hoffmeyer)

Early descriptions of coupled beam vibrations because of non-coinciding elastic and shear centres were given by Gere [2], while a thorough derivation of the coupled differential equations with contributions from rotary and warping inertia can be found in [3, 4]. Special emphasis on the effect of warping was given in [5], concluding that significant errors occurred when not taking this supplemental deformation into account. Coupled vibrations in slender beam structures are effectively analysed by beam elements [6, 7], as also shown in the present paper.

Wind turbine blades are large-scale structures with pronounced coupled bending-torsion vibrations because of asymmetric cross-section geometry and inhomogeneous material distribution, making them prone to aeroelastic flutter instability with apparent negative damping [8]. Because of the continuously increasing size of wind turbines and their blades, it is of interest to alleviate excessive dynamic vibrations, as previously proposed with tuned mass dampers [9, 10].

The coupled vibrations imposed by aeroelastic interaction is also present in streamlined bridge decks, as reported for long-span suspension bridges in [11, 12, 13]. As it may be a limiting factor in design of future multi-deck bridges, efforts are put into increasing the flutter wind speed limit by adding damping, using for example tuned mass dampers [14, 15]. Other structures with coupled bending-torsion vibrations are composite beams or plates, used in many areas of application where limited weight combined with high strength is of importance [16, 17, 18].

This paper specifically considers damping of coupled bending-torsion vibrations by partially restraining the out-of-plane, axial warping displacements that occur due to the torsional part of the fully coupled response. Figure 1a shows a viscous bimoment, restraining the cross-section warping of a 1D beam model. It has been demonstrated in [19] that the restrainment of warping by a special boundary condition for the bimoment may realize a significant increase in frequency and thereby a great damping potential. The promising results for the ideal beam model have recently been confirmed by a full three-dimensional finite element (3D FE) analysis [20], with several discrete viscous dampers placed in configurations constituting the desired bimoment on a beam cross-section, as shown in Fig. 1b

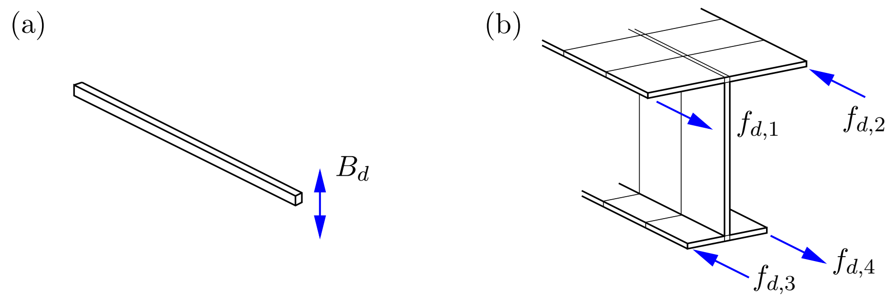

Figure 1: (a) effective beam model with actuator bimoment and (b) 3D structure with discrete, axial actuators.

for four corner forces acting oppositely on a single-symmetric cross section. However, the discrete actuators in Fig. 1b only resist warping of the cross-section locally where they are placed, thereby leaving non-vanishing warping displacements to occur in the remainder of the cross-section. This partial restrainment of warping is associated with an excess flexibility in the system, not accounted for by the beam element model in Fig. 1a. Therefore, an equivalent control law for the beam element in Fig. 1a is supplemented by an fictitious spring stiffness that represents this additional flexibility experienced by the actual model in Fig. 1b. The inclusion of the fictitious spring reduces the frequency of the system, by an elastic boundary condition, as described for torsional damping in [21] or for structures with flexible or non-ideal supports in [22, 23, 24].

For large and densely meshed structures it may be computationally ineffective to perform a detailed damping analysis with the full 3D FE model in Fig. 1b. Therefore, this paper instead solves the complex eigenvalue problem for the efficient beam element model in Fig. 1a, augmented with the fictitious spring to account for the excess warping associated with the local actuator control in Fig. 1b.

As torsional warping displacements may be quite small, an active control with positive position feedback (PPF) [25, 26, 27, 28, 29] of the warping displacement is proposed to achieve a substantial increase in attainable damping. The displacements are effectively measured by e.g. strain sensors at each actuator location and processed by a spatial filter that combines the individual signals into a resulting out-of-plane warping deflection of the cross section, without affecting deformations from the extension and bending content of the coupled response. A positive position feedback control law provides the desired damping performance and the individual target force processed to the individual actuator on the cross section is then distributed by the same spatial filter used to modulate the sensor signal. Thus, the control scheme is collectively collocated [30], although the feedback for each individual actuator is not entirely decentralized.

A proposed first-order linear filter with assumed ideal actuator dynamics has previously been proposed for vibration damping in [31, 32], and has furthermore been considered for damping of pure torsional vibrations in [33]. It is demonstrated how the excess flexibility from the partial warping restrainment, included in the beam model by the fictitious spring stiffness, affects and changes the stability limit [34, 35] of the combined system with PPF. It is finally demonstrated that substantial damping ratios are obtained by only restraining the torsional part of the coupled bending-torsion response of a beam structure.

2. Coupled vibrations with active control

A main goal of the present paper is the formulation of a simple beam model, that accurately captures the detailed dynamics of an underlying 3D beam structure with local positive position feedback (PPF) control of the out-of-plane warping displacement from torsion. This section therefore derives the governing equations for coupled bending-torsion vibrations of a pure beam model with an equivalent bimoment representing the active boundary control.

2.1. Governing differential equations

Consider a beam with length ℓ, longitudinal axis z and transverse axes $\{x_1, x_2\}$. For a cross-section without double symmetry the elastic centre $C = (c_1, c_2)$ - which also represents the centre of mass - and shear centre $A = (a_1, a_2)$ do not coincide, as shown in Fig. 2a. The $\{x_1, x_2\}$-directions are in this case not principal axes and define the translational displacements $\xi_1(z)$ and $\xi_2(z)$ with respect to the shear centre. As bending-torsion-coupling is investigated, the extension deformation is excluded in the present formulation. The angle of twist with respect to the shear centre around the z-axis is $\theta(z)$. To keep a compact notation the arguments (x_1, x_2, z) are excluded in the following.

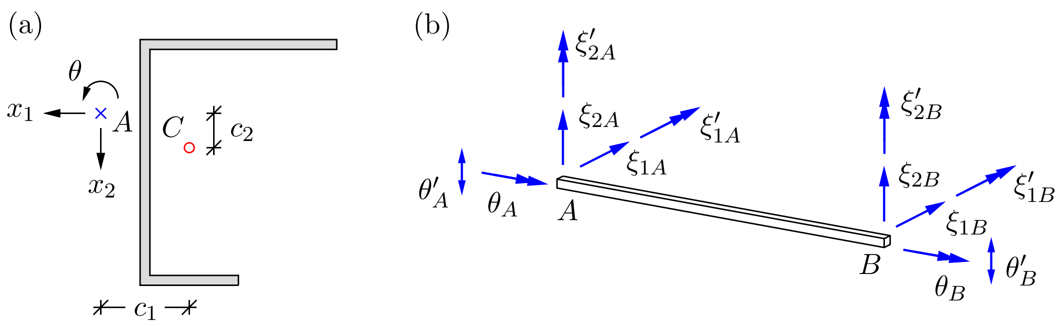

Figure 2: (a) Asymmetric cross-section with $\{x_1, x_2\}$-coordinate system, elastic centre C and shear centre A. (b) Beam element with six nodal degrees-of-freedom.

The equations governing coupled bending and torsional vibrations of a general thin-walled beam may be derived as shown in e.g. [3, 4],

$$\begin{aligned} EI_{\alpha\beta}\xi_\beta'''' + \rho A\ddot{\xi}_\alpha - \rho Ac_\beta\ddot{\theta} = 0 \quad , \quad \alpha, \beta = 1, 2 \\ EI_\psi\theta'''' - GK\theta'' + \rho Ac_1\ddot{\xi}_2 - \rho Ac_2\ddot{\xi}_1 + \rho J\ddot{\theta} = 0 \end{aligned} \tag{1}$$

where summation over repeated Greek index is implied in the top equation. The cross-sectional parameters consist of the bending stiffnesses $EI_{\alpha\beta}$, the torsional stiffness GK associated with homogeneous torsion (St. Venant), the warping stiffness EI_ψ associated with inhomogeneous torsion (Vlasov), the mass per unit length ρA and the torsional inertia per unit length ρJ. Differentiation with respect to z is indicated by $(\ )' = \partial(\ )/\partial z$, while $\dot{(\ )} = \partial(\ )/\partial t$ describes differentiation with respect to time t. Furthermore ψ is the warping function or sector-coordinate associated with free homogeneous torsion. The coupling specifically depends on the distances c_α between the elastic centre and shear centre, shown in Fig. 2a.

2.2. Discretization by beam elements

A main objective of the paper is to demonstrate the accuracy of the beam element model relative to a full 3D FE model of the beam structure. For beam elements the classic cubic Hermitian shape functions are often sufficient to interpolate between nodes, as they linearly resolve the curvature for ξ_β and θ in (1). Without the extensional deformation of the element, each node has six degrees-of-freedom, as indicated in Fig. 2b. The discretization of the beam model then yields a global stiffness matrix $\mathbf{K}$ and mass matrix $\mathbf{M}$, with further details on

the specific finite element implementation provided in the Appendix A, summarizing explicit expressions for the system matrices by appropriate sub-matrices, that may include higher-order effects, such as rotary and warping inertia, by supplemental terms.
The equations of motion for the structure modelled by beam elements are represented in terms of the n degrees-of-freedom in the displacement vector $\mathbf{q}(t)$ of the linear system,

$$\mathbf{M}\ddot{\mathbf{q}}(t) + \mathbf{K}\mathbf{q}(t) = \mathbf{0} \tag{2}$$

when neglecting any inherent structural damping. Free vibrations are throughout the paper examined by assuming harmonic solutions of the form: $\mathbf{q}(t) = \widetilde{\mathbf{q}}e^{i\omega t}$, where $\widetilde{()}$ denotes the vibration amplitude and ω is the angular frequency. By substitution into (2), the undamped eigenvalue problem takes the form

$$\Big(-\omega_{0,j}^2\mathbf{M} + \mathbf{K}\Big)\widetilde{\mathbf{q}}_{0,j} = \mathbf{0} \tag{3}$$

where $\omega_{0,j}$ are the undamped natural frequencies and $\widetilde{\mathbf{q}}_{0,j}$ are the corresponding mode shape vectors, with subscript 0 denoting the undamped structure and j referring to the specific mode number.

2.3. Damping by warping position feedback

Efficient damping of the beam element model is introduced by a PPF control, where the local actuator forces on the 3D structure in Fig. 1b act on the local axial displacements from torsional warping extracted from the coupled bending-torsion response. For the present beam model in Fig. 1a, the combined actuator forces constitute a resulting bimoment B_d that is energy conjugated to the gradient of the angle of twist θ'_d, representing the warping intensity. For the beam element model the set of equations of motion is therefore given as

$$\mathbf{M}\ddot{\mathbf{q}}(t) + \mathbf{K}\mathbf{q}(t) = -\mathbf{w}B_d(t) \tag{4}$$

The effect of the resulting bimoment is here added to the beam model by a connectivity vector $\mathbf{w}$, which identifies the specific actuator configuration and location. The connectivity vector $\mathbf{w}$ furthermore defines the representative displacement

$$\theta'_d(t) = \mathbf{w}^T\mathbf{q}(t) \tag{5}$$

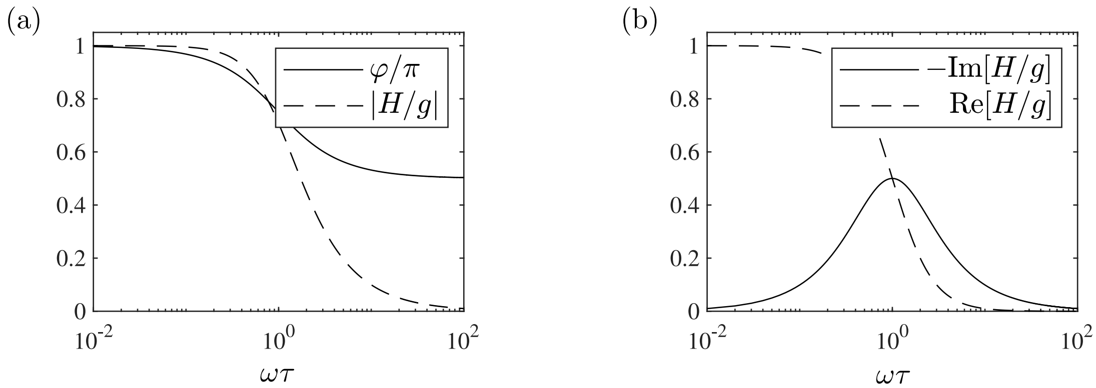

Figure 3: (a) magnitude and phase angle and (b) real and imaginary part of the frequency function H.

that produces work with the equivalent bimoment B_d in (4). For the beam model, the connectivity vector has the simple structure $\mathbf{w} = [\,\dots\,,\,1\,,\,\dots\,]^T$, where the single unit value is located at the degree-of-freedom representing the warping intensity of the controlled node. For the proposed PPF control, the bimoment is assumed linear and collocated, with the feedback force formulated as a linear filter [31, 32],

$$B_d(t) + \tau \dot{B}_d(t) = g\theta'_d(t) \tag{6}$$

where τ is a filter constant defining the cut-off frequency at $1/\tau$. Thus, the gain g here governs the magnitude of the collective feedback control for the equivalent bimoment on the simple beam model, whereas Section 5 introduces the actual control for the full 3D FE structure with a gain for the axial force actuators.

2.4. Frequency relations for PPF

Based on the measured displacement $\theta'_d(t)$, the equivalent bimoment $B_d(t)$ is fed back to the system by the control law in (6) for the representative beam model. The properties of this filter may be examined in the frequency domain by assuming the harmonic solutions $B_d(t) = \widetilde{B}_d \mathrm{e}^{i\omega t}$ and $\theta_d(t) = \widetilde{\theta}_d \mathrm{e}^{i\omega t}$, leading to the frequency control relation

$$\widetilde{B}_d = H\widetilde{\theta}_d \tag{7}$$

which introduces the temporal dependence by the frequency function

$$H = \frac{g}{1 + i\omega\tau} \tag{8}$$

Thus, the effect and tuning of the actuator is governed by the gain g, while the frequency characteristics are represented by the denominator of H. The complex $H = |H|e^{i\varphi}$ is conveniently decomposed into its phase angle φ and the magnitude $|H/g|$ of the frequency function normalized with the gain g,

$$\tan\varphi = -\omega\tau \qquad , \qquad |H/g| = \frac{1}{\sqrt{1+(\omega\tau)^2}} \tag{9}$$

The phase angle and normalized magnitude are shown in Fig. 3a. It is seen by the solid line that the PPF imposes a control component that operates ahead of velocity by a phase angle $\varphi > \pi/2$, which approaches the viscous limit $\varphi \simeq \pi/2$ in the high-frequency domain $\omega\tau \to \infty$. This phase lead $\varphi > \pi/2$ corresponds to apparent negative stiffness [32], whereby the PPF locally increases actuator deflection and improves the overall energy dissipation. Therefore, PPF is advantageous for small deformation problems, such as the warping feedback control considered in the present case.

The magnitude of the transfer function, represented by the dashed line in Fig. 3a, avoids undesirable influence from high-frequency vibrations, as $|H| \to 0$ above the cut-off frequency, whereas the filter ensures large damping in the low frequency domain below the cut-off frequency. In order for the filter in (6) to dissipate energy, the imaginary part $\mathrm{Im}[H] > 0$. Figure 3b shows both the real and imaginary part of the frequency function H, where the imaginary part of the frequency function (solid curve) is seen to be negative, whereby the gain $g < 0$. Conversely, the real part $\mathrm{Re}[H] < 0$ imposes the previously mentioned negative stiffness that locally increases the actuator stroke and improves performance over classic viscous damping or direct velocity feedback [36].

3. Beam model with warping-restrained flexibility

Figure 4a shows a flange of the thin-walled cross-section in Fig. 4b and Fig. 1b. The 3D FE structural model is discretized by finite elements and two axial actuator forces act locally at the free end. During the PPF control the actuators will restrain the warping displacements at their specific location, even completely preventing the axial motion in the limit $g \to -\infty$. However, the cross-section may still be able to warp in between the actuators locations, as indicated in Fig. 4b. This residual warping displacement is associated with an

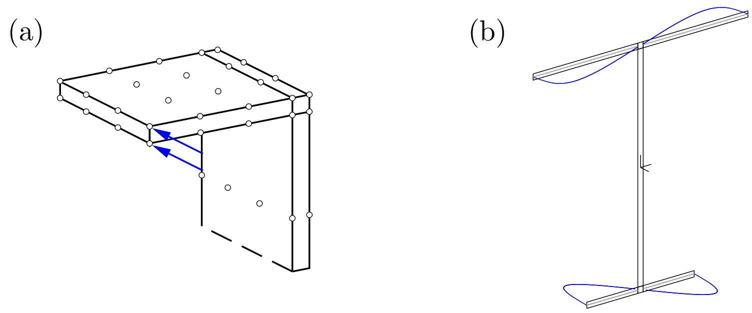

Figure 4: (a) quarter I-profile cross-section with two actuator forces at the upper left corner and (b) warping at infinitely high actuator gain.

excess flexibility, which is not included in the beam model. Thus, the PPF control law in (6) for the effective beam model must augmented to capture the correct dynamics and this additional flexibility of the underlying 3D FE model [20].

3.1. Augmented control with fictitious stiffness

The additional flexibility to be used when controlling the equivalent beam model may be modelled as a spring with stiffness k in series with the active controller in (6) with gain g, as schematically indicated in Fig. 5. The fictitious spring stiffness is introduced by the linear relation

$$B_d(t) = k\theta'_k(t) \tag{10}$$

in which the excess component θ'_k is associated with the cross-section warping in Fig. 4b for locking of the actuators at $g \to -\infty$. It follows from Fig. 5 that the total gradient of the angle of twist θ'_{d*} is given as the sum of the contributions from the bimoment and from the fictitious spring,

$$\theta'_{d*}(t) = \theta'_k(t) + \theta'_d(t) \tag{11}$$

Introducing (6) and (10) into (11) then yields the augmented control equation

$$\left(\frac{1}{g} + \frac{1}{k}\right) B_d(t) + \frac{\tau}{g}\dot{B}_d(t) = \theta'_{d*}(t) \tag{12}$$

to be used in the following for calibration of the gain g when controlling the beam model. The fictitious stiffness k is in the following determined such that the frequency of the equivalent beam at infinite gain ($g \to -\infty$) recovers the correct frequency when locking the discrete

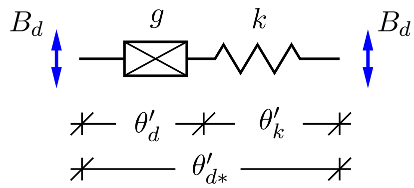

Figure 5: Boundary condition with an active element with gain g in series with a spring with stiffness k.

actuators on the actual cross-section in the full 3D FE model in Fig. 4.

The gain-dependent frequency function H_* of the augmented control equation (12) can now be written as

$$H_* = \left[\left(\frac{1}{g} + \frac{1}{k} \right) + i\omega \frac{\tau}{g} \right]^{-1} \tag{13}$$

whereby $H_* \to H$ in (8) as $k \to \infty$. When introducing the actuator force (12) in the global system (4), the equations of motion may be written in the frequency domain as

$$\Big(-\omega_j^2 \mathbf{M} + \mathbf{K} + H_* \mathbf{w}\mathbf{w}^T \Big) \widetilde{\mathbf{q}}_j = \mathbf{0} \tag{14}$$

with the effect of the augmented controller included at a specific single degree-of-freedom by the matrix $\mathbf{w}\mathbf{w}^T$. The combined controller, governing the actuator bimoment B_d, is shown in Fig. 5, where the physical controller with gain g is placed in series with the fictitious spring k. Thus, when $k \to \infty$ the fictitious spring will not be deformed, whereby the boundary condition recovers the non-modified controller in (6) with gain g. However, for a finite value of k, the additional flexibility implies an increases in displacement ($\theta'_{d*} > \theta'_d$) at the beam boundary, thus modifying both the performance, calibration and stability limit of the proposed PPF control.

3.2. Determination of residual flexibility

The accurate determination of the fictitious spring stiffness k is important for the dynamic damping analysis using the simple beam model. The residual warping-restrained stiffness k in (12) is obtained from the dynamics of the structure in the limit $g \to -\infty$, in which the controller equation (13) reduces to additional stiffness term $k\mathbf{w}\mathbf{w}^T$ in

$$\Big(-\omega_{\infty,j}^2 \mathbf{M} + \mathbf{K} + k \mathbf{w}\mathbf{w}^T \Big) \widetilde{\mathbf{q}}_{\infty,j} = \mathbf{0} \tag{15}$$

For this limiting eigenvalue problem $\omega_{\infty,j}$ is the frequency of the beam model associated with infinite gain, while $\widetilde{\mathbf{q}}_{\infty,j}$ is the corresponding mode shape vector. In the following, $\omega_{\infty,j}$ is therefore referred to as the infinitely damped (natural) frequency. In the present case the stiffness k is determined so that the infinitely damped frequency $\omega_{\infty,j}$ from (15) matches the corresponding natural frequency $\omega_{\rm 3D}$ from the full 3D FE model with infinite gain. Thus, the stiffness k is calibrated by the frequency matching $\omega_{\infty,j} = \omega_{\rm 3D}$, which only requires the solution of a real-valued eigenvalue problem for the large 3D FE model.

The fictitious stiffness k can be isolated in (15) by applying the matrix determinant lemma of the Sherman-Morrison formula [37]. Substituting the calibration frequency $\omega_{\infty,j} = \omega_{\rm 3D}$ into the beam model in (15), this lemma directly gives

$$\det\Big(-\omega_{\rm 3D}^2\mathbf{M}+\mathbf{K}+k\mathbf{w}\mathbf{w}^T\Big) = \det\big[-\omega_{\rm 3D}^2\mathbf{M}+\mathbf{K}\big]\Big(1+k\mathbf{w}^T\big[-\omega_{\rm 3D}^2\mathbf{M}+\mathbf{K}\big]^{-1}\mathbf{w}\Big) = 0 \quad (16)$$

where non-trivial solutions require the determinant to be zero. This explicitly gives the residual stiffness as

$$k = -\frac{1}{\mathbf{w}^T\big[-\omega_{\rm 3D}^2\mathbf{M}+\mathbf{K}\big]^{-1}\mathbf{w}} \quad (17)$$

based on the beam model components $\mathbf{M}$, $\mathbf{K}$ and $\mathbf{w}$, and the frequency $\omega_{\rm 3D}$ from the full 3D FE model with infinite actuator gain. As the beam model will have a limited number of degrees-of-freedom, the inversion of the matrix in (17) is computationally inexpensive.

4. Stability condition

With the warping-restrained stiffness k introduced in the modified active filter in (12) and (13), the combined system for the beam model is now described and the effect of the flexibility on the stability of the system is investigated. Fig. 6 shows a root locus tracing a damped frequency ω in the comple plane from ω_0 ($\times$) for $g = 0$ to ω_∞ ($\circ$) for $g \rightarrow -\infty$. An unbounded response occurs beyond the stability limit ($\square$), that depends on the control law (12) with the excess flexibility comprised by k.

4.1. Combined closed-loop system

When solving the combined closed-loop system, comprised by the beam structure model in (4) and the equivalent control equation (12), the damped frequencies ω_j trace a family

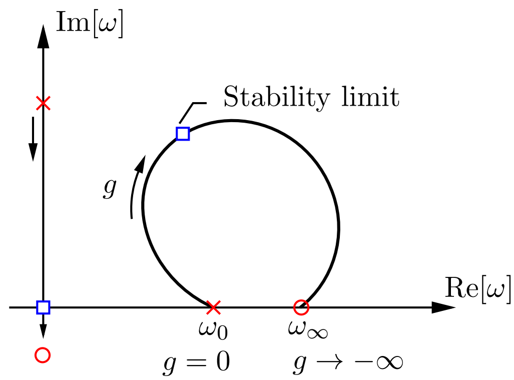

Figure 6: Root locus and indication of the stability limit when the purely imaginary eigenvalue becomes negative.

of root loci in the complex ω-plane, as indicated in Fig. 6 for gain $g = 0$ (ω_0) to $g \to -\infty$ (ω_∞). These root loci can be obtained by solving the eigenvalue problem associated with the coupled equations (4) and (12), which can be written as

$$\begin{bmatrix} \mathbf{M} & \mathbf{0} \\ \mathbf{0} & 0 \end{bmatrix} \begin{bmatrix} \ddot{\mathbf{q}}(t) \\ \ddot{B}_d(t) \end{bmatrix} + \begin{bmatrix} \mathbf{0} & \mathbf{0} \\ \mathbf{0} & \nu^{-1}\tau \end{bmatrix} \begin{bmatrix} \dot{\mathbf{q}}(t) \\ \dot{B}_d(t) \end{bmatrix} + \begin{bmatrix} \mathbf{K} & \mathbf{w} \\ -g\nu^{-1}\mathbf{w}^T & 1 \end{bmatrix} \begin{bmatrix} \mathbf{q}(t) \\ B_d(t) \end{bmatrix} = \begin{bmatrix} \mathbf{0} \\ 0 \end{bmatrix} \tag{18}$$

where $\nu = \left(1 + \frac{g}{k}\right)$ contains the correction from the fictitious stiffness k. From this block matrix formulation, the combined system is solved in the corresponding state-space format, for which the complex roots ω_n are expressed as

$$\omega_j = |\omega_j| \left(\sqrt{1 - \zeta_j^2} + i\zeta_j \right) \tag{19}$$

introducing the apparent damping ratio as the relative imaginary part

$$\zeta_j = \frac{\mathrm{Im}[\omega_j]}{|\omega_j|} \tag{20}$$

The damping ratio is therefore a rational measure for the modal damping attainable by the active PPF control.

4.2. Stability limit

It follows from Fig. 3b that $\mathrm{Re}[H] < 0$, whereby the active warping control with positive position feedback and $g < 0$ imposes apparent negative stiffness on the structure. Thus, for a limiting value of the gain $g = g_{\mathrm{stab}}$ the negative control stiffness makes the combined system non-positive definite and thus unstable with unbounded response. It is crucial to avoid instabilities when applying active control, and the determination of the precise gain limit $g = g_{\text{stab}}$ is therefore a necessity.

The equivalent first-order control equation (15) implies that a pure imaginary root is added to the family of complex conjugated natural frequencies obtained by the eigenvalue problem associated with (18). Stability requires all eigenvalues to have a positive imaginary part, whereby instability occurs when a single of these pure imaginary roots becomes negative, as indicated by the trajectory ($\times$ to $\circ$) along the imaginary axis in Fig. 6. A stability criterion is constructed by inspection of (18), in which the augmented mass and damping matrices will be guaranteed positive semi-definite for $\nu > 0$ and thus $g > -k$. Although this inequality indicates a stability gain from modal spill-over, the condition is often not limiting because of the large values of k obtained by the small to moderate reductions in the infinitely damped frequency $\omega_{\infty,j}$ found e.g. in the numerical example in Section 7.

The augmented stiffness matrix must as well be positive definite. Because of the PPF control, this introduces a limit on the negative gain $g = g_{\text{stab}} < 0$. Both the structural and controller equations are now pre-multiplied with $-g\nu^{-1}$, whereby the original structural coordinate $\mathbf{q}(t)$ is normalized as $\mathbf{q}^*(t) = -g\nu^{-1}\mathbf{q}(t)$. Hereby, the elastic energy from the augmented stiffness matrix in (18) can be expressed as

$$V_e = \begin{bmatrix} \mathbf{q}^*(t)^T & B_d(t) \end{bmatrix} \begin{bmatrix} \mathbf{K} & -g\nu^{-1}\mathbf{w} \\ -g\nu^{-1}\mathbf{w}^T & -g\nu^{-1} \end{bmatrix} \begin{bmatrix} \mathbf{q}^*(t) \\ B_d(t) \end{bmatrix} \tag{21}$$

which can be re-written into

$$\begin{aligned} V_e = \tfrac{1}{2}\mathbf{q}^*(t)^T\left[\mathbf{K} + g\nu^{-1}\mathbf{w}\mathbf{w}^T\right]\mathbf{q}^*(t) + \tfrac{1}{2}\Big(B_d(t)\big(g\nu^{-1}\big)^{1/2} - \big(g\nu^{-1}\big)^{1/2}\mathbf{w}^T\mathbf{q}^*(t)\Big)^2 \\ - B_d(t)g\nu^{-1}B_d(t) - \mathbf{q}^*(t)^T g\nu^{-1}\mathbf{q}^*(t) \end{aligned} \tag{22}$$

Stability requires the energy in (22) to be positive, i.e. $V_e > 0$, which directly identifies a limit of stability from the first term in (22), as the remaining terms are defined positive for $g < 0$. Therefore the matrix inside the square brackets of the first term (22) must be positive definite. By the matrix determinant lemma in (16) this corresponds to the determinant requirement

$$\det\left(\mathbf{K} + g\nu^{-1}\mathbf{w}\mathbf{w}^T\right) = \det\!\left(\mathbf{K}\right)\Big(1 + g\nu^{-1}\mathbf{w}^T\mathbf{K}^{-1}\mathbf{w}\Big) > 0 \tag{23}$$

which leads to an explicit solution for the stability gain g_{stab},

$$\frac{1}{g_{\mathrm{stab}}} = -\mathbf{w}^T\mathbf{K}^{-1}\mathbf{w} - \frac{1}{k} \tag{24}$$

The gain limit $g = g_{\mathrm{stab}}$ is thus comprised of the structural flexibility at the location of the control bimoment and the added flexibility from the partial warping restrainment. This added flexibility $1/k$ is seen to reduce the stability gain, which is otherwise ignored by the original PPF control equation in (6) for the beam model.

5. Spatial filtering and warping control

The accuracy of the simple beam element model with a PPF control for the equivalent bimoment relies on a precise calibration of the fictitious stiffness k in the augmented control equation (12). As mentioned previously, the stiffness k is calibrated by frequency matching $\omega_{\infty,j} = \omega_{\mathrm{3D}}$, where ω_{3D} denotes the infinitely damped frequency from the full 3D FE model with infinite actuator gains. Initially, the collective warping control for the full 3D FE model is obtained by constructing a connectivity vector $\mathbf{w}_{\mathrm{3D}}$ with a spatial filter that only restrains warping, while ignoring axial deformations from extension and bending.

5.1. Control equations for 3D FE model

The actual 3D FE model with discrete axial actuators placed as in Figs. 1b and 4a is inherently different in size and element type compared to the simple beam element model in Fig. 1a with the actuator bimoment in Fig. 5. Thus, the system matrices $\mathbf{M}$, $\mathbf{K}$ and displacement vector $\mathbf{q}(t)$ will be larger in size for the full 3D FE model. The governing system of equations for the full FE model may be written in standard form as

$$\mathbf{M}\ddot{\mathbf{q}}(t) + \mathbf{K}\mathbf{q}(t) = -\mathbf{f}_d(t) \tag{25}$$

in which the individual discrete actuator forces in Fig. 1b are contained in the force vector $\mathbf{f}_d(t)$. The present PPF on the full 3D structure is constructed in a collective format, with a single displacement

$$q_d(t) = \mathbf{w}_{\mathrm{3D}}^T\mathbf{q}(t) \tag{26}$$

introducing a connectivity vector $\mathbf{w}_{3\mathrm{D}}$, which describes the spatial filtering of the individual sensor signals. The collective displacement q_d for the full 3D FE model is then processed by a PPF control equation similar to that in (6) for the beam element bimoment B_d,

$$f_d(t) + \tau \dot{f}_d(t) = g_{3\mathrm{D}}\, q_d(t) \tag{27}$$

determining a corresponding collective control force f_d, which scales with the common control gain $g_{3\mathrm{D}}$. The actual control force provided by the individual actuator in the 3D FE model is then finally obtained by multiplication with the connectivity vector,

$$\mathbf{f}_d(t) = \mathbf{w}_{3\mathrm{D}} f_d(t) \tag{28}$$

Next, the connectivity vector $\mathbf{w}_{3\mathrm{D}}$ is constructed by a spatial filter that only targets the warping displacement of the full 3D FE model, while the relation between the actual gain $g_{3\mathrm{D}}$ and the equivalent bimoment gain g_{beam} for the beam model is established.

5.2. Connectivity and balancing

For a vibration mode with inherent coupling between torsion and bending, the axial displacements of the end cross-section may derive from a mix of inclinations associated with bending and out-of-plane warping from torsion. In the current strategy, only the axial displacements from warping are to be restrained by the PPF control, thus leaving the displacements from bending unaffected. Figure 7a,b shows the bending inclination and the warping displacement for the I-profile with a single line of symmetry, previously considered in Figs. 1 and 4. The connectivity vector $\mathbf{w}_{3\mathrm{D}}$ must now be constructed such that only warping is affected by the PPF control system for the full 3D FE model.

Multiple actuators act on the cross-section of the 3D model to realize the equivalent bimoment B_d, used in the equivalent beam model. Thus, the individual non-vanishing components in $\mathbf{w}_{3\mathrm{D}}$ must be relatively balanced to work optimally together in extracting the warping displacement in (26) and conversely imposing the ideal bimoment by the force vector $\mathbf{f}_d(t)$ in (28).

For warping different parts of the cross-section deform in opposite directions, as shown in Fig. 7b, whereby the entries in $\mathbf{w}_{3\mathrm{D}}$ must have the $\pm$-signs according to the warping function in Fig. 7c. The connectivity vector is therefore with zero entries, except at the

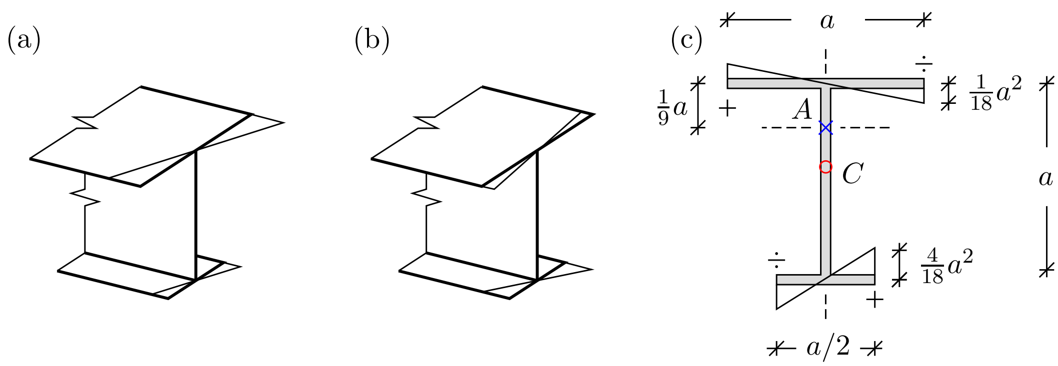

Figure 7: (a) inclination from bending, (b) warping and (c) sign of the analytical sector-coordinate ψ.

degree-of-freedom with an actuator, for which a balancing factor α_i is introduced for actuator i,

$$\mathbf{w}_{3\mathrm{D}} = [\, ... \,, \, \alpha_i \,, \, ... \,]^T \tag{29}$$

A proper balance of the individual actuators $i = 1, 2, \ldots$ is secured by balancing factors proportional to the square-root of the sector-coordinate at the actuator location

$$\alpha_i = \mathrm{sign}(\psi_i)\sqrt{|\psi_i|} \tag{30}$$

in which case the sign-function secures the desired spatial filtering that extracts the sector-coordinate in e.g. Fig. 7c, without affecting axial displacements from extension and bending. Consider the four-actuator configuration in Fig. 1b with the analytical sector-coordinate shown in Fig. 7c. In this case, the four non-zero entries in the connectivity vector will be $\pm a/\sqrt{18}$ for the two actuators placed at the free ends of the top flange and $\mp 2a/\sqrt{18}$ for the corresponding two actuators acting at the free ends of the bottom flange. When the top-flange warping function is considered as a common factor between the four entries, the connectivity vector is conveniently scaled as

$$\mathbf{w}_{3\mathrm{D}} = [\, ... \,, \, 1 \,, \, -1 \,, \, -2 \,, \, 2 \,, \, ... \,]^T \tag{31}$$

whereby the common scaling factor $a/\sqrt{18}$ is simply absorbed by the corresponding control gain $g_{3\mathrm{D}}$, as demonstrated in Section 6. Thus, for the normalized connectivity vector, the balancing factors are then $\alpha_{1,2} = \pm 1$ and $\alpha_{3,4} = \mp 2$ for the four actuator forces in Fig. 1b. For more complicated cross-section geometries and/or actuator configurations, a specific value of the sector-coordinate ψ_i at actuator location i may conveniently be obtained by available numerical cross-section analysis tools, such as [38] used in the numerical example of Section 7.

5.3. Locking cross-sectional warping

The targeted natural frequency $\omega_{3\mathrm{D}}$, used for calibration of the fictitious spring stiffness by (17), is obtained from the full 3D FE model in the gain limit $g_{3\mathrm{D}} \to -\infty$. This requires solving a large eigenvalue problem in state-space form, which may be computationally inefficient. Instead the particular locking of warping, without affecting the cross-section deformations from extension and bending, may be realized by enforcing a constraint equation based on the connectivity vector composed in the Section 5.2. This constraint condition is effectively imposed by use of Lagrange multipliers [39], with the constraint for warping simply given as $\mathbf{w}_{3\mathrm{D}}^T\widetilde{\mathbf{q}} = 0$. For free vibrations this leads to solving the following eigenvalue problem,

$$\left(\begin{bmatrix} \mathbf{K} & \mathbf{w}_{3\mathrm{D}} \\ \mathbf{w}_{3\mathrm{D}}^T & 0 \end{bmatrix} - \omega^2 \begin{bmatrix} \mathbf{M} & \mathbf{0} \\ \mathbf{0} & 0 \end{bmatrix}\right) \begin{bmatrix} \widetilde{\mathbf{q}} \\ \lambda \end{bmatrix} = \begin{bmatrix} \mathbf{0} \\ 0 \end{bmatrix} \tag{32}$$

where λ is the Lagrange multiplier and $\mathbf{w}_{3\mathrm{D}}$ specifies the constraint structure using the connectivity vector $\mathbf{w}_{3\mathrm{D}}$ established by the procedure indicated in (29). The eigenvalue problem in (32) determines the real-valued natural $\omega_{3\mathrm{D}}$ that is used by the frequency matching $\omega_{\infty,j} = \omega_{3\mathrm{D}}$ to determined the fictitious spring stiffness k by the (17).

6. Control gain equivalence

The gain g_{beam} in (12) for the beam model and $g_{3\mathrm{D}}$ for the 3D FE model in (27) are inherently different due to the different nature of the models and scaling of the respective connectivity vectors $\mathbf{w}$ and $\mathbf{w}_{3\mathrm{D}}$. The equivalence between the two models therefore requires a correct conversion between the two gains. This is achieved by equivalence of the virtual work produced by the bimoment in the beam model and the actuators in the 3D FE model. The control bimoment in the beam model produces virtual work by multiplication with the virtual rate of the angle of twist. In the frequency domain this virtual work relation can be written as

$$\delta V_{\mathrm{beam}} = -\delta\widetilde{\theta}'_d \widetilde{B}_d = -H\delta\widetilde{\theta}'_d\widetilde{\theta}'_d \tag{33}$$

introducing the frequency function H in (8). As this relation ignores the excess flexibility by $k \to \infty$, the virtual work may be considered as a perturbation from the undamped state. The virtual work in the 3D FE model consists of the virtual work produced by each of the discrete actuators,

$$\delta V_{\mathrm{3D}} = -\delta \widetilde{q}_d \widetilde{f}_d = -H \delta \widetilde{\mathbf{q}}^T \mathbf{w}_{\mathrm{3D}} \mathbf{w}_{\mathrm{3D}}^T \widetilde{\mathbf{q}} \tag{34}$$

identifying f_d and q_d as resulting scalar variables for the collective control effort. In the 3D FE model the collective displacement $\widetilde{q}_d = \mathbf{w}_{\mathrm{3D}}^T \widetilde{\mathbf{q}} = \sum_i \alpha_i \psi_i \theta_d'$ represents the sum of the magnitude of axial displacements from warping at the individual actuator locations. Thereby, the virtual work in the 3D FE model can be written as

$$\delta V_{\mathrm{3D}} = H \Big(\sum_i \alpha_i \psi_i \Big)^2 \widetilde{\theta}_d' \, \delta \widetilde{\theta}_d' \tag{35}$$

By $\delta V_{\mathrm{beam}} = \delta V_{\mathrm{3D}}$ and substitution of H from (8) with different gains in the two models, the equivalence between these gains can be obtained as

$$g_{\mathrm{3D}} = \frac{g_{\mathrm{beam}}}{\big(\sum_i \alpha_i \psi_i \big)^2} \tag{36}$$

Even though (36) describes an approximate relation, the result appears to be fairly accurate, as demonstrated in the subsequent numerical example of Section 7.

7. Numerical example

In this section an example is given to demonstrate the method of using beam elements with the warping-restrained flexibility added to analyse the damping potential of warping control applied to a beam with bending-torsion coupling. In the following the damping efficiency will be independently demonstrated for the two lowest coupled modes of a beam. The present beam is simply supported (pinned) in both ends with respect to bending in the x_1-direction, as seen in Fig. 8a, and 'simply' supported with respect to torsion, thus restraining the rotation at both beam ends while allowing warping, as indicated in Fig. 8b. The beam has length ℓ and the cross-section is seen in Fig. 8c with overall thickness $a/40$ and dimensions as depicted in the figure. The material is elastic with properties $E = 210$ GPa, $\nu = 0.3$ and $\rho = 7850$ kg/m^3. For the 3D FE model, the beam structure is discretized with isoparametric elements consisting of a bi-cubic-linear element for flange parts and a

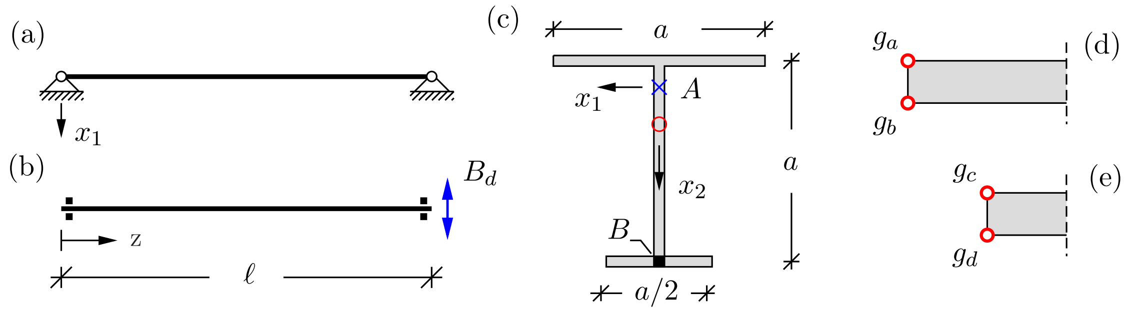

Figure 8: Simply supported beam in regards to (a) bending (b) and torsion with (c) I-profile cross-section and location of actuators in the (d) upper left corner and (e) bottom left corner.

cubic-bi-linear element for corners and junctions, as indicated in Fig. 4. The beam is discretized with 30 length-wise elements, where half of them are distributed over $\ell/25$ at the beam end where the actuators are placed, while a single element per flange part is sufficient according to [20] for the in-plane mesh. The corresponding boundary conditions in the 3D FE model restrain all nodes at both beam end cross-sections in the vertical x_2-direction, while restraining the nodes along the x_2-axis in all three directions. Thereby, the beam cross-section may rotate around the x_2-axis and displace in the axial z-direction in the flanges.

Figure 9a shows the vibration shape of the lowest mode obtained by the 3D FE model. It is seen that the torsion couples with the lateral displacement component in the x_1-direction. Figure 9b-d shows the displacement components of the coupled mode from the equivalent beam element model, with the discrete (red) circles representing average values from the full 3D FE model in Fig. 9a. It is seen that good agreement is obtained between the undamped modes from the beam element model and the full 3D FE model.

7.1. Actuator configuration

The bottom flange in Fig. 8c has half the width of the top flange, whereby the elastic and shear centres do not coincide along the x_2-axis. For the beam model, an actuator bimoment B_d is applied at the right end, as shown in Fig. 8b, which in the full 3D FE model is represented by a set of eight discrete actuators acting in the axial direction. The discrete actuators are thus structured in the connectivity vector $\mathbf{w}_{3\mathrm{D}}$ in (29) such that they collectively produce a bimoment that only operates on the warping displacement shown in

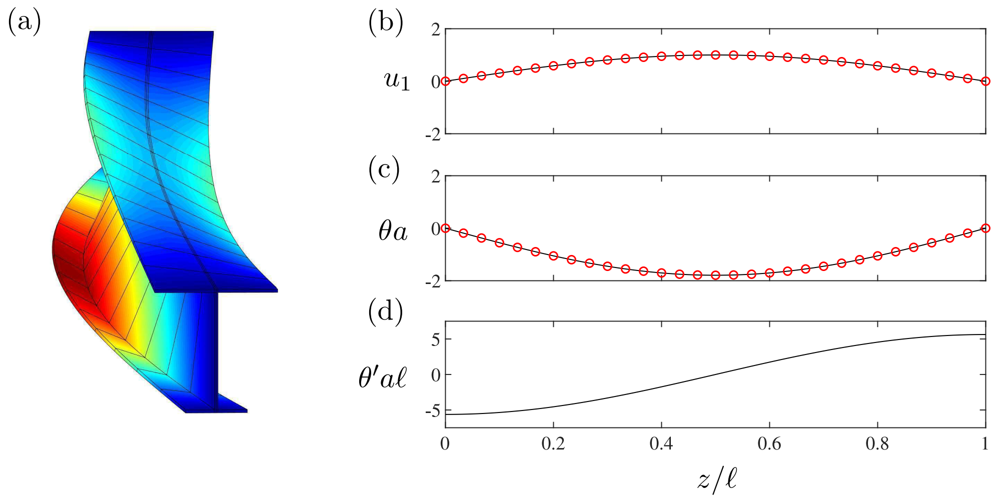

Figure 9: (a) patch plot of first vibration mode and (b-d) displacement components of the beam model, normalized with respect to maximum lateral displacement. (∘) represent averaged displacements from the 3D model.

Fig. 7c.

Two actuators are placed across the flange thickness in each corner of the four corners (free ends) of the cross-section in the 3D FE model. Because of the cross-section's symmetry with respect to the x_2-axis, the four actuators placed at the left ends of the flanges are scaled by balancing factors of same magnitude and opposite sign as their right flange counterparts. In Fig. 8d,e the circles indicate the specific location of the four left side actuators, denoted as a to d from top to bottom, respectively. The connectivity vector for the left half of the 3D FE model can therefore be expressed as

$$\mathbf{w}_{\text{left}} = [\dots, \alpha_a, \alpha_b, \alpha_c, \alpha_d, \dots]^T \tag{37}$$

with four balancing factors α_a to α_d. Conversely, the connectivity vector for the right half is simply obtained by a change of sign,

$$\mathbf{w}_{\text{right}} = -\mathbf{w}_{\text{left}} = [\dots, -\alpha_a, -\alpha_b, -\alpha_c, -\alpha_d, \dots]^T \tag{38}$$

and the total connectivity vector for all eight actuators in the 3D FE model is obtained by the assembly

$$\mathbf{w}_{\text{3D}} = [\dots, \mathbf{w}_{\text{left}}^T, \dots, \mathbf{w}_{\text{right}}^T, \dots]^T \tag{39}$$

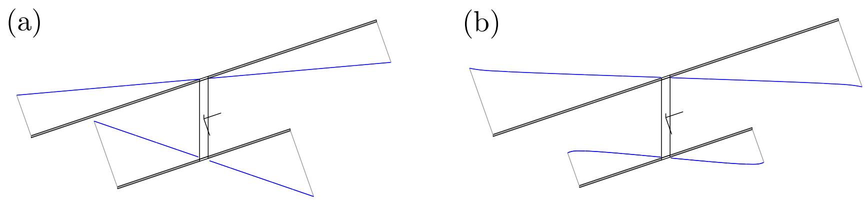

Figure 10: (a) axial displacements for the first undamped mode and (b) infinitely damped mode.

The four balancing factors α_a to α_d are then determined by (30) for the specific actuator locations shown in Fig. 8d,e. The detailed sector-coordinate is in this example obtained numerically by the cross-sectional code described in [38]. In Table 1 the balancing factors are given relative to the actuator with gain g_a in Fig. 8d.

The axial displacements of the end cross-section from the first undamped mode is seen in Fig. 10. The contribution from warping is clearly identified as the inclinations of the two flanges in Fig. 10a are not identical, which would have been the case for pure bending. With infinite gain and the chosen connectivity structure, the relative torsional warping at the four outer corners of the I-profile is restrained and leaves the axial displacements in Fig. 10b, with almost identical inclination along the flanges and a small non-linear contribution from the residual warping shown in Fig. 4b. This validates that the connectivity vector $\mathbf{w}_{3\mathrm{D}}$ effectively extracts the collective warping component due to torsion, without affecting the bending component of the coupled vibration.

7.2. Damping efficiency

With the connectivity structure determined for the 3D FE model, the objective is now to calibrate the fictitious stiffness k by (17) in order for the root locus of the beam model to initiate and terminate at the natural frequencies obtained by the full 3D FE model. The infinitely damped frequency from the 3D FE model $\omega_{3\mathrm{D}}$ is therefore be determined by solving (32).

The effect of the position feedback filter in (12) is based on the cut-off frequency $1/\tau$. In

Table 1: Balancing factors.

i	a	b	c	d
α_i/α_a	1.00	1.12	2.14	2.11

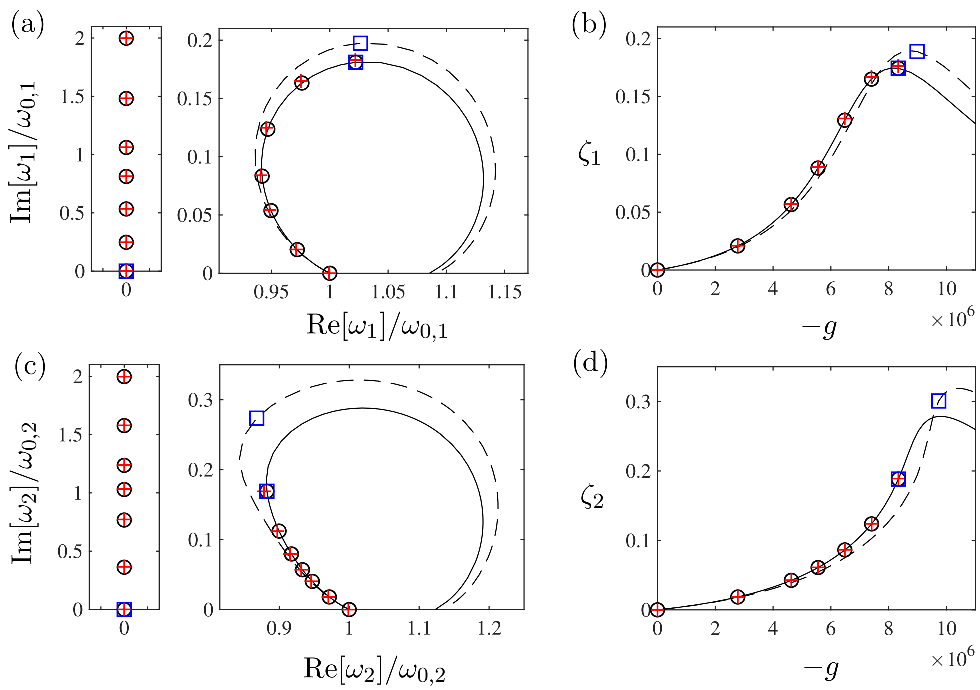

Figure 11: Frequency loci (a,c) and damping ratio (b,d) for the first mode (a,b) and second mode (c,d) of the beam model. Red markers represent the 3D FE model and the blue square indicate the gain limit. Dashed line represent $k \to \infty$.

order to damp mode j sufficiently the cut-off frequency is set to two times the corresponding undamped frequency,

$$1/\tau_j = 2\omega_{0,j} \tag{40}$$

The final step is to find the gain limit by (24), which ensures a bounded response. The results of the damping analysis for both models are seen in Fig. 11. The two lowest modes are damped independently and the corresponding frequency loci are seen in Fig. 11a,c for mode 1 and 2, respectively, while the corresponding damping ratios are plotted in Fig. 11b,d. The solid lines with circles (○ —) indicate the beam model, the red markers (+) depict the full 3D FE model solutions, the dashed line (– –) represents the beam model with $k \to \infty$ and thus no correction for the partial warping restrainment, while the blue square markers (□) represent the complex frequency at the gain limit g_{stab} in both models.

As the markers representing the beam model and 3D FE model practically coincide, very good agreement between the effective beam element model and the full 3D FE model is documented. The minor discrepancies are attributed to the non-ideal boundary conditions

Table 2: Results of analysis.

	Model	k	$(\omega_\infty - \omega_0)/\omega_0$	ζ_{stab}	$g^{\mathrm{beam}}_{\mathrm{stab}}/g^{\mathrm{3D}}_{\mathrm{stab}}$	$\left(\sum_i \alpha_i \psi_i\right)^2$
Mode 1	Beam	∞	0.092	0.189	4.57	–
		$1.15 \cdot 10^8$	0.086	0.174	4.24	4.28
	3D	–	0.086	0.176	–	–
Mode 2	Beam	∞	0.136	0.301	4.57	–
		$1.16 \cdot 10^8$	0.123	0.188	4.24	4.28
	3D	–	0.124	0.189	–	–

in the 3D FE model, which only with noticeable effort may resemble the ideal pinned boundary conditions used in the beam element model. Furthermore, the small difference in ω_0 is attributed to inherent cross-sectional distortion.

To the left in Fig. 11a,c the trace of the single pure imaginary eigenvalue is shown, for which instability is seen to occur for both models exactly when it reaches the origin. Thus, the beam model with fictitious stiffness k exactly identifies the stability limit of the collective PPF control applied for the eight actuators on the full 3D FE model.

In Table 2 the frequency increments $(\omega_\infty - \omega_0)/\omega_0$ and damping ratios at instability ζ_{stab} for the two modes are seen. The effect of taking the partial warping restrainment into account is seen to decrease the relative frequency increment and thereby the damping ratio. It is also seen that mode 2 has a larger frequency increment than mode 1, meaning that the torsional component is more pronounced, and is thus damped more than the first mode which is reflected by the damping ratios in the table. When $k \to \infty$ the damping ratio increases indicating an overestimation of damping in the beam model, when not including the fictitious stiffness k representing partial warping restrainment.

The second last column of Table 2 provides the ratio between the stability gains for the two structural models, which differ by a factor that is accurately captured by the conversion factor introduced in (36) and given in the last column of Table 2.

7.3. Free response to initial displacement

The time-response for the beam element model is determined by an initial displacement. The time response with an initial displacement corresponding to the first vibration mode,

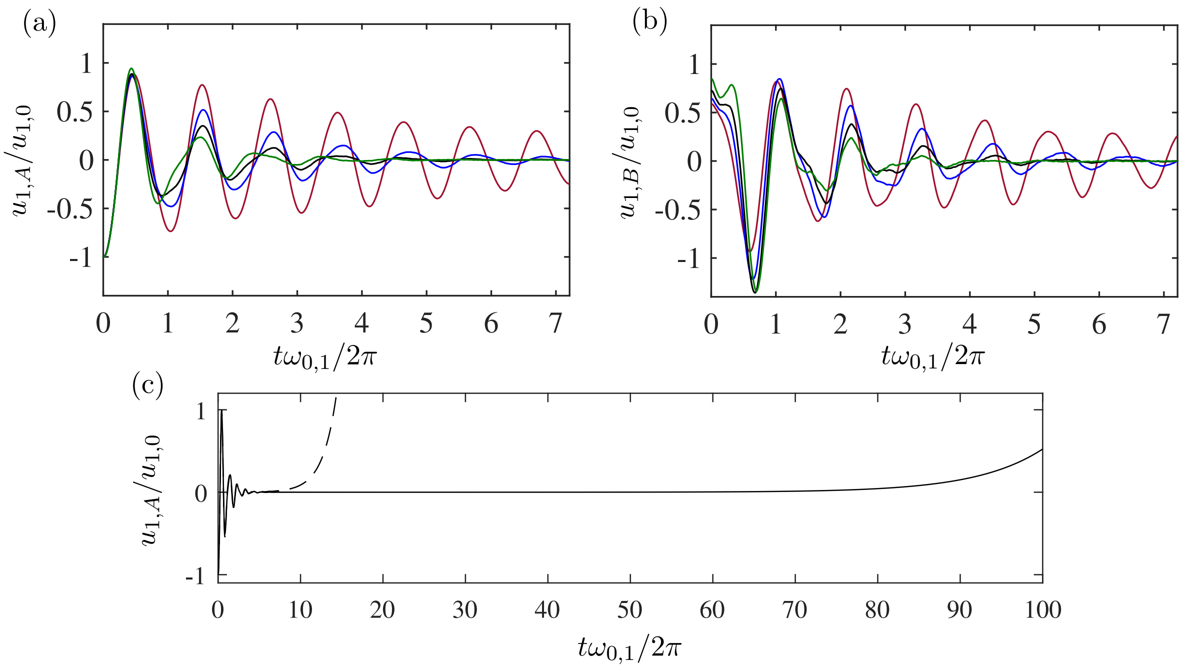

Figure 12: Free response from an initial displacement showing the horizontal displacement of (a) the shear centre and (b) point B for $0.40 \cdot g_{\rm stab}$ (red), $0.65 \cdot g_{\rm stab}$ (blue), $0.80 \cdot g_{\rm stab}$ (black) and $0.95 \cdot g_{\rm stab}$ (green). (c) shows the horizontal displacement of the shear centre for $1.01 \cdot g_{\rm stab}$ (solid) and $1.05 \cdot g_{\rm stab}$ (dashed).

using 10^3 time increments with a step size of $h = 5 \cdot 10^{-3}$ s, is obtained by the beam element model and is solved by the `ode45`-routine implemented in MATLAB. The initial displacement is based on the state vector from the eigenvalue problem in state-space with k as given for mode 1 in Table 2 and g given as a certain fraction of the gain limit. Due to the presence of the actuator, the complex state vector will contain a velocity part arising from the phase shift as well as an initial actuator force, implemented as initial displacement $\widetilde{\mathbf{q}}_0$, velocity $\dot{\widetilde{\mathbf{q}}}_0$ and actuator force $B_{d,0}$, respectively. The eigenvector is scaled such that the initial horizontal displacement of the shear centre A, as shown in Fig. 8, at the middle of the beam is $\ell/100$. Fig. 12a then shows the time history of the lateral displacement in the x_1-direction of the shear centre, while Fig. 12b shows the equivalent displacement at the joint between the lower flange and the web, denoted as point B in Fig. 8c. For point B the linearized horizontal component of the rotation of the cross-section relative to the shear centre is shown, as it describes the rotational (twist) component of the response. The response is plotted for $0.40 \cdot g_{\rm stab}$ (red), $0.65 \cdot g_{\rm stab}$ (blue), $0.80 \cdot g_{\rm stab}$ (black) and $0.95 \cdot g_{\rm stab}$

(green), approximately corresponding to the mode 1 damping ratios: $\zeta_1 = 2.9\,\%$, $8.3\,\%$, $13.8\,\%$ and $17.4\,\%$ according to Fig. 11b where the 17.4 % is recovered in Table 2.

As the response is initiated by the eigenvector, the contributions from other modes is minimized. The red curve in Fig. 12a for $g = 0.40 \cdot g_{\text{stab}}$ is rather close to an exponentially decaying cosine function. When applying very aggressive damping by $g = 0.95 \cdot g_{\text{stab}}$, the response is almost immediately cancelled. The response of point B on the lower flange is more irregular due to the presence of the torsional component. The first peak with a displacement greater than the initial displacement of point B at $t = 0$ is attributed to the apparent negative stiffness part of the filter in (12). However, the response is mitigated quite rapidly when applying aggressive damping close to the limit of stability.

In a design situation a gain close to the gain limit is not recommended, as instability should be avoided at all times with a certain margin. Various uncertainties associated with the geometry of the structure, actuator and sensor dynamics (which is not taken into account) may imply a reduced gain, slightly off the theoretical estimate. The horizontal response of the shear centre when applying a gain of $g = 1.01 \cdot g_{\text{stab}}$ and $g = 1.05 \cdot g_{\text{stab}}$ is shown in Fig. 12c, represented by the solid and dashed lines, respectively. When $g < g_{\text{stab}}$ the response becomes unbounded as observed in the figure, although for a gain only slightly above the gain limit, the increase in the response builds up more slowly over time.

8. Conclusions

Damping of coupled beam vibrations with discrete, active actuators restraining the axial warping displacements have been the objective of this paper. Emphasis has been on setting up a beam element formulation by which it is possible to perform detailed damping analyses, as verified by comparison with a large 3D FE model with isoparametric elements. On an actual structure the discrete, axial actuators only restrain warping locally, while the remaining part of the cross-section is still able to warp. This is associated with an additional flexibility, which lowers the frequency associated with infinite gain. This flexibility has been included in the beam model by a fictitious spring and it has furthermore been shown that it reduces the gain at which the combined system becomes unstable.

A numerical analysis of a beam with a single-symmetric cross-section has been used to demonstrate the accuracy of the 1D beam model and the efficiency of warping based PPF. The complex natural frequencies and corresponding damping ratios obtained by the beam model accurately reproduce the exact results from the full 3D FE model, when taking the excess flexibility from the fictitious spring into account. A key part of the analysis is the construction of the connectivity vector, which isolates the warping from torsion without affecting extension and bending. It has been demonstrated that a collective PPF control with spatial filtering imposed by the connectivity vector implies large attainable damping. The PPF control has been implemented as a simple linear filter which produces a control force that in terms of phase leads the local velocity component and therefore yields a great damping potential due to apparent negative stiffness. The combined structure and controller equation have been solved in state-space with respect to the damped frequencies and damping ratios. For the present example with an I-profile, substantial damping ratios are reached well below the system stability limit. The similarity between the two models is remarkable, suggesting that initial designs for beams with local control may successfully be carried out by a beam model with a supplemental spring that includes apparent controller flexibility. Though the gain in the two models is inherently different, it has in fact been possible to formulate a conversion factor between the two controller gains. This enables the design of the individual actuators by the beam model results when using e.g. piezoelectric, electric or hydraulic devices to realize the control effort in the actual structure.

9. Funding

This research did not receive any specific grant from funding agencies in the public, commercial, or not-for-profit sectors.

Appendix A. Implementation of beam elements

The differential equations governing fully coupled flexural and torsional vibrations of a beam can be derived as in [3, 4],

$$EI_{\alpha\beta}\xi_\beta'''' - \rho I_{\alpha\beta}\ddot{\xi}_\beta'' + \rho A\ddot{\xi}_\alpha - \rho A c_\beta \ddot{\theta} = 0 \quad , \quad \alpha, \beta = 1,2 \tag{A.1}$$

$$EI_\psi \theta'''' - GK\theta'' - \rho I_\psi \ddot{\theta}'' + \rho A c_1 \ddot{\xi}_2 - \rho A c_2 \ddot{\xi}_1 + \rho J \ddot{\theta} = 0 \tag{A.2}$$

The second term in (A.1) is the rotary inertia of the cross-section and the third term in (A.2) is the warping inertia related to the axial motion of the warping. Both of these terms are typically unimportant and therefore often discarded. However, in a finite element formulation with beam elements these effects are very easily implemented.

By discretization with the Hermitian shape functions,

$$\mathbf{N} = \left[2s^3 - 3s^2 + 1\ ,\ s(s-1)^2\ ,\ -2s^3 + 3s^2\ ,\ s^2(s-1) \right] \tag{A.3}$$

where $s = z/\ell$, the global stiffness and mass matrices may be written explicitly with appropriate sub-matrices from integration of the shape functions and their derivatives. This assumes a prismatic beam with identical cross-section. Integration of the shape functions yields the following sub-matrices,

$$\mathbf{E} = \int_0^1 \mathbf{N}^T \mathbf{N}\, ds \quad = \frac{1}{420} \begin{bmatrix} 156 & & & \\ 22 & 42 & & \\ 54 & 13 & 156 & \\ -13 & -3 & -22 & 4 \end{bmatrix} \tag{A.4}$$

$$\mathbf{F} = \int_0^1 \mathbf{N}'^T \mathbf{N}'\, ds \quad = \frac{1}{30} \begin{bmatrix} 36 & & & \\ 3 & 4 & & \\ -36 & -3 & 36 & \\ 3 & -1 & -3 & 4 \end{bmatrix} \tag{A.5}$$

$$\mathbf{G} = \int_0^1 \mathbf{N}''^T \mathbf{N}''\, ds = \begin{bmatrix} 12 & & & \\ 6 & 4 & & \\ -12 & -6 & 12 & \\ 6 & 2 & -6 & 4 \end{bmatrix} \tag{A.6}$$

The stiffness matrix does not contain coupling elements between bending and torsion, only coupling terms relating coupled bending in the case of an unsymmetric cross-section may occur. Thus a set of 4 × 4 matrices are defined as

$$\begin{aligned} \mathbf{K}_{\xi_1} &= EI_{11}\ell^{-3}\mathbf{G} \quad , \quad \mathbf{K}_{\xi_2} = EI_{22}\ell^{-3}\mathbf{G} \\ \mathbf{K}_{\xi_{12}} &= EI_{12}\ell^{-3}\mathbf{G} \quad , \quad \mathbf{K}_{\theta} = EI_{\psi}\ell^{-3}\mathbf{G} + GK\ell^{-1}\mathbf{F} \end{aligned} \tag{A.7}$$

Hereby the element stiffness matrix may be written as

$$\mathbf{K} = \begin{bmatrix} \mathbf{K}_{\xi_1} & \mathbf{K}_{\xi_{12}} & \mathbf{0} \\ \mathbf{K}_{\xi_{12}}^T & \mathbf{K}_{\xi_2} & \mathbf{0} \\ \mathbf{0} & \mathbf{0} & \mathbf{K}_{\theta} \end{bmatrix} \tag{A.8}$$

If the chosen coordinate system coincides with minimum one of the principal axes the coupling matrices vanish, $\mathbf{K}_{\xi_{12}} = \mathbf{0}$. If the elastic and shear centres do not coincide, terms in the mass matrix coupling bending and torsion arise. Thus, the diagonal terms of the mass matrix describing the inertia of bending and torsion are given as

$$
\begin{aligned}
\mathbf{M}_{\xi_1} &= \rho A \ell \mathbf{E} + \rho I_{11} \ell^{-1} \mathbf{F} \\
\mathbf{M}_{\xi_2} &= \rho A \ell \mathbf{E} + \rho I_{22} \ell^{-1} \mathbf{F} \\
\mathbf{M}_{\theta} &= \rho J \ell \mathbf{E} + \rho I_{\psi} \ell^{-1} \mathbf{F}
\end{aligned}
\tag{A.9}
$$

The last term in $\mathbf{M}_{\xi_\alpha}$ represents the rotary inertia of the cross-section and the last term in $\mathbf{M}_\theta$ represents the warping inertia. Even though these special inertia terms in most cases are vanishing it is with a minimum of effort taken into account in this way. The off-diagonal terms consist of the coupling rotary inertia and the coupling between bending and torsion, defining the matrices,

$$
\mathbf{M}_{\xi_{12}} = \rho I_{12} \ell^{-1} \mathbf{F} \quad , \quad \mathbf{M}_{\xi_1 \theta} = -\rho A c_2 \ell^{-1} \mathbf{E} \quad , \quad \mathbf{M}_{\xi_2 \theta} = \rho A c_1 \ell^{-1} \mathbf{E} \tag{A.10}
$$

The mass matrix may then be written as

$$
\mathbf{M} = \begin{bmatrix} \mathbf{M}_{\xi_1} & \mathbf{M}_{\xi_{12}} & \mathbf{M}_{\xi_1 \theta} \\ \mathbf{M}_{\xi_{12}}^T & \mathbf{M}_{\xi_2} & \mathbf{M}_{\xi_2 \theta} \\ \mathbf{M}_{\xi_1 \theta}^T & \mathbf{M}_{\xi_2 \theta}^T & \mathbf{M}_\theta \end{bmatrix} \tag{A.11}
$$

If the cross-section is double-symmetric the mass matrix contains only diagonal entries. The axial displacements are easily included in this format, yielding 14×14 stiffness- and mass matrices. For this particular structure of the governing matrices the nodal values are collected in the nodal vector $\mathbf{q}$

$$
\mathbf{q} = \left[\, \boldsymbol{\xi}_1^T \quad \boldsymbol{\xi}_2^T \quad \boldsymbol{\theta}^T \, \right]^T \tag{A.12}
$$

with the following nodal arrays,

$$
\begin{aligned}
\boldsymbol{\xi}_1 &= [\xi_{1A} \, , \, \ell \xi'_{2A} \, , \, \xi_{1B} \, , \, \ell \xi'_{2B}]^T \\
\boldsymbol{\xi}_2 &= [\xi_{2A} \, , \, -\ell \xi'_{1A} \, , \, \xi_{2B} \, , \, -\ell \xi'_{1B}]^T \\
\boldsymbol{\theta} &= [\theta_A \, , \, \ell \theta'_A \, , \, \theta_B \, , \, \ell \theta'_B]^T
\end{aligned}
\tag{A.13}
$$

where the length ℓ ensures dimensionless sub-matrices.

References

[1] Spencer, B. F. & Nagarajaiah, S. (2003). "State of the art of structural control", *Journal of Structural Engineering*, vol. 129, no. 7, 845-856.

[2] Gere, J. M. & Lin, Y. K. (1958). "Coupled vibrations of thin-walled beams of open cross-section", *Journal of Applied Mechanics*, vol. 25, 373-378.

[3] Vlasov, V. Z. (1961). "Thin-walled elastic beams", Israel Program for Scientific Translation, Jerusalem.

[4] Friberg, P. O. (1985). "Beam element matrices derived from Vlasov's theory of open thin-walled elastic beams", *International Journal for Numerical Methods in Engineering*, vol. 21, 1205-1228, DOI: 10.1002/nme.1620210704.

[5] Banerjee, J. R., Guo, S. & Howson, W. P. (1996). "Exact dynamic stiffness matrix of a bending-torsion coupled beam including warping", *Computers and Structures*, vol. 59, no. 4, 613-621, DOI: 10.1016/0045-7949(95)00307-X.

[6] Tanaka, M. & Bercin, A. N. (1997). "Finite element modelling of the coupled bending and torsional free vibration of uniform beams with an arbitrary cross-section", *Applied Mathematical Modelling*, vol. 21, no. 6, 339-344, DOI: 10.1016/S0307-904X(97)00030-9.

[7] Mei, C. (1970). "Coupled vibrations of thin-walled beams of open section using the finite element method", *International Journal of Mechanical Sciences*, vol. 12, no. 10, 883-891, DOI: 10.1016/0020-7403(70)90025-1.

[8] Hansen, M. H. (2007). "Aeroelastic instability problems for wind turbines", *Wind Energy*, vol. 10, 551-577, DOI: 10.1002/we.242.

[9] Arrigan, J., Pakrashi, V., Basu, B. & Nagarajaiah, S. (2011). "Control of flapwise vibrations in wind turbine blades using semi-active tuned mass dampers", *Structural Control and Health Monitoring*, vol. 18, no. 8, 840-851, DOI: 10.1002/stc.404.

[10] Zuo, H., Bi, K. & Hao, H. (2019). "Mitigation of tower and out-of-plane blade vibrations of offshore monopile wind turbines by using multiple tuned mass dampers", *Structure and Infrastructure Engineering*, vol. 15, no. 2, 269-284, DOI: 10.1080/15732479.2018.1550096.

[11] Ge, Y. J. & Tanaka, H. (2000). "Aerodynamic flutter analysis of cable-supported bridges by multi-mode and full-mode approaches", *Journal of Wind Engineering and Industrial Aerodynamics*, vol. 8, no. 2-3, 123-153, DOI: 10.1016/S0167-6105(00)00007-6.

[12] Zhang, X., Xiang, H. & Sun, B. (2002). "Nonlinear aerostatic and aerodynamic analysis of long-span suspension bridges considering wind-structure interaction", *Journal of Wind Engineering and Industrial Aerodynamics*, vol. 90, no. 9, 1065-1080, DOI: 10.1016/S0167-6105(02)00251-9.

[13] Øiseth, O. & Sigbjörnsson, R. (2011). "An alternative analytical approach to prediction of flutter stability limits of cable supported bridges", *Journal of Sound and Vibration*, vol. 330, no. 12, 2784-2800, DOI: 10.1016/j.jsv.2010.12.026.

[14] Casalotti, A., Arena, A. & Lacarbonara, W. (2014). "Mitigation of post-flutter oscillations in suspension bridges by hysteretic tuned mass dampers", *Engineering Structures*, vol. 69, 62-71, DOI: 10.1016/j.engstruct.2014.03.001.

[15] Mokrani, B., Tian, Z., Alaluf, D., Meng, F. & Preumont, A. (2017). "Passive damping of suspension bridges using multi-degree of freedom tuned mass dampers", *Engineering Structures*, vol. 153, 749-756, DOI: 10.1016/j.engstruct.2017.10.028.

[16] Vo, T. P. & Lee, J. (2009). "Flexural-torsional coupled vibration and buckling of thin-walled open section composite beams using shear-deformable beam theory", *International Journal of Mechanical Sciences*, vol. 51, no. 9-10, 631-641, DOI: 10.1016/j.ijmecsci.2009.05.001.

[17] Hajianmaleki, M. & Qatu, M. S. (2013). "Vibrations of straight and curved composite beams: A review", *Composite Structures*, vol. 100, 218-232, DOI: 10.1016/j.compstruct.2013.01.001.

[18] Kim, N. I. & Lee, J. (2017). "Coupled vibration characteristics of shear flexible thin-walled functionally graded sandwich I-beams", *Composites Part B: Engineering*, vol. 110, 229-247, DOI: 10.1016/j.compositesb.2016.11.025.

[19] Høgsberg, J., Hoffmeyer, D. & Ejlersen, C. (2016). "Damping of torsional beam vibrations by control of warping displacement", *Journal of Vibration and Acoustics*, vol. 138, no. 1, 229-247, DOI: 10.1115/1.4031616.

[20] Hoffmeyer, D. & Høgsberg, J. (2019). "Damping of torsional vibrations in thin-walled beams by viscous bimoments", *Mechanics of Advanced Materials and Structures*, DOI: 10.1080/15376494.2019.1567885.

[21] Christiano, P. & Salmela, L. (1971). "Frequencies of beams with elastic warping restraints", *Journal of the Structural Division*, vol. 97, no. 6, 1835-1840.

[22] Al-Jumaily, A. M. & Faulkner, L. L. (1977). "Vibration of continuous systems with compliant boundaries", *Journal of Sound and Vibration*, vol. 54, no. 2, 203-213.

[23] Kang, K. H. & Kim, K. J. (1996). "Modal properties of beams and plates on resilient supports with rotational and translational complex stiffness", *Journal of Sound and Vibration*, vol. 190, no. 2, 207-220, DOI: 10.1006/jsvi.1996.0057.

[24] Svedholm, C., Zangeneh, A., Pacoste, C., Francois, S. & Karoumi, R. (2016). "Vibration of damped uniform beams with general end conditions under moving loads", *Engineering Structures*, vol. 126, 40-52, DOI: 10.1016/j.engstruct.2016.07.037.

[25] Goh, C. J. & Caughey, T. K. (1985). "On the stability problem caused by finite actuator dynamics in the collocated control of large space structures", *International Journal of Control*, vol. 41, no. 3, 787-802, DOI: 10.1080/0020718508961163.

[26] Mahmoodi, N. & Mehdi, A. (2009). "Active vibration control with modified positive position feedback", *Journal of Dynamic Systems, Measurement and Control*, vol. 131, no. 4, 1-8, DOI: 10.1115/1.3089565.

[27] Ferrari, G. & Marco, A. (2015). "Active vibration control of a sandwich plate by non-collocated positive position feedback", *Journal of Sound and Vibration*, vol. 342, 44-56, DOI: 10.1016/j.jsv.2014.12.019.

[28] Marinangeli, L., Alijani, F. & HosseinNia, S. H. (2018). "Fractional order positive position feedback compensator for active vibration control of a smart composite plate", *Journal of Sound and Vibration*, vol. 412, 1-16, DOI: 10.1016/j.jsv.2017.09.009.

[29] Wu, Y., Zhang, W., Meng, X. & Su, Y. (2018). "Compensated positive position feedback for active control of piezoelectric structures", *Journal of Intelligent Material Systems and Structures*, vol. 29, no. 3, 397-410, DOI: 10.1177/1045389X17708045.

[30] Preumont, A. (2011). "Vibration control of active structures", *Springer*, 3rd ed., DOI: 10.1007/978-94-007-2033-6.

[31] Baz, A. & Poh, S. (1996). "Optimal vibration control with modal positive position feedback", *Optimal Control Applications and Methods*, vol. 17, no. 2, 141-149, DOI: 10.1002/(SICI)1099-1514(199604/06)17:2¡141::AID-OCA566¿3.0.CO;2-D.

[32] Høgsberg, J. & Krenk, S. (2006). "Linear control strategies for damping of flexible structures", *Journal of Sound and Vibration*, vol. 293, 59-77, DOI: 10.1016/j.jsv.2005.09.014.

[33] Hoffmeyer, D. & Høgsberg, J. (2019). "Active warping control for damping of torsional beam vibrations", *Proceedings of the 9th ECCOMAS Thematic Conference on Smart Structures and Materials*, to be published.

[34] Fanson, J. L. & Caughey, T. K. (1990). "Positive position feedback control for large space structures", *AIAA Journal*, vol. 28, no. 4, 717-724, DOI: 10.2514/3.10451.

[35] Krenk, S. & Høgsberg, J. (2013). "Equal modal damping design for a family of resonant vibration control formats", *Journal of Vibration and Control*, vol. 19, no. 9, 1294-1315, DOI: 10.1177/1077546312446796.

[36] Balas, M. J. (1978). "Active control of flexible systems", *Journal of Optimization Theory and Applications*, vol. 125, no. 3, 415-436, DOI: 10.1007/BF00932903.

[37] Cha, P. D. & Yoder, N. C. (2007). "Applying Sherman-Morrison-Woodbury formulas to analyze the free and forced responses of a linear structure carrying lumped elements", *Journal of Vibration and Acoustics*, vol. 129, no. 3, 307-316, DOI: 10.1115/1.2730537.

[38] Høgsberg, J. & Krenk, S. (2014). "Analysis of moderately thin-walled beam cross-sections by cubic isoparametric elements", *Computers and Structures*, vol. 134, pp. 88-101, DOI: 10.1016/j.compstruc.2014.01.002.

[39] Géradin, M. & Cardona, A. (2001). "Flexible Multibody Dynamics, A Finite Element Approach", Wiley.

P3

Calibration and Balancing of Multiple Tuned Mass Absorbers for Damping of Coupled Bending-Torsion Beam Vibrations

David Hoffmeyer and Jan Høgsberg

(Submitted)

Calibration and Balancing of Multiple Tuned Mass Absorbers for Damping of Coupled Bending-Torsion Beam Vibrations

David Hoffmeyer
PhD Student
Department of Mechanical Engineering
Technical University of Denmark
DK-2800, Kongens Lyngby, Denmark
Email: davhoff@mek.dtu.dk

Jan Høgsberg
Associate Professor
Technical University of Denmark
DK-2800, Kongens Lyngby, Denmark
Email: jhg@mek.dtu.dk

For damping of fully coupled beam vibrations a three-component tuned mass absorber is proposed, consisting of two translational and a single rotational absorber, which together target a specific vibration mode. The representation of the interaction with residual non-resonant vibration modes is consistently included by two supplemental terms in the absorber equation, calibrated by frequency matching with the full structural model for vanishing absorber damping. The absorber tuning directly includes these residual terms without approximation when the underlying modal representation is based on the vibration form with absorber masses rigidly attached to the structure. It is demonstrated that the desired damping behaviour require non-homogeneous absorber balancing, obtained by an approximate method for the relative sizing of each absorber mass.

1 Introduction

Supplemental damping of flexible beam structures is conveniently introduced by tuned mass absorbers [1] working as suspended masses connected to the structure by springs and viscous dashpots. Such device configurations have been used for vibration mitigation of e.g. wind turbine blades [2], suspension bridges [3] and tall buildings [4].

Tuning of the mass absorber relies on accurate frequency matching with a selected vibration mode of the flexible host structure. The classic tuning procedure of Den Hartog [5] is based on attaining equal dynamic amplification at two neutral frequencies at which the amplitude is independent of the device damping. Specifically for tuned mass absorbers this principle also implies equal damping of the two modes associated with the selected vibration form of the structure [6]. Most tuning procedures assume that the response of the structure can be represented solely by the targeted vibration mode, although the absorber will inherently experience supplemental support motion from the other non-resonant modes. This interaction with residual vibration modes deteriorates the calibration, unless corrected by e.g. the addition of a flexibility and an inertia term in the absorber equation, as proposed in [7]. The present paper adopts a slightly alternative correction approach, in which the additional parameters are calibrated based on matching of the two frequencies associated with the resonant structural modes at vanishing absorber damping, as proposed for inerter-based absorbers in [8].

Multiple absorbers may be applied to damp coupled torsion-bending vibrations in slender beam-like structures [9, 10]. As many tall buildings have an irregular shape, multiple absorbers are furthermore used to mitigate response from seismic loading [11]. However, explicit procedures for the sizing and thereby relative balancing of the individual absorbers often rely on a numerical optimization procedure [12–14], which may be inconvenient with non-parametric solutions.

The present note proposes a three-component mass absorber for damping of fully coupled beam vibrations, consisting of a single rotational and two translational absorbers. These three absorbers may be placed at the same location on the beam, as they are associated with different structural degrees-of-freedom. The configuration of the combined translational-rotational absorbers for coupled-mode vibration damping may be realized by a crucifix-type absorber [15] or a similar coupled beam-type absorber [16], both originally proposed for damping of pure bending and/or torsion modes with well-separated frequencies. For the present problem, in which the multiple absorber configuration targets a single coupled mode, the balancing between the individual absorber components becomes important. Although the method proposed in [17] has been derived for relative sizing of viscous dampers, it is directly translated to the present mass absorber problem, for which it appears to give a proper balancing of the three individual absorber components when targeting a mode with inherent bend-twist coupling.

2 Governing equations

2.1 Structure and absorber

For a general flexible structure with n degrees-of-freedom collected in the displacement vector $\mathbf{q}$, the dynamic behaviour is governed by the mass matrix $\mathbf{M}$ and the stiffness matrix $\mathbf{K}$. The general response of the structure in the frequency domain is governed by the equation of motion

$$\left(\mathbf{K} - \omega^2 \mathbf{M}\right)\mathbf{q} + \mathbf{W}\mathbf{f}_a = \mathbf{f}_e \tag{1}$$

with ω being the angular natural frequency and the external load represented by $\mathbf{f}_e$. The forces from n_a multiple tuned mass absorbers are collected in the vector $\mathbf{f}_a$ with the connectivity array

$$\mathbf{W} = [\mathbf{w}_1 \,, \mathbf{w}_2 \,, \ldots, \mathbf{w}_{n_a}] \tag{2}$$

specifying the attachment of each absorber on the structure and thus defining

$$\mathbf{u}_s = \mathbf{W}^T \mathbf{q} \tag{3}$$

as a vector containing the structural base motion experienced by each absorber. Figure 1a shows a single absorber comprising a mass m_a connected to the structure by a spring with stiffness k_a in parallel with a viscous dashpot with coefficient c_a. The absorber forces $\mathbf{f}_a$ can thus be determined as

$$\mathbf{f}_a = -\left(k_a + i\omega c_a\right)\boldsymbol{\alpha}\mathbf{u}_a = -\omega^2 m_a \boldsymbol{\alpha}\left(\mathbf{u}_a + \mathbf{u}_s\right) \tag{4}$$

where the vector $\mathbf{u}_a$ contains the relative displacements of the absorber masses, while the relative sizing of the absorbers in Fig. 1b is given by the balancing matrix

$$\boldsymbol{\alpha} = \begin{bmatrix} \alpha_1 & & & \\ & \alpha_2 & & \\ & & \ddots & \\ & & & \alpha_{n_a} \end{bmatrix} \tag{5}$$

treated in further detail in Section 6.
When introducing $\mathbf{u}_s = \mathbf{W}^T\mathbf{q}$, the latter equality in (4) gives

$$\left(k_a + i\omega c_a - \omega^2 m_a\right)\boldsymbol{\alpha}\mathbf{u}_a - \omega^2 m_a \boldsymbol{\alpha}\mathbf{W}^T\mathbf{q} = \mathbf{0} \tag{6}$$

with common absorber parameters m_a, c_a and k_a for a given balancing matrix $\boldsymbol{\alpha}$.
The corresponding structural equation (1) is obtained by elimination of the absorber force $\mathbf{f}_a$ given by the latter expression in (4). Hereby the structural equation of motion can be written as

$$\left(\mathbf{K} - \omega^2 \mathbf{M}_\infty\right)\mathbf{q} - \omega^2 m_a \mathbf{W}\boldsymbol{\alpha}\mathbf{u}_a = \mathbf{f}_e \tag{7}$$

with the augmented mass matrix

$$\mathbf{M}_\infty = \mathbf{M} + m_a \mathbf{W}\boldsymbol{\alpha}\mathbf{W}^T \tag{8}$$

containing contributions from the absorber mass, as illustrated in Fig. 1c.

2.2 Modal properties

Without absorbers and external load the original structural equation (1) defines the undamped eigenvalue problem

$$\left(\mathbf{K} - \omega_{0,j}^2 \mathbf{M}\right)\mathbf{q}_{0,j} = \mathbf{0} \tag{9}$$

in which the eigenvalue $\omega_{0,j}$ is the undamped natural frequency of mode j and $\mathbf{q}_{0,j}$ is corresponding mode shape vector. Although commonly used for a modal representation of the structure to be damped, it may appear inconsistent, as (9) is not recovered in either of the limits $c_a \to 0$ or ∞ for the absorber damping coefficient.

The alternative equation of motion (7) recovers the undamped structure in Fig. 1c for $c_a \to \infty$, with all absorber masses included in the mass matrix (8). Therefore, the corresponding eigenvalue problem

$$\left(\mathbf{K} - \omega_{\infty,j}^2 \mathbf{M}_\infty\right)\mathbf{q}_{\infty,j} = \mathbf{0} \tag{10}$$

serves as a consistent basis for a modal truncation of the flexible structure. The eigenvalue of (10) determines $\omega_{\infty,j} < \omega_{0,j}$ as the infinitely damped natural frequency, while $\mathbf{q}_{\infty,j}$ is the corresponding mode shape vector.
All absorbers are calibrated towards a single resonant vibration mode $j = r$. With the alternative problem (10) as basis, the modal expansions can be expressed as

$$\mathbf{q} = \sum_{j=1}^{n} \mathbf{q}_{\infty,j} \frac{x_j}{\nu_{\infty,j}} \quad , \quad \mathbf{u}_a = \mathbf{W}^T \mathbf{q}_{\infty,r} \frac{y_r}{\nu_{\infty,r}} \tag{11}$$

with x_j and y_r being the modal coordinates for the structure and absorber displacements, respectively. The collective absorber coordinate y_r for the target mode $j = r$ may without loss of generality be expressed directly in terms of $\mathbf{q}_{\infty,r}$, providing an identical coupling coefficient in the subsequent modal equations. A combined modal amplitude $\nu_{\infty,j}$ at the

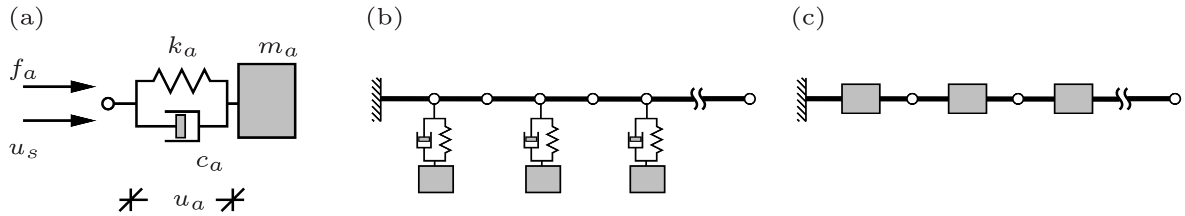

Fig. 1. (a) Tuned mass absorber, (b) structure with multiple absorbers and (c) locking of the absorber mass to the structure at $c_a \to \infty$.

absorber locations for a specific mode j is in (11) introduced by the quadratic relation

$$\nu_{\infty,j}^2 = \mathbf{q}_{\infty,j}^T \mathbf{W} \boldsymbol{\alpha} \mathbf{W}^T \mathbf{q}_{\infty,j} \tag{12}$$

comprising the location of the absorbers via $\mathbf{W}$ and the relative sizing through the balancing matrix $\boldsymbol{\alpha}$.
When introducing the expansions in (11) into the structural equation in (7) and then pre-multiplying with $\mathbf{q}_{\infty,j}^T/\nu_{\infty,j}$, the corresponding modal equation for a mode j appears in uncoupled form as

$$\big(k_j - \omega^2 m_j\big)x_j - \omega^2 m_a \eta_{jr} y_r = f_j \tag{13}$$

defining the structural modal mass, modal stiffness and external modal load as

$$m_j = \frac{\mathbf{q}_{\infty,j}^T \mathbf{M}_\infty \mathbf{q}_{\infty,j}}{\nu_{\infty,j}^2} \quad , \quad k_j = \frac{\mathbf{q}_{\infty,j}^T \mathbf{K} \mathbf{q}_{\infty,j}}{\nu_{\infty,j}^2} \quad , \quad f_j = \frac{\mathbf{q}_{\infty,j}^T \mathbf{f}_e}{\nu_{\infty,j}} \tag{14}$$

whereby the infinitely damped natural frequency $\omega_{\infty,j}$ is defined by the modal stiffness to mass ratio $\omega_{\infty,j}^2 = k_j/m_j$. In (13) the modal coupling coefficient

$$\eta_{jr} = \frac{\mathbf{q}_{\infty,j}^T \mathbf{W} \boldsymbol{\alpha} \mathbf{W}^T \mathbf{q}_{\infty,r}}{\nu_{\infty,j}\nu_{\infty,r}} \tag{15}$$

is introduced so that $\eta_{rr} = 1$. By pre-multiplication of (6) with $\mathbf{q}_{\infty,r}^T \mathbf{W}/\nu_{\infty,r}$, the associated modal absorber equation is given as

$$\big(k_a + i\omega c_a - \omega^2 m_a\big) y_r - \omega^2 m_a \sum_{j=1}^{n} \eta_{rj} x_j = 0 \tag{16}$$

with the sum containing contributions from all vibration modes through the coupling coefficient η_{rj} in (15). In the coupled modal equations (13) and (16) the n_a tuned mass absorbers act as a single unit with their individual balancing defined by the matrix $\boldsymbol{\alpha}$, while the sum with η_{rj} contains the background contributions from residual vibration modes $j \neq r$.

2.3 Modal representation with residual mode correction

Instead of truncating the sum in (16) to a single term $j = r$, the residual terms $j \neq r$ may be included by correction terms, as suggested in [7]. It follows from the modal structural equation (13) that x_j is proportional to y_r for free vibrations. Thus, the residual components of the sum in (16) may be represented consistently by a flexibility and an inertia correction term that must be proportional to y_r,

$$\sum_{j=1}^{n} \eta_{rj} x_j = x_r + \sum_{j \neq r}^{n} \eta_{rj} x_j = x_r + k_a \left(\frac{1}{k_r'} - \frac{1}{m_r' \omega^2} \right) y_r \tag{17}$$

The correction terms are directly introduced by a supplemental modal stiffness k_r' and modal mass m_r', representing base motion flexibility parameters via the sum of their reciprocal values. This modal truncation with residual mode correction eliminates the sum in the absorber equation (16), whereafter the two terms with k_r' and m_r' are fully absorbed by the corresponding physical terms proportional to y_r.
For the structural modal equation (13) the specific equation for the targeted vibration mode $j = r$ can now be normalized by the modal stiffness k_r as

$$\big(1 - \xi^2\big)x_r - \mu_r \xi^2 y_r = 0 \tag{18}$$

introducing the non-dimensional frequency

$$\xi = \frac{\omega}{\omega_{\infty,r}} = \omega \sqrt{\frac{m_r}{k_r}} \tag{19}$$

Similarly the absorber equation (16), with the sum eliminated by (17), is normalized by division with k_r. Hereby, it can be written in compact form as

$$\big(\kappa_* + i\xi\beta_* - \xi^2 \mu_*\big) y_r - \xi^2 \mu_* \kappa_* \frac{1}{\kappa_r} x_r = 0 \tag{20}$$

where the corrected mass, stiffness and damper ratios with asterisks

$$\frac{1}{\mu_*} = \frac{1}{\mu_r} + \frac{1}{\mu_r'} \quad , \quad \frac{1}{\kappa_*} = \frac{1}{\kappa_r} + \frac{1}{\kappa_r'} \quad , \quad \beta_* = \beta_r \frac{\kappa_*}{\kappa_r} \frac{\mu_*}{\mu_r} \tag{21}$$

are expressed by the physical absorber mass, stiffness and damper ratios

$$\mu_r = \frac{m_a}{m_r} \quad , \quad \kappa_r = \frac{k_a}{k_r} \quad , \quad \beta_r = \frac{c_a}{\sqrt{k_r m_r}} \tag{22}$$

and the corrected mass and stiffness ratios with primes

$$\mu_r' = \frac{m_r'}{m_r} \quad , \quad \kappa_r' = \frac{k_r'}{k_r} \tag{23}$$

representing the residual mode contributions introduced in (17). Because of the modal expansion with the infinitely damped mode shapes $\mathbf{q}_{\infty,j}$, the residual correction terms are fully included in the comprised ratios μ_* and κ_* without any approximations, as otherwise needed for tuned vibration absorbers when the undamped mode shapes $\mathbf{q}_{0,j}$ are used in the modal decomposition [7, 19].

3 Absorber tuning

The tuning of the absorbers is based on the properties of the complex poles, governed by the characteristic equation obtained by eliminating the modal coordinates between the two equations (20) and (18). By re-arranging terms the characteristic equation can be written as

$$\mu_*\left(1-\kappa_*\frac{\mu_r}{\kappa_r}\right)\xi^4 - (\mu_*+\kappa_*)\xi^2 + \kappa_* + i\xi\beta_*(1-\xi^2) = 0 \tag{24}$$

which remains within a fourth-order polynomial format because of the structural equation (7) with the augmented mass matrix $\mathbf{M}_\infty$ defined in (8).

The system parameters in (24) are determined based on a specific tuning criterium, which in the present case is the equal modal concept described in [6, 18]. For tuned mass absorbers it secures a good compromise between large attainable damping and effective response amplitude reduction. The procedure relies on the exact matching of the characteristic equation (24) with the generic polynomial

$$\xi^4 - \left(2+4\chi^2\right)\xi_0^2\xi^2 + \xi_0^4 + 4i\lambda\chi\xi_0\xi\left(\xi_0^2-\xi^2\right) = 0 \tag{25}$$

which by construction secures equal damping and obtains maximum damping ratio at a bifurcation point for $\lambda = 1$. It follows immediately by the ratio between the first and third order terms inside the last parenthesis of (24) and (25) that the reference frequency ratio

$$\xi_0 = 1 \tag{26}$$

which is a direct consequence of using the locked mode shapes $\mathbf{q}_{\infty,j}$ as the basis of the modal representation. Next the characteristic equation (24) is normalized to a unit coefficient to the leading quartic term. Then comparison of the constant terms in (24) and (25) gives

$$\frac{\kappa_*}{\mu_*} = \frac{1}{1+\mu_*\dfrac{\mu_r}{\kappa_r}} \tag{27}$$

identifying $\mu_*\mu_r/\kappa_r$ as a representative absorber parameter. Comparison of the quadratic terms gives the model parameter

$$\chi = \sqrt{\tfrac{1}{4}\mu_*\frac{\mu_r}{\kappa_r}} \tag{28}$$

while the corrected damper ratio β_* is then determined from the common factors to the odd-power terms,

$$\frac{\beta_*}{\kappa_*} = \sqrt{2\mu_*\frac{\mu_r}{\kappa_r}} \tag{29}$$

In this expression for β_* a complex pole location slightly below the bifurcation point is achieved by $\lambda = \frac{1}{2}\sqrt{2}$, which avoids structural interference of the two identical modes at $\lambda = 1$ and provides the desired flat plateau in the frequency response amplitudes [6].

Finally, the attainable modal damping ratio in the two structural modes may be estimated from (28) as

$$\zeta_r^{\text{est}} \simeq \lambda\chi = \sqrt{\tfrac{1}{8}\mu_*\frac{\mu_r}{\kappa_r}} \tag{30}$$

The above expressions ensure equal modal damping of the two structural modes based on a specified mass ratio μ_r. Furthermore, when the corrections for residual modes are not included, the expressions (27)-(30) simplify as $\mu_* = \mu_r$ and $\kappa_* = \kappa_r$.

4 Calibration of residual mode parameters

In (17) the correction modal stiffness k_r' and mass m_r' represent the influence by all other vibration modes and thus explicitly adjust the actual system parameters μ_r and κ_r in (21) by their corresponding ratios κ_r' and μ_r' defined in (23). The influence of other modes on the targeted vibration mode may be assessed in the limit $c_a = 0$, at which the homogeneous form of the governing equations (7) and (6) determine $n_a + 1$ natural frequencies for the vibration mode $j = r$ when the absorber parameters m_a and k_a are calibrated according to the tuning principle of Section 3.

Assume that the absorber mass and stiffness can be estimated as $m_a = \widetilde{m}_a$ and $k_a = \widetilde{k}_a$. For $c_a = 0$ the homogeneous form of (7) and (6) constitute the eigenvalue problem

$$\left(-\omega^2\begin{bmatrix}\mathbf{M}+\widetilde{m}_a\mathbf{W}\boldsymbol{\alpha}\mathbf{W}^T & \widetilde{m}_a\mathbf{W}\boldsymbol{\alpha}\\ \widetilde{m}_a\boldsymbol{\alpha}\mathbf{W}^T & \widetilde{m}_a\boldsymbol{\alpha}\end{bmatrix} + \begin{bmatrix}\mathbf{K} & \mathbf{0}\\ \mathbf{0}^T & \widetilde{k}_a\boldsymbol{\alpha}\end{bmatrix}\right)\begin{bmatrix}\mathbf{q}\\ \mathbf{u}_a\end{bmatrix} = \begin{bmatrix}\mathbf{0}\\ \mathbf{0}\end{bmatrix} \tag{31}$$

When $\widetilde{m}_a$ and $\widetilde{k}_a$ are chosen sufficiently accurate, this eigenvalue problem (31) identifies n_a+1 natural frequencies around $\omega_{\infty,r}$ for the targeted vibration mode r. Two of these frequencies ω_A and ω_B represent dynamic absorber-structure interaction of the actual flexible structure, while the remaining n_a-1 frequencies describe redundant absorber modes with high damping. Figure 3 shows trajectories with respect to c_a of the $n_a+1=4$ natural frequencies in the complex plane for the numerical example considered in Section 7. For $c_a=0$ the associated four real-valued frequencies are then identified in Fig. 3c, with the two outer frequencies identified or assumed as ω_A ($\circ$) and ω_B ($\square$), while the two intermediate frequencies ($\times$) then denote the redundant trajectories that approach the imaginary axis for increasing c_a.
The background correction ratios κ_r' and μ_r' are now determined such that the characteristic equation (24) exactly recovers the determined frequency ratios

$$\xi_{A,B}=\frac{\omega_{A,B}}{\omega_{\infty,r}} \tag{32}$$

in the limit $\beta_*=0$, where (24) reduces to the quadratic equation

$$\widetilde{\mu}_*\left(1-\widetilde{\kappa}_*\frac{\widetilde{\mu}_r}{\widetilde{\kappa}_r}\right)\xi^4-(\widetilde{\mu}_*+\widetilde{\kappa}_*)\xi^2+\widetilde{\kappa}_*=0 \tag{33}$$

with assumed mass and stiffness ratios $\widetilde{\mu}_r=\widetilde{m}_a/m_r$ and $\widetilde{\kappa}_r=\widetilde{k}_a/k_r$, respectively. The sum and product of the two roots ξ_A^2 and ξ_B^2 to (33) then fulfill the relations

$$\xi_A^2+\xi_B^2=\frac{\widetilde{\mu}_*+\widetilde{\kappa}_*}{\widetilde{\mu}_*\left(1-\widetilde{\kappa}_*\dfrac{\widetilde{\mu}_r}{\widetilde{\kappa}_r}\right)}\quad,\quad \xi_A^2\xi_B^2=\frac{\widetilde{\kappa}_*}{\widetilde{\mu}_*\left(1-\widetilde{\kappa}_*\dfrac{\widetilde{\mu}_r}{\widetilde{\kappa}_r}\right)} \tag{34}$$

from which the combined stiffness and mass ratios are readily obtained as

$$\begin{aligned}\widetilde{\mu}_*&=\frac{\widetilde{\kappa}_r}{\widetilde{\mu}_r}\frac{\xi_A^2\xi_B^2-\xi_A^2-\xi_B^2+1}{\xi_A^2\xi_B^2-\xi_A^2-\xi_B^2}\\ \widetilde{\kappa}_*&=-\frac{\widetilde{\kappa}_r}{\widetilde{\mu}_r}\frac{\xi_A^2\xi_B^2-\xi_A^2-\xi_B^2+1}{\xi_A^2\xi_B^2}\end{aligned} \tag{35}$$

Finally, the correction ratios μ_r' and κ_r' are then determined from (21) as

$$\frac{1}{\mu_r'}=\frac{1}{\widetilde{\mu}_*}-\frac{1}{\widetilde{\mu}_r}\quad,\quad\frac{1}{\kappa_r'}=\frac{1}{\widetilde{\kappa}_*}-\frac{1}{\widetilde{\kappa}_r} \tag{36}$$

As shown in the numerical example of Section 7 this procedure provides an accurate estimation of the residual mode correction ratios κ_r' and μ_r', provided that the initial estimates $\widetilde{m}_a$ and $\widetilde{k}_a$ are sufficiently accurate and that ω_A and ω_B can be clearly identified from the n_a+1 natural frequencies obtained for $c_a=0$.

5 Design procedure

A design procedure is now proposed and stepwise summarized in Table 1. The attainable damping ratio for mode r can be estimated by (30). Without residual mode correction $\mu_*=\mu_r$ and $\kappa_*=\kappa_r$, whereby (27) determines $\kappa_r=\mu_r(1-\mu_r)$ and (30) then gives a desired modal mass ratio

$$\mu_{\text{des}}=\frac{8\zeta_{\text{des}}^2}{1-8\zeta_{\text{des}}^2} \tag{37}$$

when $\zeta_r^{\text{est}}=\zeta_{\text{des}}$ has been introduced. This mass ratio μ_{des} can be used to determine a desired absorber mass m_a. However, the absorber ratios are defined in (22) based on the modal parameters with respect to the infinitely damped mode shape $\mathbf{q}_{\infty,r}$, for which the corresponding mass matrix $\mathbf{M}_\infty$ contains the unknown absorber mass. Thus, to estimate the desired absorber mass, the approximation $\mathbf{q}_{\infty,r}\simeq\mathbf{q}_{0,r}$ is substituted into (14b) with $\mathbf{M}_\infty$ eliminated by (8). Hereby the absorber mass is given as

$$m_a=m_{0,r}\frac{\mu_{\text{des}}}{1-\mu_{\text{des}}} \tag{38}$$

where $m_{0,r}$ is the mass ratio for the undamped structure obtained by (14a) with $\mathbf{q}_{\infty,r}=\mathbf{q}_{0,r}$ and $\mathbf{M}_\infty=\mathbf{M}$. The absorber mass m_a is kept constant during the remainder of the design procedure, whereby $\mathbf{M}_\infty$ can be constructed by (8) and the infinitely damped eigenvalue problem (10) can then be solved to give $\omega_{\infty,r}$ and $\mathbf{q}_{\infty,r}$ for the target mode $j=r$. Hereby, the modal mass m_r and stiffness k_r are determined by (14), while the modal mass ratio is finally determined as $\mu_r=m_a/m_r$.

The absorber tuning in Section 3 requires calibration of the residual mode correction ratios μ_r' and κ_r', obtained by the frequency matching procedure described in Section 4. Initially the stiffness ratio is estimated from (27) without correction and thus $\kappa_*=\kappa_r$, whereby the absorber mass and stiffness estimates are

$$\widetilde{m}_a=m_a\quad,\quad\widetilde{k}_a=k_r\mu_r(1-\mu_r) \tag{39}$$

The augmented eigenvalue problem in (31) is now solved and the natural frequencies $\omega_{A,B}$ are identified among the n_a+1 natural frequencies associated with the vibration mode r, whereby the normalized frequencies are $\xi_{A,B}=\omega_{A,B}/\omega_{\infty,r}$ from (32). Thus, the residual mode correction ratios μ_r' and κ_r' are estimated explicitly by the expressions in (35) and (36) with estimated mass ratio $\widetilde{\mu}_r=\widetilde{m}_a/m_r=\mu_r$ and stiffness ratio $\widetilde{\kappa}_r=\widetilde{k}_a/k_r=\mu_r(1-\mu_r)$ from (39).
The obtained correction ratios μ_r' and κ_r' represent the modal interaction with the non-resonant modes $j\neq r$, and thus the optimal absorber parameters must be re-tuned by the tuning expressions in Section 3. Because the absorber mass m_a is not re-evaluated, the mass ratio μ_r may not be updated by (35a). An expression for the actual stiffness ratio $\kappa_r=k_a/k_r$ is therefore obtained by elimination of κ_* between (21b) and

Table 1. Design procedure for the tuned mass absorbers with ζ_{des}.

1)	Solve the undamped eigenvalue problem (9).
2)	Determine the modal mass $m_{0,r}$.
3)	Calculate the actual absorber mass m_a by (38) and set $\widetilde{m}_a = m_a$.
4)	Solve the infinitely damped eigenvalue problem (10).
5)	Determine the modal mass m_r and stiffness k_r from (14).
6)	Determine $\widetilde{m}_a$ and $\widetilde{k}_a$ by (39)
7)	Solve the augmented eigenvalue problem (31) and choose $\omega_{A,B}$.
8)	Determine μ' and κ' from (35) and (36).
9)	Re-evaluate κ_r by (40) and κ_* by (21b).
10)	Evaluate β_* by (29) and β_r by (21c).
11)	Determined actual absorber stiffness by $k_a = \kappa_r k_r$ and absorber damping coefficient by $c_a = \beta_r \sqrt{k_r m_r}$.

the tuning relation (27), which gives

$$\kappa_r = \frac{\mu_*(1-\mu_r)}{1-\mu_*/\kappa_r'} \tag{40}$$

Without residual mode correction ($\kappa_r' \to \infty$) this expression recovers the correct solution $\kappa_r = \mu_r(1-\mu_r)$, used in (39b) to estimate the absorber stiffness. After determining κ_r by (40) the combined stiffness ratio κ_* is then finally re-calculated by (21b). As by now μ_r, κ_r, μ_* and κ_* are known, the combined damper ratio β_* follows from the tuning formula (29), while the actual damper ratio β_r is obtained from (21c). The absorber mass m_a is initially chosen by (39), while the determination of the absorber stiffness $k_a = \mu_r k_r$ and damping coefficient $c_a = \beta_r\sqrt{k_r m_r}$ finalizes the design procedure, summarized in Table 1.

6 Absorber balancing

When multiple absorbers are placed on the same structure to damp the same mode, proper balancing factors should be introduced to relatively size the individual absorbers. In the force relation (4) the common absorber parameters m_a, c_a and k_a determine the magnitude for all absorbers, while their internal scaling is governed by the balancing matrix in (5).

The absorber force vector $\mathbf{f}_a$ in (4) can be expressed by an equivalent viscous relation as

$$\mathbf{f}_a = i\omega H(\omega)\boldsymbol{\alpha}\mathbf{u}_s \tag{41}$$

introducing the frequency dependent absorber function

$$H(\omega) = m_a \frac{i\omega(k_a + i\omega c_a)}{-\omega^2 m_a + k_a + i\omega c_a} \tag{42}$$

which becomes real-valued for pure viscous dampers, as considered in [17]. An estimate of the absorber's working behavior can be gained by assuming resonance, where $m_a\omega^2 \simeq k_a$, whereby the inertia and stiffness terms in the denominator of $H(\omega)$ cancel. Thus, the absorber function can be approximated as

$$H(\omega) \simeq m_a \frac{i\omega(k_a + i\omega c_a)}{i\omega c_a} \simeq m_a \frac{k_a}{c_a} \tag{43}$$

where the last approximation assumes $k_a \gg \omega c_a$, corresponding to $\sqrt{2\mu_r} \ll 1$ for the absorber tuning assumed in Section 3 without residual mode correction. Thus, around a resonance the tuned mass absorber approximately acts as a viscous damper with apparent viscous coefficient $m_a k_a/c_a$. Thus, it seems appropriate for resonant absorber damping to determine a relative sizing of the individual absorbers by the approach for viscous dampers presented in [17].

Assume that each absorber acts directly on the structure, as indicated in Fig 1, whereby the connectivity vector for the i'th absorber

$$\mathbf{w}_i = [0\ldots, 1, \ldots, 0]^T \tag{44}$$

contains a single unit value at the degree-of-freedom to which the i'th absorber is attached. Thus, $u_{s,i} = \mathbf{w}_i^T\mathbf{q}$ defines the i'th entry of $\mathbf{u}_s$ defined in (3). The balancing procedure in [17] secures that the viscous dampers restrain the displacement of the structure at the same rate, whereby they operate together optimally. The locked vibration mode, corresponding to having support conditions at the individual points of damper/absorber attachment can mathematically be formulated by introducing n_a Lagrange multipliers in the extended eigenvalue problem [20],

$$\left(\begin{bmatrix}\mathbf{K} & \mathbf{W}\\ \mathbf{W}^T & \mathbf{0}\end{bmatrix} - \bar{\omega}_{\infty,r}^2\begin{bmatrix}\mathbf{M} & \mathbf{0}\\ \mathbf{0} & \mathbf{0}\end{bmatrix}\right)\begin{bmatrix}\bar{\mathbf{q}}_{\infty,r}\\ \boldsymbol{\lambda}_r\end{bmatrix} = \begin{bmatrix}\mathbf{0}\\ \mathbf{0}\end{bmatrix} \tag{45}$$

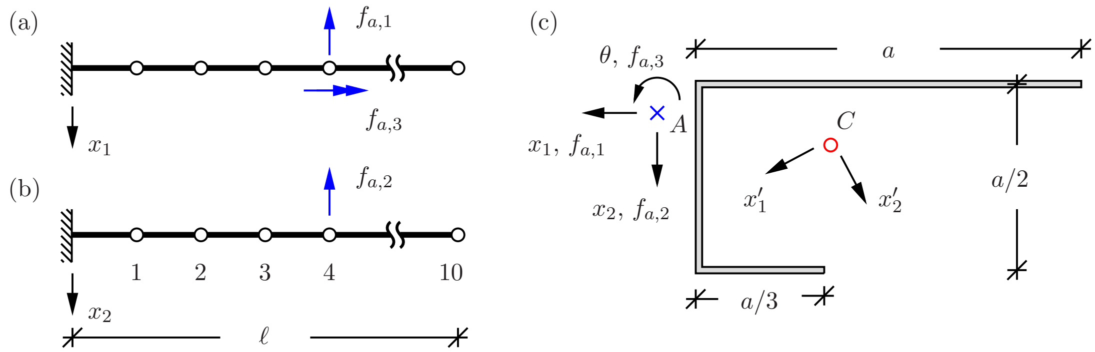

Fig. 2. (a,b) Cantilever beam with three absorber forces and (c) beam cross-section.

where the $\bar{(\,)}$ refers to this eigenvalue problem with fully restrained structure displacements at all absorber locations. However, in practice the natural frequency $\bar{\omega}_{\infty,r}$ and mode shape $\bar{\mathbf{q}}_{\infty,r}$ are conveniently determined from the undamped eigenvalue problem (9) with the additional support conditions that restrain structural motion at all absorber locations. According to [17] the appropriate balancing of an absorber i relative to a given reference $i = 1$ is then obtained by the scaling relation

$$\frac{\alpha_i}{\alpha_1} = \frac{\rho_{i,r}\mathbf{w}_1^T\mathbf{q}_{0,r}}{\rho_{1,r}\mathbf{w}_i^T\mathbf{q}_{0,r}} \tag{46}$$

in which $\mathbf{q}_{0,r}$ is the undamped vibration mode $j = r$ from (9). The constraint force components $\rho_{i,r}$ for the i'th absorber in vibration mode r are obtained by substitution of $\bar{\mathbf{q}}_{\infty,r}$ and $\bar{\omega}_{\infty,r}$ into the undamped balance equation (9) followed by pre-multiplication with $\mathbf{w}_i^T$ to extract the reaction force needed to restrain the structure,

$$\rho_{i,r} = \mathbf{w}_i^T\left(\bar{\omega}_{\infty,r}^2\mathbf{M} - \mathbf{K}\right)\bar{\mathbf{q}}_{\infty,r} \tag{47}$$

Note that the reaction force component may alternatively be extracted from (45) as the Lagrange multipliers in $\boldsymbol{\lambda}_r$. The balancing relation given by (46) ensures a uniform effect of the absorbers when working optimally together. Though the method has been formulated for viscous dampers in [17], quite good balancing factors are obtained for tuned mass absorbers, as illustrated by the following numerical example.

7 Numerical example

The calibration and balancing procedure is now illustrated by an example. The first mode of the cantilevered beam with length $\ell/a = 40$ in Fig. 2a,b is damped by three tuned mass absorbers. The beam cross-section is shown in Fig. 2c with indicated shear centre A and elastic centre C. The axes $\{x'_1, x'_2\}$ indicate the principle axes and as the two centres do not coincide the translations in the x_1- and x_2-directions couple with the angle of twist θ. The cross-section geometry is given in the figure with overall thick $a/40$. The material is isotropic with elastic modulus $E = 210$ GPa and Poisson's ratio $\nu = 0.3$. The beam is modelled by three-dimensional beam elements with six degrees-of-freedom per node, including the rate of twist θ'. The beam model is discretized by ten elements and the absorbers $f_{a,1} - f_{a,3}$ are placed in node four, as shown in Fig. 2a,b, with respect to the cross section shear centre A, as depicted in Fig. 2c. The attachment in the origin of the beam axes secures the single-unit-value construction of the connectivity vector $\mathbf{w}$ in (44), regarded by the balancing procedure in Section 6. In the present case the origin is placed in A to obtain a simple structural model. For another absorber location, the beam axes must simply be placed at the different location.

For the approximate balancing procedure of Section 6, the eigenvalue problem (45) with constraints at absorber location determines the locked vibration mode $\bar{\mathbf{q}}_{\infty,1}$ and natural frequency $\bar{\omega}_{\infty,1}$ for the target mode $r = 1$. The three constraint forces $\rho_{1,1}$ to $\rho_{3,1}$ are then determined by (47), while the components of the balancing matrix are finally evaluated by (46) as $\boldsymbol{\alpha} = \mathrm{diag}[1\,, 1.735\,, 0.038a^2]$. This balancing ensures a more consistent response compared to homogeneous balancing with $\boldsymbol{\alpha} = \mathrm{diag}[1\,, 1\,, a^2]$.

The initial desired modal damping ratio is chosen as $\zeta_{\mathrm{des}} = 0.05$, corresponding to a modal mass of $\mu_1 = 0.0206$ and stiffness ratio $\widetilde{\kappa}_1 = \mu(1-\mu) = 0.0202$. When the absorber mass $m_a = \mu_1 m_1$ has been determined, the correction parameters are obtained as $\mu'_1 = 0.433$ and $\kappa'_1 = 0.629$ according to the design procedure in Table 1. After a re-tuning according to the procedure in Section 3, the final stiffness ratio becomes $\kappa_1 = 0.0199$, thus slightly smaller than the initial value.

Figure 3 shows the root loci when varying the common viscous coefficient c_a from 0 to ∞. Figures 3a,c show the root loci for absorber tuning without residual mode correction ($1/\mu'_1 = 1/\kappa'_1 = 0$), while Figs. 3b,d show the results for the full calibration with finite correction ratios $\mu'_1 = 0.433$ and $\kappa'_1 = 0.629$. To illustrate the importance of a proper balancing, Figs. 3a,c represent the case with homogeneous balancing by $\boldsymbol{\alpha} = \mathrm{diag}[1\,, 1\,, a^2]$. It is seen from Fig. 3d that the full calibration with a proper balancing displays the desired semi-circular root loci with the asterisks indicating the optimal damping slightly below the bifurcation point. The red markers indicate the calibration frequencies ω_A (○) and ω_B (□). Homogeneous balancing is seen to provide limited tun-

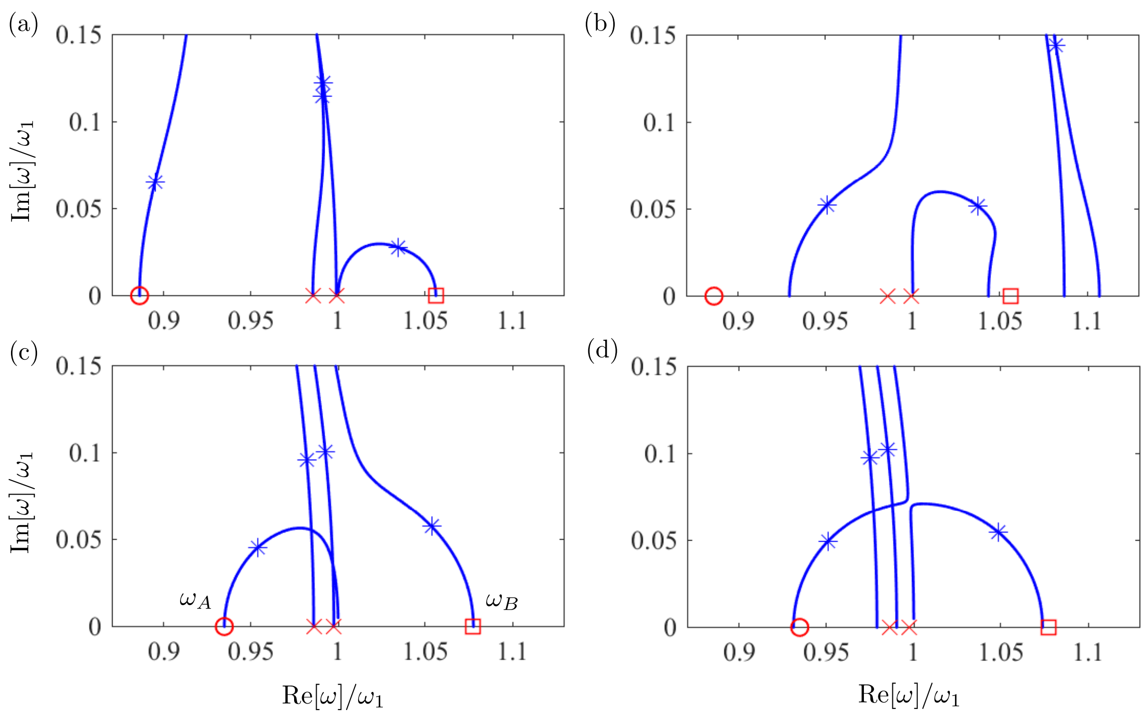

Fig. 3. Root loci (a,c) without correction, (b,d) with correction, (a,b) not balanced and (c,d) balanced.

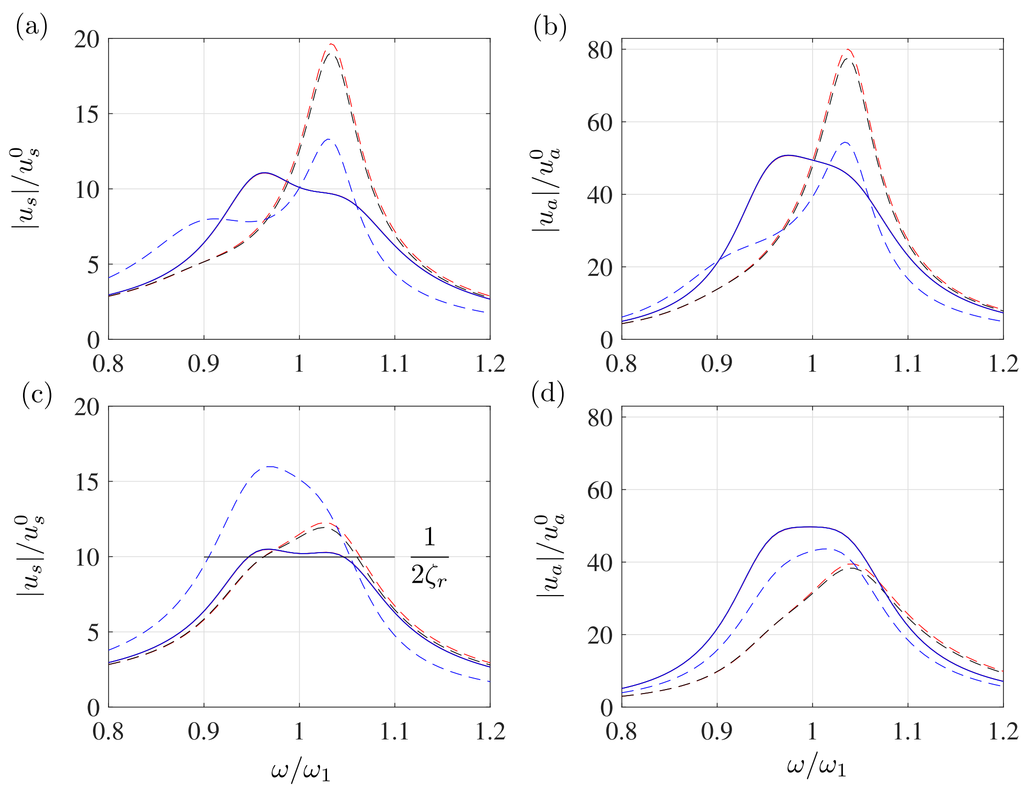

Fig. 4. Frequency response of (a,c) structure, (b,d) absorbers, (a,b) without correction and (c,d) with correction. Not balanced (dashed lines), balanced (solid lines), horizontal (red), vertical (black) and rotation (blue).

ing accuracy, whereas the inclusion of the residual mode correction improves the root locus diagrams in Fig. 3c,d compared to Fig. 3a,b. The modal damping ratios of the two split modes are according to (30) calculated to be $\zeta_1^{\text{est}} = 0.051$, while the actual damping ratios are found to be $\zeta_1 = 0.0527$ and 0.0525, with $\zeta_1 = 0.1005$ and 0.1043 for the two redundant absorber modes.

Figure 4 shows the frequency response curves for the beam loaded by a harmonic load with frequency ω. To avoid modal interaction the spatial distribution of the load is $\mathbf{f}_e = \mathbf{M}_\infty \mathbf{q}_{\infty,1}$, whereby it becomes orthogonal to the other modes ($j > 1$). The curves are normalized according to their corresponding static deflection of the structure u_s^0 at node four. Figures 4a,c represent the structure response, while Figs. 4b,d show the absorber amplitudes. The two top Figs. 4a,b are without residual mode calibration, while the two bottom figures (c,d) are for $\mu_1' = 0.433$ and $\kappa_1' = 0.629$. The dashed curves represent homogeneous balancing by $\boldsymbol{\alpha} = \mathrm{diag}[\,1\,,\,1\,,\,a^2\,]$, while the solid curves represent the optimal balancing $\boldsymbol{\alpha} = \mathrm{diag}[\,1\,,\,1.735\,,\,0.038a^2\,]$ with the colors indicating u_s as the translation in the x_1-direction (red), in the x_2-direction (black) and torsion (blue). As also observed in the root locus analysis, the proper balancing of $\boldsymbol{\alpha}$ corrects the curves to coincide and exhibit the desired plateau around the resonance associated with optimal tuning of a single degree-of-freedom structure. Furthermore, the calibration ensures a flat plateau with almost identical amplification of the two structural modes in Figs. 4a,c and a completely flat plateau for the absorber amplitude in Figs. 4b,d. It is further observed that the calibration with homogeneous absorber balancing yields a significant resonance peak, illustrating the importance of proper balancing between the $\boldsymbol{\alpha}$-components by a procedure as in Section 6.

8 Conclusions

A procedure for approximate balancing and calibration of tuned mass absorbers mounted on flexible structures has been described. The tuning of the classic mass absorber is based on a single degree-of-freedom structure and a selected vibration mode to be damped. For discrete structures, the influence of residual non-resonant vibration modes becomes important. This contribution to the absorber tuning has been included by calibrating a flexibility and inertia term with respect to two specific frequencies identified for vanishing absorber damping and sufficiently accurate estimates of the absorber stiffness. To improve the absorber efficiency for coupled bending-torsion vibrations, a set of two translational and a single rotational absorber are combined into an effective system for damping of fully coupled vibrations. As translational and torsional stiffness are inherently different, the absorbers must not be balanced homogeneously and a method for sizing of viscous dampers has been shown to provide proper balancing for tuned mass absorbers, resulting in the desired root locus and frequency response curves with equal modal damping and flat plateaus in the corresponding response amplitude curves.

References

[1] Elias, S. and Matsagar, V., 2017," Research developments in vibration control of structures using passive tuned mass dampers", Annual Reviews in Control, vol. 44, pp. 129-156, DOI: 10.1016/j.arcontrol.2017.09.015.

[2] Arrigan, J., Pakrashi, V., Basu, B. and Nagarajaiah, S., 2011, "Control of flapwise vibrations in wind turbine blades using semi-active tuned mass dampers", Structural Control and Health Monitoring, vol. 18, pp. 840-851, DOI: 10.1002/stc.404.

[3] Casalotti, A., Arena, A. and Lacarbonara, W., 2014, "Mitigation of post-flutter oscillations in suspension bridges by hysteretic tuned mass dampers", Engineering Structures, vol. 69, pp. 62-71, DOI: 10.1016/j.engstruct.2014.03.001.

[4] Zheng, L., Zhang, H., Zhao, B. and Xianjie, L., 2018, "Shaking table test and numerical simulation on vibration control effects of TMD with different mass ratios on a super high-rise structure", Structural Design of Tall and Special Buildings, vol. 27, no. 9, pp. e1470, DOI: 10.1002/tal.1470.

[5] Den Hartog, J.P., 1956, Mechanical Vibrations, 4th ed. New York, McGraw-Hill, (reprinted by Dover, New York, 1985).

[6] Krenk, S., 2005, "Frequency analysis of the tuned mass damper", Journal of Applied Mechanics, vol. 72, no. 6, pp. 936-942, DOI: 10.1115/1.2062867.

[7] Krenk, S. and Høgsberg, J., 2016, "Tuned resonant mass or inerter-based absorbers: unified calibration with quasi-dynamic flexibility and inertia correction", Proceedings of the Royal Society A - Mathematical, Physical and Engineering Sciences, vol. 472, no. 2185, pp. 20150718, DOI: 10.1098/rspa.2015.0718.

[8] Høgsberg, J., 2019, "A robust calibration procedure for multiple electromechanical shunt absorbers on a flexible structure", Proceedings of the IX ECCOMAS Thematic Conference on Smart Structures and Materials, July.

[9] Jangid, R.S. and Datta, T.K., 1997, "Performance of multiple tuned mass dampers for torsionally coupled systems", Earthquake Engineering and Structural Dynamics, vol. 26, no. 3, pp. 307-317, DOI: 10.1002/(SICI)1096-9845(199703)26:3¡307::AID-EQE639¿3.3.CO;2-#.

[10] Li, C. and Qu, W., 2006, "Optimum properties of multiple tuned mass dampers for reduction of translational and torsional response of structures subject to ground acceleration", Engineering Structures, vol. 28, no. 4, pp. 472-494, DOI: 10.1016/j.engstruct.2005.09.003.

[11] Lin, C.C., Ueng, J.M. and Huang, T.C., 2000, "Seismic response reduction of irregular buildings using passive tuned mass dampers", Engineering Structures, vol. 22, no. 5, pp. 513-524, DOI: 10.1016/S0141-0296(98)00054-6.

[12] Febbo, M. and Vera, S.A., 2008, "Optimization of a two degree of freedom system acting as a dynamic vibration absorber", Journal of Vibration and Acoustics, vol. 130, no. 1, pp. 011013, DOI: 10.1115/1.2827368.

[13] Daniel, Y. and Lavan, O., 2014, "Gradient based optimal seismic retrofitting of 3D irregular buildings using multiple tuned mass dampers", Computers and Structures, vol. 139, pp. 84-97, DOI: 10.1016/j.compstruc.2014.03.002.

[14] Zuo, H., Bi, K. and Hao, H., 2019, "Mitigation of tower and out-of-plane blade vibrations of offshore monopile wind turbines by using multiple tuned mass dampers", Structure and Infrastructure Engineering, vol. 15, no. 2,

pp. 169-284, DOI: 10.1080/15732479.2018.1550096.

[15] Snowdon, J.C., 1984, ”The cruciform dynamic vibration absorber”, Journal of the Acoustical Society of America, vol. 75, no. 6, pp. 1792-1799, DOI: 10.1121/1.390980.

[16] Mokrani, B., Tian, Z., Alaluf, D., Meng, F. and Preumont, A., 2017, ”Passive damping of suspension bridges using multi-degree of freedom tuned mass dampers”, Engineering Structures, vol. 153, pp. 749-756, DOI: 10.1016/j.engstruct.2017.10.028.

[17] Main, J. A. and Krenk, S., 2005, ”Efficiency and tuning of viscous dampers on discrete systems”, Journal of Sound and Vibration, vol. 286, no. 1-2, pp. 97-12, DOI: 10.1016/j.jsv.2004.09.022.

[18] Krenk, S. and Høgsberg, J., 2012, ”Equal modal damping design for a family of resonant vibration control formats”, Journal of Vibration and Control, vol. 19, no. 9, pp. 1294-1315, DOI: 10.1177/1077546312446796.

[19] Krenk, S. and Høgsberg, J., 2014, ”Tuned mass absorber on a flexible structure”, Journal of Sound and Vibration, vol. 333, no. 6, pp. 1577-1595, DOI: 10.1016/j.jsv.2013.11.029.

[20] Géradin, M. and Cardona, A., 2001, Flexible Multibody Dynamics, A Finite Element Approach, *Wiley*.

C1

Numerical Investigation of Damping of Torsional
Beam Vibrations by Viscous Bimoments

David Hoffmeyer and Jan Høgsberg

VII ECCOMAS Thematic Conference on
Smart Structures and Materials,
June 5-8, 2017

VIII ECCOMAS Thematic Conference on Smart Structures and Materials
SMART 2017
A. Güemes, A. Benjeddou, J. Rodellar and J. Leng (Eds)

NUMERICAL INVESTIGATION OF DAMPING OF TORSIONAL BEAM VIBRATIONS BY VISCOUS BIMOMENTS

David Hoffmeyer & Jan Høgsberg

Department of Mechanical Engineering, Technical University of Denmark
Nils Koppels Allé, building 404, DK-2800 Kongens Lyngby, Denmark
e-mail: davhoff@mek.dtu.dk, jhg@mek.dtu.dk, www.dtu.dk

Key words: Torsional beam vibrations, damping, warping, viscous bimoment, complex natural frequency, finite element method.

Abstract. Damping of torsional beam vibrations of slender beam–structures with thin–walled cross–sections is investigated. Analytical results from solving the differential equation gover– ning torsion with viscous bimoments imposed at the boundary, are compared with a numerical approach with three–dimensional, isoparametric elements. The viscous bimoments act on the axial warping displacements associated with inhomogeneous torsion, and are in a numerical format realized by suitable configurations of concentrated, axial forces describing discrete dampers. It is illustrated by an example that significant damping ratios may be obtained for a beam with an open cross–section.

1 INTRODUCTION

Torsional vibrations may be induced in slender, thin–walled beam–structures by e.g. wind, if the loads on the beam act with a certain eccentricity relative to the shear center of the cross-section. For beams with asymmetric cross-sections the elastic and shear centers do not coincide, whereby the flexural and torsional vibrations couple. In both cases the total dynamic response may be damped by damping the torsional motion of the beam. Slender structures like long bridge decks, aircraft wings or wind turbine blades may be prone to aerodynamic instabilities like flutter, where flexural and torsional vibrations couple. Flutter is associated with apparent negative damping that cannot be sufficiently compensated by the inherent structural damping. To avoid flutter and e.g. to reduce fatigue stresses by aerodynamic forces, supplemental damping is therefore required.

Torsional vibrations of thin–walled beams are associated with inhomogeneous torsion which generates out-of-plane, axial warping displacements that are often significant at the boundaries of beams with open cross-sections. The free, torsional vibration characteristics including warping were originally investigated by Gere [1] who solved for the natural frequencies and mode shapes of beams with various boundary conditions, and by Carr [2] where an energy apporach was applied to obtain approximate frequency equations for a few combinations of boundary conditions.

Subsequently Gere and Lin [3] studied the coupling between flexural and torsional vibrations, and the coupling with restrained thin–walled beams by Lin [4]. Numerical results using a finite element approach were compared with analytical results by Mei [5], and Friberg [6] derived an exact dynamic element stiffness matrix, though without the effect of warping. Analytical solutions of frequencies and mode shapes for prismatic beams excited by harmonic, torsional loads have been derived by Augustyn and Kozién [7].

Damping of torsional vibrations has only briefly been addressed in the literature. Narayanan and Malik [8] attached viscoelastic layers to the flanges of a beam with an open cross–section; Jansen and van der Steen [9] considered damping of torsional vibrations in oil well drillstrings; and recently Augustyn and Kozién [10, 11] glued piezoelectric actuators to a beam to reduce the torsional vibrations. Christiano and Salmela [12] showed that the restraining of warping results in an often considerable increase in natural frequency and change in vibration characteristics. This localized effect of restrained warping was utilized to introduce a substantial amount of supplemental damping by Høgsberg et. al. [13], where viscous boundary conditions were applied through pure bimoments at the supports. They solved the eigenvalue problem associated with free vibrations with respect to the complex-valued natural frequency and corresponding damping ratio. They demonstrated that significant damping ratios could be realized by these viscous bimoments at the beam supports.

The present paper performs a numerical investigation of the changed dynamic behaviour of thin-walled beams with applied viscous bimoments at the boundaries. The results in terms of natural frequencies and damping ratios are compared with [13]. The numerical procedure is based on a linear finite element approach with three-dimensional, isoparametric elements. In a simple numerical code, the bimoments are easily represented by concentrated, axial forces distributed over the cross-section. These viscous forces are proportional to the velocity of the given node and are added to the equations of motion by an influence vector describing the points of application. As they are proportional with velocity, they constitute a damping term and result in a modified damping matrix. Setting up the equations of motion in a state-space format yields an eigenvalue problem, from which the corresponding complex natural frequencies and damping ratios are extracted.

2 UNCOUPLED TORSIONAL VIBRATIONS

Consider a beam element of length ℓ, axial coordinate x and transverse axes $\{y, z\}$. The axial displacement is $u(x, y, z, t)$ and the angle of twist is $\theta(x, t)$ as seen in Fig. 1a. In the present analysis it is assumed that flexural and torsional vibrations uncouple because of coinciding elastic centers.

The differential equation governing the torsional vibration problem is set up by energy relations which require the elastic and kinetic energy. The elastic strain energy contains contribution from homogeneous and inhomogeneous torsion, respectively given as

$$U = \int_\ell \tfrac{1}{2}\, GK(\theta')^2 \, dx + \int_\ell \tfrac{1}{2}\, EI_\psi(\theta'')^2 \, dx \tag{1}$$

where G is the shear modulus, K is the torsion stiffness parameter, E is Young's modulus and I_ψ is the warping moment of inertia with ψ indicating the sector–coordinate or warping function.

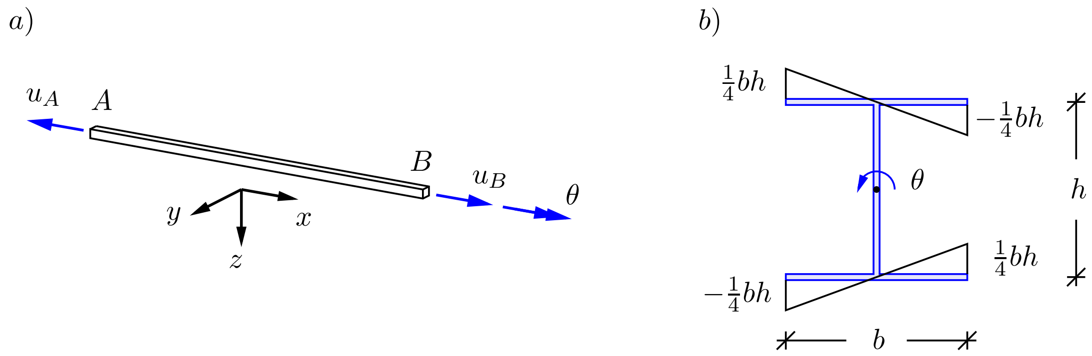

Figure 1: Degrees of freedom and coordinates a) and sector–coordinate ψ for an I–profile with a positive angle of twist b).

For an I–profile the distribution of the sector–coordinate is shown in Fig. 1b. The kinetic energy o the torsional motion is

$$T = \int_\ell \tfrac{1}{2}\,\rho J \dot{\theta}^2\,dx \tag{2}$$

where ρ is the mass density and J is the polar moment of inertia taking the distribution of the mass into account. Energy dissipation may be defined through a viscous damping coefficient either distributed along the beam by $c_0(x)$ or acting at discrete points via c described by Dirac's delta function δ. As dampers may be applied at discrete points the latter is relevant whereby the dissipated energy D then takes the form:

$$D = \int_\ell c_0(x)\,\dot{\theta}^2\,dx = \int_\ell c\,\delta(x-x_0)\,\dot{\theta}^2\,dx \tag{3}$$

where x_0 indicates the point of application of the discrete damper. In the case of damped vibrations the change in mechanical energy is balanced by the dissipated energy, $\dot{U} + \dot{T} = -D$. Performing the differentiation of the energy balance and using integration by parts yields the governing differential equation as

$$EI_\psi \theta'''' - GK\theta'' + \rho J \ddot{\theta} = 0 \tag{4}$$

As no continuous form of damping is intended, the last expression in (3) is instead applied as a boundary condition. Thus, (4) is valid between the points of application of external dampers. A time harmonic solution of the form $\theta = \varphi\,\mathrm{e}^{i\omega t}$ may be assumed with ω being the natural frequency and φ the spatial solution. Inserting the frequency solution into (4) and following the approach by Gere [1], the spatial solution may be expressed as

$$\varphi = D_1\cosh(\alpha x) + D_2\sinh(\alpha x) + D_3\cos(\beta x) + D_4\sin(\beta x) \tag{5}$$

introducing the four integrations constants D_1 to D_4 – determined by the boundary conditions – and the two apparent and real–valued wave numbers defined as

$$\alpha^2 = \sqrt{\tfrac{1}{4}k^4 + \lambda^4} + \tfrac{1}{2}k^2 \qquad , \qquad \beta^2 = \sqrt{\tfrac{1}{4}k^4 + \lambda^4} - \tfrac{1}{2}k^2 \tag{6}$$

This formulation of the solution introduces the warping length scale k, wave speed v and scaled wave number λ respectively as

$$k^2 = \frac{GK}{EI_\psi} \quad , \quad v^2 = \frac{GK}{\rho J} \quad , \quad \lambda^4 = \left(\frac{k\omega}{v}\right)^2 \tag{7}$$

It is noted that v represents the wave speed for the homogeneous torsion problem. The spatial solution to the torsion problem in terms of the vibration form is obtained from (5) by use of relevant boundary conditions. Applying the boundary conditions yields transcendental equations which must be solved iteratively for the combined set of α and β. One wave number is then given by the other through (6), and the use of the third expression in (7) determines the frequency ω. For more details see e.g. [1, 13].

2.1 Viscous Bimoment at the Boundary

A viscous condition on the boundary may be imposed in several ways. In [13] a viscous normal stress distribution was applied at the beam supports acting through the axial displacement producing a bimoment. This normal stress was distributed across the cross-section of the beam in a continuous manner. In the case of active control a discrete device would produce a concentrated force proportional to the velocity at specific points at the cross-section. A viscous, concentrated force $F_d(y,z,t)$ at the boundary is

$$F_d = \pm\, c\, \dot{u}_d \tag{8}$$

where c is a viscous damping coefficient and $\dot{u}_d(y,z,t)$ is the axial velocity, positive in the x–direction. The force is defined as positive in tension, whereby the "+" in (8) refers to the left end of the beam at $x = 0$ and the "−" refers to the right end at $x = \ell$. The axial displacement due to torsion is given through the sector–coordinate, and the corresponding velocity is

$$\dot{u}_d = -\psi\, \dot{\theta}_d' \tag{9}$$

see e.g. Vlasov [14]. A series of discrete dampers may be applied at the boundary each dissipating energy. Thus the second expression in (3) indicates a sum of the viscous damping coefficients associated with the given damper and the velocity at that particular point. In combination with (8) the rate of external work D produced by the dampers is formulated as the sum of the contributions of the viscous forces multiplied with the energy conjugate velocity by

$$D = \pm \sum_j F_{d,j}\, \dot{u}_{d,j} = \pm \sum_j c\, \dot{u}_{d,j}^2 = \pm \big(\dot{\theta}_d'\big)^2 \sum_j c\, \psi_j^2 \tag{10}$$

where ψ_j is the sector–coordinate at the location of the j'th damper and c is here assumed to be constant for all dampers. A bimoment as shown in Fig. 2a is usually noted with a double arrow due to the classical example shown in Fig. 2b. Here two opposite bending moments are applied at the flanges. Vectorially they add up to zero, and a pure bimoment is thus a kinematic and not a static condition. It does not generate a resulting force (or moment) but acts as a concentrated change in rotation curvature. The bending moments, however, may be decomposed into force couples as seen in Fig. 2c. A given configuration of concentrated, axial forces therefore generates

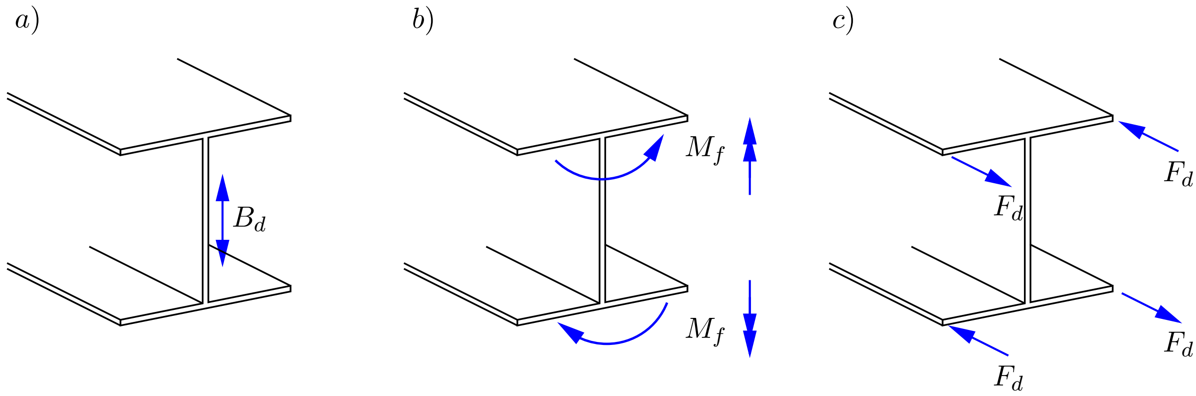

Figure 2: I–profile beam with a bimoment a), bending moments at the flanges generating the bimoment b) and equivalent configuration of concentrated, axial forces c).

a bimoment through the sector–coordinate. By definition the bimoment produces work through the negative gradient of the angle of twist, see e.g. Vlasov [14]. Thus, the rate of work produced by a bimoment is $D = -\dot{\theta}'_d B_d$. Equating this rate of work with (10) yields

$$B_d = \mp \dot{\theta}'_d \sum_j c\,\psi_j^2 \tag{11}$$

The bimoment produced by the dampers $B_d(t)$ must be balanced by the section bimoment at the boundary $B(x,t) = -EI_\psi \theta''(x,t)$. The dynamic boundary condition then takes the form

$$\theta''_d \mp \eta\,\dot{\theta}'_d = 0 \tag{12}$$

with the effective viscous damping parameter $\eta = \sum_j c\,\psi_j^2 / EI_\psi$. The form of (12) is identical to [13] with exception of the effective parameter η. Here the viscous damping coefficient c is scaled relative to the amount of dampers, the corresponding sector–coordinates at the points of application and the warping stiffness EI_ψ. Inserting the frequency solution $\theta = \varphi\,\mathrm{e}^{i\omega t}$ yields the harmonic boundary condition

$$\varphi'' \mp i\omega\eta\varphi' = 0 \tag{13}$$

which is directly applicable in connection with the transcendental equations governing the torsional vibration problem.

3 DAMPING OF TORSIONAL VIBRATIONS

When not considering a beam element but modelling the entire structure by a finite element procedure, a discretized, multi–degree–of–freedom system with n degrees of freedom may be assumed. The equations of motion are set up by the elastic, kinetic and dissipated energy. The elastic energy gives the stiffness contribution through the stiffness matrix $\mathbf{K}$, the kinetic energy gives the inertia contribution through the mass matrix $\mathbf{M}$ and the dissipated energy gives the applied, discrete viscous forces as described in (8) and in the second term in (10). The energy balance $\dot{T} + \dot{U} = -D$ then gives

$$\mathbf{M}\ddot{\mathbf{q}}(t) + \mathbf{K}\mathbf{q}(t) = -\mathbf{f}_d(t) \tag{14}$$

where $\mathbf{q}(t)$ is a column vector containing the degrees of freedom and $\mathbf{f}_d(t)$ are the externally applied viscous forces. In this case the inherent structural damping is neglected. Damping may be constituted as a series of dampers modelled as equivalent concentrated, viscous forces acting through a viscous damping coefficient c and the velocity of the corresponding nodes in the discretized system:

$$\mathbf{f}_d(t) = \left(\sum_j^{nd} c_j \mathbf{w}_j \mathbf{w}_j^T\right)\dot{\mathbf{q}}(t) = \widetilde{\mathbf{C}}\dot{\mathbf{q}}(t) \tag{15}$$

Here c_j is the viscous damping coefficient associated with the j'th damper and $\mathbf{w}_j$ is an influence vector describing the points in the structure connected to the damper. The column vector $\mathbf{w}_j$ thus contains 1 at the location of the damper and otherwise 0's. In this case, however, a constant viscous damping coefficient is used for all dampers. Inserting (15) into (14) yields the equations of motion with a modified damping matrix

$$\mathbf{M}\ddot{\mathbf{q}} + \widetilde{\mathbf{C}}\dot{\mathbf{q}} + \mathbf{K}\mathbf{q} = \mathbf{0} \tag{16}$$

These modified equations of motion with damping included yields a quadratic eigenvalue problem. However, they may be formulated in a state–space format

$$\frac{d}{dt}\begin{bmatrix}\mathbf{q}\\ \dot{\mathbf{q}}\end{bmatrix} = \begin{bmatrix}\mathbf{0} & \mathbf{I}\\ -\mathbf{M}^{-1}\mathbf{K} & -\mathbf{M}^{-1}\widetilde{\mathbf{C}}\end{bmatrix}\begin{bmatrix}\mathbf{q}\\ \dot{\mathbf{q}}\end{bmatrix} \tag{17}$$

where $\mathbf{I}$ is a $n \times n$ identity matrix. Assuming a time–dependent, partial solution the state–space format constitutes an ordinary eigenvalue problem, from which the eigenvalue $i\omega$ and corresponding eigenvector may be extracted. For damped vibrations the natural frequency ω is generally complex–valued and usually expressed as

$$\omega = |\omega|\left(\sqrt{1-\zeta^2} + i\zeta\right) \tag{18}$$

with ζ being the damping ratio defined by the imaginary part of the natural frequency

$$\zeta = \frac{\mathrm{Im}[\omega]}{|\omega|} \tag{19}$$

In the complex plane the natural frequency ω constitutes a semicircle between the undamped frequency ω_0 and the corresponding upper limit frequency ω_∞. In the former case the damper(s) have no effect and the viscous damping coefficient therefore is $c = 0$. In the corresponding extreme case where $c \to \infty$ the damper locks and the node, at which the damper is attached, simply becomes restrained against axial movement.

4 EXAMPLE

In the following an example is used to illustrate the theory from Section 2, the numerical procedure established in Section 3 and to illustrate the use of concentrated, axial forces as a measure of damping.

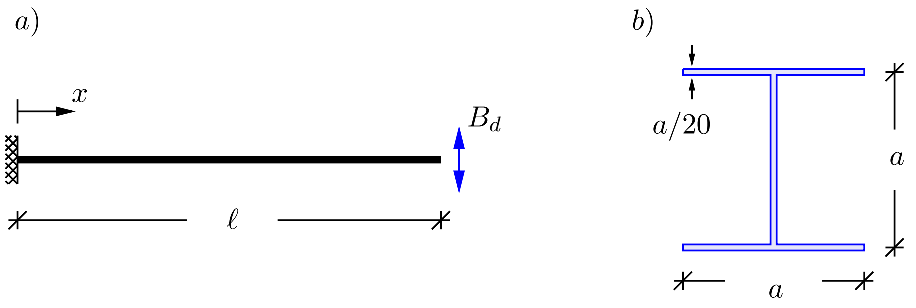

Figure 3: Fixed–free beam with viscous bimoment B_d at $x = \ell$ *a*) and I–profile cross–section *b*).

4.1 Damping of a fixed–free beam.

Consider the fixed–free beam in Fig. 3*a*. The beam has the length ℓ, is fixed at $x = 0$ with restrained rotation and warping and is free at $x = \ell$. The beam cross–section is an open I–profile with height and width a and thickness $t = a/20$, see Fig. 3b. With the chosen cross-section, material and length of the beam the warping length scale normalized with the length of the beam is $k\ell = 3$ and thus represents a slender structure. For a particular viscous bimoment at the boundary at $x = \ell$, the complex natural frequency ω and corresponding damping ratio ζ are obtained by determining the integration constants in (5) by use of the boundary conditions. For the fixed–free beam with damping at $x = \ell$ the boundary conditions are

$$\varphi(0) = 0 \quad , \quad \varphi'(0) = 0 \quad , \quad \varphi''(\ell) + i\omega\eta\varphi'(\ell) = 0 \quad , \quad k^2\varphi'(\ell) - \varphi'''(\ell) = 0 \tag{20}$$

With these homogeneous boundary conditions and the homogeneous differential equation (4) the torsion problem constitutes an eigenvalue problem where the spatial solution (5) leads to a transcendental equation. In [13] it is derived as

$$\begin{aligned} &\frac{(\alpha\ell)^4 + (\beta\ell)^4}{(\alpha\ell)^2(\beta\ell)^2}\cosh(\alpha\ell)\cos(\beta\ell) + \frac{(\alpha\ell)^2 + (\beta\ell)^2}{(\alpha\ell)(\beta\ell)}\sinh(\alpha\ell)\sin(\beta\ell) + 2 \\ &+ i\omega\eta\ell\frac{(\alpha\ell)^2 + (\beta\ell)^2}{(\alpha\ell)^2(\beta\ell)^2}\cosh(\alpha\ell)\cos(\beta\ell)\big[\alpha\ell\,\tanh(\alpha\ell) + \beta\ell\,\tan(\beta\ell)\big] = 0 \end{aligned} \tag{21}$$

This equation is solved iteratively for $\alpha\ell$ and $\beta\ell$, while the third expression in (7) determines the frequency and by (19) the damping ratio is found. In obtaining a semi–circle in the complex plane, illustrating the variation of the frequency, the viscous damping coefficient c – contained within the effective damping parameter η – is varied in the interval $c \in [0\,;\,\infty[$. In this example a series of configurations for the distribution of discrete dampers is applied, see. Fig. 4. The first configuration seen in Fig. 4*a* consists of a single damper applied at one corner of the I–profile, and the resulting warping of the cross–section is thus only partly restrained. The second configuration is a more effective measure of restraining warping as two dampers are located at opposite corners where the largest warping displacements occur, see Fig. 1*b*. The profile may though still warp, and thus the third configuration is applied which effectively prevents the cross–section from warping almost completely. The two configurations in Figs. 4*a* and 4*b* do not constitute pure bimoments as they generate a normal force – and in the first case also

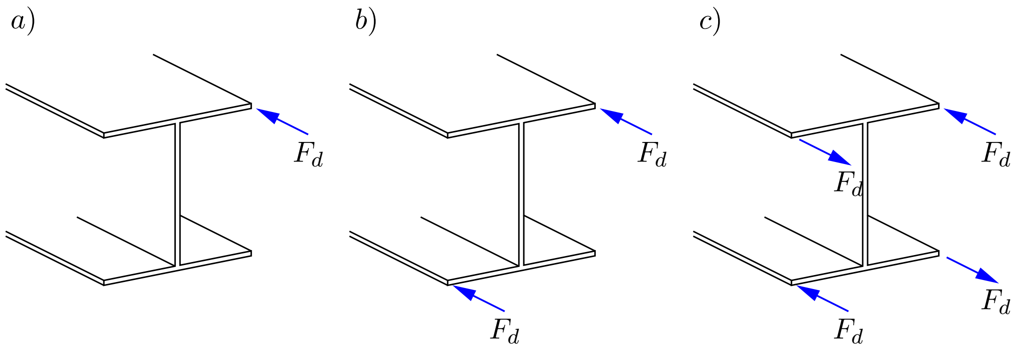

Figure 4: Three configurations of dampers; opposite corners a), all corners b) and distributed along flanges c).

bending moments – which must be accounted for. However, together with the third configuration they serve to illustrate the amount of damping that might by obtained by restraining at the right locations and with a proper number of dampers. The two configurations with non–pure bimoments may even serve to illustrate the possibility of damping coupled flexural vibrations, if the right structural set–up could be established.
The frequency loci and damping ratios for the three different configurations obtained by solving (21) are seen as the solid curves in Figs. 6a and 6b, respectively. By all three configurations of dampers the analytical model yields the same results in terms of undamped frequency ω_0 and the frequency with the dampers being locked ω_∞, corresponding to infinite damping. The dynamic boundary condition (12) restrains warping of the entire cross–section in a unified manner, and does not take the possible modes of warping with the dampers applied into account. The optimal value of the viscous damping parameter c_{opt} is therefore different in the three cases, but plotted as the effective damping parameter η the three sets of curves coincide as seen in Fig. 6b.

Frequencies and damping ratios

In the numerical comparison a standard finite element approach is used with solid, isoparametric elements. A special bi–cubic–linear element is exploited to model thin flanges and a cubic–bi–linear element for connections and corner – these are illustrated in Fig. 5.

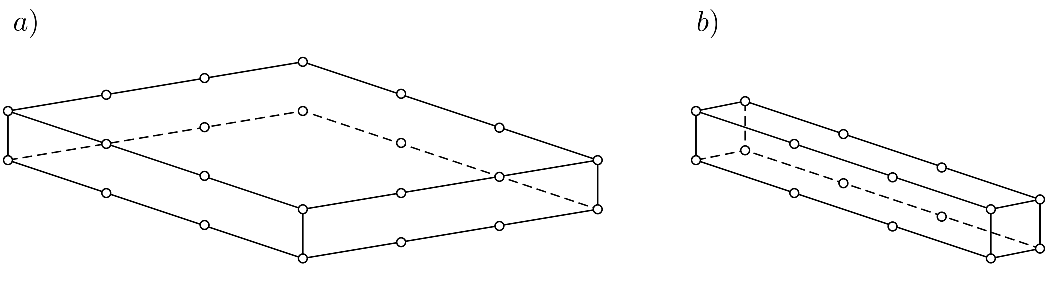

Figure 5: Isoparametric 24–node bi–cubic–linear a) and 16–node cubic–bi–linear b) element.

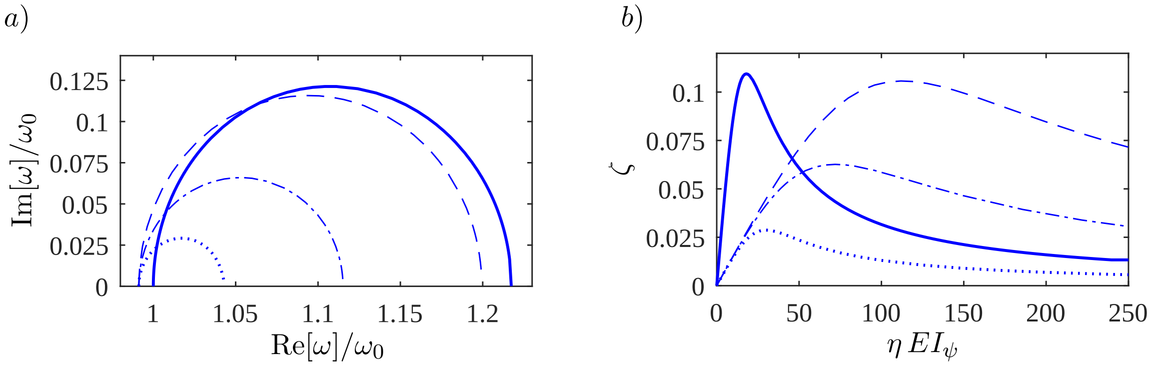

Figure 6: Frequency loci a) and damping ratios b) showing the results from (–) the analytical procedure and numerical procedure with (···), (– · –) and (– –) representing the three bimoment configurations shown in Figs. 4a, 4b and 4c respectively.

The elements are intended for modelling of thin-walled beams where a linear interpolation across the thickness is sufficient and a cubic interpolation in the flange–wise direction to capture the parabolic stress variations associated with shear. The I–profile is thus sufficiently modelled with seven elements in the cross–section in the case of a simple static analysis. See e.g. Høgsberg & Krenk [15] for the use of a two–dimensional version of these elements for general cross–sectional analyses of thin–walled beams. In the present case, however, a further discretization of the cross–section is necessary in order to capture the warping effect. As two nodes across the thickness of the flanges are present, a damper at each node of the corners are applied in order to avoid any unnecessary distortion of the cross–section as the damping effect increases. Thus, the damping forces F_d in Fig. 4 constitute a set of two dampers.

Solving the eigenvalue problem in the state–space format for the complex frequency and corresponding damping ratio for the three configurations of dampers yield the frequency loci and distribution of the damping ratio illustrated with the non–solid curves in Fig. 6. As seen the undamped frequency ω_0^{FEM} is 0.9 % lower than the analytical solution. This may be due to the torsional mode in the numerical example not representing 'pure torsion' – as the analytical method requires – but contains some minor distortion, e.g. local deformations of the flanges. The analytical approach is independent of the shape of the cross–section and only works through the cross-sectional parameters, but a three–dimensional numerical model takes this into account. In the case of $c \to \infty$ the boundary condition (12) completely restrains the warping at the free end, and the increment, $(\omega_\infty - \omega_0)/\omega_0$, in the frequency is 0.217 in the analytical case. The numerical model, however, only requires an axial restraining of the nodes at the corners of the I–profile where the dampers are attached. As the largest warping displacements occur at the corners, restraining these will have an essential influence on the warping of the rest of the cross–section. As the cross–sections in the three cases in Fig. 4 still are able to warp locally when $c \to \infty$, the corresponding frequencies ω_∞^{FEM} will be lower compared to the analytical model, which is also seen in Fig 6a. For the configurations shown in Figs. 4a, 4b and 4c the increments in frequencies, $(\omega_\infty^{FEM} - \omega_0)/\omega_0$, are 0.043, 0.115 and 0.199 relative to the analytical ω_0, corre-

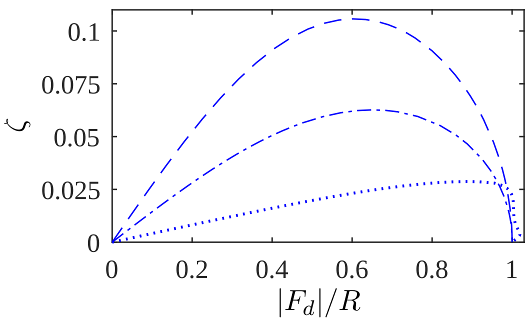

Figure 7: Damping ratio given as a function of damper force, for the three damper configurations.

sponding to an increase in stiffness from increased restraining of the warping. The increase in locked frequency has a direct consequence on the damping ratio; the bigger the frequency locus the more damping it is possible to obtain. This is also evident in Fig. 6b where the damping ratio ζ increases from 0.029 through 0.063 to 0.106 for the three configurations, compared to 0.109 in the analytical case. This should correspond to approximately half of the frequency increment, but due to ω_0^{FEM} not completely coinciding with ω_0 the values are just slightly off. By this it is noted that the numerical and analytical models match quite well, as the damping ratios are almost identical in the case 4c when restraining the entire cross–section.

In this example identical viscous damping coefficients c are used for all dampers. And larger damping ratios may be reached by application of different damping coefficients optimised for each damper. Different cross–sections where warping is more pronounced may equivalently result in even large damping ratios. However, for closed cross–sections associated with larger $k\ell$–values the obtainable damping ratios are limited due to the vanishing warping displacements. In that case an amplified warping displacement may be induced by including a slit along the beam, whereby non–vanishing, relative axial displacements occur.

Damper force

As damping of torsional vibrations by restraining of warping displacements prospectively is intended for beam–structures within civil or mechanical engineering, it is of interest to consider the magnitude of the forces occurring in the dampers. As the eigenvalue problem solved is complex, the force in the damper is also complex. Thus, the magnitude of the force vector for the j'th damper is $|F_{d,j}| = |c_j\, \mathbf{w}_j^T\, \dot{\mathbf{q}}|$. Assuming a time dependent solution of the form $\mathbf{q} = \mathbf{q}_0\, \mathrm{e}^{i\omega t}$ the force takes the form

$$|F_{d,j}| = |i\, c_j\, \omega\, \mathbf{w}_j^T\, \mathbf{q}_0| \tag{22}$$

This force, however, is scaled according to the corresponding eigenvector and does not represent the actual magnitude. But related to the reaction force R in the case of infinite damping, the relation between the two forces is comparable, provided that the eigenvectors are scaled identically. Fig. 7 shows the damping ratio given as a function of the force of the damper in a single corner of the I–beam, in Fig. 4. For the three configurations in Figs. 4a, 4b and 4c the force ratios $|F_d|/R$ corresponding to maximum damping are 0.887, 0.650 and 0.602 respectively.

It is seen that quite large portions of the reaction force must be realized at optimal damping, and for the single damper configuration almost 90 % of the reaction force is present in the damper. This indicates that a configuration of several dampers that effectively restrains warping is most advantageous.

5 CONCLUSION

A previously developed novel method for damping of torsional vibrations of thin–walled beams by control of warping displacements has been investigated and compared with a numerical finite element procedure. The torsional vibrations are damped by restraining the out–of–plane warping displacements by applying viscous bimoments at the boundary of the beam. These viscous bimoments are represented by axial, concentrated forces proportional with the velocity of a given node in the numerical model. By an example it is shown that restraining warping is associated with a significant increase in natural frequency depending on the part of the cross–section being restrained. A proper configuration of dampers results in a considerable amount of supplemental damping for a slender beam-structure, even though all dampers in the present paper are associated with identical viscous damping coefficients. The undamped and infinitely damped natural frequencies are however not exactly identical due to the numerical model taking the actual geometry of the beam into account. This suggests that a final design should be carried out by a numerical procedure to get accurate calibration of the dampers, as well as the forces in the dampers which may be close to the reaction force when locking the damper.

REFERENCES

[1] Gere, J. M., *Torsional vibrations of Beams of Thin–Walled Open Section*, ASME Journal of Applied Mechanics (1954), **21**, pp. 381–387.

[2] Carr, J. B., *The Torsional Vibration of Uniform Thin–Walled Beams of Open Section*, The Aeronautical Journal of the Royal Aeronautical Society (1968), vol. 73, pp. 672–674.

[3] Gere, J. M. & Lin, Y. K., *Coupled Vibrations of Thin–Walled Beams of Open Cross–Section*, ASME Journal of Applied Mechanics (1958), **25**, pp. 373–378.

[4] Lin, Y. K., *Coupled Bending and Torsional Vibrations of Restrained Thin–Walled Beams*, ASME Journal of Applied Mechanics (1960), **27**(4), pp. 739–740.

[5] Mei, C., *Coupled Vibrations of Thin–Walled Beams of Open Section using Finite Element Method*, International Journal of Mechanical Sciences (1970), vol. 12 no. 10.

[6] Friberg, P. O., *Coupled Vibrations of Beams – An Exact Dynamic Element Stiffness Matrix*, International Journal for Numerical Methods in Engineering (1983), vol. 19, pp. 479–493.

[7] Augustyn, E. & Kozień, M. S., *Analytical Solution of Excited Torsional Vibrations of Prismatic Thin–Walled Beams*, Journal of Theoretical and Applied Mechanics (2015), **53** no. 4, pp. 991–1004.

[8] Narayanan, S. & Malik, A. K., *Free Vibrations of Thin–Walled Open Section Beams with Constrained Damping Treatment*, Journal of Sound and Vibration (1981), **74**(3), pp. 429–439.

[9] Jansen, J. D. & van den Steen, L., *Active Damping of Self–Excited Torsional Vibrations in Oil Well Drillstrings*, Journal of Sound and Vibration (1995), **179**(4), pp. 647–668.

[10] Augustyn, E. & Kozień, M. S., *A Study on Possibility to Apply Piezoelectric Actuactors for Active Reduction of Torsional Beams Vibrations*, Acta Physica Polonica (2014), Vol. 125.

[11] Augustyn, E. & Kozień, M. S., *FEM Analysis of Active Reduction of Torsional Vibrations of Clamped–Free Beam by Piezoelectric Elements for Separated Modes*, Archives of Acoustics (2014), Vol. 39 no. 4, pp. 639–644.

[12] Christiano, P. & Salmela, L., *Frequencies of Beams with Elastic Warping Restraint*, Journal of the Structural Division (1971), **97** no. 6, pp. 1835–1840.

[13] Høgsberg, J., Hoffmeyer, D. & Ejlersen, C., *Damping of Torsional Beam Vibrations by Control of Warping Displacement*, Journal of Vibration and Acoustics (2016), vol. 138.

[14] Vlasov, V. Z., *Thin–walled Elastic Beams*, (1961) Israel Program for Scientific Translations, Jerusalem.

[15] Høgsberg, J. & Krenk, S., *Analysis of Moderately Thin–Walled Beam Cross–Sections by Cubic Isoparametric Elements*, Computers and Structures (2014), **134**, pp. 88–101.

C2

Active Warping Control for Damping of Torsional Beam Vibrations

David Hoffmeyer and Jan Høgsberg

IX ECCOMAS Thematic Conference on Smart Structures and Materials,

July 8-11, 2019

IX ECCOMAS Thematic Conference on Smart Structures and Materials
SMART 2019
A. Benjeddou, N. Mechbal and J.F. Deü (Eds)

ACTIVE WARPING CONTROL FOR DAMPING OF TORSIONAL BEAM VIBRATIONS

David Hoffmeyer* **& Jan Høgsberg**

Department of Mechanical Engineering, Technical University of Denmark
Nils Koppels Allé, building 404, DK-2800 Kongens Lyngby, Denmark
e-mail: davhoff@mek.dtu.dk, jhg@mek.dtu.dk, www.dtu.dk

Key words: Torsional beam vibrations, structural dynamics, warping, active control, position feedback, finite element method.

Abstract. This paper considers damping of torsional beam vibrations by active control of the axial warping displacements. A beam element with active positive position feedback (PPF) is set up with an additional flexibility parameter. This arises from partial restraining of warping caused by discrete actuators. The flexibility lowers the frequency associated with an infinite actuator gain and thereby the attainable damping ratio. It is shown how it furthermore affects the stability limit. Results are compared with three-dimensional finite element results, with multiple actuators acting on an end cross-section of the beam. The accuracy of the beam model is justified by an example which shows that substantial damping ratios may be achieved by active warping control.

1 INTRODUCTION

Slender structures like long bridge decks, aircraft wings, wind turbine blades and general thin-walled beams may be prone to vibrations due to loads like wind, traffic etc. If the loads act with an eccentricity relative to the shear center or if the cross-section lacks double symmetry, torsional vibrations may be induced. For some structures the aerodynamic instability phenomenon flutter may occur where flexural and torsional vibrations couple. To potentially avoid flutter or to reduce fatigue stresses, structural mass or accelerations, supplemental damping may be required.
Torsion of thin-walled beams generates out-of-plane, axial warping displacements that are often significant at the boundaries of beams with open cross-sections. Thus, for these types of thin-walled beams the restraining of warping results in an often considerable increase in the natural frequency and change in vibration characteristics as described by Gere [1]. The localized effect of restrained warping is used in [2] to introduce a substantial amount of supplemental damping by applying an energy dissipating boundary condition. In [3] discrete viscous dampers constituting a pure bimoment are placed on the beam cross-section of a three-dimensional finite element model, showing convincing agreement with the governing transcendental equation.

For beams with closed cross-sections or when torsion couples with flexure, viscous dampers may not be sufficient or even practically applicable. Thus, in the present work an active damping concept is used for damping of pure torsional vibrations. A positive position feedback (PPF) [4] signal is passed by a sensor through a simple linear filter to an actuator which produces an active force. The damping

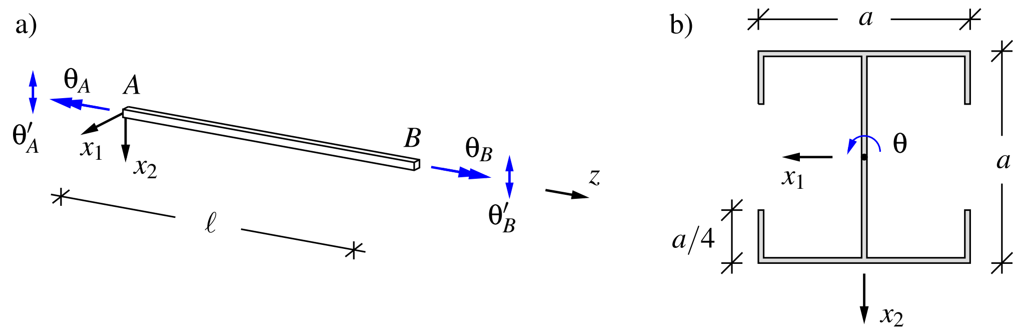

Figure 1: a) beam with degrees-of-freedom and b) thin-walled cross-section with coordinate system.

concept is applied with a beam element and compared with a full three-dimensional finite element (FE) analysis. In an actual structure the actuators are placed as discrete actuators on a beam cross-section, thus only partially restraining the warping. This is associated with an additional flexibility that lowers the frequency obtained when the actuators completely lock - which in control theory typically is refered to as a zero - and thereby also the maximum damping ratio determined as the relative imaginary part of the natural frequency. This flexibility is incorporated into the beam element as a Maxwell-type boundary condition, and is calibrated by dedicated finite element results. The system is solved in state-space form and it is shown that substantial damping ratios may be obtained for the lowest torsional mode. For the position feedback the control gain is limited by stability yielding a gain as derived in [5]. At a certain point the actuator will eliminate the structural stiffness at the location of the actuator and the response becomes unbounded. This limit, however, is based on a static condition and it is shown how the additional flexibility from restraining warping partially affects this limit.

2 STRUCTURAL EQUATIONS

In this section the governing structural equations are presented. First the differential equation governing pure torsion is presented and then the beam is discretized with beam elements, resulting in the governing multi-degree-of-freedom equations.

2.1 Uncoupled torsional vibrations

Consider the beam in Fig. 1a with length ℓ, longitudinal axis z and transverse axes $\{x_1,x_2\}$. For a cross-section like the one in Fig. 1b with double symmetry, the elastic and shear centers coincide and the torsional and flexural vibrations thereby uncouple. The rotation with respect to the shear center is denoted $\theta(t,z)$ and the warping intensity is the spatial derivative of the rotation $\theta'(t,z)$. The differential equation governing pure torsional vibrations may be derived as [1, 3, 6],

$$EI_\psi\theta''''(t,z) - GK\theta''(t,z) - \rho I_\psi\ddot{\theta}''(t,z) + \rho J\ddot{\theta}(t,z) = 0 \tag{1}$$

where E is Young's modulus, G is the shear modulus, ρ is the mass density, I_ψ is the warping moment of inertia, K is the torsion stiffness parameter, $(\,)' = \partial(\,)/\partial z$ denotes partial differentiation with respect to z and $(\dot{\,}) = \partial(\,)/\partial t$ denotes partial differentiation with respect to t. The third term is the inertia associated with the axial warping [6] and is often neglected due to its limited importance.

2.2 Discretization with beam elements

The torsion problem is now implemented in a finite element setting and the structure is discretized with beam elements. As pure torsional vibrations are considered the beam element only contains the two torsional degrees-of-freedom as depicted in Fig. 1a, that is the rotation and warping intensity. The four degrees-of-freedom for the beam element are interpolated as,

$$\theta = \mathbf{N}\left[\theta_A\,,\,\ell\theta_A'\,,\,\theta_B\,,\,\ell\theta_B'\right]^T \tag{2}$$

where the displacement interpolation array $\mathbf{N}$ contains the Hermitian shape functions,

$$\mathbf{N} = \left[2s^3-3s^2+1\;,\;s(s-1)^2\;,\;-2s^3+3s^2\;,\;s^2(s-1)\right] \tag{3}$$

where $s = z/\ell$ is a local element coordinate. The element stiffness matrix $\mathbf{K}$ and mass matrix $\mathbf{M}$ are associated with the elastic and kinetic energy respectively. Setting up the energies and assuming a prismatic beam element leads to the explicit expression for the stiffness matrix

$$\mathbf{K} = EI_\psi\ell^{-3}\begin{bmatrix} 12 & & & \\ 6 & 4 & & \\ -12 & -6 & 12 & \\ 6 & 2 & -6 & 4 \end{bmatrix} + GK\ell^{-1}\frac{1}{30}\begin{bmatrix} 36 & & & \\ 3 & 4 & & \\ -36 & -3 & 36 & \\ 3 & -1 & -3 & 4 \end{bmatrix} \tag{4}$$

with contributions from homogeneous and inhomogeneous torsion through GK and EI_ψ respectively. The mass matrix takes a similar form,

$$\mathbf{M} = \rho J\ell\frac{1}{420}\begin{bmatrix} 156 & & & \\ 22 & 42 & & \\ 54 & 13 & 156 & \\ -13 & -3 & -22 & 4 \end{bmatrix} + \rho I_\psi\ell^{-1}\frac{1}{30}\begin{bmatrix} 36 & & & \\ 3 & 4 & & \\ -36 & -3 & 36 & \\ 3 & -1 & -3 & 4 \end{bmatrix} \tag{5}$$

The first term in (5) contains the torsional inertia and the second term contains the warping inertia. The latter is usually of limited importance and often discarded but may in this format easily be implemented through the submatrices. The local elements are easily assembled and transformed to a global structure [7].

2.3 Multi-degree-of-freedom system

As the model is discretized with beam elements the equations of motion are given in terms of the displacement vector $\mathbf{q}(t)$ of the linear system and the corresponding stiffness matrix $\mathbf{K}$ and mass matrix $\mathbf{M}$ from Section 2.2. Neglecting any inherent structural damping the system has the general form,

$$\mathbf{M}\ddot{\mathbf{q}}(t) + \mathbf{K}\mathbf{q}(t) = -\mathbf{w}B_d(t) \tag{6}$$

where $B_d(t)$ represents the effect of the external actuator on the system in the form of a bimoment [6]. The corresponding connectivity vector $\mathbf{w}$ identifies the point on the structure connected to the actuator for the beam with a single actuator. The vector has the structure $\mathbf{w} = [0,...,1,...,0]^T$ with the single entry defining the degree-of-freedom associated with the actuator.
The actuator is assumed linear and collocated and may be formulated by a frequency transfer function $H(\omega)$ and gain g in the form

$$B_d(t) = gH(\omega)\mathbf{w}^T\mathbf{q}(t) \tag{7}$$

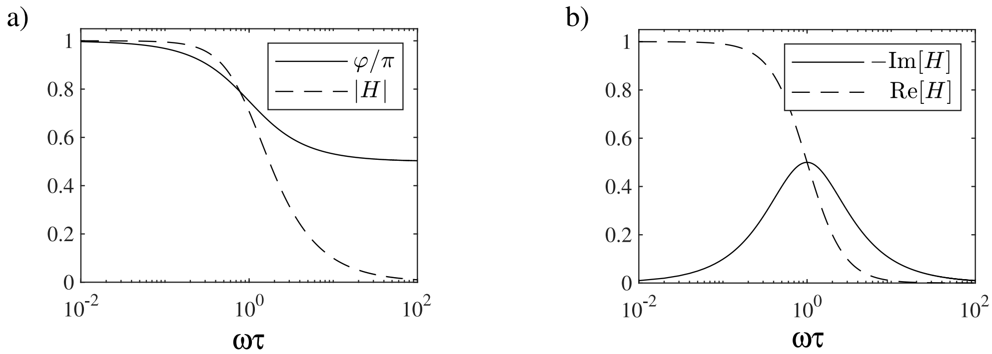

Figure 2: a) magnitude and phase angle and b) real and imaginary part of the transfer function $H(\omega)$.

The frequency function may take several different forms based on the particular control law. By introducing (7) in (6) the equations of motion may be written in the frequency domain as

$$\left(-\omega_n^2\mathbf{M}+\mathbf{K}+gH(\omega)\mathbf{w}\mathbf{w}^T\right)\tilde{\mathbf{q}}_n=\mathbf{0} \tag{8}$$

where $\widetilde{()}$ indicates the amplitude. If $g=0$ the actuator does not influence the structure and the solution to the eigenvalue problem in (8) will give real-valued solutions in form of the undamped natural frequencies $\omega_{0,n}$. If, on the other hand, $g\rightarrow\infty$ the actuator will lock and prohibit displacement at its location, whereby the solution to the eigenvalue problem provides the infinitely damped frequencies $\omega_{\infty,n}$, associated with infinite gain. The frequencies ω_0 and ω_∞ are typically denoted pole and zero respectively within control theory.

3 Active control by position feedback

Active control is now introduced by a positive position feedback. The control system detects the axial warping displacement at the end cross-section during the torsional motion, passes it through a simple linear first order filter and feeds it positively back to the structure. The position feedback is deemed appropriate as the warping displacements are small and easily measured by e.g. a piezoelectric sensor or a laser device. The filter is mathematically formulated as [8]

$$B_d(t)+\tau\dot{B}_d(t)=g\theta_g'(t) \tag{9}$$

where $\theta_g'=\mathbf{w}^T\mathbf{q}$ is the displacement at the actuator which in this case constitutes the warping intensity, B_d is the actuator force constituting a bimoment which is energy conjugate to the warping intensity and τ is a filter constant which defines the cut-off frequency at $1/\tau$. Based on the displacement $\theta_g'(t)$ the equivalent actuator force $B_d(t)$ is fed back to the system. The transfer function for the filter in (9) is hereby obtained as

$$gH(\omega)=\frac{g}{1+i\omega\tau} \tag{10}$$

The corresponding phase angle and magnitude are determined as

$$\tan\varphi=-\omega\tau \qquad , \qquad |H|=\frac{1}{\sqrt{1+(\omega\tau)^2}} \tag{11}$$

The phase angle and magnitude are seen in Fig. 2a. This specific filter ensures large damping in the low-frequency range below the cut-off frequency, while attenuating noisy high-frequency components

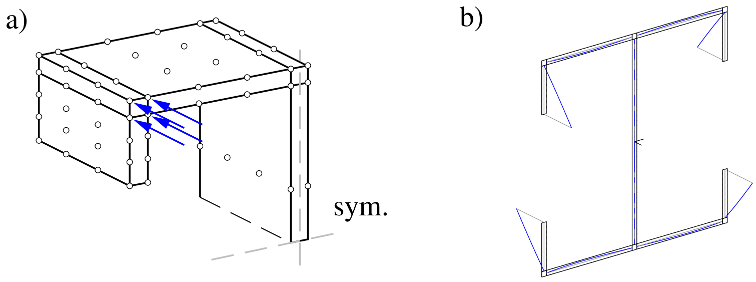

Figure 3: a) quarter cross-section discretized with isoparametric elements and with local actuators and b) altered cross-sectional warping.

which may be badly represented. By the punctured curve in Fig. 2a it is evident that this is achieved as the magnitude of the transfer function vanishes above the cut-off frequency. The major benefit of active control is the possibility of greater damping performance when the actuator leads velocity with a phase angle $\varphi > \pi/2$. Especially in the low-frequency range this filter exhibits a phase angle close to π as indicated by the solid curve, and therefore has a force component in phase with negative stiffness.
In order for the actuator to dissipate energy and not amplify the vibrations, it is required that $\mathrm{Im}[gH(\omega)] > 0$. In Fig. 2b the solid curve represent the imaginary part of the transfer function. As this is negative, it means that $g < 0$.

3.1 Warping-restrained flexibility

In practice warping control may be realized by axial actuators, acting on the cross-section as shown in Fig. 3a. In a situation with concentrated axial actuators applied at a cross-section the actuators will only fully restrain the warping displacements at the location of the actuators. At infinitely high gain, i.e. when $g \to \infty$, the axial movement at the actuator location will be completely prevented. However, the cross-section may still able to warp in between the actuators and leave an altered warping function as illustrated in Fig. 3b. This is associated with an additional flexibility compared to a fully restrained cross-section [3]. At vanishing damping ($g = 0$) the additional flexibility must however disappear. This additional flexibility may therefore be modelled as a spring in series with the actuator, as seen in Fig. 4. The warping works through the gradient of the angle of twist and therefore so does the spring. It is, however, an artificial spring as it is not physically present, but merely describes the additional flexibility due to the partial warping of the cross-section for $g > 0$. Thereby it may conveniently be modelled as a Maxwell-type boundary condition. The total gradient of the angle of twist, θ'_d, is the sum of the contribution from the actuator and spring as seen in Fig. 4,

$$\theta'_d(t) = \theta'_k(t) + \theta'_g(t) \tag{12}$$

where it works through the actuator bimoment B_d. The bimoment produced by the spring is

$$B_k(t) = k\theta'_k(t) \tag{13}$$

and the bimoment produced by the actuator is given by (9). Introducing (9) and (13) into (12) yields the modified control equation, to be used for calibration of g and identification of the stability limit,

$$\left(\frac{1}{g} + \frac{1}{k}\right) B_d(t) + \frac{\tau}{g}\dot{B}_d(t) = \theta'_d(t) \tag{14}$$

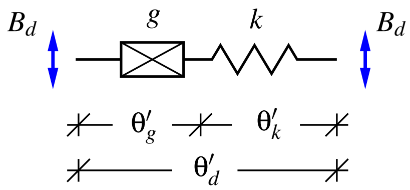

Figure 4: Maxwell-type boundary condition with an active element with gain g in series with a spring with stiffness k.

The determination of k requires in this case knowledge about the actual structure either from a full three-dimensional finite element model, from experiments or from real measurements. The stiffness k in the flexibility format reduces the infinitely damped frequency ω_∞ as the cross-section is now able to warp in between the actuator locations. However, due to the active nature of the actuator there will be a stability limit, see Section 3.3, where the response becomes unbounded. In the complex plane, however, the root locus will trace towards the correct infinitely damped frequency, as the controller equation (14) in the limit describes only the additional flexibility,

$$\left(\frac{1}{g}+\frac{1}{k}\right)B_d(t)+\frac{\tau}{g}\dot{B}_d(t)=\theta'_d \quad \rightarrow \quad B_d(t)=k\theta'_d \qquad \text{for} \quad g\rightarrow\infty \tag{15}$$

This means that the structural equations are merely supplemented with a spring, incorporated in flexibility format, when establishing the state-space equations in the following section. The stiffness k is calibrated in the unstable situation where $g\rightarrow\infty$, but this is equivalent with a situation where the actuators are replaced with supports and may thus be used for calibration.

3.2 State-space formulation

The properties of the dynamic system with damping is conveniently demonstrated in the frequency domain. The equations of motion are therefore set up in a state-space format including the feedback force from (14). With the state-vector $\mathbf{z}(t)=[\mathbf{q}(t)\,,\dot{\mathbf{q}}(t)\,,B_d(t)]^T$ the system is

$$\frac{d}{dt}\begin{bmatrix}\mathbf{q}(t)\\ \dot{\mathbf{q}}(t)\\ B_d(t)\end{bmatrix}=\begin{bmatrix}\mathbf{0} & \mathbf{I} & \mathbf{0}\\ -\mathbf{M}^{-1}\mathbf{K} & \mathbf{0} & -\mathbf{M}^{-1}\mathbf{w}\\ g/\tau\mathbf{w}^T & \mathbf{0} & -g/\tau\left(\frac{1}{g}+\frac{1}{k}\right)\end{bmatrix}\begin{bmatrix}\mathbf{q}(t)\\ \dot{\mathbf{q}}(t)\\ B_d(t)\end{bmatrix} \tag{16}$$

where $\mathbf{I}$ is the identity matrix. The presence of the actuator leads to generally complex-valued solutions of ω,

$$\omega_n=|\omega_n|\left(\sqrt{1-\zeta_n^2}+i\zeta_n\right) \tag{17}$$

where n denotes the various eigensolutions. The damping ratio is given by the imaginary part of (17) as

$$\zeta_n=\frac{\mathrm{Im}[\omega_n]}{|\omega_n|} \tag{18}$$

The mode shapes obtained from (16) are in general also complex, with the real part representing the physical vibration form and the imaginary part representing the spatial phase shift due to the presence of the energy dissipating actuator.

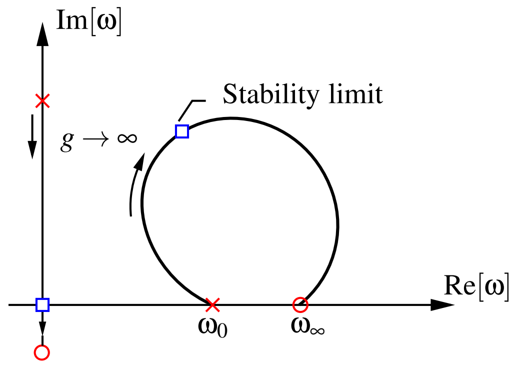

Figure 5: Root locus and indication of the stability limit when the purely imaginary eigenvalue becomes negative.

3.3 Stability and gain limit

When solving (16) varying the gain in the interval $g \in [0; \infty[$ the damped frequency will trace a root locus in the complex plane between the undamped frequency ω_0 and the infinitely damped frequency ω_∞ as shown in Fig. 5. However, as mentioned in Section 3.1 after a certain gain the response becomes unbounded. With a single actuator present, a single eigenvalue will be purely imaginary. Instability occurs when this eigenvalue becomes zero. In order for the response not to become unbounded the stability of the system must therefore be considered. This is mainly to set a limit for the gain g. The stability of the system may be checked with the Routh-Hurwitz criterion. For larger systems this typically requires determination of the Routh arrays and may not be convenient to determine an explicit limit for the gain. An alternative is to write the full system consisting of the structural equations (6) and the controller equation (14) in a block format. The structural equations and controller equation are pre-multiplied with $-g\nu^{-1}$ where $\nu = \left(1 + \frac{g}{k}\right)$, and the original structural displacement vector $\mathbf{q}$ is replaced by the modified set of variables in $\mathbf{q}^* = -g\nu^{-1}\mathbf{q}$. The equations then take the form

$$\begin{bmatrix} \mathbf{M} & \mathbf{0} \\ \mathbf{0} & 0 \end{bmatrix} \begin{bmatrix} \ddot{\mathbf{q}}^* \\ \ddot{B}_d \end{bmatrix} + \begin{bmatrix} \mathbf{C} & \mathbf{0} \\ \mathbf{0} & -g\nu^{-2}\tau \end{bmatrix} \begin{bmatrix} \dot{\mathbf{q}}^* \\ \dot{B}_d \end{bmatrix} + \begin{bmatrix} \mathbf{K} & -g\nu^{-1}\mathbf{w} \\ -g\nu^{-1}\mathbf{w}^T & -g\nu^{-1} \end{bmatrix} \begin{bmatrix} \mathbf{q}^* \\ B_d \end{bmatrix} = \begin{bmatrix} \mathbf{0} \\ 0 \end{bmatrix} \tag{19}$$

It is noted that if $|g| < k$ then $\nu > 0$. The mechanical energy is defined by the first and last matrix. The equivalent mass matrix is always positive semi-definite, and as $\tau > 0$ the equivalent damping matrix will be positive definite if the original structure has positive definite damping and is otherwise positive semi-definite. The stability is therefore entirely governed by the equivalent stiffness matrix and the corresponding reduction in stiffness caused by the actuator with the added warping-restrained flexibility. The potential energy associated with the stiffness matrix can be expressed as

$$V_e = \begin{bmatrix} \mathbf{q}^{*T} & B_d \end{bmatrix} \begin{bmatrix} \mathbf{K} & -g\nu^{-1}\mathbf{w} \\ -g\nu^{-1}\mathbf{w}^T & -g\nu^{-1} \end{bmatrix} \begin{bmatrix} \mathbf{q}^* \\ B_d \end{bmatrix} \tag{20}$$

After some rearranging it takes the form

$$\begin{aligned} V_e = \tfrac{1}{2}\mathbf{q}^{*T}\left[\mathbf{K} + g\nu^{-1}\mathbf{w}\mathbf{w}^T\right]\mathbf{q}^* + \tfrac{1}{2}\left(B_d\left(g\nu^{-1}\right)^{1/2} - \left(g\nu^{-1}\right)^{1/2}\mathbf{w}^T\mathbf{q}^*\right)^2 \\ - B_d g\nu^{-1} B_d - \mathbf{q}^{*T} g\nu^{-1}\mathbf{q}^* \end{aligned} \tag{21}$$

The time derivative of this functional is given by the second matrix in (19) as

$$\dot{V}_e = -\left[\dot{\mathbf{q}}^{*T}\mathbf{C}\dot{\mathbf{q}}^* - \dot{B}_d g \nu^{-2}\tau \dot{B}_d\right] \leq 0 \tag{22}$$

The second term in (21) is a quadratic form and thus always positive, while the third and fourth terms are also positive as $g < 0$. Stability is therefore governed by the first term of which the matrix must be positive definite for the combined system to be stable. If the matrix becomes singular it corresponds to the stiffness component of the actuator eliminating the structural stiffness at the location of the actuator and instability occurs. This corresponds to the requirement

$$\det\left(\mathbf{K} + g\nu^{-1}\mathbf{w}\mathbf{w}^T\right) > 0 \tag{23}$$

Thus the matrix in the parentheses must be invertible and the limit of the gain, g_{stab}, may be found by considering the invertibility of the matrix. The result follows from the Sherman-Morrison formula [9] as

$$\left(\mathbf{K} + g\nu^{-1}\mathbf{w}\mathbf{w}^T\right)^{-1} = \mathbf{K}^{-1} - g\nu^{-1}\mathbf{K}^{-1}\mathbf{w}\left(1 + g\nu^{-1}\mathbf{w}^T\mathbf{K}^{-1}\mathbf{w}\right)^{-1}\mathbf{w}^T\mathbf{K}^{-1} \tag{24}$$

When rigid body motion is accounted for, the stiffness matrix will be fully positive definite. Thus, if the term in the parenthesis on the right side of (24) becomes zero, the term may not be inverted. This determines the gain limit as

$$\frac{1}{g_{\text{stab}}} = -\mathbf{w}^T\mathbf{K}^{-1}\mathbf{w} - \frac{1}{k} \tag{25}$$

The above expression leaves a direct way of determining the maximum gain, which is at the same time seen to be negative. A gain that exceeds the above limit will result in an unbounded response.

4 Comparison with a 3D FEM model

The beam model is compared with a full three-dimensional FE model with isoparametric elements. The elements used are bi-cubic-linear elements for flange parts and bi-linear-cubic elements for corners and junctions. For details on the elements and discretization of the beam see [3]. The beam is discretized with 30 length-wise elements, half of them being concentrated over $\ell/25$ of the beam near the end, and a single bi-cubic-linear element per flange part as in Fig. 3a. In the three-dimensional model, actuators are applied in the corners as in Fig. 3a, and as they are placed asymmetrically they are balanced according to [3, 10]. Thus, m actuators are present and the feedback filter now contains several equations written in vector format as

$$\mathbf{f}_d + \tau\dot{\mathbf{f}}_d = \mathbf{G}\mathbf{W}^T\mathbf{q} \tag{26}$$

This equation resembles (9) but without the flexibility k. In order not to damp other modes than those associated with torsion, each connectivity vector $\mathbf{w}_j$ contains contributions from exactly four actuators constituting a pure bimoment. These four actuators are placed symmetrically in the corners with respect to the principal axes of the cross-section in Fig. 1, and thus only one of the four actuators in each corner as indicated in Fig. 6b enters each connectivity vector. Thus the structure is $\mathbf{w}_j = [0, \ldots, -\sqrt{1/4}, \sqrt{1/4}, -\sqrt{1/4}, \sqrt{1/4}, \ldots, 0]^T$. The collective array $\mathbf{W} = [\mathbf{w}_1, \mathbf{w}_2, \ldots, \mathbf{w}_{m/4}]$ contains $m/4$ connectivity vectors and $\mathbf{G} = \text{diag}[g_1, g_2, \ldots, g_{m/4}] = g^{3\text{D}}\,\text{diag}[\alpha_1, \alpha_2, \ldots, \alpha_{m/4}]$ is a diagonal matrix with all gains. The actuators are in this case not balanced equally due to the asymmetric location of the actuators in Fig. 6. Balancing factors α_j are therefore introduced according to [3] and $g^{3\text{D}}$ is a common gain. The stability requirement is derived in the same way as for the beam model with

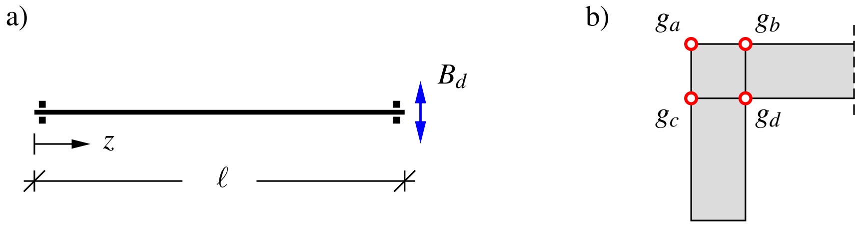

Figure 6: a) 'simple-simple' beam with damping treatment at $z = \ell$ and b) order of actuator gains at cross-section corner.

a single actuator, but the final condition is not an explicit expression for the gain. The following matrix may be derived,

$$\mathbf{H} = \mathbf{G}^{-1} + \mathbf{W}^T\mathbf{K}^{-1}\mathbf{W} \tag{27}$$

which is $m/4 \times m/4$ and will be negative definite for small values of g^{3D} and thereby have all negative eigenvalues $\lambda_i < 0$. Instability occurs exactly when the first eigenvalue of $\mathbf{H}$ becomes positive. As the beam model and three-dimensional model are inherently different, the gain at instability will not be the same as the actuators are tuned differently. However, by setting up the virtual work produced by the actuator in the beam model and the actuators in the three-dimensional model, a convertion factor can be derived as

$$g^{3D} = \frac{g}{\sum_j^m \alpha_j \psi_j^2} \tag{28}$$

where ψ_j is the sector-coordinate of the j'th actuator. In the next section it will be shown that instability occurs at the same frequency and damping ratio in the two models.

5 Damping of a 'simple-simple' beam

The accuracy of the beam model is now demonstrated by investigating the damping properties of the lowest torsional mode of the 'simple-simple' beam with length ℓ as shown in Fig. 6a. The support conditions restrain rotation but allow warping. The cross-section of the beam is shown in Fig. 1 and has thickness $t = a/40$, Young's modulus $E = 210$ GPa, Poisson's ratio $\nu = 0.3$ and density $\rho = 7850$ kg/m^3. The ratio between the cross-section height and the length of the beam is $\ell/a = 30$ and $a = 1$ m, for which the inherent distortion of the cross-section is minimal [3]. The beam model is compared with results from a three-dimensional finite element analysis. In this finite element model four actuators are placed at each corner as shown for a single corner in Fig. 6b, and balanced according to Table 1. This is done in order to avoid unnecessary distortion of the cross-section. For the beam model the first objective is to adjust the infinitely damped frequency ω_∞ to account for the partial restrainment of the warping at $z = \ell$. This is done by performing a real analysis of the 3D FE model by solving the full system in (16) with $g \to \infty$ and afterwards calibrating the flexibility parameter k by a numerical search routine to ensure that the frequency locus terminates at the correct frequency. To create the root locus the gain is varied in the interval $g \in [0; g_{\text{stab}}[$ where the stability limit is given by (25) or (27) for the beam and 3D model respectively.

The root loci for both models are seen in Fig. 7a. The solid line with black circles (—,○) are results from the beam model, the red markers (+) are results from the 3D model and the blue box marker (□) indicates the stability limits. Furthermore, the punctured line indicates results for the beam model with $k = \infty$ associated with complete restrainment of the warping of the entire cross-section. For comparison,

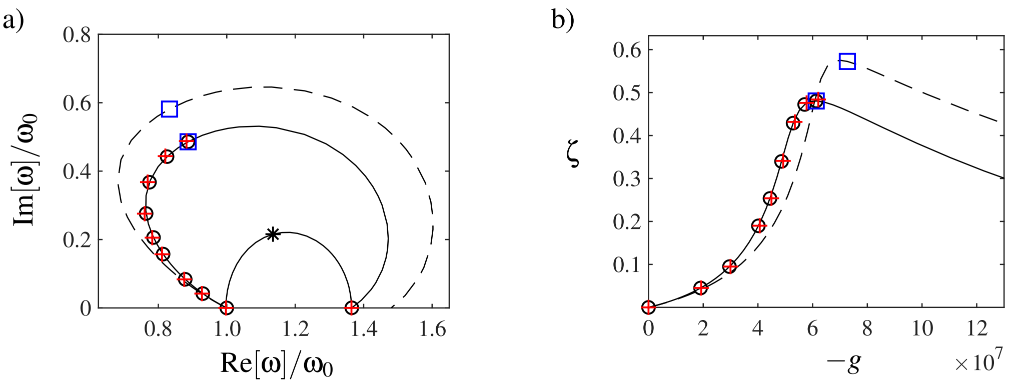

Figure 7: a) root locus and b) damping ratio for the beam analysis (—,○), FE analysis (+), gain limit (□) and $k = \infty$ (– –).

the smaller half-circular root locus is with pure viscous damping, and the asterix ($*$) indicates optimal tuning. Clearly the partial restrainment of the warping associated with the flexibility parameter k given in Table 2 results in a significant difference, lowering the relative frequency increment $(\omega_\infty - \omega_0)/\omega_0$ from 0.481 to 0.365 and the damping ratio at instability from 0.572 to 0.480 for the beam model. The damping ratio as may be seen in Fig. 7b also indicates large damping. The damping ratios at instability and the frequency increments for the two models are very similar as seen in the table, and the small deviation is due to distortional effects in the 3D model, which causes slightly different undamped frequencies ω_0. Due to the different nature of the two models and actuator configurations, the limit gains g_{stab} and g_{stab}^{3D} are not identical. The factor between these two is $g_{\text{stab}}/g_{\text{stab}}^{3D} = 50.4$ as seen in the table, and this is approximated well with (28) as seen in the last column in the table. Lastly it may be observed that the gain limit for the beam model is higher if not taking the partial warping restraining into account. This may wrongfully lead to instability.

6 CONCLUSION

In this paper a computationally efficient way of investigating the properties of damping the torsional vibrations in a simple beam with active control is considered. A beam element is set up with a single actuator acting on the warping degree-of-freedom. The actuator consists of a simple linear filter in the form of positive position feedback (PPF). It acts on the axial warping displacements, and is on an actual structure placed discretely as a set of actuators constituting a pure bimoment. This partially restrains the warping and allows for an additional flexibility in the beam model. This flexibility lowers the infinitely damped frequency and correspondingly reduces the gain limit at the point of instability. The beam model is compared with a full three-dimensional finite element model which has a set of actuators applied at discrete locations, all constituting pure bimoments. In this way only torsional modes are damped. The system equations are similar to the beam model, and instability is determined by the gain which makes the combined stiffness matrix singular. Considering a simple-simple beam as an example and plotting the root loci and damping ratios, very similar results between the two models are obtained. Only minor

Table 1: Balancing factors.

	g_a	g_b	g_c	g_d
α_j [−]	1.0	7.5	70.0	141.4

Table 2: Results of analysis.

	k	$(\omega_\infty - \omega_0)/\omega_0$	$\zeta_{\rm stab}$	$g_{\rm stab}$	$g_{\rm stab}/g^{\rm 3D}_{\rm stab}$	$\sum_j^m \alpha_j \psi_j^2$
Beam model	∞	0.481	0.572	$-7.27 \cdot 10^7$	–	–
	$3.89 \cdot 10^8$	0.365	0.480	$-6.13 \cdot 10^7$	50.4	51.0
3D model	–	0.368	0.484	$-1.22 \cdot 10^6$		

differences are observed, which may be corrected by accounting for the inherent distortion of the three-dimensional model. It is furthermore demonstrated, that the flexibility k is necessary for the beam model to reflect the 3D model. If not included, a gain exceeding the gain limit may wrongfully be chosen. The gain at instability is inherently different in the two models, but may easily be estimated considering the position of the discrete actuators. The benefits with the active filter is clear, as the beam is damped effectively, with a damping ratio of almost $\zeta = 0.5$.

REFERENCES

[1] Gere, J. M., *Torsional vibrations of Beams of Thin–Walled Open Section*, ASME Journal of Applied Mechanics (1954), vol. 21, no. 4, pp. 381-387.

[2] Høgsberg, J. & Hoffmeyer, D., *Damping of torsional beam vibrations by control of warping displacement*, Journal of Vibration and Acoustics (2016), vol. 138, DOI: 10.1115/1.4031616.

[3] Hoffmeyer, D. & Høgsberg, J., *Damping of torsional vibrations in thin-walled beams by viscous bimoments*, Mechanics of Advanced Materials and Structures (2019), DOI: 10.1080/15376494.2019.1567885.

[4] Fanson, J. L. & Caughey, T. K., *Positive position feedback control for large space structures*, AIAA Journal (1990), vol. 28, no. 4, DOI: 10.2514/3.10451.

[5] Goh, C. J. & Caughey, T. K., *On the stability problem caused by finite actuator dynamics in the collocated control of large space structures*, International Journal of Control (1985), vol. 41, no. 3, 787-802, DOI: 10.1080/0020718508961163.

[6] Vlasov, V. Z., *Thin–walled Elastic Beams*, (1961) Israel Program for Scientific Translations, Jerusalem.

[7] Cook, R. D. et. al., Concepts and Applications of Finite Element Analysis, *John Wiley and Sons*, (2002).

[8] Høgsberg, J. & Krenk, S., *Linear control strategies for damping of flexible structures*, Journal of Sound and Vibration (2006), 293, pp. 59-77, DOI: 10.1016/j.jsv.2005.09.014.

[9] Krenk, S. & Høgsberg, J., *Equal modal damping design for a family of resonant vibration control formats*, Journal of Vibration and Control (2012), vol. 19, no. 9, pp. 1294-1315, DOI: 10.1177/1077546312446796.

[10] Main, J. A. & Krenk, S., *Efficiency and tuning of viscous dampers on discrete systems*, Journal of Sound and Vibration (2005), **286**, pp. 97-122, DOI: 10.1016/j.jsv.2004.09.022.

DTU Mechanical Engineering
Section of Solid Mechanics
Technical University of Denmark

Nils Koppels Allé, Bld. 404
DK-2800 Kgs. Lyngby
Denmark

Tlf.: +45 4525 4250
Fax: +45 4525 1961

www.mek.dtu.dk

August 2019
ISBN: 978-87-7475-569-2

DCAMM
Danish Center for Applied Mathematics and Mechanics

Nils Koppels Allé, Bld. 404
DK-2800 Kgs. Lyngby
Denmark
Phone (+45) 4525 4250
Fax (+45) 4525 1961

www.dcamm.dk

DCAMM Special Report No. S263

ISSN: 0903-1685